

PROBING DYNAMICAL QUANTITIES IN THE 2D
FERMI-HUBBARD MODEL WITH QUANTUM GAS
MICROSCOPY

PETER THOMAS BROWN

A DISSERTATION
PRESENTED TO THE FACULTY
OF PRINCETON UNIVERSITY
IN CANDIDACY FOR THE DEGREE
OF DOCTOR OF PHILOSOPHY

RECOMMENDED FOR ACCEPTANCE
BY THE DEPARTMENT OF
PHYSICS
ADVISER: PROFESSOR WASEEM BAKR

SEPTEMBER 2019

© Copyright by Peter Thomas Brown, 2019.

All rights reserved.

Abstract

The recent development of fermionic quantum gas microscopes has enabled studies of cold atom Fermi-Hubbard systems with single-site resolution, revealing a variety of interesting phenomena in regimes which are difficult to access with existing theory techniques. The Fermi-Hubbard model is of great intrinsic interest as a toy model for strongly correlated quantum physics, and may also describe the phenomenology of high-temperature superconducting materials such as the cuprates. Most experimental studies of cold atom Fermi-Hubbard systems have focused on probing equal-time spin and density correlations, but a wide region of the low temperature phase diagram may be better understood by exploring dynamical (unequal-time) properties. In this thesis, we first report on an experiment exploring the response of antiferromagnetic spin correlations to a magnetic field, and find evidence for short-range canted antiferromagnetic spin correlations. Then we turn our focus to probing response functions associated with unequal-time correlations relevant for understanding the pseudogap and strange metal regimes of Fermi-Hubbard systems. First, we describe the development of a technique to measure microscopic diffusion, and hence resistivity, in doped Mott insulators. We find that this resistivity exhibits a linear dependence on temperature and violates the Mott-Ioffe-Regel limit, two signatures of strange metallic behavior. Next, we report on the development of angle-resolved photoemission spectroscopy (ARPES) compatible with quantum gas microscopy and its application to studying pseudogap physics in an attractive Fermi-Hubbard system across the BEC-BCS crossover, setting the stage for future studies of the pseudogap regime in repulsive Hubbard systems.

Acknowledgements

Thank you first to my adviser, Waseem Bakr. Waseem has been always willing to share his time, ideas, and outstanding problem solving ability with me. I have been consistently amazed at how he sees the way through or around experimental problems, sometimes before I have even understood the difficulty. It has been a privilege to work with and learn from Waseem, and many of the skills I have developed as a scientist I owe to him.

To Debayan Mitra. Debayan and I learned about vacuum, lasers, and optics and shared the excitement of achieving a first MOT, creating a molecular BEC, and building a quantum gas microscope together. To Stanimir Kondov, who taught us about atomic physics, mechanical design, and how to have fun. To Akira Kondova. To Peter Schauß who joined us just as the experiment was up and running and taught me so much about physics, computing, and microscopy. It was fun coming up with crazy ideas for experiments — and many of Peter’s actually worked! To Elmer Guardado Sanchez, who has taught me an appreciation for the finer things in life, such as the Hamilton soundtrack. It has been great fun running experiments together, and I think we have made a good team. To Ben Spar, the next generation on the lithium machine. I hope the experiment treats you as well as it has treated me. To Lysander Christakis and Jason Rosenberg. I have enjoyed talking physics and trying to help you avoid some of our early mistakes with the lithium experiment. Good luck with the molecule experiment.

To David Huse, who has been an invaluable source of physics advice and contributed in one way or another to almost every project I have worked on. David always cuts to the heart of the matter and has reframed many problems for us with a brief discussion. To Mike Romalis and the members of the Romalis group, who have contributed to the friendly atmosphere with weekly joint group lunches. In particular Junyi Lee, Vito Lucivero, Wonjae Lee, Nezih Dural, Atta Almasi, William Terrano,

Mark Limes, Morgan Hedges, Merideth Frey, Haifeng Dong, Dong Sheng, Mark Smiciklas, and many others. To Sanfeng Wu for agreeing to be a reader for this thesis and providing valuable perspective.

To the physics department staff who make it a pleasure to be in Jadwin Hall, including Antonia Sarchi, Darryl Johnson, Angela Lewis, Ted Lewis, Julio Lopez, Karen Kelly, Regina Savadge, Kate Brosowsky, and others. Thank you to Geoff Gettelfinger, Bob Rickett, Chris Jones, Ralph Searfoss and other members of the facilities staff who have played a tremendous role in keeping our experiment running.

To my friends in the department, particularly Tom Hazard and Mallika Randeria for many good times, great hiking, and good cooking. Also to Junyi Lee, Laura Chang, and many others. To the members of our short lived condensed matter journal club, Tong Gao, Wudi Wang, Yonglong Xie, Tom, and Mallika. We certainly had fun, and maybe learned a little physics while we were at it.

To Dave Schuster and the members of his group at Chicago who first introduced me to physics research. I had no idea experimental work could be so much fun! To Ge Yang who inspired my initial interest in programming and physics simulations.

To my parents, Sue and Tom, for their unwavering love and support. You have always encouraged me to pursue my interests and to above all do my best. I would never have made it this far without you. To my brother, Bryan, your enthusiasm and passion are an inspiration to me. I always enjoy hearing about whatever mathematical idea you are thinking about. To my uncle John, I have enjoyed learning about radio and electronics from you. I don't know if I appropriately venerate vacuum tubes, but I am developing a certain reverence. To my wife, Isabel, you have been my rock these past six years. Your love, support, and understanding sustain and motivate me. I am looking forward to our next adventure together!

To the many other friends and teachers from Rockhurst, Chicago, and elsewhere who have inspired me to learn, to seek, and to discover.

To my family.

Contents

Abstract	iii
Acknowledgements	iv
List of Tables	xii
List of Figures	xiii
1 Introduction	1
1.1 High temperature superconductivity and the Fermi-Hubbard model .	3
1.2 Realizing the Fermi-Hubbard model in optical lattices	5
2 Apparatus and experimental techniques	10
2.1 Experimental sequence	10
2.2 Raman imaging	14
2.3 Laser frequency stabilization	19
2.4 Observables	23
2.4.1 Singles density	24
2.4.2 Single-species density	24
2.4.3 Single-species singles density	26
2.4.4 Doublon density	26
2.4.5 Derived observables	27
2.4.6 Correlator statistical uncertainty	28
2.4.7 Correlator systematic uncertainties	29

2.5	Optical lattice	31
2.5.1	Depth calibration	36
2.5.2	Phase stability	37
2.5.3	Pointing noise	39
2.5.4	Intensity noise	40
2.6	Laser intensity stabilization	43
2.7	Spatial light modulator setup	45
2.8	Bias magnetic field stabilization	48
2.9	Magnetic field gradient calibration	51
3	Theoretical background	54
3.1	The Fermi-Hubbard Model	55
3.1.1	Hubbard parameters in cold atoms and the cuprates	57
3.1.2	Particle-hole symmetry	58
3.1.3	Attractive and repulsive symmetry	59
3.1.4	SU(2) spin symmetry	61
3.1.5	SU(2) pseudospin symmetry	62
3.1.6	Higher symmetry	64
3.1.7	Connection to the $t - J$ model	64
3.1.8	Connection to the Heisenberg model	65
3.2	The non-interacting Fermi gas	66
3.2.1	Equation of state	67
3.2.2	Fermi gas correlations	69
3.2.3	Magnetism	73
3.3	The local density approximation	74
3.4	The atomic limit	76
3.5	The infinite temperature limit	77
3.6	Parameter fitting	78

3.6.1	Fermi gas	80
3.6.2	Determinantal quantum Monte Carlo	81
3.7	Linear response theory	84
3.7.1	Matsubara Green's function	88
4	Canted antiferromagnetism in a Fermi-Hubbard system	91
4.1	Magnetic fields and correlated quantum systems	93
4.2	Quantum magnetism in the Fermi-Hubbard model	96
4.3	Experimental preparation	97
4.4	Measuring spin correlations	98
4.5	Calibration of Hubbard parameters	99
4.6	Spin canting at half-filling	101
4.7	Sign change of spin z -correlation for large polarizations	105
4.8	Spin correlations versus doping	106
4.9	Singles density correlations	108
4.10	Magnetic susceptibility versus polarization	110
4.11	Relationship between susceptibility and local polarization	112
4.12	Outlook	113
5	Bad metallic transport in a Fermi-Hubbard system	114
5.1	Transport in strongly-interacting quantum systems	116
5.2	Experimental preparation	118
5.3	Density modulation decay	119
5.4	Atomic tunneling time	122
5.5	Linear response theory	124
5.6	Phenomenological hydrodynamic model	125
5.7	Determining experimental hydrodynamic parameters	127
5.8	Experimental hydrodynamic parameters versus temperature	128

5.9	Linearity	131
5.10	Thermoelectric effects	133
5.11	The Nernst-Einstein relation	134
5.12	Compressibility versus temperature	135
5.13	Experimental DC conductivity	137
5.14	Comparison of theory techniques	140
5.15	Outlook	141
6	Angle-resolved photoemission spectroscopy of a Fermi-Hubbard system	142
6.1	Photoemission spectroscopy	143
6.2	Experimental preparation	146
6.3	Radiofrequency spectroscopy	147
6.4	Band mapping simulation	150
6.5	The single-particle spectral function	151
6.6	Linear response theory	153
6.7	Spectral function trap averaging	158
6.8	LDA versus full trap simulation	160
6.9	Spectral function versus interaction	162
6.10	Dispersion from $A(k, \omega)$ versus $A_{\text{occ}}(k, \omega)$	167
6.11	Spectral function versus temperature	168
6.12	Outlook	172
7	Conclusion	173
A	Properties of 6-lithium	175
A.1	Branching ratios	175
A.2	Feshbach resonances	178

B Optical lattice	180
B.1 Band structure for an arbitrary periodic potential	180
B.2 Wannier Functions	183
B.3 Determining tight-binding parameters	185
B.4 Interactions in the tight-binding model	187
B.5 Four-fold interfering lattice	188
C Static spin structure factor	189
Bibliography	195

List of Tables

2.1	Preparation of a degenerate Fermi gas	11
2.2	Four-fold lattice Fourier components for $\alpha = 0$	33
A.1	Feshbach resonances in ${}^6\text{Li}$	179
B.1	Four-fold lattice Fourier components, arbitrary α	188

List of Figures

2.1	Single-site reconstruction algorithm visualization.	18
2.2	Laser frequency stabilization servo circuit diagram.	21
2.3	Lattice geometry at various linear polarizations.	31
2.4	Lattice potential non-idealities.	32
2.5	Tight-binding parameters versus lattice depth.	35
2.6	Lattice intensity modulation spectroscopy.	36
2.7	Lattice phase drift.	38
2.8	Lattice pointing stability.	39
2.9	Lattice intensity noise spectra.	41
2.10	Laser intensity stabilization servo circuit diagram.	44
2.11	Digital mirror device optical setup.	45
2.12	Magnetic bias field stabilization setup.	49
2.13	Magnetic field gradient calibration.	52
3.1	Non-interacting Fermi gas equation of state.	70
3.2	Non-interacting Fermi gas correlations versus temperature and filling.	71
3.3	Local density approximation in-trap profiles.	75
3.4	Fermi gas parameter fitting.	81
3.5	Fermi gas trap parameter determination.	82
3.6	DQMC parameter fitting, repulsive interaction.	83
3.7	DQMC parameter fitting, attractive interaction.	84

4.1	Site-resolved imaging of a spin-imbalanced Fermi gas in an optical lattice.	95
4.2	RF spectroscopy Hubbard interaction calibration.	100
4.3	Spin-correlation spatial anisotropy due to canting.	102
4.4	Anisotropic spin-correlation matrices due to canting.	104
4.5	Nearest-neighbor spin correlations versus doping at finite polarization.	107
4.6	Singles density correlations versus local polarization.	109
4.7	Nonmonotonic dependence of local polarization on doping at strong interactions.	110
4.8	Local polarization linearity with Zeeman field	112
5.1	Measuring charge transport in the Hubbard model.	120
5.2	Decay of density modulation pattern versus time.	121
5.3	Hubbard charge transport hydrodynamic model parameters.	129
5.4	Density modulation linearity.	131
5.5	Hubbard compressibility versus temperature.	136
5.6	Hubbard conductivity versus temperature.	138
6.1	ARPES experiment schematic.	148
6.2	Band mapping simulation.	150
6.3	Trap-averaged single-particle spectral function.	159
6.4	Occupied spectral function from LDA versus trap simulation.	161
6.5	Occupied single-particle spectral function versus interaction.	163
6.6	Energy distribution curves versus interaction.	165
6.7	Trap-average spectral function versus interaction.	166
6.8	Dispersion from occupied spectral function versus full spectral function.	167
6.9	Occupied single-particle spectral function versus temperature.	169
6.10	Energy distribution curves versus temperature.	170
6.11	Trap-average spectral function versus temperature	171

A.1	Lithium branching ratios from the $D2$ line.	176
C.1	Static spin structure factor near half-filling, $U/t = 8$.	191
C.2	Static spin structure factor versus doping, $U/t = 8$.	192
C.3	Static spin structure factor near half-filling, $U/t = 4$.	193
C.4	Static spin structure factor versus doping, $U/t = 4$.	194

Chapter 1

Introduction

The theory of quantum mechanics provides an exquisitely accurate description of microscopic physics at low energies. Part of the power of the theory lies in the ideas of superposition and entanglement, concepts which have no analog in classical physics. The price for this added descriptiveness is the necessity to simultaneously consider *every* possible state of the system in its mathematical description, which leads to an exponential growth of the size of the Hilbert space as the number of degrees of freedom is increased. This makes quantum mechanics unwieldy in situations where the full quantum nature of problem must be considered. In such cases, determining the ground state or calculating the time evolution of the system (e.g. after a quench) are both very difficult problems and cannot be solved exactly for more than a few tens of particles. In consequence, our understanding of generic interacting quantum systems is severely limited.

Strongly-correlated quantum materials are one important example of such intrinsically “quantum” problems. These systems include high- T_c superconducting cuprates, heavy-fermion metals, interacting topological quantum materials such as the fractional quantum hall state and many others that exhibit novel states of matter which are poorly understood and may lead to groundbreaking technological applications.

As there are no small parameters in these problems, there is no obvious perturbative approach to understand their properties. In particular, interaction effects must be treated on equal footing with other parameters. Strong correlation effects cause naïve mean-field approaches to break down, and there is a dearth of applicable theory techniques. In most cases such problems cannot be solved exactly, and numerics are limited to small systems due to the large Hilbert space dimensions and therefore often suffer from finite size effects.

This situation has motivated the development of *quantum simulation* as an alternate approach for understanding quantum systems. In 1982 Richard Feynman suggested that a natural way to model one quantum system is to simulate it using a “computer” built from quantum components [1]. This suggestion has motivated tremendous effort to develop fully programmable “digital” quantum computers capable of solving a large class of problems. However, for the purpose of understanding strongly correlated quantum systems, we are interested in a more restricted class of problems: finding the ground state of a given Hamiltonian and probing its properties by measuring various observables, or modeling the time evolution of an initial state under the action of the Hamiltonian.

To solve this more constrained class of problems, we emulate the Hamiltonian of interest using a synthetic quantum system. This approach, referred to as quantum simulation or “analog” quantum computing, is very useful if we choose a synthetic quantum system which is more broadly tunable, easier to study, and contains fewer extraneous degrees of freedom than the system we would like to understand. Over the past several decades, a number of synthetic quantum systems have been developed, including trapped ions, quantum dots, superconducting qubits, photonic structures, and ultracold atoms. These various approaches are complementary, and each has proven more suitable for certain applications. One outstanding challenge for many of these platforms is scalability, which is vital as studying many-body physics is

facilitated by large system sizes. However, confounding effects such as decoherence and disorder often scale unfavorably with system size.

Ultracold atoms in optical lattices have distinguished themselves as one of the few synthetic systems which can simultaneously access many-body physics and reach system sizes of thousands of particles. These systems have a number of advantages, including that they are well-isolated from the environment because they are confined using magnetic or optical traps in ultra-high vacuum (UHV) systems which routinely reach background pressures on the order of 10^{-12} torr. Optical lattices have no disorder, no impurities, and no phonons. The relative simplicity of the alkali atoms commonly employed allows parameters to be extracted from *ab initio* calculations. Furthermore, ultracold atom systems are highly tunable. The geometry and dimensionality can be adjusted by using different optical potentials. It is possible to work in 1D, 2D, or 3D and to dynamically adjust the potential landscape. Interactions between particles can be tuned by adjusting the magnetic field using Feshbach resonances.

1.1 High temperature superconductivity and the Fermi-Hubbard model

The Bardeen-Cooper-Schrieffer (BCS) theory [2] provides an effective description of most of the superconducting systems studied from Onnes' initial 1911 discovery in mercury [3] to the early 1980's. The BCS theory is a mean-field theory which describes how an arbitrarily weak attractive interaction can lead to superconductivity with a transition temperature that is exponentially small in the interaction strength, $T_c \propto \exp[-1/g(\mu)V_o]$ where $g(\mu)$ is the density of states at the Fermi level and V_o is the interaction strength. In real materials a weak attractive interaction between electrons

is mediated by electron-phonon interactions. This mechanism sets an upper limit on the superconducting critical temperature around 30 K [4].

Therefore, it was a surprise when the first superconductor with a transition temperature near 35 K, LBCO, was discovered in 1986 [5]. Soon after, the maximum observed T_c was pushed above liquid nitrogen temperatures in YBCO [6]. These high- T_c cuprate materials are anisotropic layered ceramic structures, consisting of CuO₂ planes separated by layers of dopant atoms. At filling of one electron per copper-oxygen unit cell, cuprates are antiferromagnetic Mott insulators, but upon hole doping they exhibit *d*-wave superconductivity with short coherence length [7, 8, 9]. In fact, the coherence length is shorter than the spacing between copper-oxygen planes implying that the pairing physics happens in 2D. These materials also show anomalous behavior in the normal state, including a pseudogap regime for hole-doped systems below optimal doping, and a strange metal regime characterized by unconventional transport characteristics that may imply it is not a Fermi liquid [9]. These various phenomena are not explained by the BCS theory and seem incompatible with electron-phonon coupling mediating the superconductivity.

Soon after the initial HTSC discovery, Anderson suggested that the essential physics of the cuprates might be due only to the electronic sector and captured by the 2D Fermi-Hubbard model [10]. The (repulsive) Fermi-Hubbard model was initially introduced to explain the behavior of electrons in bands composed of *d*-orbitals in transition metals, where it was argued the band widths should be narrow compared to the interaction energy, leading to enhanced interaction effects, and that on-site interaction should dominate due to local character of these orbitals [11, 12, 13, 14]. Initially a three-band Hubbard model was proposed to describe the cuprates [15, 16, 17] accounting for bands formed from the $2p_x$ and $2p_y$ orbitals in oxygen and the $3d_{x^2-y^2}$ orbital in copper, but soon after it was realized that a simplified one-band model should be sufficient [18, 19]. It is now generally believed that the essential physics of

HTSC is the physics of doping a Mott insulator [9] as described by this single-band Hubbard model.

The discovery of the HTSC materials catalyzed a tremendous amount of further experimental and theoretical studies, but progress understanding the origin of the curious phenomenology was slow and uncertain. Almost ten years after the initial discovery of cuprate HTSC's it was appropriate to write,

“ It seems that over 30000 papers have been written in the field of high T_c superconductivity since the fundamental discovery of G. Bednorz and K.A. Müller in 1986. Considering that, despite the enormous effort, progress has been little, the mean field expected information per paper is “little” /30000, Therefore it is probably not worth to read papers and it may be even less reasonable to write them. ” [20]

Almost twenty-five years later the situation is fundamentally similar in the sense that there is still no unifying theory or deep theoretical understanding of the origins of cuprate HTSC. Once more, it is still unclear how much of the HTSC physics the Fermi-Hubbard model captures in spite of the development of a variety of new analytic and numerical techniques [21]. This situation provides tremendous incentive to adopt an alternative approach – simulating the Fermi-Hubbard model using ultracold fermions in optical lattices.

1.2 Realizing the Fermi-Hubbard model in optical lattices

Since the first realization of a Bose-Einstein condensate (BEC) in a dilute atomic vapor in 1995 [22, 23] the scope of so called *ultracold atom* physics has grown enormously, progressing from studying weakly interacting quantum systems to exploring strongly correlated physics. At first glance, it is surprising that it is possible to reach

a quantum regime in these dilute systems at all. Typical densities in cold atomic gases are $n = 10^{12} - 10^{14} \text{ /cm}^3$, at least five orders of magnitude less dense than air, $n \sim 10^{19} \text{ /cm}^3$. To determine where quantum mechanical effects become important the interparticle spacing should be compared with the thermal de Broglie wavelength, $\lambda_{\text{dB}} = h/\sqrt{2\pi mk_b T}$. We define the phase space density as the ratio of these volumes, $\rho = n\lambda_{\text{dB}}^3$. For air $\lambda_{\text{dB}} \sim 0.2 \text{ \AA}$, giving a phase space density of $\rho \sim 10^{-7}$. On the other hand, typical electrons in a solid at room temperature have densities of $10^{21} - 10^{23} \text{ /cm}^3$, and $\rho = 10^2 - 10^4$ aided by the electron's small mass. Because alkali gases are metastable systems with lifetimes typically limited by three-body loss at high densities, achieving large phase space densities requires extremely low temperatures. Temperatures on the order of nanokelvin can now be routinely achieved in a variety of atomic species, including many of the alkalis, some alkaline earth elements, and some lanthanides.

Reaching a strongly correlated many-body regime with fermions has been enabled by the development of degenerate Fermi gases of dilute atomic gases [24, 25] and early work on bosons in optical lattices. This many-body regime can be contrasted with early work on BEC's, which despite their quantum nature can be described by a single macroscopic wave function and understood using the mean-field Gross-Pitaevskii equation [26]. The first proposal to realize Hubbard systems using optical lattices was introduced around the same time as the first degenerate atomic Fermi gas [27], although the study of atoms in optical lattices predates the realization of a BEC in cold atoms [28]. Hubbard systems were first realized using bosons, where the study of the superfluid (SF) to Mott insulator (MI) transition in the Bose-Hubbard model firmly established the possibility of reaching a many-body regime in cold atom experiments [29, 30, 31, 32, 33].

Early suggestions that ultracold fermions in optical lattices could be used as a tool to address outstanding questions about the Fermi-Hubbard model came around

the same time as the early Bose-Hubbard experiments [34]. A 3D Fermi-Hubbard system was first realized in 2005 [35], and early experiments focused on thermometry [36, 37, 38] and found evidence of Mott insulating behavior [39, 40, 41]. Later experiments explored local spin correlations [42, 43], large spin degeneracy [44, 45], hexagonal lattices [46, 47], the equation of state [48], and antiferromagnetism [49, 50]. Other experiments studied 2D Fermi-Hubbard systems, mapping the equation of state [51], exploring short-range correlations [52, 53], and observing evidence of antiferromagnetic correlations [54, 55].

The development of the quantum gas microscope (QGM) [56, 57] expanded the capabilities of cold atom experiments by enabling lattice site resolved measurements of atomic density distributions and correlations. The QGM fluorescence imaging techniques (see section 2.2) give exquisite signal-to-noise compared with other common approaches, and enabled the first studies of single-layer 2D systems. QGM's were first developed for bosonic atoms, where they reexamined the SF to MI transition in the 2D Bose-Hubbard model [58] among many other experiments [59]. The development of QGM's for the fermionic alkali atoms ^6Li [60, 61] and ^{40}K [62, 63, 64] in 2015 catalyzed rapid progress in studying static properties of Fermi-Hubbard systems, including observation of the Mott insulating state [65, 66] and antiferromagnetic spin correlations in 1D [67] and 2D [68, 69].

This work has been followed by various other probes of static properties of the Fermi-Hubbard model, including observation of canted antiferromagnetic spin correlations (chapter 4 and reference [70]), charge-density wave correlations in the attractive model [71], magnetic polarons in the doped repulsive model [72], development of techniques aiming to reach lower temperatures [73, 74], and further exploration of spin correlations to test parton theories of the doped Mott insulating state [75]. The static properties of the 1D model have been extensively studied, including observations of

spin-charge separation by measuring string correlations [76] and incommensurate antiferromagnetism [77].

In contrast, the dynamical properties of Fermi-Hubbard systems have received much less experimental attention. Experiments without microscopes have largely explored far-from-equilibrium settings [78, 79, 80, 81], however near-equilibrium dynamics is also extremely interesting. Near-equilibrium experiments can be described in terms of linear response functions which are related to unequal-time correlation functions (see section 3.7). These functions provide a wealth of detail about a given many-body system, but are often more difficult to calculate in theory than static correlators and therefore are not accessible at the same low temperatures. This opens the possibility that quantum simulators may provide experimental results that can test different theoretical approximations or distinguish between competing theories. However the variety of techniques available for measuring dynamical quantities in QGM experiments is rather limited.

In this thesis, we develop several new tools to study dynamical quantities in the Fermi-Hubbard model. In particular, in chapter 5 we develop a technique to measure the charge diffusion constant and resistivity of a 2D Fermi-Hubbard system [82]. In chapter 6 we develop a technique which is analogous to angle-resolved photoemission spectroscopy (ARPES) and apply this to measure the occupied single-particle spectral function in an attractive Fermi-Hubbard system [83]. These techniques, in combination with other work studying the optical conductivity [84], spin-diffusion [85], and hole dynamics [86], constitute an emerging toolkit for quantum gas microscopy which realizes some of the promises of quantum simulation by probing regimes inaccessible to theory.

The major impediment to fully mapping the phase diagram of the Fermi-Hubbard model using ultracold atom experiments is the achievable temperature. The extremely low absolute temperatures are counterbalanced by correspondingly low Fermi temper-

atures due to the dilute nature of these systems. Current Fermi-Hubbard experiments reach values of $T/T_f = 0.05 - 0.1$, which is comparable to the value for electron systems at 10^3 K. The very low absolute energy scales required in cold atoms are the penalty for the large characteristic length scales and slow dynamics which make them so attractive to study. Already at current temperature scales, cold atom experiments can explore dynamical quantities which are poorly understood theoretically. Nevertheless, achieving the ambitious goal of “solving” the Fermi-Hubbard model using quantum simulation will require reaching lower temperatures. This aim may not be as daunting as it sounds — a factor of ~ 10 decrease in temperature is all that is required.

Chapter 2

Apparatus and experimental techniques

The experiments discussed in this thesis were carried out with an apparatus for producing a degenerate Fermi gas of 6-lithium in an optical lattice using an all optical evaporation with a cycle time of ~ 15 s and imaging the atomic density with single-site resolution using quantum gas microscopy techniques. In this chapter we outline the function of this apparatus, first describing the experimental sequence, then considering various details of the optical lattice, imaging techniques and experimentally accessible observables, stabilization electronics, and recently implemented spatial light modulator setup. More detailed descriptions of the design and construction of the apparatus and diagrams of the laser systems are available in [87]. Portions of the apparatus are similar to that of the Heidelberg group, which is well documented in [88, 89]. Similar QGM techniques for lithium are described in [90, 91].

2.1 Experimental sequence

The vacuum chamber is divided into two sections: an “oven chamber” where a thermal vapor of lithium is produced, and a “science chamber” where lithium atoms are cooled

Step	n_{center}	T	T_f	λ_{dB}	ρ_{center}
MOT	$1 \times 10^9 / \text{cm}^3$	1.5 mK		20 nm	7×10^{-9}
CMOT	$2 \times 10^{10} / \text{cm}^3$	300 μK		40 nm	1×10^{-6}
ODT	$1 \times 10^{12} / \text{cm}^3$	200 μK		50 nm	1×10^{-4}
evaporated ODT	$1 \times 10^{12} / \text{cm}^3$	2 μK	400 nK	500 nm	0.13
light sheet	$1.4 \times 10^{12} / \text{cm}^3$	2 μK	500 nK	550 nm	0.2
evaporated light sheet	$1.5 \times 10^{12} / \text{cm}^3$	$400 \text{ nK} <$	500 nK	1.1 μm	
unevaporated 2D trap	$1.4 \times 10^8 / \text{cm}^2$	$300 \text{ nK} <$	350 nK	1.3 μm	
2D lattice	$2 \times 10^8 / \text{cm}^2$	15 nK	200 nK	6 μm	

Table 2.1: Preparation of a degenerate Fermi gas. For the initial stages of preparation, temperature is determined from time of flight measurements, and density from absorption imaging. In the lattice, temperature is determined from correlation functions, and density from fluorescence imaging. Estimating the temperature in the intermediate regime, where $T \approx T_f$, is more challenging.

and trapped, and the experiments take place. The two sections are separated by a differential pumping tube, which allows the oven chamber pressure to be on the order of 10^{-9} torr while the science chamber pressure is 10^{-11} torr, two orders of magnitude smaller. We also separate the two chambers with a gate valve, which allows the lithium source to be exchanged without breaking vacuum in the science chamber.

We produce a sufficient vapor pressure in the oven chamber by heating a block of solid lithium metal to 360 °C. At this temperature the atoms have a mean velocity of $\langle v \rangle = \sqrt{\frac{8k_b T}{\pi m}} \sim 1500 \text{ m/s}$. Thermal atoms travel through a collimating aperture near the beginning of a Zeeman slower. The Zeeman slower reduces their axial velocity to $\sim 50 \text{ m/s}$ which is slow enough to allow them to be captured by the magneto-optical trap (MOT).

We load the MOT for 5 s to accumulate sufficient atom number for further stages of cooling at an initial temperature of 1.5 mK. Under optimal conditions, we load 10^9 atoms in the MOT. Under more typical conditions, we operate with $\sim 200 \times 10^6$

atoms. Next, we produce a compressed MOT (CMOT) by ramping the laser frequencies closer to the atomic resonance and lowering the power in the MOT beams, which reduces the temperature and increases the density further. The temperature of the cloud is typically a factor of 1.5-2 greater than the Doppler temperature for the lithium D -line, $T_D = 140 \mu\text{K}$.

Sub-Doppler cooling techniques, such as Sisyphus cooling [92], are not effective for lithium due the unresolved hyperfine structure of the $2P_{3/2}$ state. In early experiments, we utilized D_1 gray molasses cooling [93] to reach lower temperatures. However, we found that the experimental complexity of the additional laser system that was required outweighed the modest benefits in phase space density. Instead, following the CMOT stage we load the atoms directly into a crossed beam optical dipole trap (ODT) consisting of 110 W of 1070 nm light in each arm. The waists of the beams are about 90 μm and the maximum trap depth is 1 mK. The ODT is generated by a multi-mode Ytterbium fiber laser, IPG PHOTONICS YLR-200-LP-AC-Y11, with spectral line width $< 4 \text{ nm}$.

After the atoms are trapped in the ODT we optically pump them to the $F = \frac{1}{2}$ hyperfine manifold to prevent spin-exchange collisions. We then ensure the populations in the $|1\rangle$ and $|2\rangle$ states are equal using a sequence of 10 radiofrequency pulses performed at a magnetic field of 545 G. Finally, we create a balanced $|1\rangle - |3\rangle$ mixture by transferring the $|2\rangle$ atoms to state $|3\rangle$ using an rf Landau-Zener sweep at 790 G.

We perform an optical evaporation at 700 G near the $|1\rangle - |3\rangle$ Feshbach resonance at 690 G [94] by lowering the ODT laser intensity using an exponential shape for 2 s. We stop the evaporation before the gas is cold enough to form Feshbach molecules. After this initial stage of evaporation we ramp the field away from the Feshbach resonance and evaporate further to produce a degenerate Fermi gas which is adiabatically connected to the upper branch of the resonance. We first set the field in the range 50-500 G where the $|1\rangle - |3\rangle$ scattering length is large and attrac-

tive, $a_{13} \sim -900 - -450 a_0$ where a_0 is the Bohr radius. We load the gas into an anisotropic “light sheet” beam which has an in-plane waist of $50 \mu\text{m}$, and an out of plane waist of $5 \mu\text{m}$. The light sheet is also anisotropic in-plane, with aspect ratios $\omega_x : \omega_y : \omega_z = 1 : 2 : 10$. In preparation for later stages of the sequence, we turn on an additional “bottom beam” that provides radial confinement. We evaporate in this combined potential by ramping down the depth of the light sheet trap in the presence of a magnetic gradient created by the MOT coils.

Next we compress the gas into 2D by loading the atoms into a single fringe of an accordion lattice [95, 96] formed by 532 nm light. The initial lattice spacing is $7 \mu\text{m}$. After loading this fringe, we turn off the light sheet potential entirely. We compress the accordion lattice to a final spacing of $3.5 \mu\text{m}$ where the trap frequency is $\omega = (2\pi)20 \text{ kHz}$. At this point the gas is quasi two-dimensional in the sense that only the ground state of the axial potential is occupied. The trap is approximately circular, with an aspect ratio $\omega_x/\omega_y \approx 1.2$.

We perform a final stage of evaporation in the 2D potential by ramping down the bottom beam intensity in the presence of a magnetic gradient created by the MOT coils. Due to the different magnetic moments of the $|1\rangle$ and $|3\rangle$ states, the final spin imbalance of the system can be adjusted by changing the evaporation field and the value of the magnetic field gradient. We produce a balanced cloud by evaporating near 500 G , or a nearly polarized gas of state $|1\rangle$ atoms by evaporating near 50 G . At the end of this evaporation, we adiabatically load a 2D in-plane optical lattice formed by a single laser beam which interferes with itself four times (see section 2.5). We ramp the magnetic field to set the scattering length, typically using values between 100 mG and 620 G . At larger fields, the proximity of the Feshbach resonance leads to atom loss.

During each stage of the experimental preparation, we assess the degree of degeneracy using several metrics. The first is the phase space density, $\rho = n\lambda_{\text{dB}}^3$ which is

the number of particles in a cubic thermal de Broglie wavelength, $\lambda_{\text{dB}} = h/\sqrt{2\pi m k_b T}$. The phase space density is appropriate when the gas is not degenerate and the fact we work with a spin mixture is less relevant. The second is the temperature relative to the Fermi temperature, T/T_f . At sufficiently low temperature, we can estimate the Fermi temperature from the central density. For a 3D sample, $k_f = (6\pi^2 n_{\sigma,\text{center}})^{1/3}$ and $k_b T_f = \hbar^2 k_f^2 / (2m)$, where $n_{\sigma,\text{center}}$ is the density of spin σ atoms at the center of the trap [25]. For a 2D sample, $k_f = (4\pi n_{\sigma,\text{center}})^{1/2}$. This is the more relevant quantity in the degenerate regime. Typical atomic densities, temperatures, and phase space densities during various phases of the preparation are summarized in table 2.1.

2.2 Raman imaging

After performing an experiment, we image the atomic density by freezing the atoms in place (“pinning” them on individual sites of the optical lattice), causing them to fluoresce, and collecting the fluorescence photons with a high-resolution imaging system. To prevent the atoms from being heated out of the lattice during the imaging process, we simultaneously cool them using a Raman sideband cooling scheme similar to [60, 61]. We find this technique to be more efficient for lithium than EIT cooling [97], which has been used for ^{40}K [62].

To realize Raman sideband cooling, we couple the $2S_{1/2} |F = 3/2\rangle |n\rangle$ state to the $|F = 1/2\rangle |n - 1\rangle$ state using a pair of Raman beams and drive cooling by optically pumping atoms from the $|F = 1/2\rangle |n - 1\rangle$ state to the $2P_{1/2} |F = 3/2\rangle$ state. Here n refers to the vibrational level in the harmonic trap, and we describe the Raman scheme for a one-dimensional trap for simplicity. In the Lamb-Dicke regime, the $2P_{1/2} |F = 3/2\rangle |n - 1\rangle$ state preferentially decays to the $2S_{1/2} |F = 3/2\rangle |n - 1\rangle$ state, leading to net cooling via removal of vibrational energy. The cooling process terminates once the atoms reach the $|F = 3/2\rangle |n = 0\rangle$ state, which is a dark state

in this one-dimensional picture. For Raman cooling to work efficiently, spontaneous emission from the $2P_{1/2}$ $|F = 3/2\rangle |n - 1\rangle$ must preserve the vibrational quantum number. Transitions between different motional quantum numbers $|n\rangle$ and $|n \pm d\rangle$ are suppressed by a factor of η^{2d} , where $\eta = kl_o$ is the Lamb-Dicke parameter, k is the wave vector of the emitted photon, and $l_o = \sqrt{\hbar/2m\omega}$ is the harmonic oscillator length.

We pin the atoms on-site in the optical lattice using 20 W of 1064 nm light from a 42 W master oscillator power amplifier (MOPA) laser (COHERENT Mephisto MOPA) focused to a beam waist of 70 μm . The on-site trapping frequency is $\omega = (2\pi)1.5$ MHz. The vibrational levels in the lattice are well resolved, as the effective line width of the states is only due to the Raman lasers dressing the ground state with a fraction of the $2P$ excited states. This tight trapping frequency leads to a Lamb-Dicke parameter of $\eta_{x,y} = 0.2$. The confinement in the axial direction due to the lattice is much weaker, so to increase it we turn on the light sheet using 12 W of light, producing a trapping frequency of $\omega = (2\pi)70$ kHz. This leads to a Lamb-Dicke parameter of $\eta_z = 1$.

The Raman beams are detuned 5 GHz to the red of the D_1 line. We typically operate with 50 μW focused to a waist of about 1 mm for the pump beam and 3 mW focused to a waist of 75 μm for each Raman beam. We estimate the Rabi frequency, $\Omega = (2\pi)180$ kHz, from the scaling of the width of Raman spectra with power. The Raman axis is along the diagonal of the square lattice tilted $\sim 10^\circ$ out of plane, the maximum angle allowed by our chamber geometry, to ensure coupling to all three trap axes. The beams are in a retro-reflected lin- \perp -lin configuration meaning that the incoming beam has a vertical polarization and the retro-reflection has a horizontal polarization. The incoming beam has higher frequency and couples the $F = 1/2$ ground states to the excited states. We observe that the Raman sideband cooling is most efficient when we adjust the bias magnetic field to 200 mG pointing in the plane and roughly perpendicular to the Raman axis. From the perspective of the atoms

the incoming Raman beam has an equal mixture of σ_{\pm} polarizations, and the retro-reflection has π polarization. The finite field detunes some of the transitions between $F = 1/2$ and $F = 3/2$ ground states, most likely the $|1\rangle = |F = 1/2 m_f = 1/2\rangle$ to $|6\rangle = |F = 3/2 m_f = 3/2\rangle$ transition. We find adjusting the field in this way enhances the efficiency of the cooling process, leading to less tunneling of atoms between sites.

We simultaneously optically pump the atoms using a beam which is near resonant to the $2S_{1/2} |F = 1/2\rangle$ to $2P_{1/2}$ transition. The optical pumping beam is circularly polarized and travels along the diagonal of the lattice, but is tilted out of the plane a few degrees less than the incoming Raman beam. From the perspective of the atoms this beam has 0.5π polarization and 0.25 of each σ_{\pm} polarization. More efficient pumping could be achieved by using a purely σ polarized beam along the quantization axis.

The interplay between the cooling of the strongly confined lattice directions with small Lamb-Dicke parameter and the weakly confined light sheet direction with large Lamb-Dicke parameter has not been studied in detail. One possibility is that the Raman beams effectively couple the weakly confined direction with the strongly confined directions, and thus the cooling in the strongly confined direction also cools the weakly confined direction. Similar approaches have been used in other 3D cooling schemes [62].

During each cycle of the optical pumping, the atoms spontaneously emit a photon which we collect using a high-resolution objective made by SPECIAL OPTICS with numerical aperture of 0.5 , allowing us to collect 6.7% of the total scattered photons. The objective has a working distance of 24.7 mm and is corrected for our 5 mm thick fused silica vacuum window. We find a -0.5 spherical aberration corrector (EDMUND OPTICS #66-758) improves the point spread function. An achromatic doublet with $f = 750\text{ mm}$ gives an imaging system magnification of ~ 30 which we verify using Kapitza-Dirac scattering of a molecular BEC. We block stray light using a 671 nm

band pass filter with 10 nm width (EDMUND OPTICS #65-172) and a short pass filter, which provides additional rejection for scatter from the powerful infrared beams in the experiment.

We perform Raman imaging for 800 – 1200 ms and collect \sim 1000 photons per atom using an sCMOS camera, ANDOR TECHNOLOGY Zyla 4.2, with a quantum efficiency of 75 % near 671 nm. The measured point spread function (PSF) has a full-width half-maximum of 900(20) nm, slightly larger than expected for our numerical aperture [87]. This is sufficient for a numerical algorithm to distinguish occupied and unoccupied sites, as illustrated in fig. 2.1. Our reconstruction algorithm is similar to that described in [57], and is also described in the supplement to [70]. The reconstruction allows us to reduce the data from the fluorescence pictures to binary matrices that are the basis for all further data processing.

After binarization, we identify sites in lattice coordinates, which we define by $(\eta_1, \eta_2) = \eta_1 \mathbf{a}_1 + \eta_2 \mathbf{a}_2$ where \mathbf{a}_i are the lattice vectors. The lattice coordinates are related to the real space coordinates by the transformation

$$\begin{pmatrix} \eta_1 \\ \eta_2 \end{pmatrix} = \frac{1}{\sin(\theta_2 - \theta_1)} \begin{pmatrix} \frac{1}{a_2} & 0 \\ 0 & \frac{1}{a_1} \end{pmatrix} \begin{pmatrix} -\sin(\theta_1) & \cos(\theta_1) \\ \sin(\theta_2) & -\cos(\theta_2) \end{pmatrix} \begin{pmatrix} x \\ y \end{pmatrix} + \begin{pmatrix} \phi_2 \\ \phi_1 \end{pmatrix}, \quad (2.1)$$

where θ_i is the angle between \mathbf{a}_i and the x -axis. When the lattice axes are orthogonal, the lattice and real space coordinates are related by a rotation and scale factor, and this transformation therefore preserves angles. When the axes are not orthogonal this is a more general affine transformation, which can include different magnifications along the two directions and shearing. The parameters θ_i and a_i are only sensitive to gross beam alignment changes and therefore stable over several weeks. On the other hands, ϕ_i are sensitive to lattice phase changes and must be determined for each image.

We estimate fidelity errors due to Raman imaging imperfections by taking 40 consecutive images of the same atom cloud and determine the shot-to-shot differences. This leads to a tunneling rate during one picture of < 1 % and a loss rate of < 2 %.

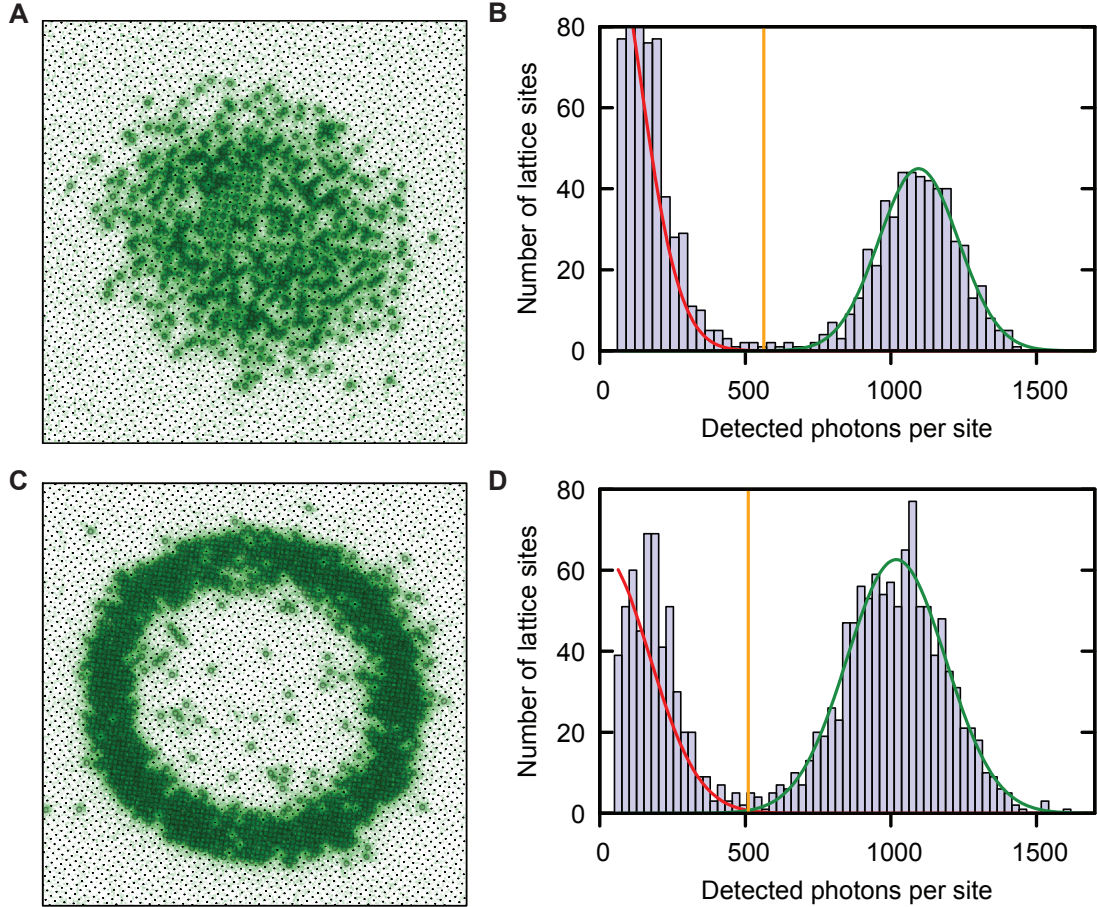


Figure 2.1: Reconstruction visualization. **A**, A fluorescence image with lattice sites overlaid, showing occupied sites (circles) and unoccupied sites (points). The field of view is $46 \mu\text{m} \times 46 \mu\text{m}$. **B**, Histogram of detected photons on each site for panel A. We identify the lower peak with unoccupied sites and the upper with occupied sites. By fitting Gaussians to these peaks, we determine a threshold value (orange line). We identify any site with more counts than the threshold as occupied. **C**, Fluorescence image showing a band insulator in the center of the cloud, surrounded by a Mott insulator region. **D**, Histogram of detected photons for panel C.

2.3 Laser frequency stabilization

For addressing atoms with near resonant light, which is required for cooling and trapping atoms in a MOT, absorption imaging, and Raman cooling, it is necessary to control the laser frequency to a precision much better than the line width of the atomic transition. In this case, the relevant transitions are the D_1 and D_2 lines in ${}^6\text{Li}$, which have line widths of $\Gamma = (2\pi)6\text{ MHz}$. Diode laser frequencies can drift on the order of hundreds of MHz due to thermal fluctuations and vibrations. To achieve the required frequency stability, it is necessary to control the frequency of the laser using a servo loop [98, 99].

Before the laser frequency can be electronically controlled, it must be read out and converted to an electronic signal. The frequency can be read out by comparing it to a frequency reference, such as an atomic transition, optical cavity mode, or stable laser. The difference in frequency is then converted to an electronic error signal. The error signal must give two types of information: a measure of how far the current frequency is from the desired set-point, and a measure of which direction the frequency should change to go towards the set-point. An absorption spectra for an atomic medium such as obtained from Doppler-free spectroscopy does not meet these criteria because this signal is symmetric above and below the atomic resonance. Although it provides a measure of how far the frequency is from the set-point, it is not possible to determine how the frequency should be modified to approach the set-point from a single measurement.

Instead, most schemes compare the phase of light interacting with the frequency reference with the phase of light which does not. Many suitable schemes exist, including Pound-Drever-Hall locking [100], optical heterodyne spectroscopy [101], and modulation transfer spectroscopy [102]. If one laser has been stabilized using these techniques, other lasers can be stabilized to nearby ($< \sim 10\text{ GHz}$) frequencies using offset locking, which relies on measuring the beat note between the lasers frequencies

on a photodiode and producing an error signal using heterodyne [103, 104] or digital techniques [105, 106, 107, 108, 109]. In our experiment, we utilize two master lasers, one locked to the ${}^6\text{Li } D_2$ line to generate trapping and cooling light, and another to the D_1 line to generate light for the Raman imaging. We use modulation transfer spectroscopy for both, which has the advantage that the error signal offset is independent of the laser power [110]. We lock various auxiliary lasers to the masters using the offset locking scheme described in [104].

Controlling the frequency of an external cavity diode laser (ECDL) in the Littrow configuration can be accomplished either by changing the current passing through the laser diode, or by adjusting the angle of the diffraction grating, which can be done using a piezoelectric actuator. It is often beneficial to control both of these parameters, as the piezoelectric actuator can correct large frequency fluctuations but is relatively slow (typically $\leq 10 \text{ kHz}$) whereas the current can correct fast frequency fluctuations ($\sim 1 \text{ MHz}$ or more) but has limited range.

We did not have a preexisting design for a laser lock and therefore we chose to design our own instead of buying a commercial controller, due to the expense of these units and the large number of lasers required for our experiment. Our circuit, shown in fig. 2.2, accepts a user supplied error signal from either the inverting or non-inverting input. These inputs use ANALOG DEVICES AD8429 low noise instrumentation amplifiers which have large input impedance, high bandwidth (gain-bandwidth product 15 MHz), and low noise ($1 \text{ nV}/\text{Hz}^{1/2}$). If both inputs are used simultaneously the two signals are subtracted from each other, allowing one to be used as a variable set-point adjustment. An offset voltage is added to the result, allowing the zero point of the error signal to be adjusted. This error signal is passed to piezo and current stabilization circuits, and is also available to be read out from an error monitor output.

A major challenge is to ensure the system is stable when operating with both piezo and current feedback simultaneously. It is possible for the two feedback loops

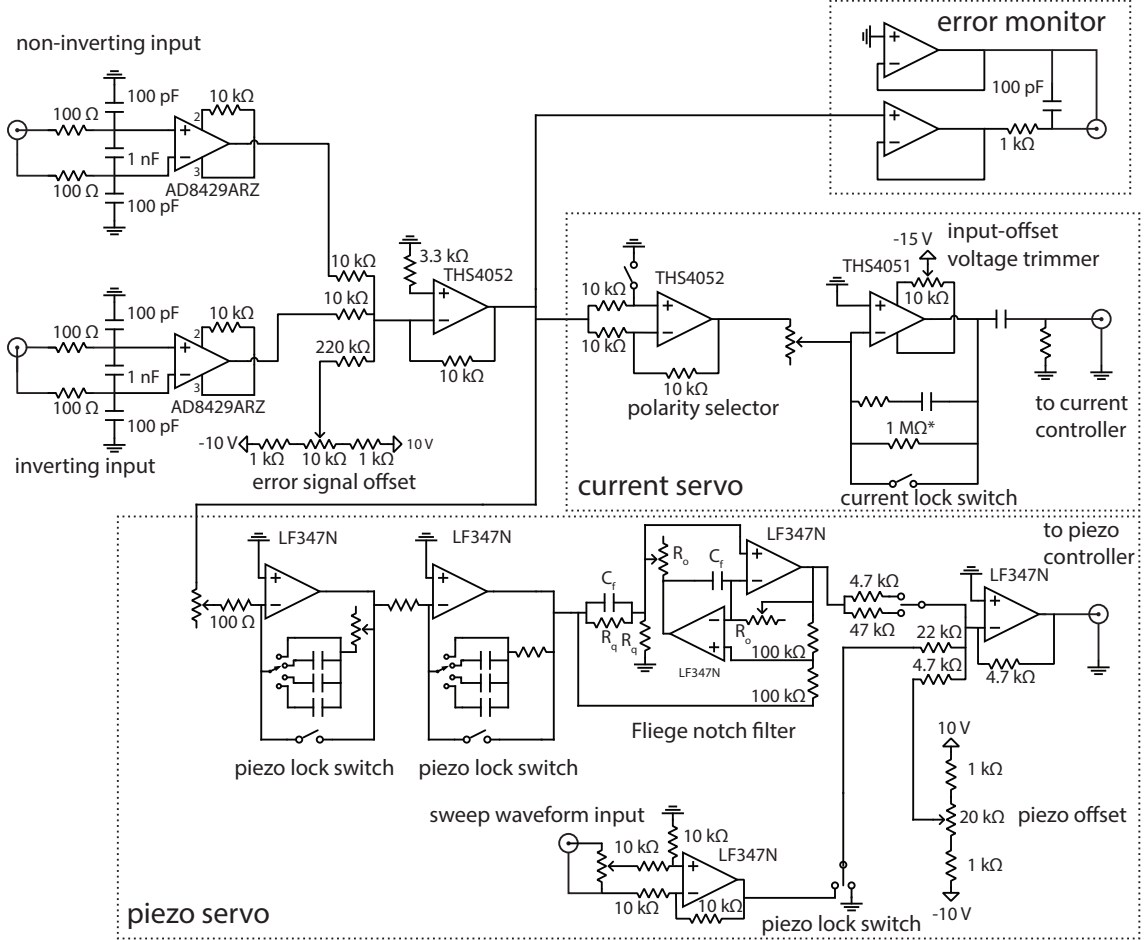


Figure 2.2: Laser frequency stabilization servo circuit diagram. Circuit diagram for the laser frequency stabilization circuit board. Components with values marked by an asterisk are optional as explained in the text. A voltage signal which is proportional to the laser frequency enters through either the inverting or non-inverting input as is added to an offset signal which determines the lock point. The resulting error signal can be read out through the error monitor path. It is passed on to the servo sections, which produce appropriate control signals for the laser diode current and piezo voltage.

to compete if, for example, the zero points of the error signals are not identical. This is a common problem in circuits based on operational amplifiers (op amps) because many op amps have significant input offset voltage, which can be as large as ~ 10 mV for certain designs. Some op amp designs are optimized for extremely low input offset voltage, but these often have other drawbacks. There are two methods of avoiding this issue. The first is to include an adjustable knob in the circuit to fine tune the

zero points of the error signal along the two paths so they are the same. The second is to separate the frequency response of the feedback loops so that the current loop does not respond to noise at frequencies where the piezo loop has large gain. Similar issues are discussed in more detail in [111]. Our circuit is flexible enough to allow both possibilities. The second option is easier, and is the one we typically choose for our diode lasers. However, when better noise performance is desired the first option is superior.

The piezo path of our circuit is based on a pair of cascaded PI stages, similar to the design described in [112]. In typically operation, one PI stage is tuned (e.g. using the Ziegler-Nichols method [113]) so that its knee frequency is large, and the other has a knee frequency \sim 10 times smaller. This allows the circuit to have large gain near DC with little phase shift at higher frequency. The PI stages are followed by a notch filter using the Fliege topology [114]. The notch frequency is adjustable and may be used to null one of the piezo resonances, which is important for achieving high gain. However, this is not a scalable solution for piezo systems with many resonances. Those sorts of systems may be stabilized using digital techniques [115]. A better approach is to design the piezo to maximize the resonance frequency [116].

To facilitate locking the piezo at a certain position, an offset voltage is added to the servo signal. Typically, this voltage should be chosen to position the piezo near the desired lock point. This offset is applied even when the piezo locking section is switched off. In the off position, an external triangular sweep signal can be added to the piezo, and the amplitude of the sweep is adjustable using a potentiometer. This allows the piezo to be swept near a set-point, which is useful for observing nearby features in the error signal and selecting an appropriate atomic transition. In typical operation, an atomic transition is selected by iteratively adjusting the voltage set-point and turning down the amplitude of the sweep. Once the set-point is near the

zero crossing of the error signal, the lock can be engaged. Typically, the output signal is passed through a high voltage amplifier before it is applied to the piezo.

The current control consists of a single PI stage implemented using a TEXAS INSTRUMENTS THS4051 op amp with a 40 MHz bandwidth. This op amp design includes pins which allow the input offset voltage to be adjusted using an external potentiometer. By tuning this potentiometer, it is possible to avoid competition between the current and piezo feedback loops. In some situations it is useful to have no current response at low frequency, and therefore we include an optional high pass filter at the current output. When this high pass filter is implemented, the PI stage will tend to saturate due to its large gain at DC. To mitigate this issue, we include an optional $1\text{ M}\Omega$ resistor which gives the PI stage finite DC gain. The output signal is intended to drive a current modulation, and unlike the piezo path does not include a voltage set-point. Typically, the laser current is driven by a separate controller with a modulation input.

In principle the bandwidth of the current path may be pushed to very high frequency, but this requires high-bandwidth, low-noise detection circuitry, minimization of coaxial cable path lengths, and other high-effort optimizations that are not necessary for achieving the required stability to create a MOT.

2.4 Observables

The Raman imaging technique is sensitive to the parity of the on-site atomic density. Using various spin manipulation techniques, we can measure a variety of other on-site density quantities, which are described in detail in this section. A single measurement corresponds to one projection of the many-body wave function onto a certain real space density basis. By making many measurements, we infer expectation values for densities and density correlations. Although we have access to many different

observables, we cannot directly measure correlations between different types of observables because each measurement is destructive. In some special cases, these sorts of correlations can be extracted from several different measurements.

2.4.1 Singles density

When near resonant light is incident on a single tightly confined lattice site containing multiple atoms, light-assisted collisions occur leading to pairwise atom loss. For this reason, the natural observables Raman imaging provides access to are the atomic singles density and singles-density correlations defined by

$$n_i^s = n_{i\uparrow} + n_{i\downarrow} - 2n_{i\uparrow}n_{i\downarrow} \quad (2.2)$$

$$C_s(d) = \langle n_i^s n_{i+d}^s \rangle - \langle n_i^s \rangle \langle n_{i+d}^s \rangle. \quad (2.3)$$

The singles density is closely related to the *local moment*, which is defined by $m_i^z = (n_{i\uparrow} - n_{i\downarrow})^2$. These two quantities are identical for fermions. One limitation of measuring the singles density is that both doublons and holes appear as empty sites, and we cannot distinguish between them.

2.4.2 Single-species density

The single-species densities $n_{i\uparrow}$ and $n_{i\downarrow}$ and correlations,

$$C_\sigma(d) = \langle n_{i\sigma} n_{i+d\sigma} \rangle - \langle n_{i\sigma} \rangle \langle n_{i+d\sigma} \rangle \quad (2.4)$$

are also accessible in the experiment. Raman imaging drives transitions between different spin states, and therefore is not directly sensitive to spin. To measure this quantity we ramp the lattice depth to $60 E_r$ in $100 \mu s$ and ramp the magnetic field to 595 G . Then we shine light resonant with only one of the spin states on the atoms for

30 μ s. The length of this pulse was determined by observing atom loss for different pulse lengths. The atom loss curve exhibits two well-separated time scales, which we interpret as resonant heating and off-resonant heating of the two spin states, and fit with the sum of two decaying exponentials [69]. We find time constants 4.5(2) μ s and 1.7(5) ms, from which we estimate that 0.2% of resonantly blown atoms remain, and up to 2% of the off-resonant state atoms are ejected.

This is possible because the lithium ground and excited states are in the high-field (Paschen-Back) regime at moderately large fields and thus the high-field seeking states have nearly closed cycling transitions $2S_{1/2} |m_j = -1/2, m_i\rangle$ to $2P_{3/2} |m_j = -3/2, m_i\rangle$ which are also optically resolved. However, these transitions are not perfectly closed and the resonant pulse also pumps some of state $|1\rangle$ ($|2\rangle$) atoms into state $|5\rangle$ ($|4\rangle$). For more discussion of ${}^6\text{Li}$ branching ratios versus field, see appendix A.

We take advantage of the cycling state $|3\rangle = |m_j = -1/2, m_i = -1\rangle$ to calibrate the pumped fraction. To measure the probability of pumping $|1\rangle$ into $|5\rangle$ we prepare a $|1\rangle - |3\rangle$ Mott insulator and compare the results blowing both states with blowing only state $|3\rangle$. We find that we pump 0.8(1)% of the atoms from $|1\rangle$ to $|5\rangle$. We separately measured the probability of pumping $|2\rangle$ into state $|4\rangle$ to be 1.2(1)% by preparing a $|1\rangle - |2\rangle$ Mott insulator and comparing blowing both states with blowing $|2\rangle$ only.

We find this procedure ejects one spin state without affecting the other with high fidelity. This situation is in contrast to the behavior observed in [68, 69], where resonant light causes both spin states to be lost. We attribute the absence of these light-assisted collisions in our system to the much weaker axial confinement used (see section 2.2).

2.4.3 Single-species singles density

By first removing doublons and then performing spin resolved detection, the single-species singles densities are accessible. These are defined by

$$n_{i\sigma}^s = n_{i\sigma} - n_{i\uparrow}n_{i\downarrow} \quad (2.5)$$

$$C_{s,\sigma}(d) = \langle n_{i\sigma}^s n_{i+d\sigma}^s \rangle - \langle n_{i\sigma}^s \rangle \langle n_{i+d\sigma}^s \rangle. \quad (2.6)$$

We again prepare the system in a $60 E_r$ lattice, but now before performing resonant pushing we “hide” doublons by ramping slowly across one of the narrow Feshbach resonances (see section A.2). Doublons are either lost or transferred to deeply bound molecules that are not observed in Raman imaging. Finally, we remove the undesired spin state using resonant light.

To characterize the fidelity of doublon hiding, we first prepare a band insulator. We take images with neither doublon hiding nor blowing to determine the number of singles in the band insulator. We then compare this to the number of singles we observe after performing doublon hiding and removing one of the spin states with a blowing pulse, which leaves behind single atoms on sites where the doublon hiding failed. We find a doublon hiding fidelity of 90(3)%.

2.4.4 Doublon density

The doublon density is accessible through rf techniques. The doublon density and density correlations are given by

$$d_i = n_{i\uparrow}n_{i\downarrow} \quad (2.7)$$

$$C_d(d) = \langle d_i d_{i+d} \rangle - \langle d_i \rangle \langle d_{i+d} \rangle. \quad (2.8)$$

Again we prepare the gas in a deep lattice and ramp the field to 595 G. We can selectively transfer doublons using two different schemes. One, we can rely on the strong repulsive interaction to spectroscopically resolve doubly and singly occupied sites. Two, we can take advantage of the tight axial confinement from the accordion lattice by applying an rf pulse to transfer $|1\rangle$ atoms to state $|2\rangle$ and add two vibrational quanta. As momentum must be conserved in an rf transfer, this process can only occur on sites where there are two atoms. This technique is closely related to the trap sideband resolved spectroscopy discussed in [94]. We apply this second method in the experiment because the accordion lattice trapping frequency is larger than the interaction energy, leading to larger separation between the singly and doubly occupied site resonances. After the rf transfer, we push out both states $|1\rangle$ and $|3\rangle$. The remaining $|2\rangle$'s correspond to sites which were doubly occupied.

2.4.5 Derived observables

The four observables described in the previous section can be combined to obtain other interesting correlations which are more suited to illuminating certain kinds of physics.

The spin correlations can be obtained by combining the singles correlations and the single-component singles correlations, [67, 68, 69, 70]

$$S_i^z = \frac{1}{2}(n_{i\uparrow} - n_{i\downarrow}) \quad (2.9)$$

$$C_{\text{spin}}^z(d) = 4(\langle S_i^z S_{i+d}^z \rangle - \langle S_i^z \rangle \langle S_{i+d}^z \rangle) \quad (2.10)$$

$$= 2[C_{s,\uparrow}(d) + C_{s,\downarrow}(d)] - C_s(d). \quad (2.11)$$

Correlations between up spins and down spins, which are characteristic of interacting systems, can be inferred from the spin correlations and the single-component

density correlations,

$$C_{\uparrow\downarrow}(d) = \langle n_{i\uparrow}n_{i+d\downarrow} \rangle - \langle n_{i\uparrow} \rangle \langle n_{i+d\downarrow} \rangle \quad (2.12)$$

$$C_{\uparrow\downarrow}(d) + C_{\downarrow\uparrow}(d) = C_{\uparrow}(d) + C_{\downarrow}(d) - C_{\text{spin}}^z(d). \quad (2.13)$$

Density correlations can be inferred from a similar combination of spin correlations and single-component density correlations

$$C_n(d) = \langle n_i n_{i+d} \rangle - \langle n_i \rangle \langle n_{i+d} \rangle \quad (2.14)$$

$$= C_{\uparrow}(d) + C_{\downarrow}(d) + C_{\uparrow\downarrow}(d) + C_{\downarrow\uparrow}(d) \quad (2.15)$$

$$= 2 [C_{\uparrow}(d) + C_{\downarrow}(d)] - C_{\text{spin}}^z(d). \quad (2.16)$$

These derived correlators require measuring many different correlations to determine, and are thus more experimentally “expensive” than the directly accessible quantities. Nevertheless, they are frequently of great interest and reveal information which is not apparent from the component correlators.

2.4.6 Correlator statistical uncertainty

Quantifying the uncertainty in measured correlators is important to draw scientific conclusions, but due to correlations which exist between $\langle n_i n_j \rangle$ and $\langle n_{i,j} \rangle$, we cannot apply naïve uncertainty analysis to the correlation functions discussed above. Here we use n_i as a stand in for any of the previous density observables discussed in the previous section. To estimate the uncertainty, we note that the correlation functions can be recast as the covariance between the variables n_i and n_j , $\langle n_i n_j \rangle_c = \text{Cov}(n_i, n_j)$. The expectation value of the covariance we calculate in the experiment is therefore the *sample covariance*, S . The uncertainty in the sample covariance is related to its

variance which can be calculated

$$\text{Var}[S(n_i, n_j)] = \frac{1}{N} \left(\delta_2 + \frac{1}{N-1} \text{Var}(n_i) \text{Var}(n_j) - \frac{N-2}{N-1} \text{Cov}^2(n_i, n_j) \right) \quad (2.17)$$

As the number of measurements, N , becomes large, $S \rightarrow \frac{1}{N} (\delta_2 - \text{Cov}^2(n_i, n_j))$ where $\delta_2 = \langle (n_i - \langle n_i \rangle)^2 (n_j - \langle n_j \rangle)^2 \rangle$.

Bootstrap techniques [117] yield similar error estimates, but are more computationally expensive.

2.4.7 Correlator systematic uncertainties

In addition to statistical uncertainties, the various density and correlator expectation values are affected by systematic effects such as atom loss and imperfect resonant pushing or radiofrequency manipulation. We estimate the impact of various imaging imperfections here. Related discussion of similar effects can be found in [68].

Atoms that are lost from the trap after tunneling dynamics are frozen can reduce the measured correlations. We estimate this effect by introducing the probability of an atom being lost before imaging, ϵ_l , and the probability ϵ_r that we identify an empty site as occupied. ϵ_r is a result of both tunneling and recapture of atoms during imaging. We find

$$\tilde{n}_i^s = n_i^s (1 - \epsilon_l) + (1 - n_i^s) \epsilon_r \quad (2.18)$$

$$C_s(d) = \frac{\tilde{C}_s(d)}{1 - 2(\epsilon_l + \epsilon_r)}, \quad (2.19)$$

to first order in ϵ . Using the estimates from section 2.2 for imaging loss rate, tunneling rate, and loss during pinning hold times leads to an expected multiplicative reduction in measured correlators to $1 - 2(\epsilon_l + \epsilon_r) = 0.92(2)$ of the actual values. Since the

imaging procedure is not affected by differences in sample preparation, such as lattice depth or spin removal pulses, this correction applies to all measured correlators.

Imperfections in the spin imaging process can also affect correlators. The blowing pulse off-resonantly ejects an atom in the spin state of interest with probability ϵ_σ and fails to eject an atom in the other spin state with probability $\epsilon_{f\sigma}$, leading to

$$\tilde{n}_{i\sigma} = n_{i\sigma}(1 - \epsilon_\sigma) + n_{i,-\sigma}\epsilon_{f\sigma}. \quad (2.20)$$

A similar expression holds for the n_σ^s . The errors considered here are due to the resonant blowing pulses and do not affect the value of C_s . However, they do affect the $C_{s,\sigma}$ and C_σ . To first order in ϵ , the reduction in these correlators is

$$C_\sigma(d) - \tilde{C}_\sigma(d) = 2\epsilon_\sigma C_\sigma(d) - \epsilon_{f,\sigma} [\langle n_{i\sigma} n_{i+d,-\sigma} \rangle_c + \langle n_{i,-\sigma} n_{i+d,\sigma} \rangle_c]. \quad (2.21)$$

A similar expression holds for $C_{s,\sigma}$ with the replacement $n_{i\sigma} \rightarrow n_{i\sigma}^s$.

Imperfect doublon hiding affects the $C_{s,\sigma}$ correlators. If we fail to hide a doublon with probability ϵ_d , we find

$$\tilde{n}_{i\sigma}^s = n_{i\sigma}^s + \epsilon_d d_i \quad (2.22)$$

$$C_{s,\sigma}(d) - \tilde{C}_{s,\sigma}(d) = -\epsilon_d (\langle n_i^s d_{i+d} \rangle_c + \langle d_i n_{i+d}^s \rangle_c). \quad (2.23)$$

Imperfect doublon transfer reduces the observed doublon correlations. Suppose that we fail to transfer doublons with a rate ϵ_{df} and we unintentionally transfer a spin-up or down atom on a singly occupied site with rate ϵ_s . We find,

$$\tilde{d}_i = (1 - \epsilon_{df})d_i + \epsilon_s(n_{i\uparrow} + n_{i\downarrow}) \quad (2.24)$$

$$C_d(d) - \tilde{C}_d(d) = 2\epsilon_{df}C_d(d) - \epsilon_s [\langle d_i n_j^s \rangle_c + \langle d_j n_i^s \rangle_c]. \quad (2.25)$$

In most circumstances, the effect of the mixed correlators (e.g. $\langle d_i n_j^s \rangle$) are small and we only consider the effect of the terms proportional to the given correlator itself.

2.5 Optical lattice

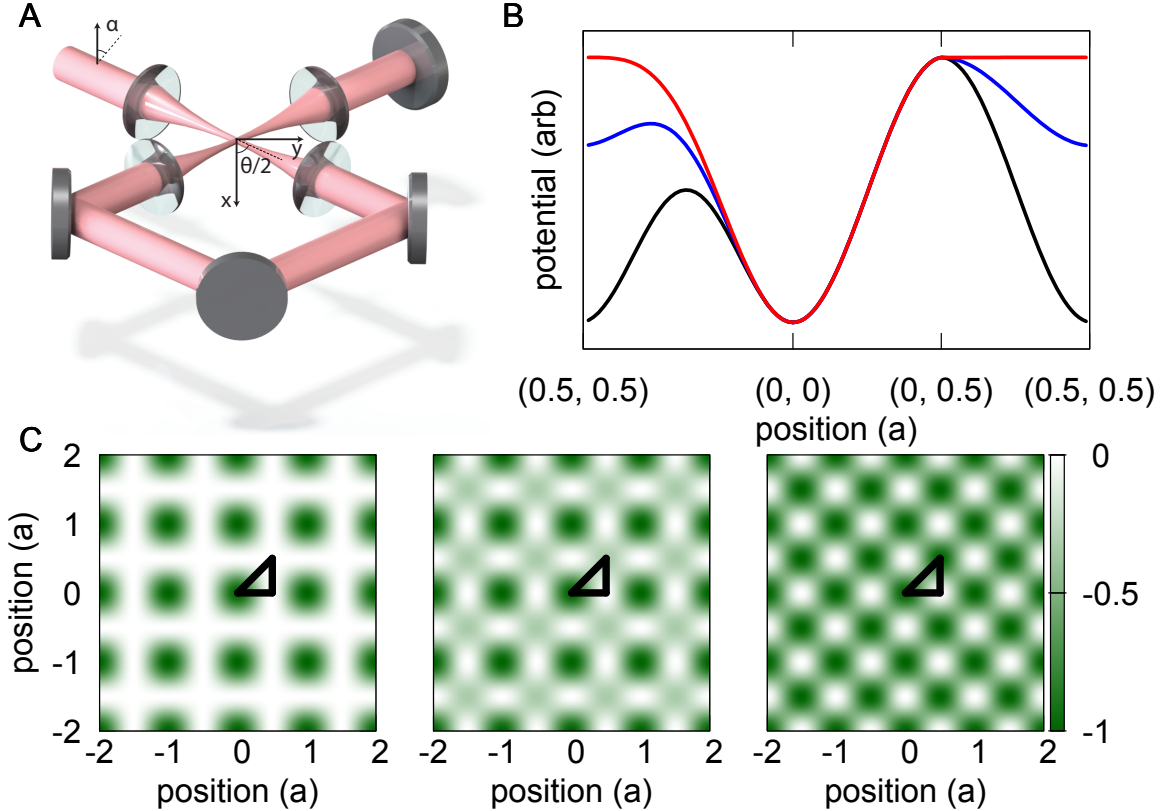


Figure 2.3: **Lattice geometry.** **A**, Lattice beams are shown in pink, mirrors in gray and lenses in blue. All four lattice beams cross at the origin and can interfere depending on the polarization angle α . The incoming beam makes an angle of $\theta/2$ with the x -axis. **B**, Lattice potential shown along lines of high-symmetry in the unit cell for polarization angles $\alpha = 0^\circ$ (red), 45° (blue), and 90° (black). The global minimum occurs at position $(0, 0)$, whereas a local minimum occurs at position $(\lambda/2\sqrt{2}, \lambda/2\sqrt{2})$. **C**, 2D lattice potentials for $\alpha = 0^\circ$ (left), 45° (center), and 90° (right). Black lines show the path traversed for the plots in panel B. The leftmost panel is the four-fold interfering lattice with lattice axis along the coordinate axes. As the laser polarization is varied, the lattice develops a second local minimum (center panel), and the local minimum becomes equivalent to the global minimum and the lattice has shorter periodicity and axes diagonal to the coordinate axes (right panel).

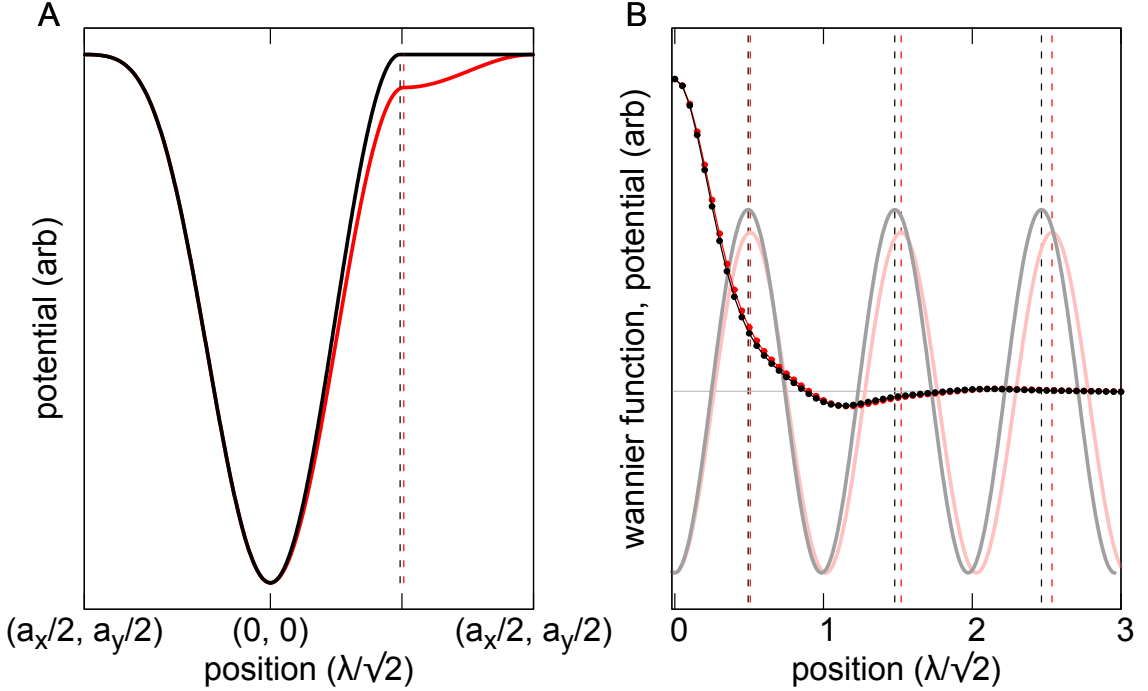


Figure 2.4: **Lattice potential non-idealities.** **A**, Lattice potential along high-symmetry directions in the unit cell, including the path shown in fig. 2.3C (red) which travels from $(a_x/2, a_y/2)$ to $(0, 0)$ to $(a_x/2, 0)$, and the complementary path for the y -direction (black) which passes through $(a_x/2, a_y/2)$, $(0, 0)$, and $(0, a_y/2)$. Dotted lines delineate the edge of the unit cell along the lattice axes. **B**, Lattice potential along the x (light-red line) and y (gray line) directions and the (purely real) Wannier function (red and black) for lattice depth $5 E_r$. The edges of successive unit cells (dotted lines) illustrate the different lattice constants along the two directions.

Precise knowledge of the optical lattice potential is required for comparing the experimental results in this thesis to theory. In this section, we discuss the optical lattice in detail. The optical lattice is a 2D square lattice formed by four interfering passes of a single vertically polarized beam at 1064 nm, as illustrated in fig. 2.3A. Compared to the commonly used lattice configuration created by two non-interfering orthogonal retro-reflected beams, this lattice has a spacing a factor of $\sqrt{2}$ larger and a much larger depth because of the 4-fold interference, features that facilitate quantum gas microscopy. Furthermore, the tunneling barrier between sites is the full lattice depth, compared with half the depth in the two-beam setup.

The lattice geometry may be changed by adjusting the angle the linear polarization makes with the vertical, α [118]. For vertical polarization, $\alpha = 0$, all four passes interfere and the resulting potential is non-separable with lattice axes along the x and y axes and spacing $\lambda/\sqrt{2}$. As the polarization is adjusted away from $\alpha = 0$, the lattice exhibits a double well structure with the global minimum at $(x, y) = (0, 0)$ and a local minimum at $(\lambda/2\sqrt{2}, \lambda/2\sqrt{2})$. For $\alpha = 90^\circ$ these two minima are equivalent, and the lattice potential is separable with lattice basis vectors along the diagonals and spacing $\lambda/2$.

We suppose the lattice is red detuned and the first two passes travel in the xy plane at angles $\pm\theta/2$ to the x -axis and that the electric field of the retro-reflected beam is attenuated by a factor of r . The lattice principal axes are along the x - and y -axes independent of the angle θ , and we choose the phase of the lattice so that the minimum occurs at the origin. We write the lattice potential in terms of its Fourier components,

$$V(\mathbf{r}) = \sum_{\mathbf{K}} V_{\mathbf{k}} e^{i\mathbf{K}\cdot\mathbf{r}} \quad (2.26)$$

where the Fourier components for polarization $\alpha = 0$ are given in table 2.2 and for arbitrary polarization in table B.1.

K_x	K_y	$V_{\mathbf{K}}$
0	0	$-V_o \frac{2(1+r^2)}{4(1+r)^2}$
$\pm 2k \cos(\theta/2)$	0	$-V_o \frac{2r}{4(1+r)^2}$
0	$\pm 2k \sin(\theta/2)$	$-V_o \frac{1+r^2}{4(1+r)^2}$
$\pm 2k \cos(\theta/2)$	$\pm 2k \sin(\theta/2)$	$-V_o \frac{r}{4(1+r)^2}$
$\pm 2k \cos(\theta/2)$	$\mp 2k \sin(\theta/2)$	$-V_o \frac{r}{4(1+r)^2}$

Table 2.2: Four-fold lattice Fourier components for $\alpha = 0$.

We can also write the potential as

$$= -V_0 \frac{(1 + r^2 + 2r \cos[2k \sin(\theta/2)x]) (1 + \cos[2k \cos(\theta/2)y])}{2(1+r)^2}, \quad (2.27)$$

where V_0 is the full lattice depth and $k = 2\pi/\lambda$. Note that eq. 2.27 differs from the expression given in [70] by a phase factor to ensure that the potential minimum occurs at $(x, y) = (0, 0)$.

For $\theta = 90^\circ$ the lattice constant is $\frac{\lambda}{\sqrt{2}}$. Deviations from this condition preserve the lattice axes but result in different spacing along the two directions,

$$a_x = \frac{\lambda}{2 \cos(\theta/2)} \quad (2.28)$$

$$a_y = \frac{\lambda}{2 \sin(\theta/2)} \quad (2.29)$$

$$\theta = 2 \arctan \left(\frac{a_x}{a_y} \right). \quad (2.30)$$

This spacing asymmetry results in asymmetric tunneling along the two directions which we compensate by adjusting the attenuation of the retro-reflected beam. We display the effect of these non-idealities on the potential (fig. 2.4A,B) and the Wannier function (fig. 2.4B), for $\theta = 91.6267^\circ$, which is the lattice angle inferred from a_x and a_y determined during binary reconstruction (see section 2.2), and $r = 0.6$, which is near the value that equalizes the x - and y -direction tunneling rates for lattice depth $5 E_r$.

For a lattice with equal spacing, we define the recoil energy in terms of the magnitude of the reciprocal lattice vectors, $|b|$ by $E_r = \frac{\hbar^2}{2m} (|b|/2)^2$. For lattices with unequal spacing, we take instead the geometric mean of the reciprocal lattice vectors $b_{\text{mean}} = \sqrt{|b_1||b_2|}$. However, here we will express all quantities in terms of the recoil energy of the ideal lattice, i.e. $\theta = 90^\circ$, $E_r = \frac{\hbar^2}{2m} \frac{2\pi^2}{\lambda^2}$, which is 14.65 kHz for ${}^6\text{Li}$ and $\lambda = 1064$ nm.

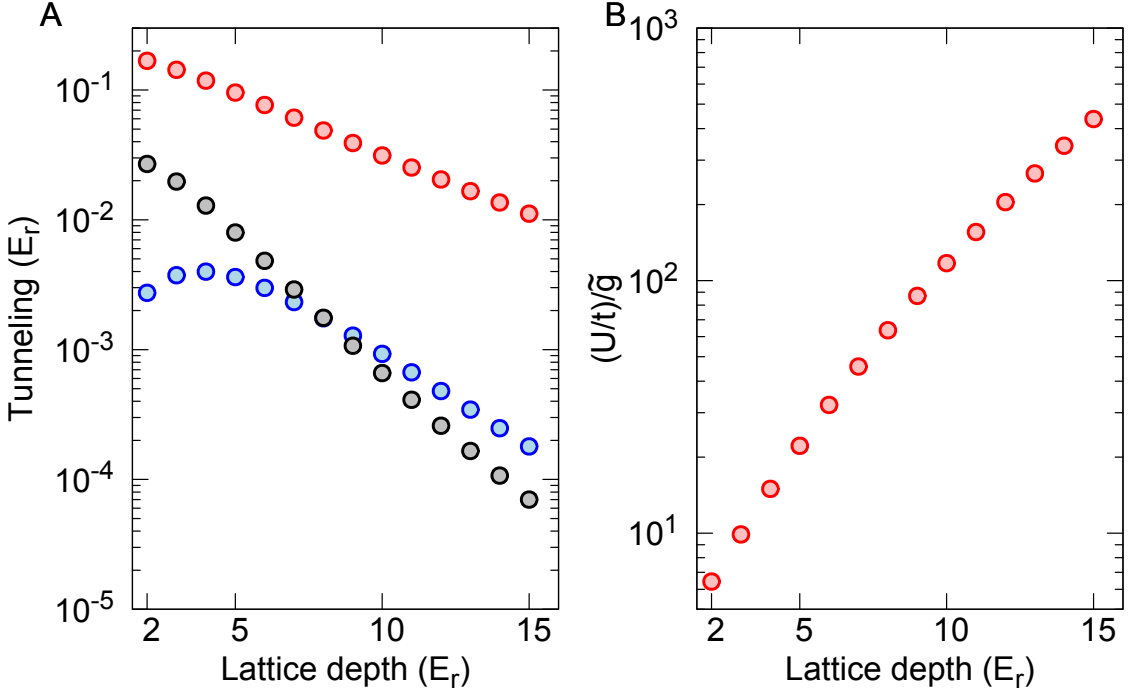


Figure 2.5: **Lattice parameters versus depth.** **A**, Lattice nearest-neighbor tunneling energy (red), diagonal (blue), and second neighbor (gray) determined from a Wannier function calculation. We verify these values by comparing them with the values obtained by fitting the shape of the band structure. **B**, Ratio of the Wannier interaction integral, $\int dx dy |w(x, y)|^4$, over the hopping. Equivalently, this is $(U/t)/\tilde{g}$, where $\tilde{g} = g/E_r a^2$ and $g = \frac{4\pi a_s \hbar^2}{m} \sqrt{\frac{m\omega_z}{\hbar}}$. This quantity allows U/t to be easily calculated for various atomic parameters (see text).

The tunneling and interaction energies can be determined by solving a single-particle problem (see appendix B). For lattices deeper than a few recoil energies, tunneling between sites is strongly suppressed with distance and we can approximate the potential using a tight-binding model. We plot the first few tunneling energies in fig. 2.5A determined from a Wannier function calculation. We confirm these results by comparing them with tunneling parameters obtained from fitting the dispersion of the ground band. We also extract the interaction energy from the Wannier functions and plot the ratio U/t up to a factor of $\tilde{g} = g/(E_r a^2)$, where $g = \frac{4\pi a_s \hbar^2}{m} \sqrt{\frac{m\omega_z}{\hbar}}$ in fig. 2.5B. The connection between the Wannier integral and the interaction energy in quasi-2D is given by $U = g \int dx dy |w(x, y)|^4$ (see section B.4).

2.5.1 Depth calibration

Knowing the optical lattice depth is important both as a tool for aligning the lattice potential and because it can be used to determine the tunneling rate from a band structure calculation. This approach is useful because measuring the tunneling rate directly is more challenging. In early experiments, we calibrated the lattice depth using Kapitza-Dirac scattering (see e.g. [119]) of a molecular BEC. We aligned the potential by monitoring the strength of scattered orders, a process we found to be time consuming and imprecise. It is easier to align the lattice beams by imaging the position of the atoms along vertical and horizontal imaging axes and then calibrate the depth using amplitude modulation in a deep lattice. The lattice depth at lower intensity can be estimated by scaling this measured depth.

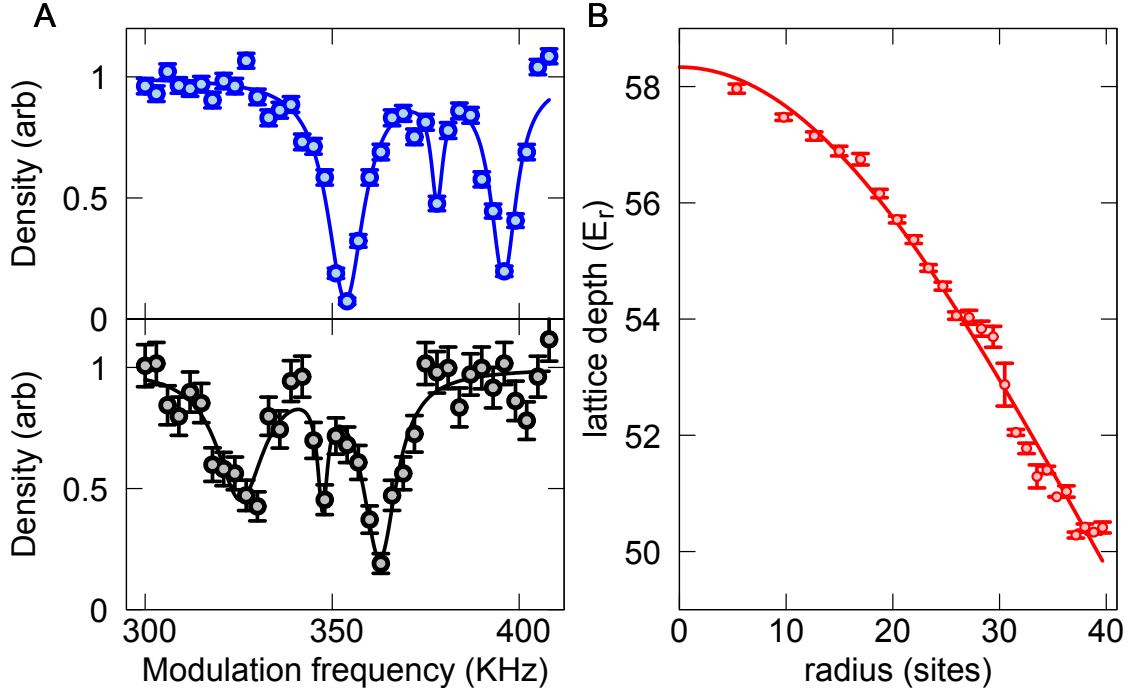


Figure 2.6: **Lattice intensity modulation spectroscopy.** **A**, Atomic density versus modulation frequency (points) and a three Lorentzian fit (line) for atoms in the center of the trap, $r = 0 - 8$ sites (upper, blue) and at the edge $r = 37.5 - 38.5$ sites (lower, black). **B**, Experimental lattice depth obtained from locally resolved intensity modulation spectroscopy versus spatial position (points) and a Gaussian fit to the experimental result (line).

We perform amplitude modulation spectroscopy by combining the lattice intensity stabilization servo output with a modulation signal using a bias-T. We work in a deep lattice, $\sim 60 E_r$ to easily resolve different bands, and measure atom loss versus frequency, scaling the modulation time to keep the number of periods fixed. We typically observe loss features due to transitions between the s -band and the three d -bands, and fit these to Lorentzians to determine their centers and widths, as shown in fig. 2.6A. Then, we determine the lattice depth V_o and the retro-reflection electric field amplitude attenuation factor r by performing a least squares fit to the band gaps, determined from a band structure calculation, with the Lorentzian centers.

Due to the Gaussian shape of the lattice beams, the depth of the lattice varies away from the beam center with a Gaussian envelope. We measure this variation in depth using locally resolved intensity modulation spectroscopy (fig. 2.6B). The relatively large trap variation is caused by the small 70 μm waist beams we employ. The small beam waist is necessary to obtain sufficient trapping frequency for efficient Raman imaging. However, it leads to several undesirable effects in the science lattice configuration, including strong variation of the atomic density versus position and variation of U/t across the trap.

2.5.2 Phase stability

The optical lattice potential, eq. 2.27, is stable against changes in the beam path lengths without active phase stabilization [118]. This is because, compared with a four beam lattice derived from two separate lasers with the same polarization (which *requires* phase stabilization), this topology has one fewer phase degree of freedom.

For this lattice we have three degrees of phase freedom which are the phase of the incoming beam (which can be neglected), the path length between the first and second passes, l , and the path length from the second pass to the retro-reflection

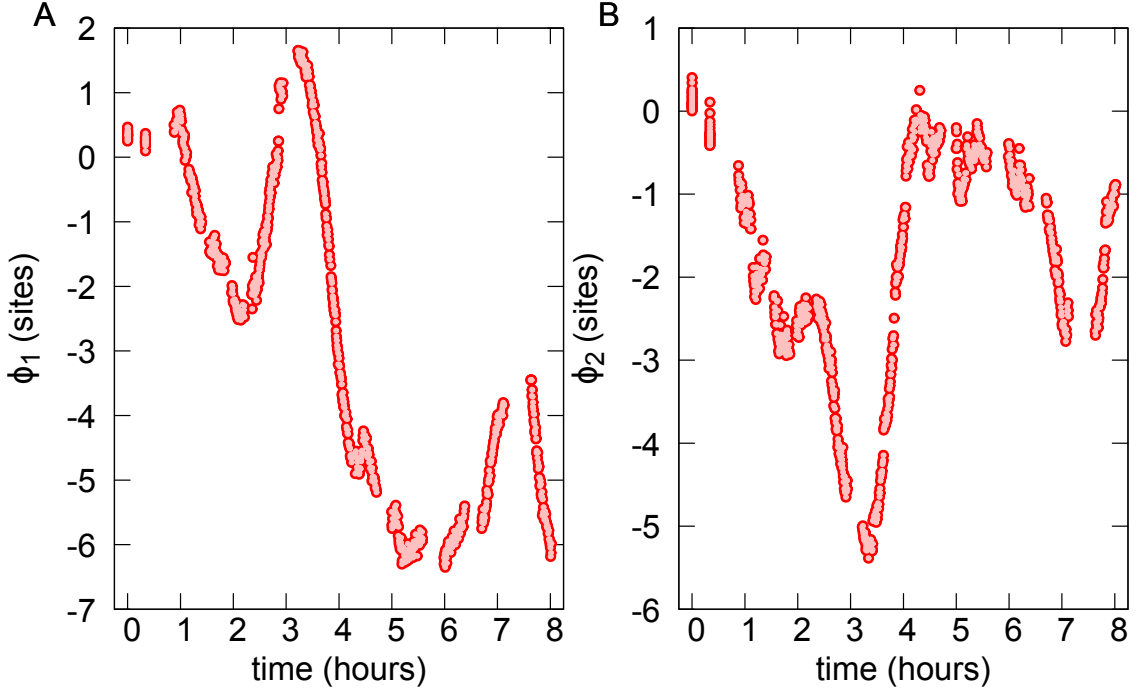


Figure 2.7: **Lattice phase drift.** **A**, Lattice phase ϕ_1 inferred from reconstruction after phase unwinding over the course of 8 hours. The phase drifts slowly, at most a few lattice sites per hour. **B**, Lattice phase ϕ_2 .

mirror l_r . We find that the potential V can be written

$$V(x, y) = V_o(x - \delta l - \delta l_r, y - \delta l_r), \quad (2.31)$$

where V_o is the potential with zero phase factors. We find that changing the path length between the first and second pass by δl shifts the lattice along the x -direction by δl , whereas changing the path length to the retro-reflection mirror by δl_r shifts the lattice along the $x + y$ -direction by length $\sqrt{2}\delta l_r$.

We observe long term phase drifts in the lattice potential by using our reconstruction algorithm to determine the quantities ϕ_1 and ϕ_2 , defined by eq. 2.1, from a sequence of fluorescence images. Over the course of 8 hours, the position of the lattice minimum drifts by a few sites, with typical drift rate less than 2 sites/h (fig. 2.7). The slow scale of the drift is consistent with thermal effects, which can change the path

lengths l and l_r . Abrupt changes in the lattice phase may be caused by adjusting the focus of the camera. This phase drift is not important for the experiments considered in this work, but might pose difficulties for experiments that require single-site addressing.

2.5.3 Pointing noise

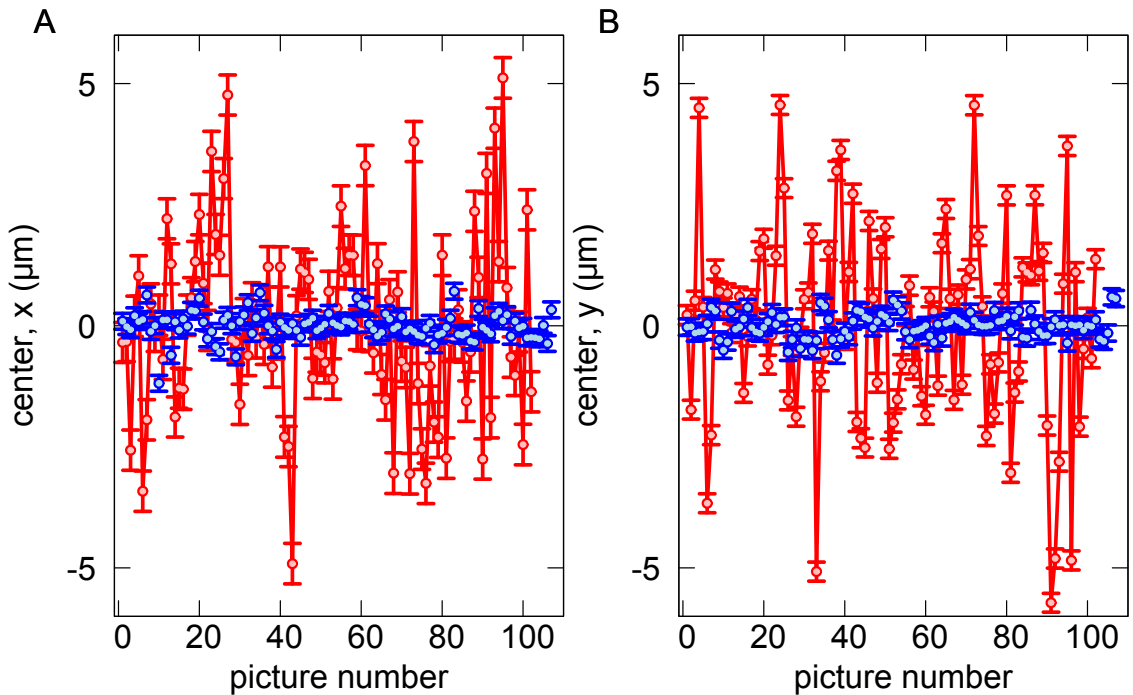


Figure 2.8: **Optical lattice pointing stability.** **A**, Beam x -position versus shot number for the MOPA laser (red) and the laser after being fiber coupled (blue). **B**, Beam y -position. The beam position is significantly more stable after being coupled into a fiber.

In addition to phase drift of the lattice, we observe shot-to-shot fluctuations in the center of mass of the atom cloud with typical standard deviation 1-2 sites. This effect is significant enough that it is difficult to e.g. flatten the optical potential using the DMD. Due to this shaking it is possible to produce a potential that is flat *on average*, but individual shots have densities concentrated to one side or another. This effect appears to originate from positional instability of the laser used to generate the

lattice. We quantify the shaking amplitude by focusing the beam to a waist of 175 μm using a test setup and imaging the position on a ALLIED VISION TECHNOLOGIES Guppy F-080B CCD camera with a repetition rate of 4 Hz and imaging exposure time of 1 ms. The total beam path is $\sim 1 \text{ m}$, similar to that used in the experiment. We determine the beam center using a Gaussian fit, and find a standard deviation of about 2 μm in the position (fig. 2.8), which is already smaller than the 4.65 μm camera pixels. To verify this effect is due to beam shaking, we compare these results with measurements taken after coupling the beam into a fiber. The standard deviation in position of the fiber coupled beam is less than 0.3 μm , similar to the fitting uncertainty due to the spatial digitization of the image.

2.5.4 Intensity noise

Reaching the low temperatures required to access interesting physics in the experiment requires mitigation of optical intensity noise, which causes heating in optical traps. Intensity noise heating is characterized by an exponential energy increase with rate constant Γ . For atoms in a harmonic trap, this rate is [120],

$$\Gamma = \frac{\pi}{2} \omega^2 \frac{S_{PP}(2\omega)}{\langle P \rangle^2}, \quad (2.32)$$

where ω is the harmonic trap frequency, $\langle P \rangle$ is the mean optical power, and S_{PP} is the one-sided power-spectral density of the optical power.

For a noisy signal $P(t)$, the one-sided power spectral density is given by

$$S_{PP}(\omega) = 2 \langle |P(\omega)|^2 \rangle \quad (2.33)$$

$$= \int_0^\infty d\tau \langle P(t)P(t+\tau) \rangle e^{-i\omega\tau}. \quad (2.34)$$

where $P(\omega)$ is the Fourier transform of $P(t)$ over a finite time T given by

$$P(\omega) = \frac{1}{\sqrt{T}} \int_0^T dt P(t) e^{-i\omega t}. \quad (2.35)$$

Eq. 2.34 expresses the power spectral density as the Fourier transform of the autocorrelation of the noisy signal, a result known as the *Wiener-Khinchin theorem*, which provides a convenient method of calculating this quantity. If P is an optical power signal, the power spectral density has units of W^2/Hz . However, it is more common to quote $\sqrt{S_{PP}(\omega)}$ in units of $\text{W}/\text{Hz}^{1/2}$.

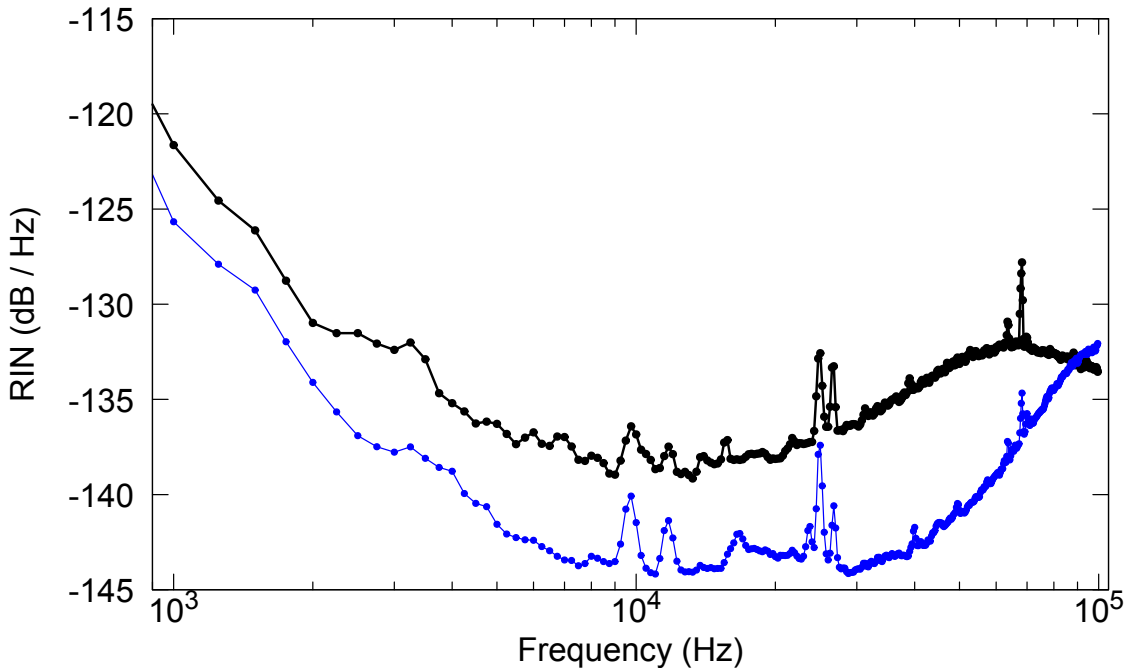


Figure 2.9: **Optical lattice intensity noise spectra.** Lattice intensity noise for depths of $8.4 E_r$ (black) and $50 E_r$ (blue). Minimum RIN values are obtained at frequencies ranging from several hundred Hz to several kHz, on the range of the tunneling rate and Hubbard interaction.

As eq. 2.32 demonstrates, the fractional power fluctuations are the relevant quantity to assess heating processes. We will quote these in terms of the residual intensity

noise (RIN) defined by

$$\text{RIN}_{PP}(\omega) = \frac{S_{PP}(\omega)}{\langle P \rangle^2}, \quad (2.36)$$

which has units of $1/\text{Hz}$. We more typically quote $10 \log_{10}(\text{RIN})$ in units of dB/Hz . The fundamental lower limit on the obtainable RIN for optical power comes from shot noise. For an optical signal with frequency ν , $S_{pp}(\omega) = 2h\nu \langle P \rangle$, giving $\text{RIN} = \frac{2h\nu}{\langle P \rangle}$.

We assess the noise performance of the optical lattice intensity stabilization (see section 2.6) by measuring the intensity noise on a THORLABS PDA36A amplified photodiode, similar to the setup discussed in [121]. The photodiode produces a current which is proportional to the incident optical power. We then measure a voltage across a resistor using an SR770 Fourier transform network analyzer (STANFORD RESEARCH SYSTEMS). The voltage signal is proportional to the intensity signal, and therefore will have the same RIN as long as intensity noise dominates sources of electronic noise, such as Johnson noise in the photodiode and detection circuitry. The photodiode noise sources are quantified in terms of the *noise equivalent power* (NEP), which is often massaged to produce a single number on a data sheet by defining

$$\text{NEP}_{\text{spec}} = \frac{\sqrt{S_{II}}}{\max_{\lambda}[R(\lambda)]}, \quad (2.37)$$

where R is the photodiode sensitivity in A/W and S_{II} is the total electronic noise written as a current spectral density. The NEP at a given wavelength is then $\text{NEP}(\lambda) = \max_{\lambda}[R(\lambda)]/R(\lambda) \times \text{NEP}_{\text{spec}}$. The PDA36A is specified to have $\text{NEP}(1064 \text{ nm}) = 4.55 \times 10^{-11} \text{ W/Hz}^{-1/2}$.

We reach minimum RIN for the optical lattice intensity near 300-5000 Hz of -135 dB/Hz (fig. 2.9). Minimizing noise in this frequency range is critical because the Hubbard energy scales t and U are typically of a similar order. We find that the RIN improves at larger intensities, as expected. At beam power 80 mW and lattice

depth $8.4 E_r$ the minimum RIN is -135 dB/Hz , whereas for 450 mW or $50 E_r$ the minimum RIN is -140 dB/Hz (fig. 2.9). These values are similar to what was achieved in [121]. The shot noise limits for these two powers are -173 dB/Hz and -180 dB/Hz respectively. The photodetector noise floor is expected to be smaller than the shot noise limits, corresponding to RIN's of -185 dB/Hz and -200 dB/Hz respectively.

2.6 Laser intensity stabilization

The laser intensity stabilization discussed in section 2.5.4 is accomplished using an acousto-optic modulator (AOM) driven with variable rf power, which is controlled by servo electronics. The servo electronics detect the current laser intensity, compare it with the desired set-point, and adjust the rf power to correct any deviation.

We developed a home built intensity stabilization servo circuit based on a pair of cascaded PI stages and a transistor emitter follower output driver stage, shown in fig. 2.10. To avoid integrator windup, we also include MOSFET based relays which short the PI stages when they receive a TTL signal. This circuit is relatively simple and flexible enough to be used not only for power stabilization, but also magnetic field stabilization and other general purpose use in the lab.

The servo is designed as follows. A set-point voltage and the signal to be stabilized are connected to differential amplifier inputs. One input is inverting, and other is non-inverting, therefore adding the outputs together subtracts the set-point and signal, creating the error signal. The error signal is passed to a pair of cascaded PI stages. The PI stage frequency response is adjustable using a pair of potentiometers and switchable capacitors. The output of the PI stage is fed to a transistor emitter follower driver stage, capable of supplying moderate current.

The servo voltage signal is sent to either a voltage variable attenuator (VVA) or a mixer which modulates the rf intensity. For non-critical applications, we use VVAs

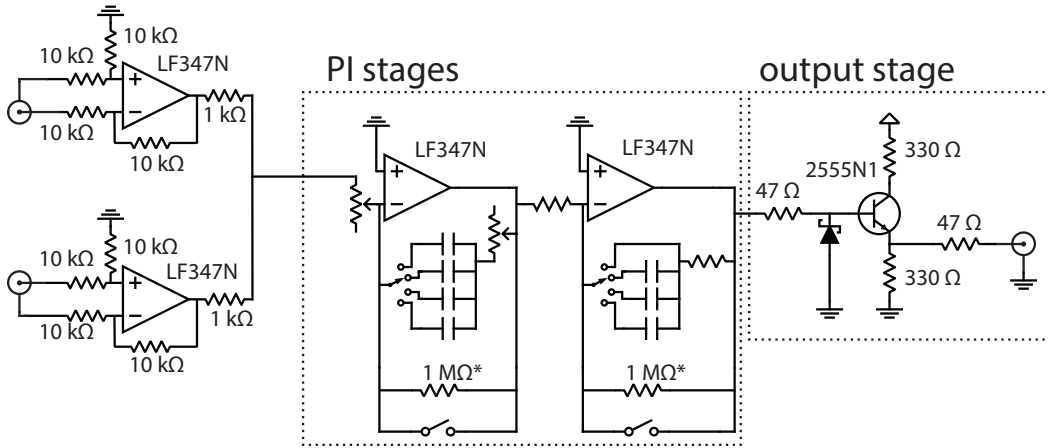


Figure 2.10: **Laser intensity stabilization servo circuit diagram.** Circuit diagram for the laser intensity stabilization circuit board. On the left are the inverting and non-inverting input differential amplifiers. These are summed, and the error signal is passed to the PI stages. The output stage is an emitter follower driver which can supply more current than the op amps. The 330Ω collector resistor limits the current, and should be selected based on the current limit of the component being driven to prevent damage. Components with values marked by an asterisk are optional.

which have the advantage that they can suppress the rf power more than 40 dB, but typically have low bandwidth ($< 100\text{ kHz}$) and small input impedance. Driving a VVA in the on state can require upwards of 20 mA , which is more than some op amps can supply. This current is supplied by the driver output stage of the intensity servo. Mixers provide less power suppression, but are much faster than VVAs.

The noise suppression performance of our laser intensity servos are limited by the maximum achievable bandwidth of the feedback loop. The bandwidth is fundamentally limited by the speed of sound in the AOM crystal to about $300\text{-}400\text{ kHz}$, meaning noise can be efficiently suppressed at frequencies up to a few tens of kilohertz. Faster servo response requires a power modulation device which is not based on acoustic waves, for example a Pockels cell based on an electric field modulating the phase delay through a crystal.

2.7 Spatial light modulator setup

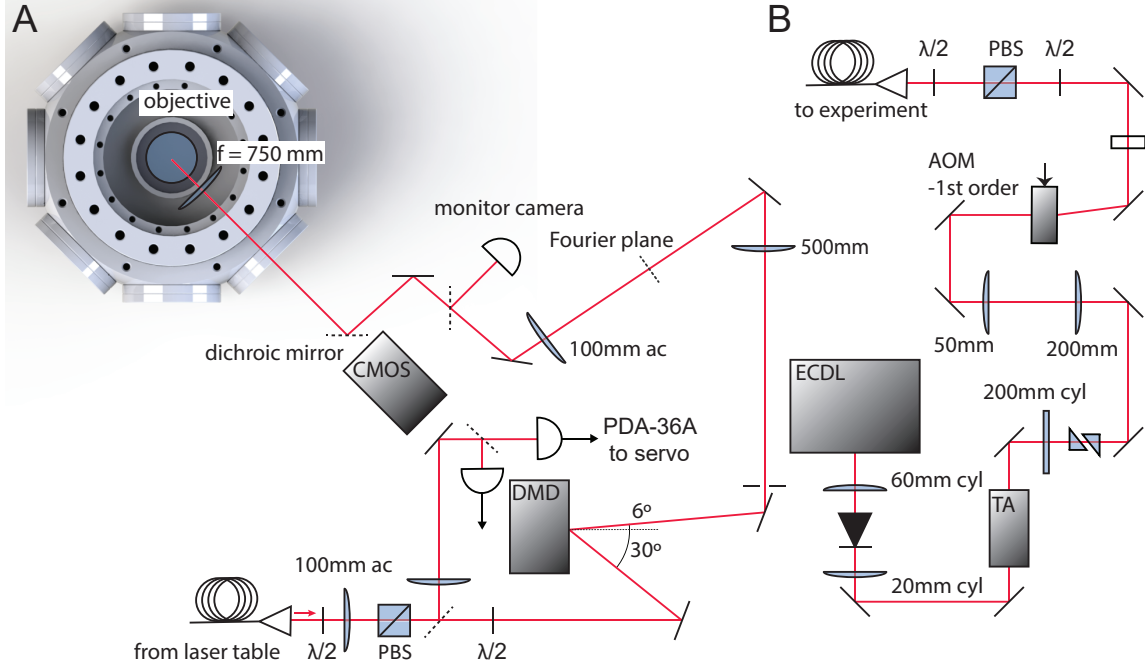


Figure 2.11: **DMD optical setup.** **A**, DMD optical system including intensity stabilization monitors, demagnification optics, and the imaging system. **B**, Coherent 650 nm light generation setup. A home built ECDL seeds a tapered amplifier. Intensity of the light is controlled by an AOM and servoed using the photodiodes shown in panel A.

We use a digital mirror device (DMD) as a spatial light modulator (SLM) to project arbitrary potential patterns on the atoms. The DMD is arranged in an imaging plane configuration because we typically project patterns with large spatial frequencies, and the imaging plane configuration is more efficient than the Fourier plane configuration for this application [122, 123, 124].

To produce the optical potentials we use up to 15 mW of 650 nm coherent light derived from a tapered amplifier (EAGLEYARD EYP-TPA-0650-00250-2007-CMTO02-0000) seeded by a home built external cavity diode laser (ECDL) using a TOPTICA LD-0650-0040-AR-2 laser diode. The ECDL is based on the design described in [125]. The laser system used to produce this light, shown in fig. 2.11B, is located on a separate table from the experiment. The light is coupled into an optical fiber and guided

to the DMD setup, shown in fig. 2.11A. We illuminate the DMD with a Gaussian beam of waist ~ 1 cm, which is intensity stabilized by an INTRAACTION model ATM 1141A1 AOM.

We use a TEXAS INSTRUMENTS DLP Discovery 4100 development kit with a DLP7000 DMD. The mirrors are arranged on a square grid with a mirror separation of $a = 13.68 \mu\text{m}$. The mirrors swivel at 45° to the grid axis. In the on (off) state the normal of the micromirror plane makes an angle of $12^\circ(-12^\circ)$ with the underlying device. We mount the DMD at a 45° angle compared to the grid axis so that the micromirrors swivel in a plane parallel to the optical table.

The path of the incoming light forms an angle of $\theta_{\text{in}} = 30^\circ$ with the normal to the DMD and we utilize the $m = 6$ diffraction order leading to an outgoing angle of $\theta_{\text{out}} = 6^\circ$. These choices satisfy both the diffraction condition and the Blaze condition which are

$$m = \frac{d}{\lambda} [\sin(\theta_{\text{in}}) - \sin(\theta_{\text{out}})] \quad (2.38)$$

$$\theta_{\text{out}} = \theta_{\text{in}} - 2\theta_{\text{Blaze}}, \quad (2.39)$$

where $d = a/\sqrt{2} = 9.8 \mu\text{m}$ is the distance between mirrors along horizontal direction and $\theta_{\text{Blaze}} = 12^\circ$.

We image this light onto the atoms using two stages of demagnification. First, we demagnify the DMD image by a factor of 5 using a telescope formed by the 500 mm and 100 mm lenses shown in fig. 2.11A. These two lenses form a $4f$ imaging system with the DMD in the imaging plane. The Fourier plane of this imaging system may be used to spatially filter the light pattern. Next we combine the DMD projection path with the imaging path on long-pass dichroic mirror, SEMROCK BrightLine Di03-R635-t1. The imaging system demagnifies the light by an additional factor of 30. A square of approximately 8×8 mirrors determines the potential at a single lattice

site. We produce binary images from continuous potential profiles using the Floyd-Steinberg error diffusion algorithm [126]. The imaging system spatially filters the binary image, resulting in a smooth potential at the atoms.

We can either project a single static pattern, or change the pattern dynamically with a maximum frame rate of ~ 20 kHz. When running in dynamic mode the DMD displays successive images after receiving a trigger, and it is therefore possible to use arbitrary timings for each frame. By default, each image is displayed for a fixed time and then the DMD reverts to the off state. We use the ALP-4.2 API “uninterruptible binary mode” to keep the image on the DMD until the next trigger. The DMD transitions between images in approximately $10\text{ }\mu\text{s}$. During this time, all mirrors go to the off state, and then the mirrors needed for the next image are turned to the on state. The motion of the mirrors is underdamped, and we observe the mirrors bouncing by measuring diffracted light on a photodiode.

The DMD setup is programmed by the factory to cycle all mirrors from their initial position to the off position and back every 10 s to prevent any mirror from becoming stuck. This time is sufficiently long compared to the ~ 100 ms that the DMD is used for in the experiment that such events rarely affect the atoms. In some DMD devices the refresh rate is much faster and requires significant effort to modify [127].

We can regard the imaging system as a coordinate transformation between the object space with coordinates (x_o, y_o) aligned with the DMD and the image space with coordinates (x_i, y_i) aligned with the camera sensor. The transformation between these coordinates involves a rotation parameterized by angle θ between the coordinate axes, a scale factor S , and a shift in origin. It is given by

$$\begin{pmatrix} x_o \\ y_o \end{pmatrix} = T \begin{pmatrix} x_i \\ y_i \end{pmatrix} = \frac{1}{S} \begin{pmatrix} \cos(\theta) & -\sin(\theta) \\ \sin(\theta) & \cos(\theta) \end{pmatrix} \left(\begin{pmatrix} x_i \\ y_i \end{pmatrix} - \begin{pmatrix} c_x \\ c_y \end{pmatrix} \right). \quad (2.40)$$

Composing this transformation with eq. 2.1 gives the transformation between the DMD coordinate space and the lattice coordinate space.

The relationship between the electric field at the DMD, $E_o(x_o, y_o)$, and the electric field at the atoms is given in terms of the point-spread function of the imaging system, P , and the object to image space coordinate transformation, T ,

$$E(x_i, y_i) = \int dx_o dy_o E_o(x_o, y_o) P \left(T \begin{pmatrix} x_i \\ y_i \end{pmatrix} - \begin{pmatrix} x_o \\ y_o \end{pmatrix} \right). \quad (2.41)$$

To determine the relationship between the intensity pattern at the DMD and the atoms, we must distinguish two different regimes. In the first, the size of the point-spread function is less than the size of a DMD pixel. In this case, we only have a smooth intensity pattern if we coarse grain the intensity distribution in the imaging plane. Then the coarse grained intensity is proportional to the density of “on” pixels. In the second regime, the size of the point-spread function is greater than the size of a single pixel. In this case, light from different pixels interferes, and the intensity in the imaging plane is proportional to the square of the number of “on” pixels. We operate our setup in the second regime, and we account for this fact when generating DMD patterns to be projected on the atoms.

2.8 Bias magnetic field stabilization

Many atomic properties are dependent on the magnetic field intensity, including the energy difference between hyperfine states and scattering properties of various spin mixtures. Typical ambient magnetic field fluctuations in the lab are on the order of 1 mG. To perform experiments where these field fluctuations cause significant changes in atomic parameters, it is necessary to stabilize at least one component of the magnetic field.

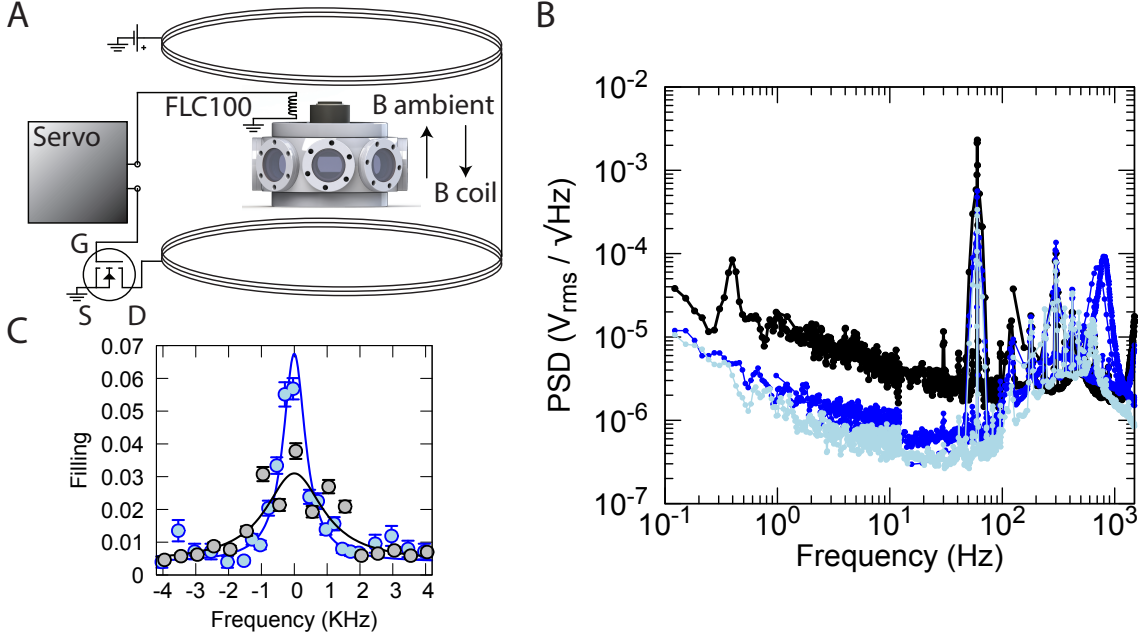


Figure 2.12: Magnetic bias field stabilization setup. **A**, Schematic of the bias magnetic field stabilization setup. **B**, Power spectral density of the fluxgate sensor signal for the unstabilized field (black), stabilized field using a single integrator (dark blue), and stabilized field using two integrators (light blue). The servo improves the noise performance by roughly an order of magnitude for frequencies below 100 Hz. **C**, Rf spectra taken both with (blue) and without (black) magnetic field stabilization. When the stabilization is on, the spectral line narrows and the variance in the atom transfer decreases.

These issues arise most commonly when working at low bias fields, $< 1 \text{ G}$, where the background magnetic field fluctuations are fractionally much larger than when working at hundreds of Gauss. Although many ${}^6\text{Li}$ experiments work in the vicinity of the broad Feshbach resonance, this atom has a number of desirable scattering properties at small bias fields, $< 200 \text{ mG}$. Here the scattering length a_{13} becomes large [128], while the other scattering lengths among the lowest three hyperfine states are negligible. However, the $|1\rangle - |2\rangle$ and $|2\rangle - |3\rangle$ splittings are field sensitive, with approximate slopes 0.93 MHz/G and 1.87 MHz/G respectively at 100 mG .

Reaching stable bias fields which are smaller than Earth's field, $\sim 500 \text{ mG}$, requires control over all three field directions and active stabilization. To produce a bias field in the z -direction, it is necessary to null the ambient fields in the x - and y -

directions. We do this using two pairs of coils driven by stable current sources. Even at 100 mG the quadrature addition of field components suppresses the effect of fluctuations in these directions. We then actively stabilize the field in the z -direction. We measure the z -field using a Stefan Mayer FLC100 fluxgate sensor [129] positioned above the vacuum chamber, and control it using a Helmholtz coil of radius ~ 0.5 m and a home built servo (described in section 2.6) driving an n-channel power MOSFET (STMICROELECTRONICS STW20NM60FD) as shown in fig. 2.12A.

This geometry is susceptible to several undesirable effects. The fluxgate sensor is far from the atoms and thus only fields which are uniform in space can be nulled. Furthermore, the sensor is sensitive to fringing fields from the x - and y -coils, and as such will respond to any current noise from these supplies.

We assess the stabilization at the sensor position by measuring field noise on the fluxgate sensor using an SR770 Fourier transform network analyzer (STANFORD RESEARCH SYSTEMS). We find this setup suppresses the noise by about one order of magnitude in the frequency range 1-100 Hz (fig. 2.12B). Achieving higher low-frequency gain to suppress this noise further requires increasing the bandwidth of our sensor, which is about 1 kHz.

We characterize the field stability at the position of the atoms by measuring the width of an rf transition between two hyperfine states. We determine the magnetic field fluctuations by measuring the width of a series of rf spectra with increasing pulse length and decreasing power. For the shortest pulses, the spectral width is dominated by Fourier broadening. As the power is decreased and the time is increased, the field noise eventually dominates the spectral width. Because the field fluctuations are typically slow compared with the length of the rf pulse, the signal is extremely noisy in this regime and requires substantial averaging to obtain an accurate width. The best compromise is to find a point where the Fourier broadening is comparable to the field broadening, and a spectrum can still be measured with only a few averages.

To eliminate the effects of interactions, we perform this measurement on a polarized gas of $|3\rangle$'s in a deep optical lattice ($\sim 60 E_r$), which suppresses tunneling, and measure spectra using the $|2\rangle - |3\rangle$ transition. We fit the resulting spectra to a Lorentzian line shape and find a minimum half-width at half-maximum of ~ 300 Hz. The full width corresponds to a field fluctuation of 0.3 mG.

We assess the long term stability of our field by measuring the resonance frequency of the polarized gas at different times during the course of a day. We observe frequency drifts of ~ 1 kHz (0.5 mG) over a period of ~ 1 h.

2.9 Magnetic field gradient calibration

The magnetic field gradients used during several stages of the evaporation procedure are critical to reaching low temperatures in the experiment. Field gradients are also an important tool which can be used to prepare spin patterns in the gas [130], measure spin correlations [55], or probe the magnetic susceptibility of the gas. Therefore, it is desirable to have a method of calibrating the strength of the field gradient.

We calibrate magnetic field gradients in the imaging plane by preparing a polarized gas in a $60 E_r$ lattice and performing a Ramsey sequence. In the Ramsey sequence, we first apply a $\pi/2$ pulse to rotate the spins into a coherent mixture of up and down, allow these to precess for time τ , then perform a second $\pi/2$ pulse, and detect the up spins. In a magnetic field gradient, spins at different positions will evolve at different speeds, leading to a sinusoidal distribution of probability to be in one spin state. An imperfect $\pi/2$ pulse reduces the amount of contrast but does not affect the shape of this pattern.

Given an rf rotation about the x -axis through an angle θ and a magnetic field $B(z) = z\partial_z B$ the probability of measuring a down spin at position z is

$$\mathbb{P}(\downarrow, z) = 2 \sin^2(\theta/2) \cos^2(\theta/2) [1 + \cos(\partial_z B(m_\uparrow - m_\downarrow)z\tau/\hbar)] \quad (2.42)$$

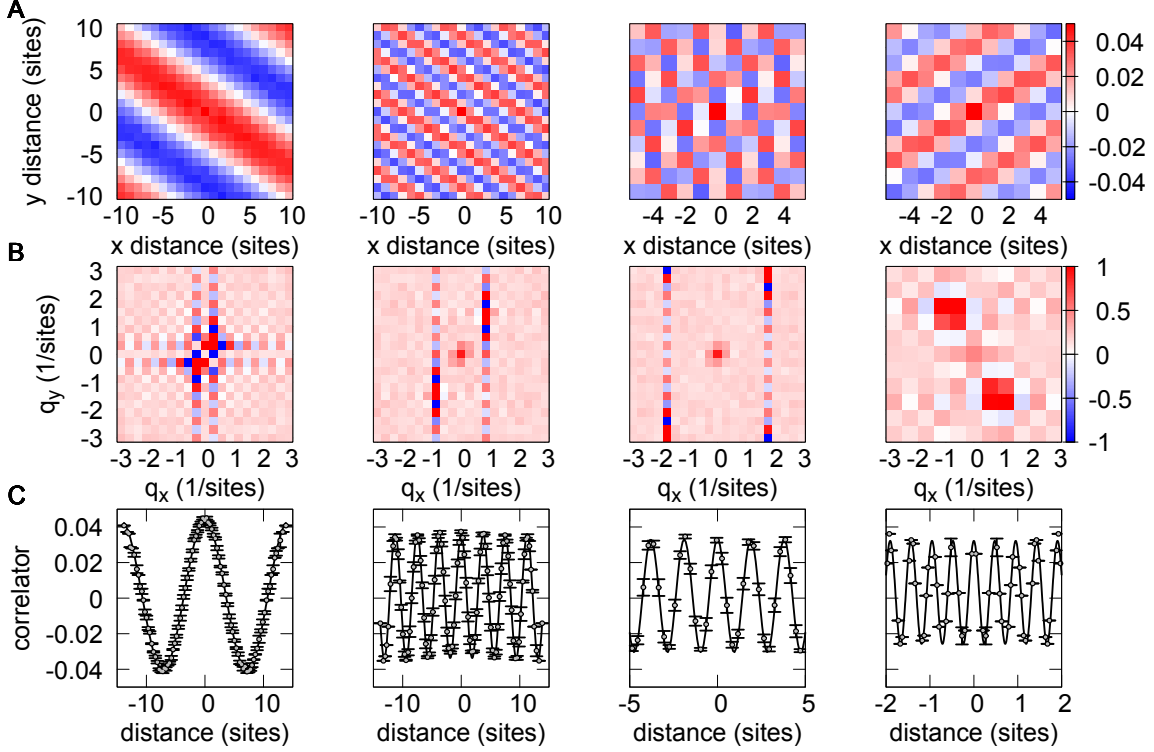


Figure 2.13: **Magnetic field gradient calibration.** **A**, Correlation versus distance for the spin spiral pattern using a series of Ramsey hold times $\tau = 250 \mu\text{s}, 1 \text{ ms}, 2 \text{ ms}, 8 \text{ ms}$ (left to right). **B**, 2D Fourier transforms associated with the panels in A. **C**, 1D averages of the correlation matrices taken along an angle of -57° and sinusoidal fits to these patterns which give periods of $14.34(2) a$, $3.757(2) a$, $1.870(4) a$ and $0.4766(2) a$.

where m_σ are the magnetic moments of the two spin states. The magnetic field gradient in terms of the wavelength λ of the spin spiral is

$$\partial_z B = \frac{1}{\left(\frac{m_\uparrow - m_\downarrow}{h}\right) \lambda \tau}. \quad (2.43)$$

In the experiment, we look at spatial correlations between spins instead of the spin density because these correlations are insensitive to overall field drifts which can shift the location of the spin pattern. By measuring these for a variety of Ramsey hold times, we determine the strength of the gradient with high precision. We show the full correlation matrices for a variety of hold times in fig. 2.13A, and the associated structure factors in fig. 2.13B. For the two rightmost panels, the period of the density

pattern is less than the lattice spacing, which leads to aliasing effects. The true periodicity of the pattern corresponds to the visible peaks in the structure factor shifted by $\pm 2\pi$ in the y -direction. To determine the periodicity, we average the correlation matrix along the direction orthogonal to the pattern and fit the result to a cosine, as shown in fig. 2.13C. We find that at a bias field of 50 G the MOT coils produce a maximum gradient in the imaging plane of $1.75 \times 10^{-4} \text{ G}/a = 2.33 \text{ G}/\text{cm}$.

Chapter 3

Theoretical background

In this chapter we introduce the Fermi-Hubbard model, which describes the cold atom gas prepared using the apparatus outlined in chapter 2, and discuss various theoretical tools required to understand the Fermi-Hubbard gas. Many tutorial reviews (e.g. [131, 132, 133, 134, 135]) and more complete references [136, 137, 138, 139, 140] on Fermi-Hubbard physics are available, but most are written from a condensed matter point of view. Cold atom systems have very different capabilities than condensed matter experiments, meaning that quantities or regimes of little interest in condensed matter are relevant to cold atom experimentalists. It is our aim to collect many of these results in a coherent framework useful for those working in cold atoms, and more specifically with fermion QGM's.

We structure this chapter as follows. First, we introduce the Fermi-Hubbard Hamiltonian and discuss a number of its properties, including its symmetries and close connection to the Heisenberg and $t-J$ models. Next, we discuss several tractable limiting cases of the Hubbard model, including the non-interacting Fermi gas, the infinite temperature limit, and the atomic limit. These cases provide valuable perspective as they reveal which aspects of Hubbard physics are due to strong interactions, and which are a result of Fermi statistics or other features. Finally, we review the linear

response formalism which is used extensively to compare experimental results with theory calculations in chapters 4, 5, and 6.

3.1 The Fermi-Hubbard Model

The Fermi-Hubbard Hamiltonian is a model for strongly correlated physics which is widely studied because of the rich structure present in its phase diagram, a result of competition between the interaction, temperature, doping, and dimensionality. Although we often consider the Hubbard system because it may describe the essential physics of high- T_c superconductivity, it is an interesting and important subject in its own right.

There has been immense theoretical effort to elucidate the physics of the Fermi-Hubbard model using a wide variety of analytic and numerical techniques. A handful of cases can be exactly solved or efficiently simulated. These are primarily the 1D Hubbard chain, which can be solved using a Bethe ansatz solution [141], a single hole in a half-filled background for $U = \infty$ in arbitrary dimension [142], and the infinite-dimensional model [143, 144] which can be simulated efficiently using dynamical mean-field theory [145, 146, 147]. On the other hand, the two-dimensional model is neither amenable to the same methods as the one-dimensional model nor well captured by mean-field theory. Therefore, numerical techniques on small clusters are the primary tools used to study the 2D case in the strong interaction regime [21]. For attractive interactions, the ground state of the model can be explored using determinantal quantum Monte Carlo (DQMC). For repulsive interactions, the Fermion sign problem prevents DQMC from accessing this regime, and the nature of the ground state remains an open question.

The two-dimensional Fermi-Hubbard Hamiltonian describes two species of fermions on a lattice interacting via an on-site interaction. On a square lattice, it is

written

$$\mathcal{H}_o = -t \sum_{\langle i,j \rangle \sigma} \left(c_{i\sigma}^\dagger c_{j\sigma} + \text{h.c.} \right) + U \sum_i n_{i\uparrow} n_{i\downarrow} \quad (3.1)$$

where $c_{i\sigma}^\dagger$ is the creation operator for a particle of spin $\sigma \in \{\uparrow, \downarrow\}$ on site $i = (i_x, i_y)$, $\langle i, j \rangle$ denotes a sum over nearest-neighbor sites, and $n_{i\sigma} = c_{i\sigma}^\dagger c_{i\sigma}$. The first term represents the kinetic energy and describes the tendency of particles to tunnel between sites, with a characteristic tunneling energy t . The second term describes the on-site interaction between particles of opposite spins of strength U , which may be either attractive or repulsive. Pauli exclusion forbids two particles of the same spin occupying the same site.

The model describes competition between the tunneling term, which favors delocalizing particles, and the interaction term, which favors localizing particles. For weak interactions, $U/t \ll 1$ the tunneling term dominates and the system is metallic for fillings $n_\sigma < 1$. At $n_\sigma = 1$ the system forms a band insulator. For strong interaction, $U/t \gg 1$, a repulsive interaction strongly penalizes double occupancies. The intermediate regime is characterized by the interaction energy and band width being comparable, $U/t \sim 8$ in the 2D model. For intermediate and strong repulsive interactions and low temperature, a Mott insulating state develops at *half-filling*, $n_\sigma = 0.5$. At even lower temperature, antiferromagnetic correlations develop, driven by *superexchange* interactions [148, 149]. Superexchange is a second-order virtual process whereby a particle tunnels to a neighboring occupied site and tunnels back. This process is only allowed if the other site is occupied by an opposite spin particle.

We can make explicit the role of the particle number, or doping, in the problem by writing the Hamiltonian in the grand canonical ensemble. In terms of the mean chemical potential, $\bar{\mu} = \frac{1}{2}(\mu_\uparrow + \mu_\downarrow)$, and the chemical potential imbalance, $h = \frac{1}{2}(\mu_\uparrow - \mu_\downarrow)$, this is

$$\mathcal{H}_{\text{GC}} = \mathcal{H}_o - \bar{\mu} \sum_i (n_{i\uparrow} + n_{i\downarrow}) - h \sum_i (n_{i\uparrow} - n_{i\downarrow}). \quad (3.2)$$

It is well known that strong quantum fluctuations destroy true long-range order in one- or two-dimensions [150, 151]. However, the existence of a superfluid like state with algebraically decaying correlations is possible through the BKT mechanism [152, 153]. The 2D attractive Fermi-Hubbard model has an *s*-wave superfluid ground state [154]. Numerical evidence from looking at the *d*-wave pairing susceptibility suggests the repulsive model may possess a *d*-wave superfluid state at low temperature and finite doping [155].

3.1.1 Hubbard parameters in cold atoms and the cuprates

The Hubbard model describes ultracold fermions in optical lattices, and is also believed to describe the essential physics of the cuprate superconductors. The difference between typical energy scales for ultracold atomic systems and electrons in cuprates is nearly 11 orders of magnitude. Nevertheless, the Hubbard model can describe both because the relevant parameters are ratios between the absolute energies and a characteristic energy scale, typically the tunneling energy, t .

In cold atom Fermi-Hubbard systems, typical tunneling energies are $t = \hbar \times 0.1 - 1 \text{ kHz}$, corresponding to temperatures of a few tens of nK. Interaction energies are $U = \hbar \times 1 - 10 \text{ kHz}$, and a wide range of U/t values can be obtained. Temperatures as low as $T = 0.25t$ [73] and as large as the band width, $T = 8t$ [82] have been realized.

In the cuprates, the tunneling parameter is roughly the same for various materials and can be obtained from band structure calculations, which find $t = 300 - 400 \text{ meV}$ [9, 156]. The tunneling energy corresponds to a temperature of roughly 4000 K. The diagonal tunneling term is also significant, with $t' = -0.1 - -0.3t$. The on-site interaction energy is $U = 2 - 3 \text{ eV}$ [157], implying that $U/t = 4 - 10$.

Near room temperature, the ratio of the temperature to the tunneling for the cuprates is smaller than what is currently achievable in ultracold gases, reaching $T/t \sim 0.08$ at 300 K. The highest temperature any cuprate material has been studied at is

~ 1100 K or $T/t \sim 0.3$ [158], near the *lowest* temperature achievable in ultracold gases. Achieving temperatures at and above this range is limited by structural transitions or other effects. Superconducting transition temperatures range from about 35 K in the Ba-La-Cu-O system [5] to 130 K in the Hg-Ba-Ca-Cu-O system [159] corresponding to $T_c/t = 0.01 - 0.04$.

3.1.2 Particle-hole symmetry

The Hubbard model on a bipartite lattice has particle-hole symmetry which gives a one-to-one correspondence between states above and below half-filling. Due to this symmetry the Hubbard phase diagram is symmetric about the half-filling point and it is sufficient to consider either the case of particle or hole doping. On a square lattice, we implement a particle-hole transformation which acts on real space and momentum space as follows

$$\Gamma c_{i\sigma} \Gamma^\dagger = (-1)^{i_x+i_y} c_{i\sigma}^\dagger \quad (3.3)$$

$$\Gamma c_{k\sigma} \Gamma^\dagger = c_{k+Q\sigma}^\dagger, \quad (3.4)$$

where $Q = (\pi, \pi)$. This is called a particle-hole transformation because it acts on number operators by $\Gamma n_{i\sigma} \Gamma^\dagger = (1 - n_{i\sigma})$. For a general bipartite lattice, a similar transformation law holds if we replace $(-1)^{i_x+i_y}$ by a factor which is 1 on the *A* sublattice and -1 on the *B* sublattice. For lattices which are not bipartite, particle-hole symmetry is not relevant.

Acting on the Fermi-Hubbard Hamiltonian, this transformation leaves the tunneling and interaction terms unchanged but shifts the chemical potential

$$\Gamma \mathcal{H}(U, \bar{\mu}, h) \Gamma^\dagger = \mathcal{H}(U, U - \bar{\mu}, -h) + N(U - 2\mu), \quad (3.5)$$

where N is the number of sites. Exactly at half-filling, we expect that the Hamiltonian is invariant under the particle-hole transformation, i.e. $\mathcal{H}(n) = \mathcal{H}(2 - n)$, which implies that $\mu = U/2$. Away from half-filling this transformation provides a correspondence between eigenstates of $\mathcal{H}(n)$ and $\mathcal{H}(2 - n)$. In particular,

$$\mathcal{H}(\bar{\mu}, h) |l\rangle = \epsilon_l |l\rangle \quad (3.6)$$

$$\mathcal{H}(U - \bar{\mu}, -h)\Gamma |l\rangle = \tilde{\epsilon}_l \Gamma |l\rangle, \quad (3.7)$$

where $\tilde{\epsilon}_l = \epsilon_l - N(U - 2\mu)$.

This correspondence relates the Green's functions and spectral functions of the two Hamiltonians,

$$G^R(k, t, \bar{\mu}, h) = G^R(k + Q, -t; U - \bar{\mu}, -h) \quad (3.8)$$

$$A(k, \omega, \bar{\mu}, h) = A(k + Q, -\omega; U - \bar{\mu}, -h), \quad (3.9)$$

where $Q = (\pi, \pi)$. In the balanced gas, this implies that the spectral functions below and above half-filling are related by $A(k, \omega, n) = A(k + Q, -\omega, 2 - n)$.

3.1.3 Attractive and repulsive symmetry

The Hubbard model on a bipartite lattice also has a symmetry which connects systems with attractive and repulsive interactions. This transformation exchanges the role of doping and spin-imbalance and provides a correspondence between the spin-balanced repulsive model at various dopings with the half-filled attractive model at various spin polarizations and vice versa.

The attractive-repulsive symmetry is realized by a partial particle-hole transformation which acts only on the down-spins [160]

$$\Lambda c_{i\uparrow} \Lambda^\dagger = c_{i\uparrow} \quad (3.10)$$

$$\Lambda c_{i\downarrow} \Lambda^\dagger = (-1)^{i_x+i_y} c_{i\downarrow}^\dagger. \quad (3.11)$$

We find as in the particle-hole case this transformation leaves the tunneling term invariant, but modifies the interaction and chemical potential terms

$$\Lambda \mathcal{H}(U, \bar{\mu}, h) \Lambda^\dagger = \mathcal{H} \left(-U, h - \frac{U}{2}, \bar{\mu} - \frac{U}{2} \right) - (\bar{\mu} - h) N. \quad (3.12)$$

This transformation changes the sign of the interaction and exchanges the roles of $\bar{\mu}$ and h . The offset of $-U/2$ sets up a correspondence between half-filling and spin-balance and vice versa. This proves the correspondence between spin-balanced systems at finite doping and spin-imbalanced systems at half-filling which we alluded to above, $\mathcal{H}(U, \bar{\mu}, 0) \leftrightarrow \mathcal{H}(-U, -U/2, \bar{\mu} - U/2)$.

This mapping provides a correspondence between the Green's function and spectral function for the two parameter sets. As the mapping does not affect the spin up fermion operators, the Green's function and spectral function become

$$G_\uparrow^R(k, t; U, \bar{\mu}, h) = G_\uparrow^R \left(k, t; -U, h - \frac{U}{2}, \bar{\mu} - \frac{U}{2} \right) \quad (3.13)$$

$$A_\uparrow(k, \omega; U, \bar{\mu}, h) = A_\uparrow \left(k, \omega; -U, h - \frac{U}{2}, \bar{\mu} - \frac{U}{2} \right) \quad (3.14)$$

On the other hand, the mapping is a particle hole transformation for the down spins, and therefore analogous to eqs. 3.8 and 3.9, the spin down Green's function and

spectral function become

$$G_{\downarrow}^R(k, t; U, \bar{\mu}, h) = G_{\downarrow}^R \left(k + Q, -t; -U, h - \frac{U}{2}, \bar{\mu} - \frac{U}{2} \right) \quad (3.15)$$

$$A_{\downarrow}(k, \omega; U, \bar{\mu}, h) = A_{\downarrow} \left(k + Q, -\omega; -U, h - \frac{U}{2}, \bar{\mu} - \frac{U}{2} \right). \quad (3.16)$$

3.1.4 SU(2) spin symmetry

The Hubbard model describes a system of itinerant particles of two species which we refer to as “spins”. This analogy is natural because the Fermi-Hubbard Hamiltonian respects spin rotations. To bring out this symmetry, we define local spin operators

$$S_i^{\alpha} = \frac{1}{2} \begin{pmatrix} c_{i\uparrow}^{\dagger} & c_{i\downarrow}^{\dagger} \end{pmatrix} \sigma_{\alpha} \begin{pmatrix} c_{i\uparrow} \\ c_{i\downarrow} \end{pmatrix}, \quad (3.17)$$

where σ_{α} are the Pauli matrices for $\alpha = x, y, z$. The z -component of the spin operator, $S_i^z = \frac{1}{2}(n_{i\uparrow} - n_{i\downarrow})$, measures the difference in spin populations, whereas the x -component measures the difference in populations of the superposition states $\frac{1}{\sqrt{2}}(c_{i\uparrow}^{\dagger} \pm c_{i\downarrow}^{\dagger})|0\rangle$. The y -component is similar. The corresponding raising and lowering operators are $S_i^+ = c_{i\uparrow}^{\dagger}c_{i\downarrow}$ and $S_i^- = c_{i\downarrow}^{\dagger}c_{i\uparrow}$.

The spin operators obey the usual SU(2) algebra commutation relations, $[S_i^{\alpha}, S_i^{\beta}] = i\epsilon_{\alpha\beta\gamma}S_i^{\gamma}$, where $\epsilon_{\alpha\beta\gamma}$ is the Levi-Civita symbol. The global spin operators, $S^{\alpha} = \sum_i S_i^{\alpha}$, have the following commutation relations with the Hamiltonian

$$[\mathcal{H}, S^+] = -2hS^+ \quad (3.18)$$

$$[\mathcal{H}, S^z] = 0 \quad (3.19)$$

$$[\mathcal{H}, S^2] = 0 \quad (3.20)$$

which show we can choose eigenstates of \mathcal{H} of definite total spin and z -spin projection. When $h = 0$, the Hamiltonian is invariant under spin rotations which implies that the spin correlations along any direction must be equal. For finite h , only rotations about the z -axis preserve \mathcal{H} and the total symmetry is reduced from SU(2) to U(1). In this case, the x and y spin correlations are still constrained to be equal but the z spin component develops a finite expectation value. We discuss experimental realization of this canted antiferromagnetism in chapter 4.

3.1.5 SU(2) pseudospin symmetry

The Hubbard model has a second SU(2) symmetry, referred to as the *pseudospin symmetry*, which is closely connected with s -wave superfluidity and charge density wave order. This symmetry was first noticed decades after the initial development of the Hubbard model [161].

We define the pseudospin operators for $\alpha = x, y, z$ by

$$\eta_i^\alpha = \frac{1}{2} \begin{pmatrix} c_{i\uparrow}^\dagger & (-1)^{i_x+i_y} c_{i\downarrow} \end{pmatrix} \sigma_\alpha \begin{pmatrix} c_{i\uparrow} \\ (-1)^{i_x+i_y} c_{i\downarrow}^\dagger \end{pmatrix}, \quad (3.21)$$

from which it is clear that Λ maps the pseudospin operators onto the spin operators

$$\Lambda \eta_i^\alpha \Lambda^\dagger = S_i^\alpha. \quad (3.22)$$

We also have the raising and lower operators $\eta_i = (-1)^{i_x+i_y} c_{i\uparrow} c_{i\downarrow}$ and $\eta_i^\dagger = (-1)^{i_x+i_y} c_{i\uparrow}^\dagger c_{i\downarrow}^\dagger$.

The pseudospin operators satisfy the SU(2) algebra commutation relations and the global pseudospin operators have the following commutation relations with the

Hamiltonian

$$[\mathcal{H}, \eta^\dagger] = -(2\bar{\mu} - U)\eta^\dagger \quad (3.23)$$

$$[\mathcal{H}, \eta^z] = 0 \quad (3.24)$$

$$[\mathcal{H}, \eta^2] = 0, \quad (3.25)$$

which follow from applying Λ to the corresponding relations for the S^α 's. Analogous to the case of spin symmetry, we can choose eigenstates of definite η^2 and η^z .

At half-filling, pseudospin rotations are a symmetry of the model. Away from half-filling, the full rotational SU(2) symmetry is reduced to rotations about the z -axis. This U(1) symmetry is the phase symmetry associated with charge conservation.

The pseudospin is closely connected with s -wave superfluidity and charge density wave order. Performing an appropriate pseudospin rotation transforms one into the other [162], implying that charge density wave correlations and s -wave superfluid correlations have equal strength at half-filling. Recent experiments in our group explored charge density correlations in the attractive Hubbard model [71].

The Hamiltonian commutation relations with η^\pm imply the existence of three collective modes in the attractive model, which are visible as poles in various response functions [162, 163, 164]. These are a massless Goldstone mode associated with the U(1) charge symmetry, and two partners which are massive, except at half-filling where they are also massless [162]. The massless mode corresponds to long-wavelength rotations of the superconducting phase. The massive modes couple density fluctuations to superconducting fluctuations and may be observable in the system's density response [164].

3.1.6 Higher symmetry

The $SU(2)$ spin and pseudospin symmetries combine to form an $SO(4) = SU(2) \times SU(2)/\mathbb{Z}_2$ symmetry in the Hubbard model [165, 166]. The reduction from $SU(2) \times SU(2)$, as we might naïvely expect based on the two individual $SU(2)$ symmetries, to $SO(4)$ is associated with the additional attractive-repulsive symmetry discussed in section 3.1.3. An interesting consequence of this is that all eigenstates of the Hubbard model can be obtained from those at half-filling by the action of S^\pm and η^\pm [167]. In some sense, the full Hubbard problem can be understood from the half-filled case.

Due to the natural relationship between the pseudospin operators and s -wave superfluidity, the $SO(4)$ symmetry associated with spin and pseudospin rotations is suited to studying properties of the attractive Hubbard model, which has an s -wave superconducting ground state. However, it would be desirable to find a symmetry that respects d -wave superfluidity, which is expected to exist in the repulsive model. To this end, the possibility that the Hubbard model has an approximate $SO(5)$ symmetry which connects d -wave superconductivity to antiferromagnetism has also been explored [168].

3.1.7 Connection to the $t - J$ model

The repulsive Hubbard model is frequently considered in the strong interaction limit, $U \gg t$. In this parameter range, double occupancies are very energetically costly. True doublon excitations are rare, but play an important role as virtual excitations (i.e. second order or higher processes).

A low-energy effective Hamiltonian describing the Hubbard model near the ground state can be derived by projecting out double occupancies but retaining the effect of leading order virtual processes, which can be formally done using a Schrieffer-Wolff

transformation [169]. This leads to the Hamiltonian

$$\mathcal{H} = -t \sum_{\langle i,j \rangle \sigma} \left(c_{i\sigma}^\dagger c_{j\sigma} + \text{h.c.} \right) + J \sum_{\langle i,j \rangle} \left(\mathbf{S}_i \cdot \mathbf{S}_j - \frac{n_i n_j}{4} \right), \quad (3.26)$$

which is referred to as the $t-J$ model. Here t is the tunneling energy and $J = 4t^2/U$ is the superexchange energy. Unlike the Hubbard system, this effective Hamiltonian has an on-site basis with three states, $|0\rangle$, $|\uparrow\rangle = c_{i\uparrow}^\dagger |0\rangle$ and $|\downarrow\rangle = c_{i\downarrow}^\dagger |0\rangle$ making the $t-J$ model somewhat more tractable for numerical simulations [170].

3.1.8 Connection to the Heisenberg model

At half-filling and large U/t , itinerant fermions can be thought of as a collection of spins on a lattice, because the only degrees of freedom are the particle species on each site. Here, the $t-J$ model reduces to a Heisenberg spin model [171] with Hamiltonian,

$$\mathcal{H} = J \sum_{\langle i,j \rangle} \mathbf{S}_i \cdot \mathbf{S}_j - 2h \sum_i S_i^z, \quad (3.27)$$

where the spin operators S^α are defined by eq. 3.17 and we include a magnetic field along the z -direction. This effective Hamiltonian has two on-site basis states, which are $|\uparrow\rangle = c_{i\uparrow}^\dagger |0\rangle$ and $|\downarrow\rangle = c_{i\downarrow}^\dagger |0\rangle$. The Heisenberg interaction, which manifestly depends only on the relative orientation of spins on neighboring sites, makes plain the SU(2) spin symmetry of the model and emphasizes the role of superexchange interactions.

Similarly, the balanced gas at strong interactions can be written in terms of the pseudospin operators [163]

$$\mathcal{H} = J \sum_{\langle i,j \rangle} \vec{\eta}_i \cdot \vec{\eta}_j - (2\bar{\mu} - U) \sum_i \eta_i^z, \quad (3.28)$$

which emphasizes the pseudospin symmetry of the model. As we expect, the chemical potential plays the role of an effective magnetic field in this case.

3.2 The non-interacting Fermi gas

We consider the problem of non-interacting fermions on a 2D square lattice as a means of understanding which aspects of Hubbard physics may be due to Fermi statistics or dimensionality alone, and which are due to interaction effects. This problem is exactly solvable, but Fermi statistics still lead to non-trivial correlations between particles. Furthermore, the 2D situation is particularly interesting because of the presence of a Van Hove singularity at the half-filling point, where the density of states diverges logarithmically. Early studies emphasized the role Van Hove singularities can play in enhancing T_c in interacting systems [172].

We suppose we have two spin components, as in the Hubbard case. The Hamiltonian for a mixture of non-interacting Fermions is

$$\mathcal{H}_{\text{fg}} = \sum_{k\sigma} \epsilon_k n_{k\sigma} - \bar{\mu} \sum_{k\sigma} n_{k\sigma} - h \sum_k (n_{k\uparrow} - n_{k\downarrow}), \quad (3.29)$$

where ϵ_k is the dispersion relation. This is identical to the Fermi-Hubbard Hamiltonian with $U = 0$. We will consider the tight-binding dispersion relation $\epsilon_k = -2t(\cos(k_x) + \cos(k_y))$. Due to particle-hole symmetry, the half-filling point occurs at $\mu = 0$.

Most experimental properties of the model, such as spin or density correlations and response functions, can be determined from Green's functions. Response functions are particularly important because they contain information about the system's response to external perturbations through the Kubo formula and fluctuation-dissipation theorem (see section 3.7). In the non-interacting case, higher order Green's functions can be reduced to products of single-particle Green's functions using Wick's theorem

[173, 174, 175]. We obtain the single-particle retarded Green's function by solving the Heisenberg equations of motion for c_k ,

$$G_\sigma^R(k, t) = -\frac{i}{\hbar} \theta(t) e^{-i\xi_{k\sigma}t/\hbar} \quad (3.30)$$

$$G_\sigma^R(k, \omega) = \frac{1}{\hbar(\omega + i\eta) - \xi_{k\sigma}}, \quad (3.31)$$

where $\xi_{k\sigma} = \epsilon_k - \mu_\sigma$ and we always work in the limit $\eta \rightarrow 0^+$.

3.2.1 Equation of state

We determine thermodynamic properties of the Fermi gas through the equation of state, $n(\mu, h, T)$, which can be written in terms of the dispersion relation

$$n_\sigma = \int d\epsilon F(\xi_{k\sigma}, T) g(\epsilon) \quad (3.32)$$

$$= \frac{1}{N} \sum_k F(\xi_{k\sigma}, T), \quad (3.33)$$

where g is the density of states, F is the Fermi function, $\xi_{k\sigma} = \epsilon_k - \mu_\sigma$, and N is the number of lattice sites. The first equation is useful for analytic calculations when the density of states has a closed form expression. The second form is convenient for numerics. To evaluate this equation, consider a system with N_x and N_y lattice sites in the x and y directions with periodic boundary conditions. The allowed k vectors are $k_x = 2\pi n/N_x$ and $k_y = 2\pi m/N_y$ for $n \in \{0, \dots, N_x - 1\}$ and $m \in \{0, \dots, N_y - 1\}$. The size of the lattice must be chosen so that the characteristic energy spacing is small compared with the temperature.

In cold atom experiments gases are subject to spatially varying potentials, and therefore it is natural to ask how the system responds to an external potential which varies in space and time. This is formally described by the density response function, which can be determined by computing the Matsubara Green's function $G(\tau) =$

$-1/\hbar \langle \mathcal{T}n_{k\sigma}(\tau)n_{-k\sigma}(0) \rangle$ using Wick's theorem and analytically continuing to real-frequency (see e.g.[174] or section 3.7), where k is the wave vector of the perturbation and ω is the angular frequency. The result is

$$\chi_c(q, \omega) = \sum_{k\sigma} \frac{F(\xi_{k\sigma}) - F(\xi_{k+q,\sigma})}{\hbar\omega + \xi_{k\sigma} - \xi_{k+q,\sigma} + i\eta}. \quad (3.34)$$

The imaginary part of this response function represents dissipation from the production of particle-hole pairs.

The density distribution of the gas in a static trap can be understood from eq. 3.33 above and the static compressibility. We determine the static compressibility either by differentiating eq. 3.33 or taking the limit of the response function $\lim_{q \rightarrow 0} \chi_c(q, 0)$ from eq. 3.34 to find

$$\left. \frac{\partial n}{\partial \mu} \right|_T = \int d\epsilon \partial_\mu F(\xi_k) g(\epsilon) \quad (3.35)$$

$$= \frac{2\beta}{N} \sum_k [1 - F(\xi_k)] F(\xi_k). \quad (3.36)$$

We display this equation of state (eqs. 3.33 and 3.36) for a 2D gas with a tight binding dispersion in fig. 3.1. In the high-temperature limit, we expect $\chi_c(T) \rightarrow n(1 - n/2)/T$ (see section 3.5). We find this estimate is quite accurate at half-filling for $T > 5$. Away from half-filling, agreement occurs at even lower temperature.

In the low temperature limit, $T \rightarrow 0$, the compressibility saturates $\chi_c \rightarrow g(\mu)$, as long as the density of states is finite. The 2D tight-binding density of states is finite away from half-filling ($\epsilon = 0$) where it has a logarithmic Van Hove singularity, $g(\epsilon) \sim -\log(\epsilon/t)$. At half-filling, the compressibility diverges $\chi(n = 1) \sim \log(T/t)$. Near quarter-filling, saturation occurs at moderately low temperature $T \sim 0.5t$, and the onset of saturation is pushed to lower temperature as n approaches half-filling.

The compressibility is closely connected with the Fermi gas density correlations, which we discuss in more detail section 3.2.2. The two are related through the fluctuation-dissipation theorem (see section 3.7),

$$\chi_c = \beta \sum_d C_n(d). \quad (3.37)$$

The $d = 0$ term, which is the variance of the atom number, gives the strongest contribution. At high temperatures, all off-site correlations vanish and this relation recovers the high temperature limit compressibility.

3.2.2 Fermi gas correlations

Despite the absence of an explicit interaction term, the Fermi gas develops correlations at low temperatures due to Fermi statistics. The ground state of the gas is a Fermi sea, and Pauli exclusion between the momentum states induces density correlations in real space. We can also deduce these using Wick's theorem. The single-component density correlations are given by

$$\begin{aligned} C_\sigma(d) &= \delta_{0d} \langle n_\sigma \rangle - \left| \left\langle c_{i\sigma}^\dagger c_{i+d\sigma} \right\rangle \right|^2 \\ &= \delta_{0d} \langle n_\sigma \rangle - \left| \frac{1}{N} \sum_k F(\xi_k, T) e^{ikd} \right|^2, \end{aligned} \quad (3.38)$$

which are negative for $d \neq (0, 0)$. The nearest-neighbor correlations, $C_\sigma(1, 0)$ provide a good thermometer in the temperature range $T/t = 0.1 - 1$ near half-filling, as shown in fig. 3.2A. For a 2D gas with tight binding dispersion at half-filling and zero temperature, $C_\sigma(1, 0) \approx -0.041$. Away from half-filling these correlations remain significant, and we display the variation in correlation strength with density at a variety of temperatures in fig. 3.2B. Correlations between sites with larger separation are extremely small.

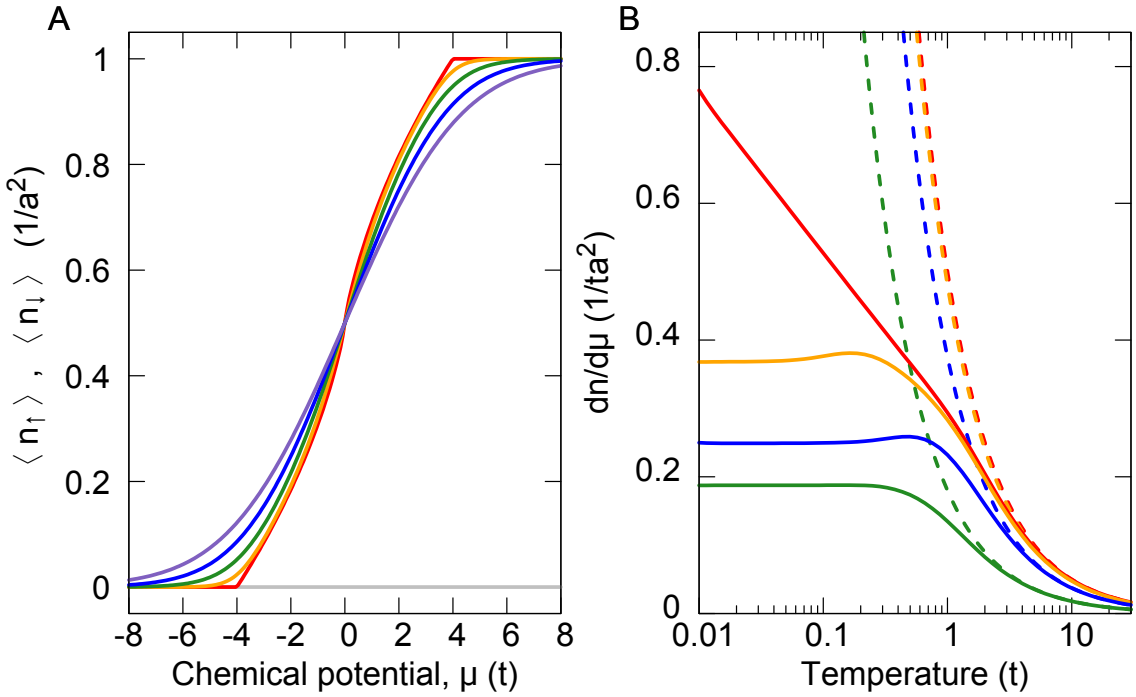


Figure 3.1: **Fermi gas equation of state.** **A**, Density n_σ versus chemical potential μ for temperatures $T/t = 0$ (red), 0.4 (orange), 0.8 (green), 1.2 (blue), and 1.6 (purple). At zero temperature the density saturates when the chemical potential reaches the edge of the energy band and the compressibility diverges at half-filling. At higher temperature the density depends less strongly on the chemical potential, and sharp features of the zero temperature equation of state are smoothed. **B**, Fermi gas compressibility at $n = 1$ (red solid line), 0.8 (orange line), 0.6 (blue), 0.2 (green) and the infinite-temperature limits (dotted lines). The compressibility saturates at low temperature away from half-filling, and scales as $1/T$ at high temperature. We calculate these quantities for increasing lattice sizes to verify that the numerics are converged.

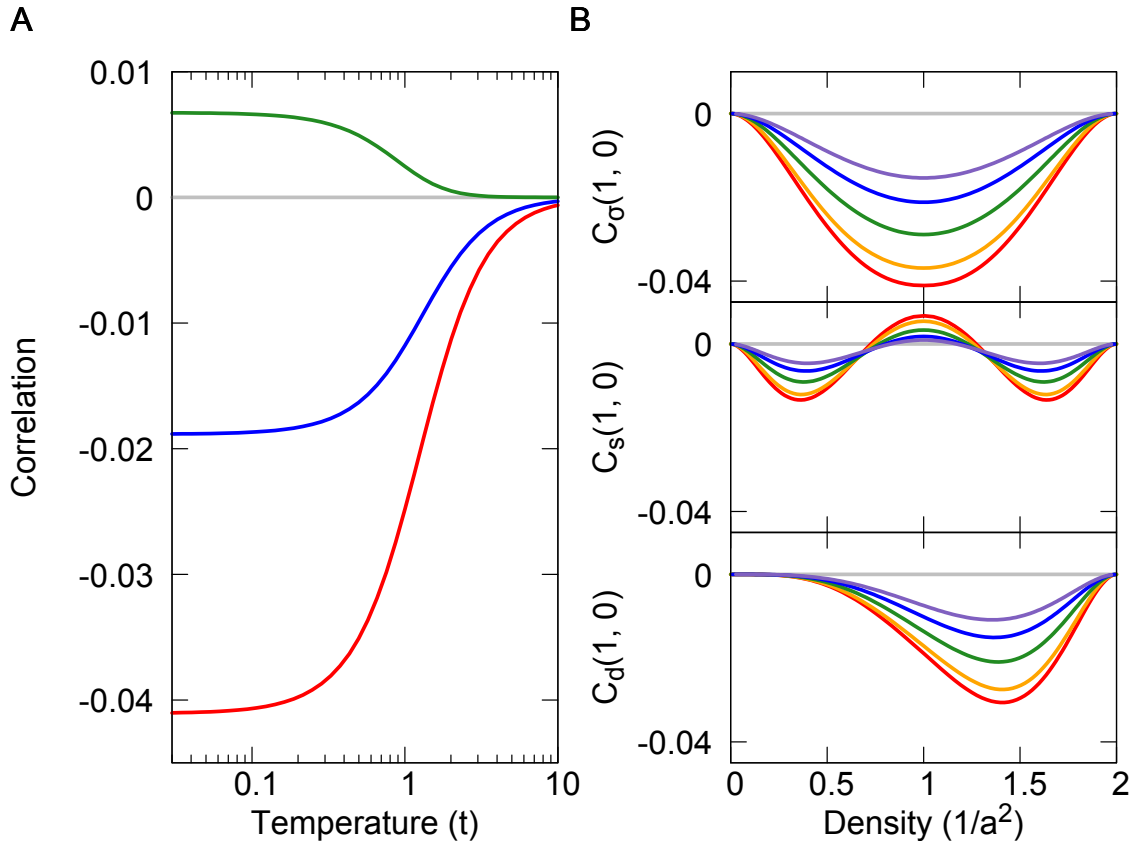


Figure 3.2: **Fermi gas correlators versus temperature and filling.** **A**, Correlators versus temperature for a 2D Fermi gas with tight-binding dispersion at half-filling including $C_{\uparrow}(1, 0) = C_{\downarrow}(1, 0)$ (red), $C_s(1, 0)$ (green), and $C_d(1, 0)$ (blue). These correlators are useful thermometers for $T/t = 0.1 - 1$. **B**, Correlators versus density at temperatures $T/t = 0$ (red), 0.4 (orange), 0.8 (green), 1.2 (blue), and 1.6 (purple) including $C_{\sigma}(1, 0)$ (top panel), $C_s(1, 0)$ (middle panel), and $C_d(1, 0)$ (bottom panel). The single-species density correlator and singles correlators are symmetric about half-filling due to particle-hole symmetry. The doublon correlator reaches maximum strength above half-filling.

The fermion density correlations induce a variety of other correlations, including doublon-doublon, doublon-hole, and single-single correlations which are given by

$$C_d(d) = C_\uparrow(d) \langle n_{i\downarrow} \rangle \langle n_{i+d\downarrow} \rangle + \langle n_{i\uparrow} \rangle \langle n_{i+d\uparrow} \rangle C_\downarrow(d) + C_\uparrow(d)C_\downarrow(d) \quad (3.39)$$

$$C_{dh}(d) = -C_\uparrow(d) \langle n_{i\downarrow} \rangle - C_\downarrow(d) \langle n_{i\uparrow} \rangle \quad (3.40)$$

$$\begin{aligned} C_s(d) = & C_\uparrow(d) (1 + 4 \langle n_{i\downarrow} \rangle \langle n_{i+d\downarrow} \rangle - 2 \langle n_{i\downarrow} \rangle - 2 \langle n_{i+d\downarrow} \rangle) \\ & + C_\downarrow(d) (1 + 4 \langle n_{i\uparrow} \rangle \langle n_{i+d\uparrow} \rangle - 2 \langle n_{i\uparrow} \rangle - 2 \langle n_{i+d\uparrow} \rangle) \\ & + 4C_\uparrow(d)C_\downarrow(d). \end{aligned} \quad (3.41)$$

It is instructive to compare the structure of Fermi gas correlators to those of the Hubbard system to assess the significance of interaction effects compared with fermionic statistics.

The doublon correlations are always negative and their strength can be enhanced or reduced compared with the single-component density correlators based on the filling, which affects the probability a doublon exists in the first place. We show the doublon correlation at half-filling versus temperature in fig. 3.2A, and versus density in fig. 3.2B. Similar negative nearest-neighbor correlations have been observed in the attractive Hubbard system [71] where they are further enhanced by superexchange.

The doublon-hole correlations are always positive, similar to the situation in the repulsive Hubbard model [68]. For the non-interacting case the positivity is a result of fermion antibunching, whereas in the interacting system superexchange processes enhance these correlations because they are energetically favorable.

The singles correlator is negative away from half-filling and positive near half-filling. The negative correlation comes from the single-component density correlations in the low density regime where doublons are rare and $n^s \sim n_\uparrow + n_\downarrow$, or in the high-density regime where most sites contain doublons. The first two terms in eq. 3.41 describe this contribution. The third term describes a positive contribution to the

correlator which competes with the negative contribution. We can understand the situation by considering two sites with an up spin on the left site and a down spin on the right. Fermion antibunching then leads to a lower probability that either site has a second atom. Therefore it is more likely that we have singly occupied sites of opposite spin next to each other than in an uncorrelated system, where at least one of these sites would be more likely to contain a doublon. We display the single correlations versus temperature in fig. 3.2A and versus density in fig. 3.2B. This behavior is qualitatively similar to that observed in the repulsive Hubbard model [68], but in that case the strength of the positive correlations near half-filling is enhanced by superexchange.

3.2.3 Magnetism

A two-component Fermi gas exhibits paramagnetism in response to an applied magnetic field. This is referred to as *Pauli paramagnetism*, and can be understood as the magnetic field inducing a differential shift in the chemical potentials of the two components. The magnetic susceptibility immediately follows from the density response,

$$\chi_m(q, \omega) = \chi_c(q, \omega) \quad (3.42)$$

$$\left. \frac{\partial(n_\uparrow - n_\downarrow)}{\partial h} \right|_T = \lim_{q \rightarrow 0} \chi_m(q, \omega = 0). \quad (3.43)$$

In the $T \rightarrow 0$ limit, the magnetic susceptibility is again given by the density of states.

Fermi statistics induce negative nearest-neighbor spin correlations,

$$C_{\text{spin}}^z(d) = C_\uparrow(d) + C_\downarrow(d) \quad (3.44)$$

$$\begin{aligned} C_{\text{spin}}^x(d) &= C_{\text{spin}}^y(d) \\ &= \delta_{0d} \langle n \rangle - \left\langle c_{i\uparrow}^\dagger c_{i+d,\uparrow} \right\rangle \left\langle c_{i+d,\downarrow}^\dagger c_{i\downarrow} \right\rangle - \left\langle c_{i\downarrow}^\dagger c_{i+d,\downarrow} \right\rangle \left\langle c_{i+d,\uparrow}^\dagger c_{i\uparrow} \right\rangle. \end{aligned} \quad (3.45)$$

For $U/t = 8$ at half-filling and $T \rightarrow 0$, $C_{\text{spin}}^z(1, 0) = -0.36$ for the Hubbard system [69], whereas $C_{\text{spin}}^z(1, 0) = -0.082$ for the Fermi gas. A large portion of the Hubbard correlations are due to correlations between different spin states, $C_{\uparrow\downarrow}(1, 0)$ and $C_{\downarrow\uparrow}(1, 0)$ (due to the decomposition of eq. 2.13), which are induced by the Hubbard interaction.

For a spin-balanced gas, SU(2) spin symmetry ensures that $C_{\text{spin}}^z = C_{\text{spin}}^{x,y}$ in both Fermi and Hubbard gases. For the Fermi gas, the three spin correlators are equal at half-filling even in the presence of imbalance, due to particle-hole symmetry. In contrast, the spin imbalanced repulsive Hubbard gas at half-filling develops stronger antiferromagnetic correlations along the x - and y -directions, compared with the z -direction. We discuss this canted antiferromagnetism in more detail in chapter 4.

The magnetic susceptibility and spin correlations are related through the fluctuation-dissipation theorem (see section 3.7),

$$\chi_m = \beta \sum_d C_{\text{spin}}^z(d). \quad (3.46)$$

3.3 The local density approximation

In previous sections we have discussed homogeneous systems, but cold atom experiments are frequently performed in harmonic trapping potentials. Simulating a trapped system is solving a less general problem than the homogeneous system, and can require more effort because the trap breaks translational symmetry. Therefore, it is desirable to apply the solution of the homogeneous problem to understand the trapped system. As long as the trapping potential varies slowly compared with relevant length scales in the problem, such as the lattice spacing, correlations lengths, mean free paths, etc., the gas appears locally homogeneous. Given such a separation of length scales, the potential can be treated as a spatially varying chemical potential

and an observable at position \mathbf{r} in the trap can be calculated from the solution to the homogeneous problem at $\mu(\mathbf{r}) = \mu_o - V(\mathbf{r})$, where μ_o is the chemical potential at the center of the trap. This semiclassical approximation called the *local density approximation* (LDA). The density profile in the LDA is

$$\langle n(\mathbf{r}, T) \rangle = \langle n(\mu(\mathbf{r}), T) \rangle, \quad (3.47)$$

which can be determined from eq. 3.33 for the non-interacting system, or from quantum Monte Carlo or other techniques for the Hubbard system.

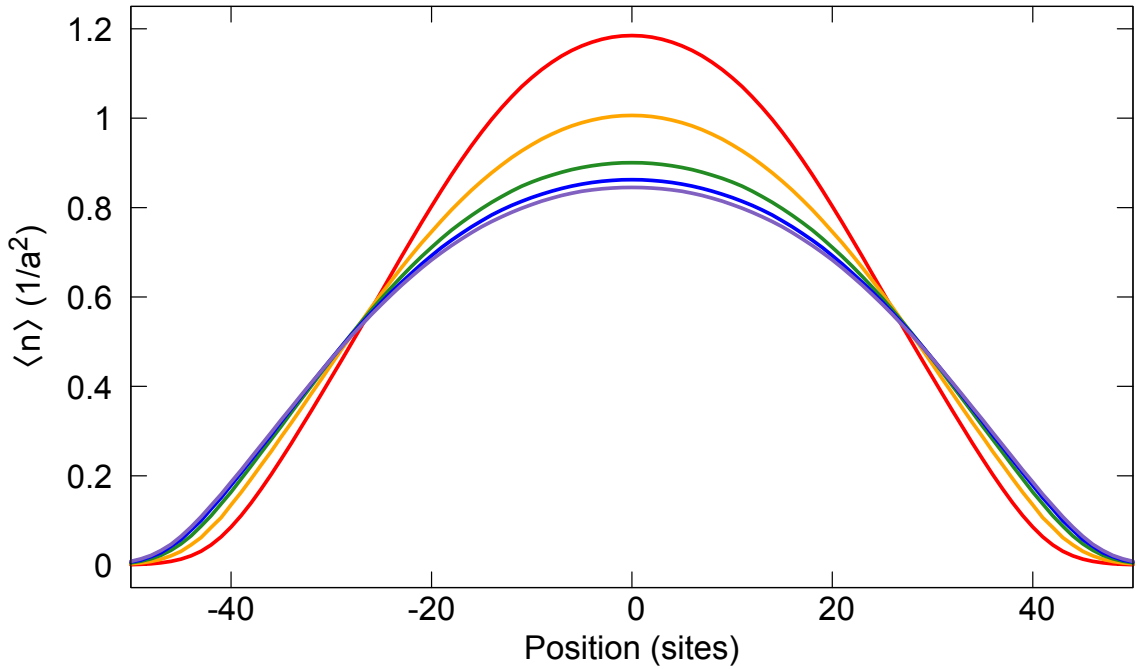


Figure 3.3: Density profiles along one dimension for a non-interacting Fermi gas (red) and Hubbard systems at $U/t = 2$ (orange), 4 (green), 6 (blue), and 8 (purple) at fixed atom number $N = 2770$ and $T/t = 0.3$ in the local density approximation for a harmonic trap with trapping frequency $\omega = (2\pi)150$ Hz. Stronger interactions favor lower central density in the trap, leading to broader profiles.

We consider LDA density profiles for a non-interacting gas, determined from eq. 3.33, and a Hubbard gas at several different repulsive interactions, determined from DQMC (fig. 3.3). For all profiles, we work with a fixed number, and $T/t = 0.3$.

The trapping potential is harmonic, $\mu(\mathbf{r}) = \mu_o - \frac{1}{2}m\omega^2\mathbf{r}^2$, where $\omega = (2\pi)150\text{ Hz}$ is the trapping frequency. As the strength of the repulsive interaction increases, the peak density in the trap decreases.

3.4 The atomic limit

We considered the situation when the Hubbard interaction U vanishes in the previous section. Here we consider the opposite limit, where the tunneling energy vanishes. We note that this case should be distinguished from the large U -limit, $U \gg t, T$, because in that case tunneling processes are still present [140]. In this case, we have a system of decoupled sites which we refer to as the *atomic limit*. The Hamiltonian is $\mathcal{H} = Uc_\uparrow^\dagger c_\uparrow c_\downarrow^\dagger c_\downarrow$. This problem can be easily solved because there are only four allowed quantum states on a single site, $|0\rangle$, $c_\uparrow^\dagger|0\rangle$, $c_\downarrow^\dagger|0\rangle$ and $c_\uparrow^\dagger c_\downarrow^\dagger|0\rangle$, nevertheless it frequently provides useful intuition.

All thermodynamic information comes from the grand partition function

$$Z = 1 + 2e^{\beta\mu} + e^{-\beta(U-2\mu)}, \quad (3.48)$$

and the grand potential $\Omega(T, \mu) = -k_b T \log(Z)$. In particular, the atomic density and entropy are,

$$n_{\text{atomic}} = -\left.\frac{\partial\Omega}{\partial\mu}\right|_T = \frac{1}{Z}(2e^{\beta\mu} + 2e^{-\beta(U-2\mu)}) \quad (3.49)$$

$$S_{\text{atomic}} = -\left.\frac{\partial\Omega}{\partial T}\right|_\mu = k_b \log(Z) - \frac{k_b}{Z}\beta(2\mu e^{\beta\mu} + (2\mu - U)e^{-\beta(U-2\mu)}). \quad (3.50)$$

The local density and entropy in the trap can be determined using the LDA.

Dynamical information is contained in the Green's function and single-particle spectral function which are

$$G_{\uparrow}^R(k=0, \omega) = \frac{1}{Z} \left(\frac{1 + e^{\beta\mu}}{(\omega + i\eta) - \mu} + \frac{e^{\beta\mu} + e^{-\beta(U-2\mu)}}{(\omega + i\eta) + \mu - U} \right) \quad (3.51)$$

$$\begin{aligned} A_{\uparrow}(k=0, \omega) &= \frac{1}{Z} [(1 + e^{\beta\mu}) \delta(\omega - \mu) \\ &\quad + (e^{\beta\mu} + e^{-\beta(U-2\mu)}) \delta(\omega + \mu - U)], \end{aligned} \quad (3.52)$$

where we write $k = 0$ to emphasize that because the sites are decoupled there is no momentum resolution in the problem. The spectral function exhibits a two peak structure split by the interaction energy U . These features correspond to an extreme limit of the upper and lower Hubbard bands.

3.5 The infinite temperature limit

Both the Hubbard model and the non-interacting Fermi gas are single band models which have bounded energy spectra, and therefore we can sensibly speak of a high-temperature limit where the temperature is much larger than other energy scales in the problem, $T \gg t, U, W$, where $W = 8t$ is the band width. The high temperature behavior of a wide variety of thermodynamic quantities and response functions can be derived as a series expansion in powers of T^{-1} [176].

For many quantities, the leading order term in the high-temperature limit comes from the atomic limit [176]. From this perspective, it is easy to show that we have the following expressions for the chemical potential and compressibility at given density n in either a finite- U Hubbard system or a two-component non-interacting Fermi gas,

$$\mu(T) = \log \left[\frac{n}{2-n} \right] / T + \mathcal{O}(T^{-2}) \quad (3.53)$$

$$\chi_c(T) = \frac{n(1-n/2)}{T} + \mathcal{O}(T^{-2}), \quad (3.54)$$

where \log is the natural logarithm. To this order, the coefficients are independent of U , but this will not be true in general. As noted in section 3.2.1, $n(1 - n/2)$ is the variance in the on-site density, and therefore the compressibility equation above can also be thought of as a manifestation of the fluctuation-dissipation theorem.

A wide variety of other quantities, including spectral functions and correlation functions can also be obtained in the high temperature limit. For these quantities, which are frequency dependent, the terms of the expansion are functions of frequency and can be written [176],

$$\frac{\chi''(k, \omega)}{\omega} = \frac{1}{t^2} \sum_{i=1}^{\infty} \left(\frac{t}{T}\right)^i f^{(i)}(k, \omega/t, U), \quad (3.55)$$

where χ'' is the imaginary part of a susceptibility function (see section 3.7). Reconstructing the full frequency dependence of the $f^{(i)}$ is a challenging problem, but many moments of these terms can be calculated [176]. Some useful general features of various correlations can be ascertained from this expression, including the fact that the conductivity, $\sigma(\omega = 0)$ scales like $1/T$ at high temperature. We discuss the connection between this scaling and strange metallicity in chapter 5.

3.6 Parameter fitting

In previous sections we have discussed obtaining the expectation values of various observables in the grand canonical ensemble, where the observables, $\mathcal{O}(\mu, T, P)$, are naturally functions of temperature, chemical potential and other parameters P of the system. However, these parameters are generally not known experimentally. To determine them it is necessary to compare measured quantities with theory results.

In the experiment it is more natural to work with the density, which is directly measurable, rather than the chemical potential. Working in the LDA, the chemical potential effectively varies across the trap, and determining its variation requires a

detailed knowledge of the trapping potential. This could be extracted from an additional experiment, but if the equation of state, $n(\mu, T)$, can be calculated theoretically we can invert the relationship between n and μ to determine $\mu(n, T)$ and $\mathcal{O}(n, T, P)$. The density can be measured using QGM techniques, which leaves T and P as free parameters in the problem.

We determine T and P as follows. Suppose we measure a family of observables $\{\mathcal{O}_j\}$ and the density at a number of spatial positions indexed by i . Then we use a nonlinear least squares procedure to minimize

$$\chi^2 = \sum_{ij} \frac{1}{\sigma_{ij}^2} \left| \mathcal{O}_j(n_i, T, P) - \mathcal{O}_j^{\text{theory}}(n_i, T, P) \right|^2, \quad (3.56)$$

where σ_{ij} is the standard error of the mean in the measurement of $\mathcal{O}_j(n_i, T, P)$.

When the equation of state can be determined analytically, the functions $\mathcal{O}_j^{\text{theory}}(n, T, P)$ can be directly implemented on a computer. For numerical methods, such functions can be constructed using interpolation techniques. We typically generate theory values on a grid of chemical potential and temperature points (μ_r, T_s) , which are not necessarily equally spaced, and calculate the observables $\mathcal{O}_j^{rs} = \mathcal{O}_j(\mu_r, T_s)$. We rewrite the observables as a function of density and temperature, $\mathcal{O}_j^{rs} = \mathcal{O}_j(n_{rs}, T_s)$. However, interpolation is not efficient because the points (n_{rs}, T_s) are not on a grid. Therefore, we perform a first (slow) interpolation to obtain $\mathcal{O}_j^{ts} = (n_t, T_s)$ on a grid. Subsequent (fast) interpolations can be performed efficiently using these points.

Parameters of the problem include the effective field h and the interaction energy U . In addition, we can include experimental efficiencies, such as the imaging fidelity (see section 2.4.7). Typically we determine the imaging fidelities using other techniques, but it is also possible to include them as fitting parameters.

To increase the signal-to-noise of experimental observables, we typically compute their average over some spatial region. In many cases, we choose elliptical contours and perform an azimuthal average before applying the above fitting procedure. If the cloud does not have elliptical symmetry, we can apply alternative averaging schemes.

This fitting scheme can be modified to account for real space variations in the trap, such as a spatially varying U/t . In this case, we consider also the real space coordinates (x_i, y_i) associated with density n_i . If the functional form of the varying parameter is known, we can write $P_i = f(P_o, x_i, y_i)$, and substitute this dependence in eq. 3.56.

3.6.1 Fermi gas

Using this fitting technique combined with the Fermi gas equation of state discussed in section 3.2.1 and the correlators discussed in section 3.2.2, we can determine the parameters of the weakly interacting gas from experimental data. The parameters of the problem are $(\bar{\mu}/t, T/t, h/t)$, and accessible experimental observables are $\langle n_\sigma \rangle$, $C_\sigma(1, 0)$, $\langle n^s \rangle$, $C_s(1, 0)$, $\langle d \rangle$, and $C_d(1, 0)$. We show the result of the fitting technique described above for a weakly interacting $|1\rangle - |3\rangle$ mixture in fig. 3.4. We prepare this system by adjusting the magnetic bias field near 568 G, where the $|1\rangle - |3\rangle$ scattering length vanishes. This fit yields a temperature of $T/t = 0.40(5)$, where we have fixed $h = 0$ and used an imaging fidelity of 0.96 and doublon transfer efficiency of 0.9.

After determining the temperature and other parameters of the system, the chemical potential across the trap is known through the equation of state. We display the chemical potential in fig. 3.5, and a harmonic fit to determine the trapping frequency. The potential appears to be harmonic out to a radius of 35 sites and the trapping frequency is $\omega = (2\pi)0.011(1)\sqrt{\frac{2h}{ma^2}}\sqrt{\frac{t}{h}}$. This unconventional unit of frequency is obtained from fitting the chemical potential curve after writing the chemical potential

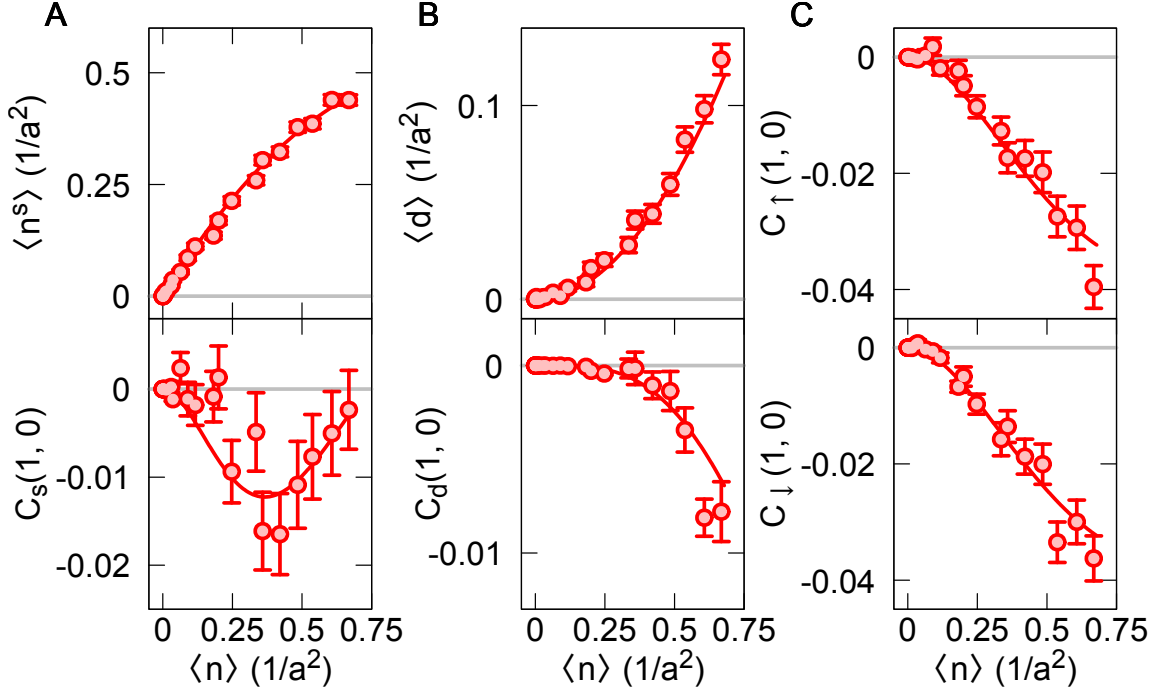


Figure 3.4: **Fermi gas parameter fitting.** Experimental data (points) and Fermi gas fit (line) for various observables versus total density. Experimental points are adjusted to account for imaging efficiencies. **A**, Singles density (top) and nearest-neighbor singles density correlations (bottom). The singles correlations are negative far from half-filling, reflecting the negative single-component density correlations. **B**, Doubles density (top) and nearest-neighbor doubles density correlations (bottom). The doublon correlations are negative, reflecting the influence of the single-component density correlators. **C**, Spin-up density correlator (top) and spin-down density correlator (bottom). These correlators are the most important observables for determining the temperature from the fit. Error bars standard error of the mean.

in units of t and distance in units of lattice sites. Here $t/h \approx 1250$ Hz leading to a trapping frequency $\omega = (2\pi)180$ Hz, a typical value in the experiment.

3.6.2 Determinantal quantum Monte Carlo

For the Hubbard gas the parameters are $(\bar{\mu}/t, T/t, U/t, h/t)$, and we consider the same observables as for the Fermi gas versus total density, $\langle n \rangle$. These various observables are each useful under certain conditions, but it is not necessary to include all of them simultaneously in most cases. For example, the correlators $C_\sigma(1, 0)$ are useful

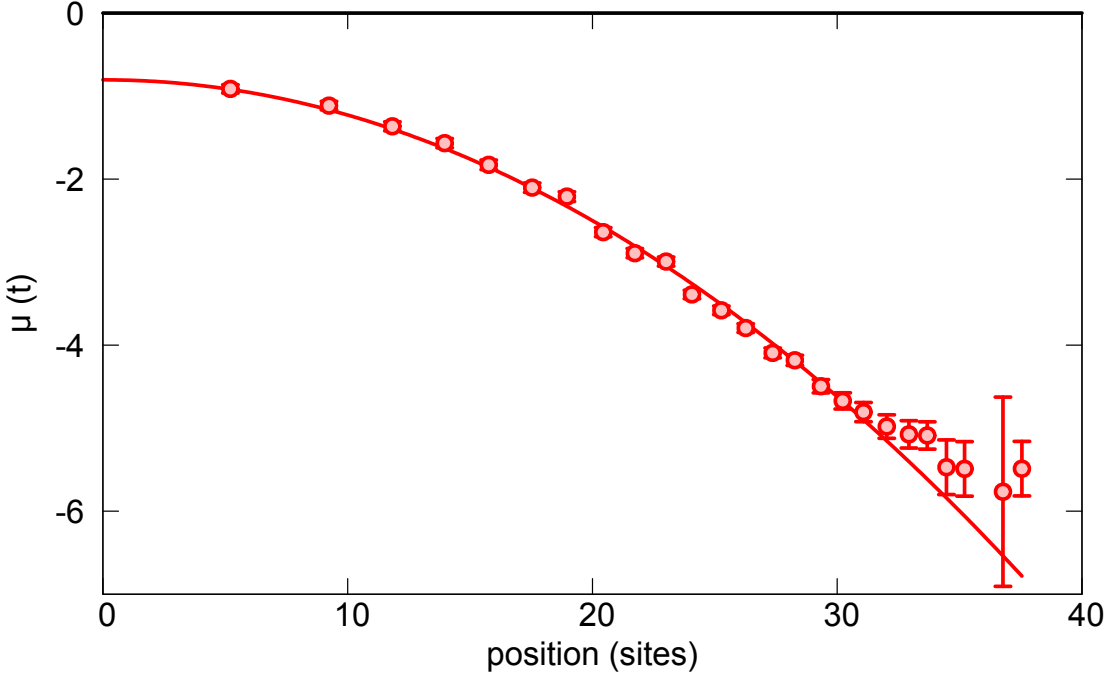


Figure 3.5: **Fermi gas trap parameter determination.** Chemical potential determined from the Fermi gas equation of state (points), and a parabolic fit to these points (line). The potential is harmonic to a radius of about 30 sites, where the Gaussian shape of the trapping beam becomes significant. Error bars standard error of the mean.

thermometers for temperature $T/t \sim 0.1 - 1$. The singles and doubles densities are sensitive to the interaction strength at low temperatures and serve as useful thermometers at temperature $T/t \sim 1 - 10$. The doublon-density correlator is a useful thermometer for attractive interaction. The single-species densities are useful for determining h/t in a spin imbalanced system. In principle it is possible to include other observables, such as further neighbor correlators.

We display the results of a fit used to determine the temperature T/t for a repulsive gas at fixed interaction strength $U/t = 8$ and field $h/t = 0$ in fig. 3.6. This fit only considers $\langle n^s \rangle$ and $C_\sigma(1, 0)$. The correlator acts as a thermometer at low temperatures, whereas the singles density is more sensitive at higher temperatures. Combining the two gives temperature sensitivity over a wider range. This fit yields

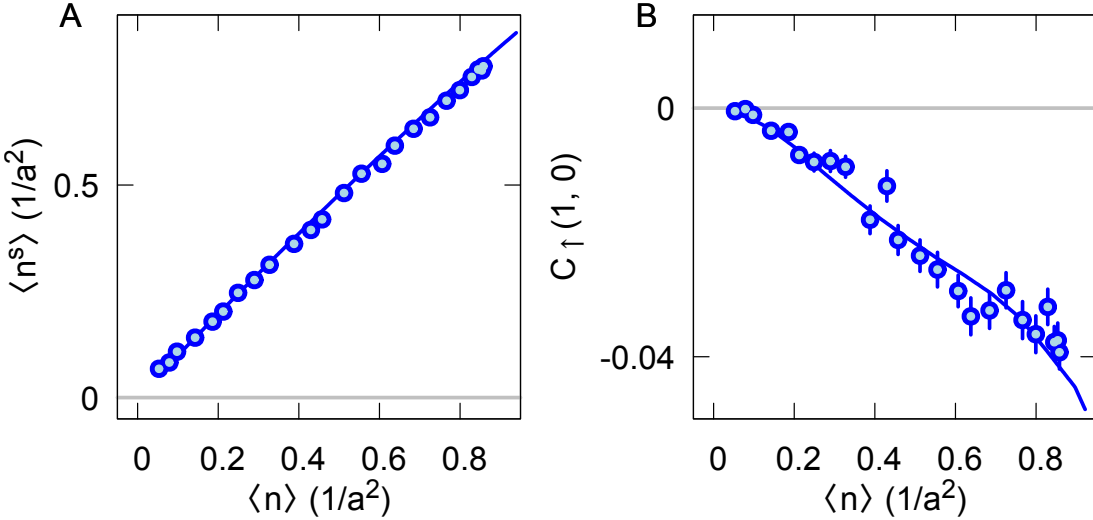


Figure 3.6: **DQMC parameter fitting, repulsive interaction.** Experimental data corrected for imaging efficiencies (points) and DQMC fit (lines) for various quantities versus total density. This fit yields $T/t = 0.39(2)$ for DQMC data at $U/t = 8$. **A**, Experimental results (points) and DQMC fit (lines) for the singles density versus total density. **B**, Spin-up density correlator, $C_{\uparrow}(0, 1)$, for nearest-neighbor sites. Error bars standard error of the mean.

a temperature $T/t = 0.39(2)$ accounting for an imaging fidelity of 0.96. Similar fits are used for thermometry in chapter 5.

The result of an exemplary fit used to determine T/t and U/t is shown in fig. 3.7. At low temperatures, the correlators provide thermometry while the singles and doubles densities help determine the interaction. We assume a doublon transfer efficiency of 0.9 and an imaging fidelity of 0.96. The net doublon imaging fidelity is the product of these factors. The densities are corrected by a single factor of the relevant efficiency, and correlators are corrected by the efficiency squared. The fit in fig. 3.7 yields a temperature of $T/t = 0.38$ and interaction of $U/t = -4.2$. Similar fits are used to determine T/t and U/t in chapter 6.

We obtain the DQMC results used for parameter fitting in this thesis from the Quantum Electron Simulation Toolbox (QUEST) software [177]. The simulations are run on an 8×8 homogeneous square lattice with the inverse temperature split into $L = 40 - 80$ imaginary time slices, where $L\Delta\tau = \beta$. We perform 5000 warm

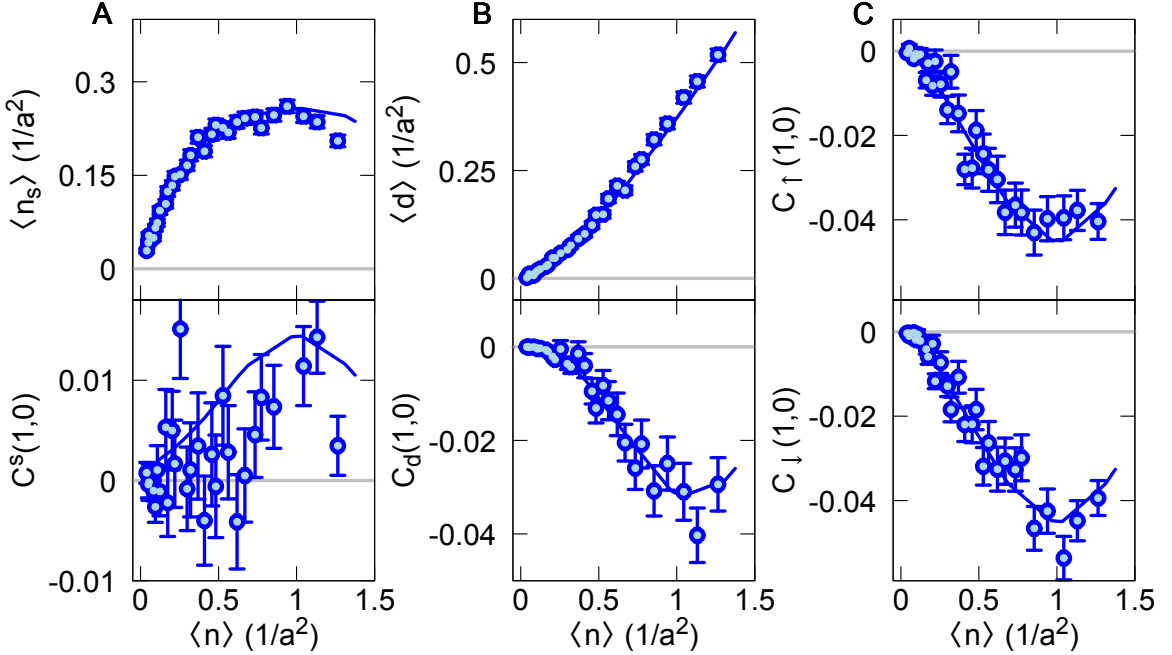


Figure 3.7: **DQMC parameter fitting, attractive interaction.** The experimental data corrected for imaging efficiencies (points) and DQMC fit (lines) for various quantities versus total density. This fit yields $T/t = 0.38$ and $U/t = -4.2$. **A**, Singles density (top) and nearest-neighbor singles density correlator (bottom). The singles density constrains the interaction. The singles density correlations are small, of the same order as the error bars. **B**, Doubles density (top) and nearest-neighbor doubles density correlator (bottom). The doubles density constrains the interaction, providing similar information to the singles density. The doubles density correlations are a thermometer. **C**, Spin-up density correlator (top) and spin-down density correlator (bottom). The single-component density correlators are good thermometers in this temperature range. Error bars standard error of the mean.

up sweeps, 50000 measurement sweeps and between 100 and 1000 passes to accumulate adequate statistics. Using these parameters, a single simulation at fixed $(\bar{\mu}/t, T/t, U/t, h/t)$ takes several hours to run. We perform up to 100 simulations in parallel using Princeton's Feynman cluster.

3.7 Linear response theory

Many of the experiments considered in this thesis involve perturbing a strongly-interacting system with a probe and observing the response of the system. In the

limit of a weak probe, these experiments can be understood using perturbation theory. In this section, we provide a brief outline of linear response theory. Although this material is available in a variety of textbooks (see for example [174, 175, 178]) it is rarely collected in a manner that is useful for the experimentalist.

We suppose we have a strongly interacting Hamiltonian and a weak probing field $h(r, t)$ which is coupled to an observable $M(r, t)$ of the system and we observe the system response by measuring observable $\mathcal{O}(r, t)$. We think of h as a generalized force which is conjugate to the observable M . Then the full Hamiltonian is $\mathcal{H} = \mathcal{H}_o + \mathcal{H}'(t)$, where \mathcal{H}_o is the unperturbed Hamiltonian and

$$\mathcal{H}' = \int dr M(r, t)h(r, t) \quad (3.57)$$

$$= \int dq M(-q, t)h(q, t). \quad (3.58)$$

In the second line we have taken the Fourier transform of both the observable and the field, which makes clear that a field with wave vector q couples to the observable at wave vector $-q$.

We apply first-order time dependent perturbation theory to determine the response of \mathcal{O} to this perturbation,

$$\langle \mathcal{O}(r, t) \rangle_{\mathcal{H}} - \langle \mathcal{O}(r, t) \rangle_{\mathcal{H}_o} = -\frac{i}{\hbar} \int_{-\infty}^t dt' \int dr' \langle [\mathcal{O}(r, t), M(r', t')] \rangle_{\mathcal{H}_o} h(r', t'), \quad (3.59)$$

which depends only on expectation values taken with respect to the *unperturbed* system. We can write the change in expectation value of \mathcal{O} due to the perturbation

$$\langle \delta \mathcal{O}(r, t) \rangle = \int_{-\infty}^{\infty} dt' \int dr' \Phi_{\mathcal{O}M}(r, t, r', t') h(r', t') \quad (3.60)$$

$$\Phi_{\mathcal{O}M}(r, t, r', t') = -\frac{i}{\hbar} \theta(t - t') \langle [\mathcal{O}(r, t), M(r', t')] \rangle, \quad (3.61)$$

where $\Phi_{\mathcal{O}M}$ is the *response function*. From eq. 3.61, we see it is identical with the retarded Green's function $G_{\mathcal{O}M}^R(r, t, r', t')$. This expression, referred to as the *Kubo formula*, gives a method for calculating response functions in terms of correlation functions [179].

Often the frequency domain version of the response function is more useful

$$\chi_{\mathcal{O}M}(r, r', \omega) = \int dt e^{i(\omega+i\eta)(t-t')} \Phi_{\mathcal{O}M}(r, t, r', t'), \quad (3.62)$$

which we will refer to as the *susceptibility*. Here we add a small positive imaginary part, $i\eta$, to the frequency so that the integral converges, but always work in the limit $\eta \rightarrow 0$. The susceptibility can be calculated from the eigenstates, $|n\rangle$ of \mathcal{H}_o with energies ϵ_n according to

$$\chi_{\mathcal{O}M}(\omega) = \frac{1}{Z} \sum_{m,n} (e^{-\beta\epsilon_n} - e^{-\beta\epsilon_m}) \frac{\langle n | \mathcal{O} | m \rangle \langle m | M | n \rangle}{\hbar(\omega + i\eta) + \epsilon_n - \epsilon_m}. \quad (3.63)$$

This relation makes clear that when $\mathcal{O} = M$ and \mathcal{O} is Hermitian, then the real (imaginary) part of the susceptibility is symmetric (antisymmetric) in ω .

In many cases of interest, our systems are translationally invariant. In that case, Φ and χ only depend on r and r' through the combination $r-r'$. Similarly, when \mathcal{H}_o is time-independent these only depend on t and t' through $t-t'$. In the translationally invariant case, it is useful to consider the response function and susceptibility in Fourier space,

$$\Phi_{\mathcal{O}M}(q, t) = -\frac{i}{\hbar} \theta(t-t') \langle [\mathcal{O}(q, t), M(-q, t')] \rangle, \quad (3.64)$$

where we have the particularly simple relation

$$\langle \delta \mathcal{O}(q, \omega) \rangle = \chi_{\mathcal{O}M}(q, \omega) h(q, \omega). \quad (3.65)$$

The susceptibility is convenient to work with because it is analytic in the upper-half plane. For example, this implies that the full susceptibility can be obtained from the real or imaginary part alone through the *Kramers-Kronig relation*

$$\chi(\omega) = \frac{1}{i\pi} \mathcal{P} \int_{-\infty}^{\infty} \frac{\chi(\omega')}{\omega' - \omega} d\omega', \quad (3.66)$$

where \mathcal{P} denotes the Cauchy principal value of the integral. Taking the real or imaginary part of the above equation leads to expressions for the real part of χ in terms of the imaginary part or vice-versa.

Many response functions are directly accessible through hydrodynamics in the long-wavelength and low frequency limit ($k \rightarrow 0, \omega \rightarrow 0$) [180], a fact we will take advantage of to measure the diffusion constant and conductivity of a repulsive Hubbard system in chapter 5.

The Kubo formula is closely connected with the *fluctuation-dissipation theorem*, which relates the correlation function,

$$S_{OM}(t) = \langle \mathcal{O}(t)M(0) \rangle - \langle \mathcal{O}(t) \rangle \langle M(0) \rangle \quad (3.67)$$

to the dissipative part of the susceptibility function [181]. Comparing the spectral representation of the susceptibility (eq. 3.63) to that of the correlation function S demonstrates that,

$$S_{OM}(\omega) = 2\hbar [1 + B(\omega)] \chi''_{OM}(\omega). \quad (3.68)$$

Here B is the Bose distribution function, and χ'' is the imaginary part of the response function. In the limit $\beta\omega \rightarrow 0$, this expression recovers the classical result, $S(\omega) = \frac{2}{\beta\omega} \chi''(\omega)$. Applying the Kramers-Kronig relation in this limit gives an expression for

the $\omega = 0$ susceptibility in terms of the $t = 0$ correlation function,

$$\chi'_{\mathcal{O}M}(\omega = 0) = \beta S_{\mathcal{O}M}(t = 0), \quad (3.69)$$

where χ' is the real part of the susceptibility. This form of the fluctuation-dissipation theorem leads to the expressions for the charge compressibility (eq. 3.37) and magnetic susceptibility (eq. 3.46) given earlier. For example, we obtain eq. 3.37 by identifying $\mathcal{O}(r_i, t) = n_i(t)$ and $M(t) = \sum_i n_i(t)$. These are exact relations because they are taken at $\omega = 0$.

3.7.1 Matsubara Green's function

Linear response calculations are frequently easier to perform working in imaginary time, as opposed to directly in real time. We briefly introduce the Matsubara Green's function and discuss its close connection to the retarded Green's function.

The Matsubara Green's function at imaginary time $\tau = it$ is defined by

$$G_{AB}(\tau) = -\frac{1}{\hbar} \langle \mathcal{T}A(\tau)B(0) \rangle, \quad (3.70)$$

where $A(\tau) = e^{\tau\mathcal{H}}A(0)e^{-\tau\mathcal{H}}$. Here \mathcal{T} is the time ordering operator given by

$$\mathcal{T}A(\tau)B(0) = \theta(\tau)A(\tau)B(0) \mp \theta(-\tau)B(0)A(\tau) \quad (3.71)$$

for fermionic and bosonic operators respectively. The Matsubara Green's function is periodic for bosons and antiperiodic for fermions, i.e. $G(\tau + \beta) = G(\tau)$ for bosons and $G(\tau + \beta) = -G(\tau)$ for fermions. This property implies it has a discrete frequency

spectrum, and we write its Fourier transform

$$G(i\Omega_n) = \int_0^\beta d\tau \mathcal{G}(\tau) e^{i\Omega_n \tau} \quad (3.72)$$

$$\mathcal{G}(\tau) = \frac{1}{\beta} \sum_n \mathcal{G}(i\Omega_n) e^{-i\Omega_n \tau}, \quad (3.73)$$

where Ω_n are the *Matsubara frequencies* given by $\Omega_n = \frac{2\pi n}{\beta}$ for bosons and $\Omega_n = \frac{\pi(2n+1)}{\beta}$ for fermions.

The utility of working with the Matsubara Green's function comes from the many nice properties of the time ordering operator. For example, Wick's theorem applies to time ordered Green's functions which enables the apparatus of many-body perturbation theory. The Matsubara Green's function is useful for linear response because it can be analytically continued to yield the retarded Green's function. This follows from the spectral representation,

$$G_{AB}(i\Omega_n) = \frac{1}{Z} \sum_{n,m} (e^{-\beta\epsilon_n} \pm e^{-\beta\epsilon_m}) \frac{A_{nm}B_{mn}}{\hbar(i\Omega_n) + \epsilon_n - \epsilon_m}, \quad (3.74)$$

which is identical with the retarded Green's function (eq. 3.63) under the substitution $i\Omega_n \rightarrow \omega + i\eta$. Here the upper sign is for fermionic operators, and the lower for bosonic. Indeed, we can define an analytic function $G(z)$ everywhere on the complex plane away from the real axis which coincides with the Matsubara Green's function at the Matsubara frequencies, matches the retarded Green's function when approaching the real axis from above ($\lim_{\eta \rightarrow 0} G(\omega + i\eta) = G^R(\omega)$), and matches the advanced Green's function when approaching from below ($\lim_{\eta \rightarrow 0} G(\omega - i\eta) = G^A(\omega)$). This is an example of the principle of *analytic continuation*. An expression for an analytic function on an open set can be extended to a larger open set, provided it is well defined.

The Matsubara Green's function is also closely connected to the spectral function,

$$A(\omega) = -\frac{1}{\pi} \text{Im} [G^R(\omega)]. \quad (3.75)$$

Using contour integration techniques (see e.g. [174, 175]) this connection can be expressed

$$G(\tau) = \int_{-\infty}^{\infty} d\omega F/B(-\omega) e^{-\omega\tau} A(\omega) \quad (\tau \geq 0) \quad (3.76)$$

$$G(\tau) = \int_{-\infty}^{\infty} d\omega F/B(\omega) e^{-\omega\tau} A(\omega) \quad (\tau \leq 0) \quad (3.77)$$

$$G(i\Omega_n) = \mp \int_{-\infty}^{\infty} d\omega \frac{A(\omega)}{i\Omega_n - \omega}, \quad (3.78)$$

where as above the upper and lower symbols are for fermionic and bosonic operators. Here B and F are the Bose and Fermi distribution functions respectively. Eqs. 3.76 and 3.77 are the basis for numerical analytic continuation techniques, which given $G(\tau)$ or $G(i\omega_n)$ attempt to invert one of the integral equations to obtain $A(\omega)$ [182]. Eq. 3.78 has a broader domain of validity than given above. If we take $i\Omega_n \rightarrow z$, where z is a general complex argument, this provides an expression for $G(z)$ off the real axis.

Chapter 4

Canted antiferromagnetism in a Fermi-Hubbard system

Portions of this chapter are based on work previously published as

P. T. Brown, D. Mitra, E. Guardado-Sánchez, P. Schauß, S. S. Kondov, E. Khatami, T. Paiva, N. Trivedi, D. A. Huse, and W. S. Bakr. [Spin-imbalance in a 2D Fermi-Hubbard system](#). *Science* **357**, 6358, 1385–1388 (2017).

The Fermi-Hubbard model exhibits quantum magnetism near half-filling in the sense that up and down spins are strongly correlated. Observing an up spin next to a down spin is more likely than observing two particles with the same spins next to each other. These *antiferromagnetic* spin correlations are favored by the superexchange interaction which we introduced in section 3.1. The superexchange physics can be made more transparent by mapping the Fermi-Hubbard model onto a Heisenberg spin model at half-filling and strong interaction (see sections 3.1.7 and 3.1.8).

To gain more insight into quantum magnetism, we can ask what happens when we introduce an external magnetic field which also couples to the spins. Does the com-

petition between the external magnetic coupling and the antiferromagnetic coupling lead to new and interesting physics?

Magnetic fields couple to particles in two ways. The first is through the Lorentz force which affects the motion of charged particles. This orbital magnetic coupling is extremely important in real materials and leads to interesting physics such as the Meissner effect, a form of perfect diamagnetic behavior observed in superconductors. More generically, it leads to the weak Landau diamagnetism predicted in electron systems [183]. However, this magnetic coupling is not relevant for cold atom systems, because atoms are charge neutral. The second mechanism is Zeeman coupling, i.e. magnetic dipole coupling between the magnetic field and the particle spin. This effect shifts the energy of spins with different angular momentum projections along the directions of the field. In a system with spin-exchange this leads to imbalanced spin populations. For weakly interacting particles the Zeeman shift increases the population of spins pointing in the same direction as the field, an effect referred to as *Pauli paramagnetism* (see section 3.2.3). We can also adopt a complementary viewpoint, and regard a spin population imbalance as an effective Zeeman magnetic field.

In real materials, Lorentz effects typically mask Zeeman field effects. For example, in superconducting materials Lorentz effects lead to the destruction of superconductivity above a certain critical field, which occurs before Zeeman effects became noticeable. One method of suppressing Lorentz effects is to work with a 2D material and apply a magnetic field parallel to the material plane.

Even when such techniques suppress Lorentz effects, observing significant Zeeman effects requires the Zeeman shift to be comparable to the superexchange energy. We can make a rough estimate of the fields required by comparing the superexchange energy to $g\mu_b B$, where $g \approx 2$ is the Landé g -factor of the electron and μ_b is the Bohr magneton. For a typical superexchange energy in a cuprate material, $J \sim 0.13 \text{ eV}$ [9],

this implies a field strength of $B \approx 10^3$ T. Typical laboratory magnetic fields are in the range of a few tens of Tesla. Therefore, even in situations where Lorentz magnetic field effects can be suppressed, it is difficult to reach significant Zeeman fields.

Atomic systems appear to have little advantage over electron systems because atoms inherit magnetic moments from their constituent particles. Since electrons in closed shells have zero net magnetic moment, we might expect an enhancement of at most a factor of the number of valence electrons for a given atomic species. However, atomic systems are capable of achieving extremely strong effective fields by taking advantage of the analogy between a spin population imbalance and a Zeeman field. In these systems spin exchange can be avoided, so a prepared spin-imbalanced will be conserved. Spin exchange only occurs through spin-changing collisions, which are energetically forbidden at cold temperatures and finite Zeeman splitting for certain initial states, or through magnetic dipolar interactions which are extremely weak because these systems are dilute. From this point of view, preparing a nearly polarized cold atom system corresponds to applying a magnetic field orders of magnitude stronger than achievable in the lab.

4.1 Magnetic fields and correlated quantum systems

The interplay of strong interactions and magnetic fields gives rise to novel forms of superconductivity and magnetism in quantum many-body systems. Here we present an experimental study of the two-dimensional Fermi-Hubbard model—a paradigm for strongly-correlated fermions on a lattice—in the presence of a Zeeman field and varying doping. Using site-resolved measurements, we reveal spin-anisotropic antiferromagnetic correlations, a precursor to long-range canted order. We observe nonmonotonic behavior of the local polarization with doping for strong interactions,

which we attribute to the evolution from an antiferromagnetic insulator to a metallic phase. Our results pave the way to experimentally mapping the low-temperature phase diagram of the Fermi-Hubbard model as a function of both doping and spin polarization, for which many open questions remain.

Magnetic fields can significantly modify the behavior of strongly-correlated condensed matter systems in important ways, even leading to new phases of matter. Well-known examples include superconductors with finite-momentum pairing induced by Zeeman effects and fractional quantum Hall states induced by orbital effects [184]. Theoretically, a cornerstone model for studying strongly-interacting fermions on a lattice is the Fermi-Hubbard model [185]. This model has been the topic of intense study over several decades because of its potential implications for understanding high-temperature superconductors and other quantum many-body systems [9, 10]. The phase diagram of the Fermi-Hubbard model in the presence of a Zeeman field is qualitatively understood at half-filling, with a canted antiferromagnetic state expected at low temperatures [186]. Much less is known, even on a qualitative level, about the phase diagram away from half-filling, where the interplay of doping, spin polarization, and strong correlations can lead to rich physics.

The difficulty of numerical simulations of the Fermi-Hubbard model at low temperatures has motivated quantum simulations that use two-component Fermi gases in optical lattices [39, 40]. Rapid developments have been achieved by the recent introduction of quantum gas microscopes for fermionic atoms [60, 61, 62, 63, 64, 65, 187]. The reduction of density fluctuations in the Mott insulating phase—previously inferred from bulk measurements [39, 40]—has been explicitly revealed. Furthermore, site-resolved measurements probe antiferromagnetic correlations at all distances and sites in the trapped gas directly[67, 68, 69], complementing other techniques that detect these correlations by measuring the fraction of singlets on neighboring sites [43],

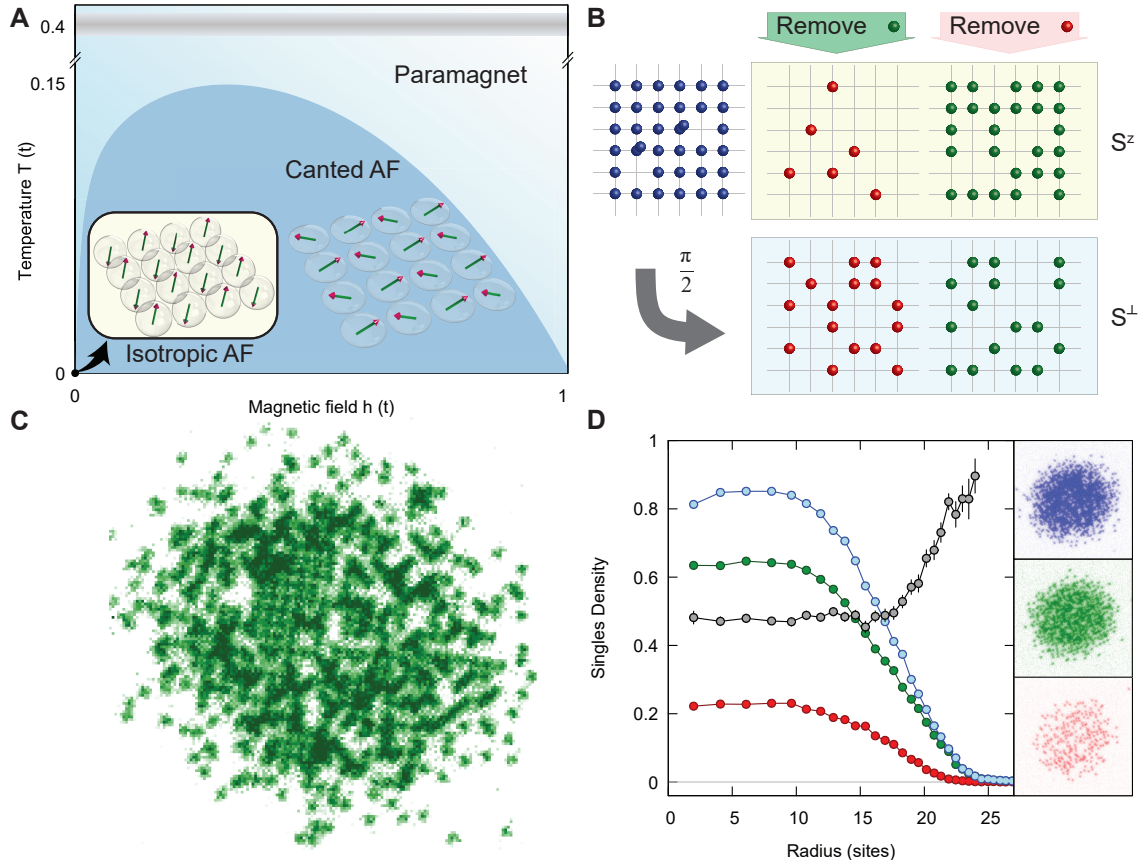


Figure 4.1: Site-resolved imaging of a spin-imbalanced Fermi gas in an optical lattice. **A**, Schematic phase diagram of the Fermi-Hubbard model at half-filling. T is the temperature, and h is the effective Zeeman field controlled experimentally by the global polarization P_g , both in units of the tunneling energy, t . At $h = 0$, the ground state is an antiferromagnet with SU(2) symmetry. For non-zero h , there is a finite temperature transition to a canted antiferromagnetic phase. Antiferromagnetic correlations persist at experimental temperatures (gray band). The ellipsoids surrounding the spins illustrate the magnitude of correlations in a given direction. **B**, We prepare a spin mixture (blue) in an optical lattice and then selectively remove one spin state (red or green) and doublons. We extract spin correlations from the resulting density correlations for the S^z spin projection and the S^\perp projection after a global spin rotation ($\pi/2$ -pulse). **C**, Site-resolved fluorescence image after removal of one spin state. Field of view is $35\text{ }\mu\text{m} \times 35\text{ }\mu\text{m}$. **D**, Azimuthally averaged profiles and single fluorescence images showing the total singles density n^s (purple), n_\uparrow^s (green), n_\downarrow^s (red), n^s (blue), and local polarization p^s (gray) over the trap at $U/t = 8.0(5)$. Insets are corresponding exemplary single-shot pictures. Field of view is $48\text{ }\mu\text{m} \times 48\text{ }\mu\text{m}$. Error bars standard error of the mean.

using Bragg scattering [49] or taking advantage of the fluctuation-dissipation theorem [54].

In this work, we probe the magnetic response of a two-dimensional Fermi-Hubbard system using a spin-imbalanced Fermi gas that has so far been studied mostly by theoretical means [188, 189, 190]. Thermodynamically, a non-zero polarization corresponds to the introduction of an effective Zeeman field $h = (\mu_{\uparrow} - \mu_{\downarrow})/2$, where $\mu_{\uparrow,\downarrow}$ are the chemical potentials of the two spin components. The system is described by the Hubbard Hamiltonian given in eq. 3.2.

4.2 Quantum magnetism in the Fermi-Hubbard model

At low temperatures and in the absence of a field, the half-filled Fermi-Hubbard model exhibits isotropic antiferromagnetic correlations along any projection of the spin owing to the SU(2) spin symmetry (see section 3.1.4). The correlations decay exponentially with distance, and the correlation length diverges at zero temperature. A non-zero magnetic field reduces the spin symmetry to U(1), leading to a finite temperature Berezinskii-Kosterlitz-Thouless (BKT) phase transition to a canted antiferromagnet, where the correlations decay algebraically [188] (fig. 4.1A). Canting accommodates magnetization along the field while still benefiting from the superexchange interactions by building up long-range antiferromagnetic correlations of the spin components perpendicular to the magnetization. The BKT phase transition boundary has been calculated for the Fermi-Hubbard model, but until recently different methods had large discrepancies [154]. Even above this boundary, precursor canted correlations are present and we directly detect them in our experiment. Furthermore, we probe the spin-imbalanced Fermi-Hubbard model in the presence of

doping, where theory is challenged by the fermion “sign problem”, revealing a non-monotonic behavior of the local polarization.

4.3 Experimental preparation

We realize the 2D Fermi-Hubbard model using a degenerate mixture of two hyperfine states, $|\uparrow\rangle = |1\rangle$ and $|\downarrow\rangle = |3\rangle$ in the ground state hyperfine manifold of ${}^6\text{Li}$ in an optical lattice. Here $|i\rangle$ is the i th lowest Zeeman sublevel. The global spin imbalance $P_g = (N_\uparrow - N_\downarrow)/(N_\uparrow + N_\downarrow)$ can be varied continuously from 0-0.9 by evaporating the gas in the presence of a magnetic gradient leading to preferential loss of one of the spin states. The final temperature is weakly affected by choice of imbalance.

To create the sample we load a magneto-optical trap (MOT) from a Zeeman slower, then use a compressed MOT stage to load a $\approx 1\text{ mK}$ deep optical trap, and evaporatively cool that atoms by lowering the optical trap depth near the 690 G Feshbach resonance. We stop the evaporation before Feshbach molecules form and transfer the atoms to a highly anisotropic light sheet trap where it undergoes further evaporation near 300 G. Next, we transfer the atoms into a single layer of a 532 nm accordion lattice with trapping frequency $\omega_z = 2\pi \times 19.9(3)\text{ kHz}$ in the axial direction, and utilize a 1070 nm beam to provide radial confinement. For further details, see [87, 191] and section 2.1.

The spin populations are imbalanced by evaporating the mixture in a magnetic gradient of up to 40 G/cm along the same direction as the magnetic bias field, which we set in the range 75-500 G depending on the targeted imbalance. We then adjust the bias field near 494 G which sets the scattering length to be $448(9)\text{ a}_\text{o}$, where a_o is the Bohr radius, and adiabatically load into a 2D square lattice with a 50 ms long ramp to a depth of $10.5(3)\text{ E}_\text{r}$. Here, $E_\text{r} = h \times 14.66\text{ kHz}$ is the lattice recoil energy. We estimate the tunneling rate to be $t = h \times 450(25)\text{ Hz}$ at this lattice depth. For these

parameters, we obtain $U/t = 8.0(5)$, where strong antiferromagnetic correlations are expected at half-filling in the balanced gas.

We detect site occupations using Raman fluorescence imaging with an exposure time of 1200 ms, during which we collect \sim 1000 photons/atom. We estimate the imaging fidelity using the techniques described in section 2.2 and find a tunneling rate of 0.4(2) % and a loss rate of 1.6(3) % per picture. In addition, while holding the atoms in a deep lattice for spin manipulations and doublon hiding, we lose 2(1) % of the atoms, leading to a net detection efficiency of 96 %.

4.4 Measuring spin correlations

Fluorescence images obtained with quantum gas microscopy techniques enable us to identify singly occupied sites in the lattice, regardless of the spin state (see section 2.4). Doubly occupied sites undergo light assisted collisions and appear empty. We can also identify singly occupied sites where the atoms are projected onto a chosen eigenstate of S^z by illuminating the cloud with a short pulse of resonant light that ejects atoms in the other eigenstate (fig. 4.1B,C). By first converting atoms on doubly occupied sites to deeply bound molecules, we ensure that they are not affected by this light pulse and they are subsequently lost in light-assisted collisions during imaging. From these images we extract the azimuthally-averaged density of atoms on singly-occupied (s) sites in a particular spin (σ) state $n_\sigma^s(r)$ and the total density $n^s = n_\uparrow^s + n_\downarrow^s$, shown in fig. 4.1D for an imbalanced gas. We observe a plateau in n^s over an extended region near the center of the trap, indicating a reduction in compressibility owing to the charge gap. The deviation of n^s from unity within this region is primarily due to doublon-hole quantum fluctuations, which are non-negligible at our interaction strength. We characterize the local polarization in terms of the measured quantities $p^s = (n_\uparrow^s - n_\downarrow^s)/(n_\uparrow^s + n_\downarrow^s)$. This definition coincides with the true polar-

ization in the absence of doubly occupied sites. At the accessible temperatures, the local polarization is constant throughout the central reduced compressibility region.

We measure spin correlators along two different spin projections, both parallel to the field, C_{spin}^z , and orthogonal to it, C_{spin}^\perp . The spin correlators between sites separated by a displacement $d = (d_x, d_y)$ are defined by eq. 3.17. S^\perp is the spin along an undetermined direction in the plane orthogonal to the field, where rotational symmetry ensures $\langle S^\perp \rangle = \langle S^{x,y} \rangle$. Similarly, $C_{\text{spin}}^\perp(d) = C_{\text{spin}}^{x,y}(d)$.

$C_{\text{spin}}^z(d)$ is obtained from the singles density correlators $C_s(d)$, and the single-component singles density correlators $C_{s,\sigma}(d)$ according to eq. 2.11. The procedures for measuring C_s and $C_{s,\sigma}$ are described in detail in section 2.4.

To extract $C_{\text{spin}}^\perp(d)$, we insert a radiofrequency pulse to coherently rotate the spins by $\pi/2$ before initiating the measurement protocol. Because a direct rf transition between states $|1\rangle$ and $|3\rangle$ is forbidden by selection rules we perform the $\pi/2$ spin rotation using a two step protocol described below. After freezing tunneling dynamics in a 55 E_r lattice, we convert the $|1\rangle - |3\rangle$ mixture to a $|1\rangle - |2\rangle$ mixture by driving a radio-frequency Landau-Zener transition between states $|3\rangle$ and $|2\rangle$ in 10 ms with efficiency of 0.99(1). Next we hide all doublons in our sample by converting them to molecules, employing a ramp across a narrow Feshbach resonance near 543 G (as discussed in section 2.4.3). Then we either drive a $\pi/2$ spin rotation to measure correlations for the spin component perpendicular to the effective magnetic field, or omit this to measure correlations for the spin component parallel to the field.

4.5 Calibration of Hubbard parameters

We extract our lattice parameters from atom resolved images, as described in section 2.2. We determine that the lattice axes are at an angle of $90.02(2)^\circ$ and the lattice

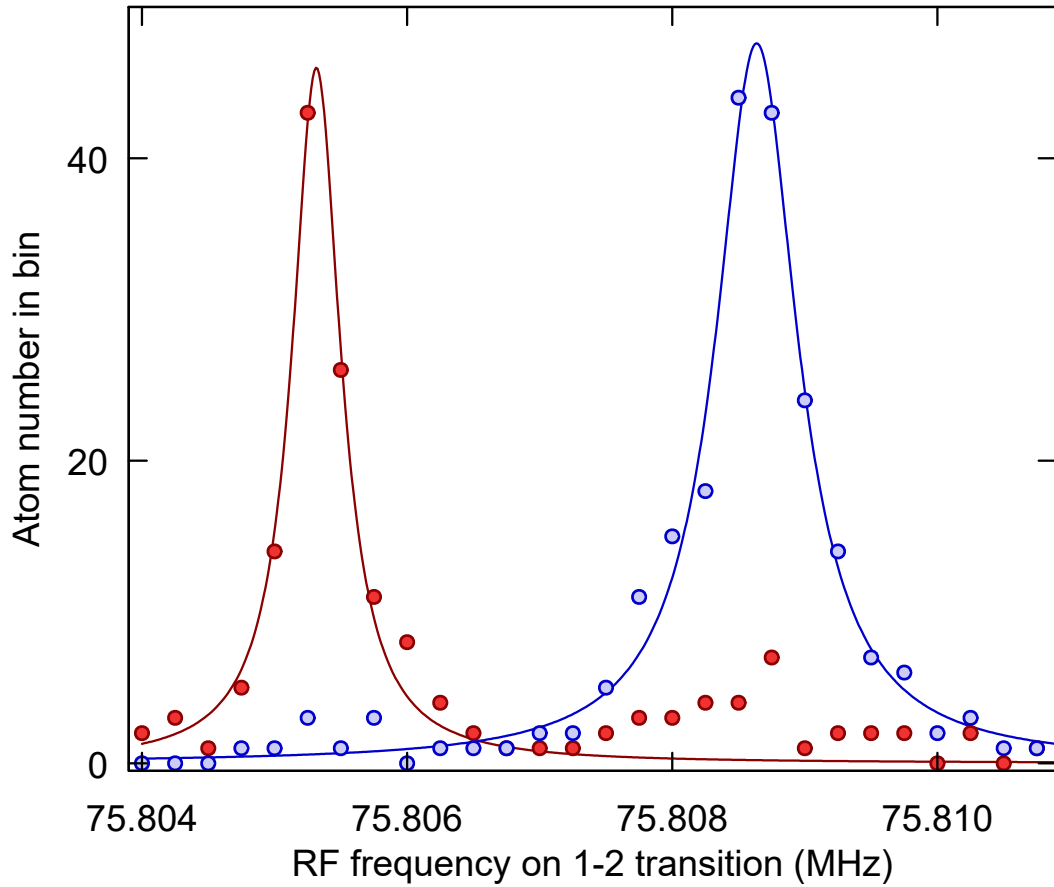


Figure 4.2: **RF spectroscopy Hubbard interaction calibration.** Spectroscopy signal from a band insulator at lattice depth of $10.5 E_r$ and scattering length $448 a_0$. Shown is the transferred atom number in the center of the cloud (red), where sites are doubly occupied and in the surrounding Mott insulator region (blue) where most sites are singly occupied. To determine the interaction energy the final state interaction must accounted for (see text).

constants are $a_x = 762$ nm and $a_y = 741$ nm, from which we extract the intersection angle of the lattice beams, $\theta = 91.63(2)^\circ$, using eq. 2.30.

Using the lattice depth calibration procedure described in section 2.5.1 we infer the depth of the lattice in which our measurements are performed to be $10.5(3)$ E_r and the retro-reflected electric field attenuation factor to be $r = 0.54$. From this we obtain tight-binding tunneling values $t_x = 442$ Hz, $t_y = 462$ Hz ($t_x/t_y = 0.96$), and $t_d = 12$ Hz. The reduction of the lattice depth across the cloud due to the Gaussian profile of the lattice beams (see section 2.5.1) leads to an increase in the tunneling by 10 % at the edge of the cloud compared to the central value.

We measure the interaction energy U using radio frequency spectroscopy (fig. 4.2). We transfer atoms from state $|1\rangle$ to $|2\rangle$ and resolve the frequency shift between singly and doubly occupied sites. We determine

$$U_{13} = \delta U \frac{a_{13}}{a_{13} - a_{23}}, \quad (4.1)$$

taking into account a small correction due to weak final state interactions. The experimentally measured value agrees with the value determined from band structure calculations including higher band corrections [192] to within 10 %.

4.6 Spin canting at half-filling

We observe short-range canted antiferromagnetism at half-filling with stronger spin correlations in the direction orthogonal to the magnetization, in contrast to the spin-balanced case where identical correlations are measured for any projection of the spin. To investigate the dependence of the spin correlations on p^s , we varied the global polarization P_g and extracted the correlations in the half-filled central region. The measured nearest and next-nearest-neighbor correlators $C_{\text{spin}}^{\perp,z}$ are shown in fig. 4.3A and the correlator anisotropies, defined as $A = 1 - C_{\text{spin}}^z/C_{\text{spin}}^\perp$, are shown in fig. 4.3B.

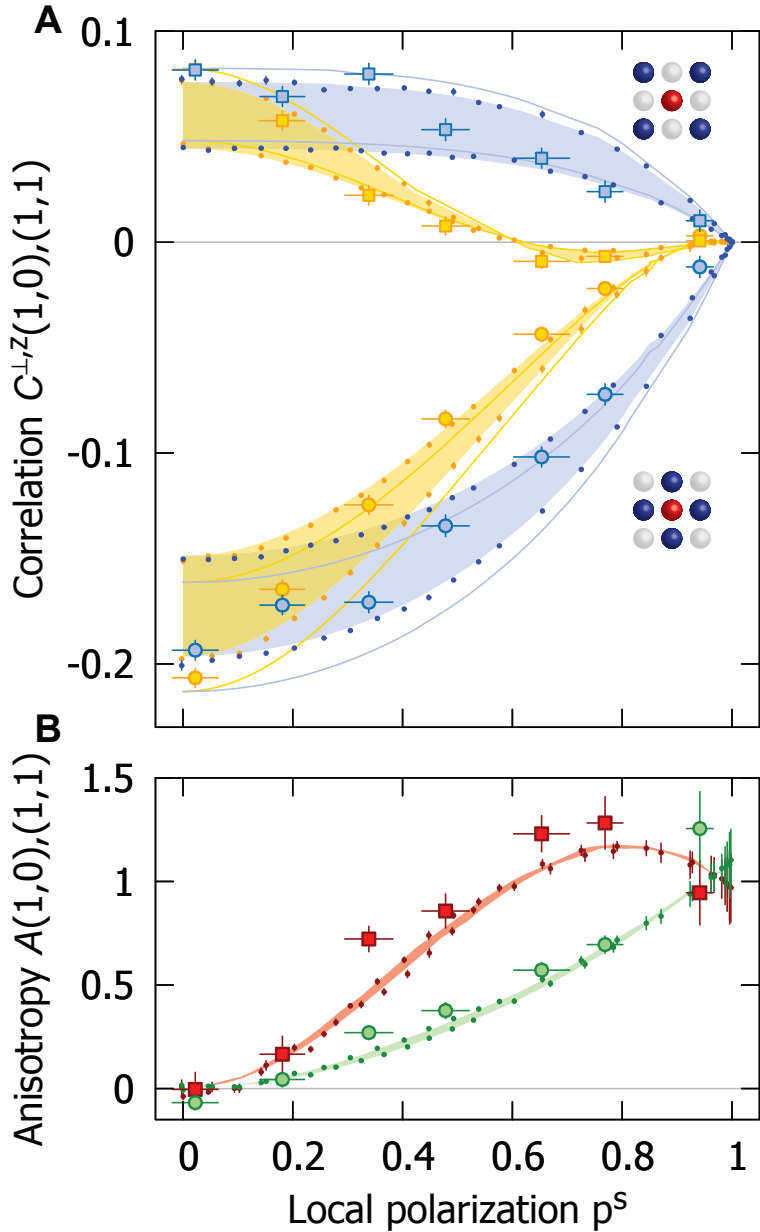


Figure 4.3: **Anisotropic spin correlations.** **A**, Experimental nearest-neighbor (large circles) and diagonal-neighbor (squares) spin correlations for the S^z (yellow) and S^\perp (blue) spin projections versus local polarization p^s at half-filling. We show NLCE (edges of shading) and DQMC (small circles) results at $U/t = 8$ corrected for our detection efficiency of 0.96 and uncorrected NLCE results (solid lines). For the simulations, a temperature band from $T/t = 0.38 - 0.53$ is shown. **B**, Anisotropy A of nearest-neighbor (large green circles) and diagonal-neighbor (red squares) spin correlations with NLCE (solid lines) and DQMC (small circles) results. A is insensitive to detection efficiency. Error bars standard error of the mean. Experimental data averaged over ~ 50 images and azimuthally.

For an almost unpolarized gas, with local polarization $p^s = 0.02(4)$ at half-filling, we find isotropic correlations: $A = -0.06(7)$ for the nearest-neighbor and $A = 0.0(2)$ for the next-nearest-neighbor. The consistency of these values with zero verifies the SU(2) spin symmetry of the Fermi-Hubbard Hamiltonian at $h = 0$. As the polarization is increased, we observe an overall decrease in correlations, with C_{spin}^z decreasing faster than C_{spin}^\perp , leading to growing nearest-neighbor anisotropy with polarization.

The system's preference to build correlations in the plane orthogonal to the field can already be understood at the level of a classical Heisenberg model because spins oriented with the staggered magnetization in the xy -plane can lower their energy by uniformly canting in the direction of the field. In the quantum system, strong quantum fluctuations in two-dimensions reduce the magnitude of the nearest-neighbor correlator in the balanced gas from 1 to 0.36 in the ground state [69], and thermal fluctuations and imaging fidelity further reduce it to the experimentally measured value of 0.207(4). At non-zero polarization, we observe that the correlator anisotropy is stronger when the sites are further apart. For example, at local polarization $p^s = 0.48(4)$, $A = 0.38(9)$ for the nearest-neighbor, while $A = 0.8(2)$ for the next-nearest-neighbor. The increase of the correlation anisotropy with distance can be partly understood by considering what happens at lower temperatures as we approach the BKT transition. There the C_{spin}^\perp correlations become long range while the C_{spin}^z do not, so at long distance A approaches one.

We compare our measurements to results from determinantal quantum Monte Carlo (DQMC) [193, 194] and numerical linked cluster expansion (NLCE) [195, 196] simulations of the Fermi-Hubbard model at half-filling in the presence of a chemical potential imbalance with the temperature as a free parameter. For the balanced gas, the measured nearest-neighbor correlators give a fitted temperature of $T/t = 0.40(5)$. The temperature increases with polarization, rising to $T/t = 0.57(5)$ at local polarization $p^s = 0.77(3)$. This trend may be caused by a reduction of the efficiency

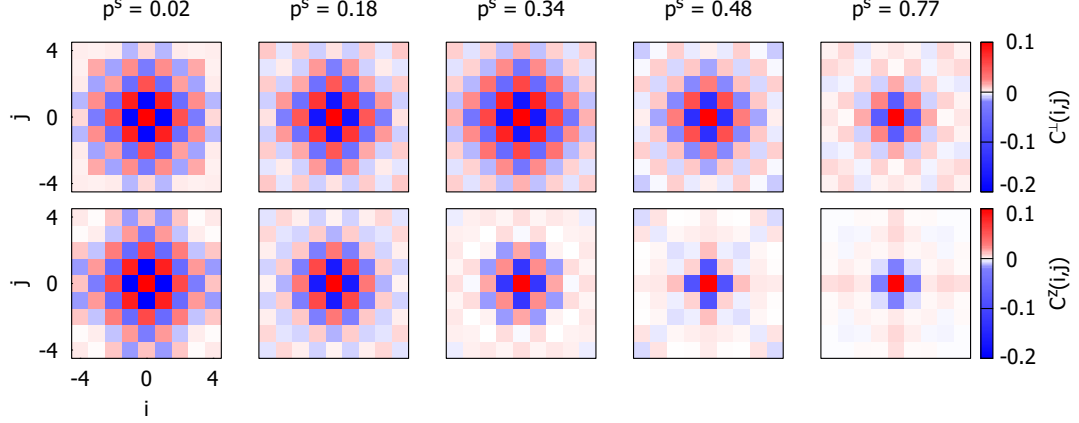


Figure 4.4: **Spin correlation matrices.** Full spin correlation matrices for different site displacements $d = (i, j)$, shown at half-filling for different local polarizations p^s . Top row shows S^\perp correlators, C_{spin}^\perp , and bottom row shows S^z correlators, C_{spin}^z . Correlator values are averaged over equivalent points using the symmetry of the square. Each panel is calculated from ~ 50 images.

of evaporative cooling with increasing spin imbalance. The calculated anisotropy is almost independent of temperature over this range, and shows excellent agreement with the experiment (fig. 4.3B). The temperatures obtained from the spin correlations agree with those calculated from the singles density correlations (see section 4.9).

Insight into the range of the antiferromagnetic order can be gained by examining 2D plots of the spin correlators as a function of the displacement vector between the sites (fig. 4.4). The checkerboard pattern is visible for displacements of up to four sites in the almost unpolarized gas, and the overall decrease of all correlations with polarization, as well as the suppression of C_{spin}^z relative to C_{spin}^\perp is evident. The C_{spin}^\perp correlations remain antiferromagnetic at all polarizations, but the C_{spin}^z correlations can be viewed as the density correlations of the gas of minority spins [197] whose modulation becomes longer wavelength as the density of this gas decreases (see section 4.7). This leads to a change in the sign of $C_{\text{spin}}^z(1, 1)$ near local polarization $p^s = 0.6$ (figs. 4.3A and 4.4). The observation of this percent-level negative correlation is only possible because of the superb sensitivity of quantum gas microscopy.

4.7 Sign change of spin z -correlation for large polarizations

To understand why $C_{\text{spin}}^z(1,1)$ becomes negative near $p_s = 0.6$ at half filling, it is instructive to consider what happens in the Heisenberg model with a nearly fully polarized gas. We can regard the fully polarized gas as a vacuum state and the minority spins as a dilute gas of magnons [197, 198]. These magnons are bosons and can form a Bose-Einstein condensate (BEC) at low temperatures. We will find that the BEC off-diagonal order is associated with the spin correlations perpendicular to the magnetization, and the density correlation of the magnons are associated with the spin correlations parallel to the magnetization.

To make this argument more concrete, we rewrite the Heisenberg Hamiltonian using operators defined by $\beta_i^\dagger = S_i^+$, $\beta_i = S_i^-$ and $S_i^z = \beta_i^\dagger \beta_i - 1/2$,

$$\mathcal{H} = \frac{J}{2} \sum_{\langle i,j \rangle} \left(\beta_i^\dagger \beta_j + \beta_j^\dagger \beta_i \right) + \sum_i (h - 4J) \beta_i^\dagger \beta_i + J \sum_{\langle i,j \rangle} \beta_i^\dagger \beta_j^\dagger \beta_i \beta_j. \quad (4.2)$$

The β_i and β_j satisfy bosonic commutation relations for $i \neq j$. To avoid difficulty at $i = j$ we introduce an infinite on-site repulsion, or hard-core constraint, and can then regard β_i^\dagger as the creation operator for a boson on site i [197]. From the middle term in Eq. 4.2, we see the field h is the chemical potential of the magnons (up to a constant offset). The last term describes nearest-neighbor repulsion of magnons. The first term describes the bosons tunneling. Transforming to momentum space, this term becomes $\sum_q \epsilon(q) \beta_q^\dagger \beta_q$ with $\epsilon(q) = J(\cos(q_x a) + \cos(q_y a))$ where a is the lattice constant. In contrast to the typical case, the tunneling term here is positive and the condensate forms at the band minimum, $q = (\pi, \pi)$. Condensation is signaled by non-zero expectation value of off-diagonal density matrix elements. For system of

volume V and total particle number N these elements are

$$\begin{aligned}\langle \beta_i^\dagger \beta_{i+d} \rangle &= \frac{1}{V} \int dq \exp(iq \cdot d/\hbar) \langle \beta_q^\dagger \beta_q \rangle \\ &= \frac{N}{V} (-1)^{d_x + d_y}.\end{aligned}\quad (4.3)$$

Using the identity $\beta_i^\dagger \beta_{i+d} + \beta_{i+d}^\dagger \beta_i = 2(S_i^x S_{i+d}^x + S_i^y S_{i+d}^y)$, we see the BEC off-diagonal order is associated with spin correlations perpendicular to the magnetization, and the anti-ferromagnetic checkerboard is associated with the condensate quasimomentum, (π, π) .

The spin correlations parallel to the magnetization are associated with the density correlations of the magnons, which can be written $\langle \beta_i^\dagger \beta_i \beta_{i+d}^\dagger \beta_{i+d} \rangle_c = \langle S_i^z S_{i+d}^z \rangle_c \propto C_{\text{spin}}^z(d)$. These are the density correlations of a liquid of bosons on the lattice, with hard core exclusion and nearest-neighbor repulsion. These are expected to be typical liquid correlations, starting negative at short distances and oscillating and damping with distance, first becoming positive at a distance of order the inter-particle spacing. As we go to high polarization and thus low density of these bosons, this inter-particle distance grows and moves beyond the diagonal-neighbor distance, resulting in the sign change in $C_{\text{spin}}^z(1, 1)$.

4.8 Spin correlations versus doping

Introducing doping decreases the magnitude of the spin correlations, but canted anti-ferromagnetism persists for small dopings. For fixed Zeeman field h , both $C_{\text{spin}}^z(1, 0)$ and $C_{\text{spin}}^\perp(1, 0)$ decrease with increasing doping (decreasing singles filling n^s), as shown in fig. 4.5. For small but finite field, C_{spin}^\perp is more negative than C_{spin}^z at half-filling due to canting, and this anisotropy persists over a finite range of dopings. For example, at a field of $h/t = 0.52$ canted antiferromagnetic correlations are present down to a

doping of $n^s \approx 0.6$ (fig. 4.5B). Once the doping is large enough ($n^s < 0.6$ in fig. 4.5B), the anisotropy is destroyed. This behavior changes at extremely large fields. For large enough fields, canted antiferromagnetic correlations are still present near half-filling, but for large doping C_{spin}^z becomes more negative than C_{spin}^\perp . This effect is visible in fig. 4.5C at $h/t = 0.94$.

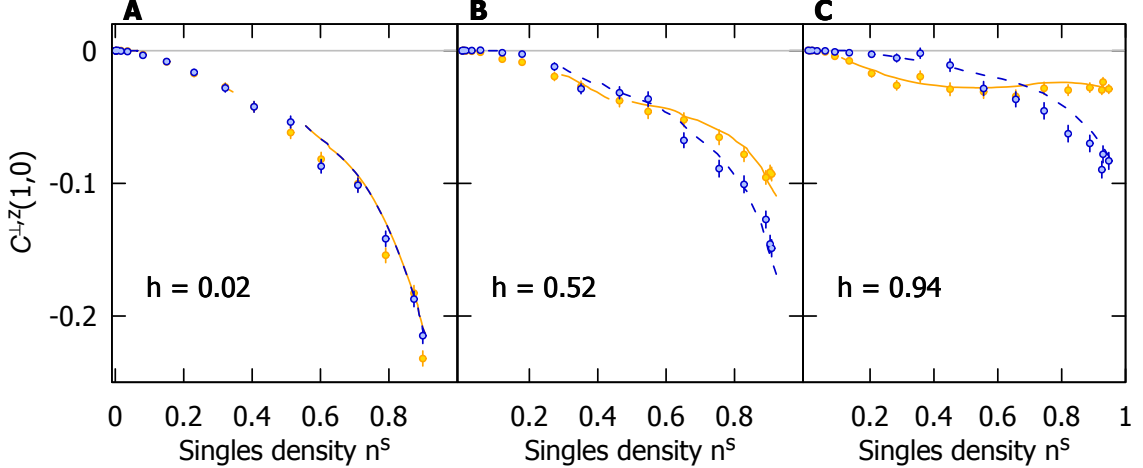


Figure 4.5: Spin correlators versus doping. Nearest-neighbor spin correlators C_{spin}^z (yellow) and C_{spin}^\perp (blue) versus singles density n^s for different Zeeman fields, h . Experimental values (points) and 8th order NLCE results (solid and dashed lines) are shown for several local polarizations at half-filling. **A**, $p^s = 0.02$, $h/t = 0.02$, $T/t = 0.38$. **B**, $p^s = 0.48$, $h/t = 0.52$, $T/t = 0.38$. **C**, and $p^s = 0.77$, $h/t = 0.94$, $T/t = 0.53$. The Zeeman field used in NLCE is determined from the singles polarization at half-filling. Experimental data averaged over ~ 50 images and azimuthally. Error bars are standard error of the mean.

The suppression of C_{spin}^\perp relative to C_{spin}^z at large doping and large fields reflects the transition to a nearly fully polarized Fermi gas at low densities. In this limit, $C_{\text{spin}}^z(d) \rightarrow 2C_\uparrow(d)$, the density correlator of the majority atoms. This correlator is negative for all displacements, as demonstrated by eq. 3.38. On the other hand, C_{spin}^\perp contains only mixed spin operators, such as $\langle c_{i\uparrow}^\dagger c_{i\downarrow} c_{i+d,\uparrow}^\dagger c_{i+d,\downarrow} \rangle$ which vanish in a polarized gas.

The regime of finite doping and low temperatures considered here is difficult for NLCE, which fails for a range of dopings $n^s \approx 0.2 - 0.5$ for $T/t \approx 0.4$ as shown in

fig. 4.5A and B. For higher temperatures, such as $T/t = 0.53$ in fig. 4.5C, convergence is restored.

4.9 Singles density correlations

In addition to spin correlations our data gives access to density correlations between singly occupied sites, also referred to as *local moment* correlations, defined by eq. 2.3. Previous analysis of this correlator in a balanced gas revealed a dominant positive contribution at half-filling from doublon-hole virtual excitations and a smaller negative contribution from hole-hole correlations due to Pauli repulsion [68]. In fact, this positive correlation is already present in the non-interacting system (see section 3.2.2 and fig. 3.2C), but the doublon-hole virtual excitations enhance the strength of the correlator.

We observe the behavior of the nearest-neighbor singles density correlations as the effective magnetic field (polarization) is varied. For increasing polarization, singles density correlations decrease as Pauli blocking suppresses double occupancy in the gas. The results of NLCE and DQMC calculations at $U/t = 8$ show good agreement with the data using the same temperature range extracted from the spin correlations, as shown in fig. 4.6.

In the inset of fig. 4.6, we show the singles density correlation versus singles density for different polarizations. As was observed in the balanced case, the correlator changes sign as the filling is reduced, an effect that has been attributed to Pauli repulsion in the metallic regime [68]. This repulsion becomes more pronounced as the polarization is increased, leading to negative correlations over a wider range of fillings. This interpretation is further supported by our calculations of this quantity in the non-interacting Fermi gas, where we find qualitatively similar behavior (see section 3.2.2 and fig. 3.2C).

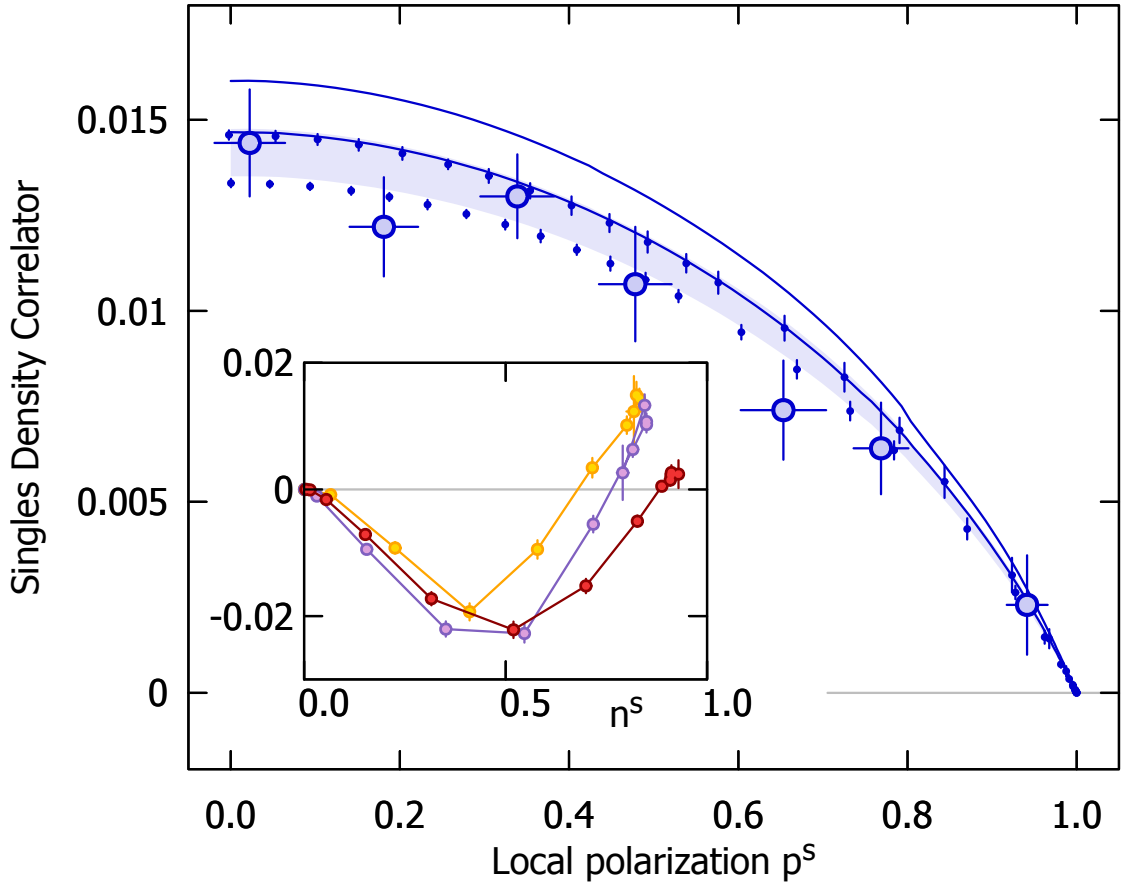


Figure 4.6: **Singles density correlations.** Nearest-neighbor singles density correlations versus local singles polarization p^s at half-filling. We show NLCE (edges of shading) and DQMC (small circles) results corrected for our detection efficiency, and uncorrected NLCE results (solid lines). We show a temperature band from $T/t = 0.38$ to 0.53, which is determined from spin correlators. **Inset,** Singles density correlations versus density for $p^s = 0.02$ (yellow), 0.48 (purple), and 0.94 (red). Lines are guides to the eye. Error bars standard error of the mean. Experimental data averaged over ~ 50 images and azimuthally.

4.10 Magnetic susceptibility versus polarization

The polarization profile of the imbalanced gas in the trap gives insight into the magnetic susceptibility of the Fermi-Hubbard model in the doped regime. For strong interactions we observe that the in-trap polarization profile can exhibit nonmonotonic behavior as shown in fig. 4.7A for $U/t = 14.7(8)$ obtained by increasing the scattering length to $793(12)$ a_0 . For these experiments, we extract the true local polarization $p = (n_\uparrow - n_\downarrow)/(n_\uparrow + n_\downarrow)$, rather than p^s . The local polarization shows a shallow rise near the edge of the half-filled region then drops in the metallic region, before rising rapidly at the edge of the cloud.

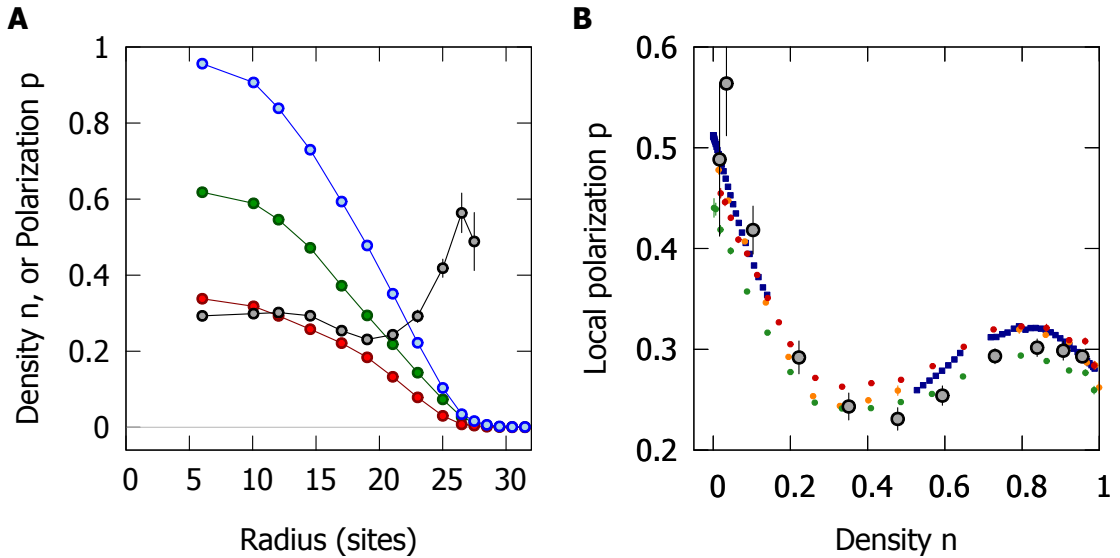


Figure 4.7: **Nonmonotonic dependence of local polarization on doping at strong interactions.** **A**, Azimuthally averaged density profiles showing the total density n (blue), n_\uparrow (green), n_\downarrow (red), and p (gray) for a spin-imbalanced cloud at $U/t = 14.7(8)$ with global polarization $P_g = 0.29(3)$. **B**, Local polarization as a function of density (gray circles) assuming linear response. NLCE (blue squares) at $U/t = 15$ for $T/t = 0.35$ and $h/t = 0.20$. DQMC results (small circles) at $U/t = 15$ for $T/t = 0.42$ and $h/t = 0.22$ (red), $T/t = 0.36$ and $h/t = 0.20$ (orange) and $T/t = 0.42$ and $h/t = 0.20$ (green). Experimental data averaged over ~ 55 images and azimuthally. Error bars standard error of the mean.

These effects can be understood qualitatively in terms of the magnetic susceptibility of the gas at different fillings,

$$\chi = \frac{1}{n} \left. \frac{\partial \langle S^z \rangle}{\partial h} \right|_{\bar{\mu}}, \quad (4.4)$$

because the susceptibility is proportional to the local polarization $\chi = \frac{p}{2h}$. Here the field h is constant across the trap since the gas is in chemical equilibrium. At half-filling, the susceptibility is expected to be that of an antiferromagnet $\chi_{\text{AF}} \propto 1/J = U/4t^2$, while for small doping at our temperatures there is a non-degenerate gas of holes in the lower Hubbard band and as a result a weak maximum in the susceptibility. At intermediate hole doping the susceptibility crosses over to that of a metal, $\chi_m \propto 1/t$, which is smaller than χ_{AF} for large U/t . Similar behavior has been observed in the cuprates in the normal phase [199, 200, 201] and studied theoretically [202, 203]. At even lower filling, the gas is non-degenerate and there is no filled Fermi sea to hinder spins from aligning with the effective field, leading to an enhanced magnetic susceptibility.

We show the polarization versus density in fig. 4.7B and compare it with NLCE and DQMC calculations in the local density approximation, which reproduce the nonmonotonic behavior described above. The strength of the field, $h/t = 0.21(1)$, is determined from the polarization at half-filling, which exhibits only a weak dependence on temperatures for $T/t < 0.5$. These calculations are near the limit of these numerical techniques for the doped system, as evidenced by the region from $n \approx 0.2 - 0.5$ where NLCE fails to converge. Comparing DQMC and NLCE in this challenging regime controls for systematic errors.

4.11 Relationship between susceptibility and local polarization

This analysis of the polarization relies on the claim that the local polarization is proportional to the spin susceptibility of the gas. This connection holds in the *linear regime*, where the spin imbalance can be approximated by,

$$\langle S^z \rangle = \left. \frac{\partial \langle S^z \rangle}{\partial h} \right|_{\bar{\mu}} h. \quad (4.5)$$

We can rewrite this equation using the polarization and spin susceptibility as $p = 2h\chi$, which verifies the relationship we asserted above.

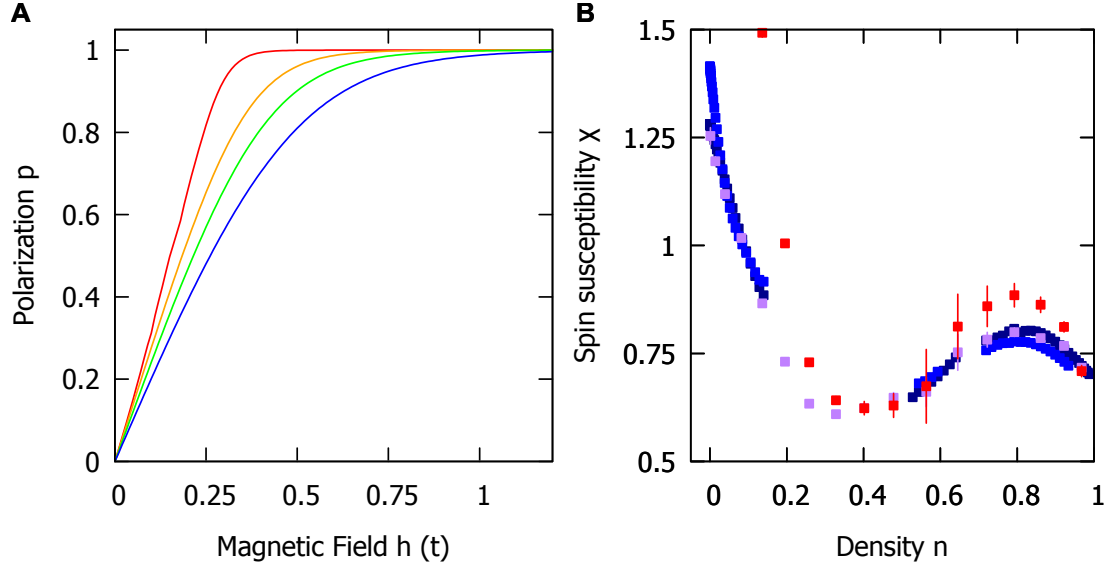


Figure 4.8: **Linearity with Zeeman field.** **A**, Local polarization at half-filling versus Zeeman field. NLCE results for $T/t = 0.15$ (red), 0.35 (orange), 0.49 (green) and 0.67 (blue) at $U/t = 15.0$. The magnetic field is measured in units of the tunneling energy, t . **B**, NLCE results for $p/2h$ (dark-blue) and χ (light-blue) versus density n for $U/t = 15.0$ at $T/t = 0.35$ and $h/t = 0.20$.

We numerically verify that we are in the linear regime at half-filling by considering the dependence of the local polarization p on the field h . This plot is shown in fig. 4.8A

for $T/t = 0.15 - 0.67$ at $U/t = 15.0$. The experimental polarization at half-filling, $p \approx 0.3$, falls within the linear regime for even the highest temperature considered.

To verify that we are in the linear regime away from half-filling, we compare the polarization to the spin-susceptibility determined from NLCE simulations using the fluctuation-dissipation theorem (see eq. 3.46) in fig. 4.8B. The susceptibility determined this way differs by less than 10 % from $p/2h$. The missing points in this curve are dopings where NLCE failed to converge.

4.12 Outlook

In this chapter we have presented the first experimental study of a 2D spin-imbalanced Fermi-Hubbard system in a regime near the edge of what state-of-the-art numerical techniques can simulate. The high effective fields reached in our experiments allow us to explore canted antiferromagnetic correlations above the BKT transition and to observe an interesting dependence of the local polarization on doping. Future directions for both experimental and theoretical work include investigation of spin-imbalance in the attractive 2D Hubbard model where Fulde-Ferrell-Larkin-Ovchinnikov superfluid correlations should be detectable at the entropies achieved in repulsive experiments [204] and mapping out the BKT transition in the imbalanced repulsive gas phase diagram which would require lower temperatures. Finally, the achievement of cold spin-imbalanced clouds in an optical lattice suggests a new route for local entropy reduction using adiabatic demagnetization cooling, a technique previously demonstrated in bosonic lattice experiments [205].

Chapter 5

Bad metallic transport in a Fermi-Hubbard system

Portions of this chapter are based on work previously published as

P. T. Brown, D. Mitra, E. Guardado-Sánchez, R. Nourafkan, A. Reymbaut, C.-D. Hébert, S. Bergeron, A.-M. S. Tremblay, J. Kokalj, D. A. Huse, P. Schauß, and W. S. Bakr. [Bad metallic transport in a cold atom Fermi-Hubbard system](#). *Science* **363**, 6425, 379–382 (2019).

Although experiments have studied a variety of static properties of the Fermi-Hubbard model, exploring the full phase diagram requires measurement of dynamical properties. This is because many of the interesting phases in the cuprate phase diagram, which we expect may also exist in the Fermi-Hubbard model, are defined in terms of such dynamical observables and it is not clear that static observables can provide the same information, although this is also an active area of research. Therefore, in this chapter and the next we focus on developing new experimental techniques to explore dynamical properties of the Fermi-Hubbard model using a quantum gas microscope. In this chapter, we focus on measuring the resistivity of a repulsive Fermi-Hubbard gas at finite doping — parameters that would put us in the “strange

metal” regime in a cuprate system. We investigate whether or not similar strange metal phenomenology occurs in a Fermi-Hubbard system.

Transport measurements are both the most common experimental and simplest conceptual techniques for exploring the properties of materials. The basic premise is to connect a macroscopic sample to a number of terminals, then connect some of these terminals to reservoirs or sources (of voltage, current, heat, etc.), and observe the response at other terminals. Transport experiments have been instrumental in the discovery a variety of interesting phenomena, including the quantum Hall effect [206], fractional quantum Hall effect [207], and superconductivity among many others. It is illustrative of the influence of these techniques that superconductors, which are quantum materials with a variety of interesting characteristics, are primarily defined in terms of their charge transport properties.

Transport measurements reveal information about the underlying nature of the constituents of a material — for example Hall voltage measurements can reveal the sign of charge carriers, and similar techniques led to the discovery of fractionally charged quasiparticles. Recently, heat conductivity measurements may even have exposed information about the nature of the wave function for certain fractional quantum Hall states [208]. Transport measurements can also reveal situations where strongly interacting quantum systems no longer behave as if they are composed of discrete particles. In such situations, many of the most common techniques for studying transport break down, such as the Boltzmann transport equation, and a general framework for understanding such systems is lacking. Despite the lack of a unifying theoretical framework, there are hints that various incoherent systems may have deep connections to one another [209, 210].

Transport coefficients can often be understood as unequal-time correlation functions, as discussed in section 3.7. These objects are challenging to calculate theoretically, particularly for strongly interacting quantum systems. This poses a diffi-

cult challenge to understanding strongly-correlated transport using existing theory techniques, as calculations cannot probe low temperature physics. We adopt a complementary approach by using a quantum simulator to explore charge transport in the Fermi-Hubbard model at temperatures below what is accessible to some exact theory methods. In this chapter, we find evidence for strange metallic transport in this model which shares much of the phenomenology observed in real materials.

5.1 Transport in strongly-interacting quantum systems

Strong interactions in many-body quantum systems complicate the interpretation of charge transport in such materials. To shed light on this problem, we study transport in a clean quantum system: ultracold ${}^6\text{Li}$ in a 2D optical lattice, a testing ground for strong interaction physics in the Fermi-Hubbard model. We determine the diffusion constant by measuring the relaxation of an imposed density modulation and modeling its decay hydrodynamically. The diffusion constant is converted to a resistivity using the Nernst-Einstein relation. That resistivity exhibits a linear temperature dependence and shows no evidence of saturation, two characteristic signatures of a bad metal. The techniques we develop here may be applied to measurements of other transport quantities, including the optical conductivity and thermopower.

In conventional materials, charge is carried by quasiparticles and conductivity is understood as a current of these charge carriers developed in response to an external field. For the conductivity to be finite, the charge carriers must be able to relax their momentum through scattering. The Boltzmann kinetic equation in conjunction with Fermi liquid theory provides a detailed description of transport in conventional materials, including two trademarks of resistivity. The first is the Fermi liquid prediction that the temperature-dependent resistivity $\rho(T)$ should scale like T^2 at low

temperature [175]. The second is that the resistivity should not exceed a maximum value ρ_{\max} , obtained from the Drude relation assuming the Mott-Ioffe-Regel (MIR) limit which states that the mean free path of a quasiparticle cannot be less than the lattice spacing [211, 212]. This resistivity bound itself is sometimes referred to as the MIR limit.

Strong interactions can however lead to a breakdown of Fermi liquid theory. One signal of this breakdown is anomalous scaling of ρ with temperature, including the linear scaling observed in the “strange metal” state of the cuprates [213] and other anomalous scalings in d - and f - electron materials [214]. Another is the violation of the resistivity bound $\rho < \rho_{\max}$, which is observed in a wide variety of materials [215]. Additionally, interactions may lead to a situation where the momentum relaxation rate alone does not determine the conductivity, in contrast to the semiclassical Drude formula, generalizations of which hold for a large class of systems called coherent metals [210]. Approaches introduced to understand these anomalous behaviors include hidden Fermi liquids [216], marginal Fermi liquids [217], proximity to quantum critical points [218] and associated holographic approaches [219], and many numerical studies of model systems, most notably the Hubbard [220] and $t - J$ [170] models.

Disentangling strong interaction physics from other effects, such as impurities and electron-phonon coupling, is difficult in real materials. Cold atom systems are free of these complications, but transport experiments are challenging due to the finite and isolated nature of these systems. Most fermionic charge transport experiments have focused on either studying mass flow through optically structured mesoscopic devices [221, 222, 223, 224] or bulk transport in lattice systems [78, 79, 80, 81, 84]. Here, we explore bulk transport in a Fermi-Hubbard system by studying charge diffusion, which is a microscopic process related to conductivity through the Nernst-Einstein equation $\sigma = \chi_c D$, where D is the diffusion constant and $\chi_c = \left(\frac{\partial n}{\partial \mu}\right)_T$ is the compressibility. This relation requires only the assumption of linear response and absence

of thermoelectric coupling and does not rest on assumptions concerning quasiparticles.

5.2 Experimental preparation

We realize the 2D Fermi-Hubbard model using a degenerate spin-balanced mixture of two hyperfine ground states of ${}^6\text{Li}$ in an optical lattice which we label $|\uparrow\rangle = |1\rangle$ and $|\downarrow\rangle = |3\rangle$ [70]. Our system is well described by the Hubbard Hamiltonian given in eq. 3.2 with $h = 0$. Our lattice beams produce a harmonic potential, which leads to a varying atomic density in the trap. To obtain a system with uniform density, we flatten the trapping potential over an elliptical region of mean diameter 30 sites using a repulsive potential created with a spatial light modulator (for more details see section 2.7). We superimpose an additional sinusoidal potential that varies slowly along one direction of the lattice with a controllable wavelength (fig. 5.1, A and B).

By adiabatically loading the gas into these potentials, we prepare a Hubbard system in thermal equilibrium with a small amplitude (typically 10 %) sinusoidal density modulation. The average density in the region with the flattened potential is the same with and without the sinusoidal potential. Next, we suddenly turn off the added sinusoidal potential (but not the flattening potential) by changing the DMD image in less than 10 μs , and observe the decay of the density pattern versus time (fig. 5.1, C and D). We measure the density of a single spin component, $\langle n_{\uparrow} \rangle$ using techniques described in [70], giving us access to the total density through $\langle n \rangle = 2 \langle n_{\uparrow} \rangle$.

We work at average total density $\langle n \rangle = 0.82(2)$. This value is close to a conjectured quantum critical point in the Hubbard model [225]. Our lattice depth is $6.9(2) E_r$, where $E_r/h = 14.66 \text{ kHz}$ is the lattice recoil. We estimate the tunneling rate $t/h = 925(10) \text{ Hz}$ from a band structure calculation. We adjust the Hubbard interaction by tuning the bias magnetic field in the vicinity of the Feshbach resonance centered near

690 G. We work at 616.0(2) G where the scattering length is $a_{13} = 1070(10)$ a_o and the interaction energy is $U = 7.0(7)$ kHz, determined from a spectroscopic measurement (see section 4.5). These parameters lead to an on-site interaction to tunneling ratio $U/t = 7.4(8)$, which is in the strong-interaction regime and close to the value that maximizes antiferromagnetic correlations at half-filling [196].

To image the density of a single spin state, we freeze the motion of the atoms by ramping the lattice depth to $60 E_r$ in approximately 100 μ s. We check this ramp effectively freezes the atomic motion by comparing the density amplitude modulation pattern without turning off the DMD potential, and with turning off the DMD potential and then immediately ramping the lattice depth for our shortest wavelength at our lowest temperatures (where the modulation decays fastest). The modulation depths agree, indicating that the atomic motion is effectively frozen well before the lattice reaches $60 E_r$.

5.3 Density modulation decay

We observe the decay of the initial sinusoidal density pattern over a period of a few tunneling times. The short timescale ensures that the observed dynamics are not affected by the inhomogeneous density outside of the central flattened region of the trap. To obtain better statistics, we apply the sinusoidal modulation along one dimension and average along the other direction (fig. 5.1, A and C). We fit the average modulation profile to a sinusoid, where the phase and frequency are fixed by the initial pattern (fig. 5.2A). The time dependence of the amplitude of the sinusoid quantifies the decay of the density modulation, fig. 5.2B. Our experimental technique is analogous to that of [130], which studied the decay of a spin pattern in a bosonic system.

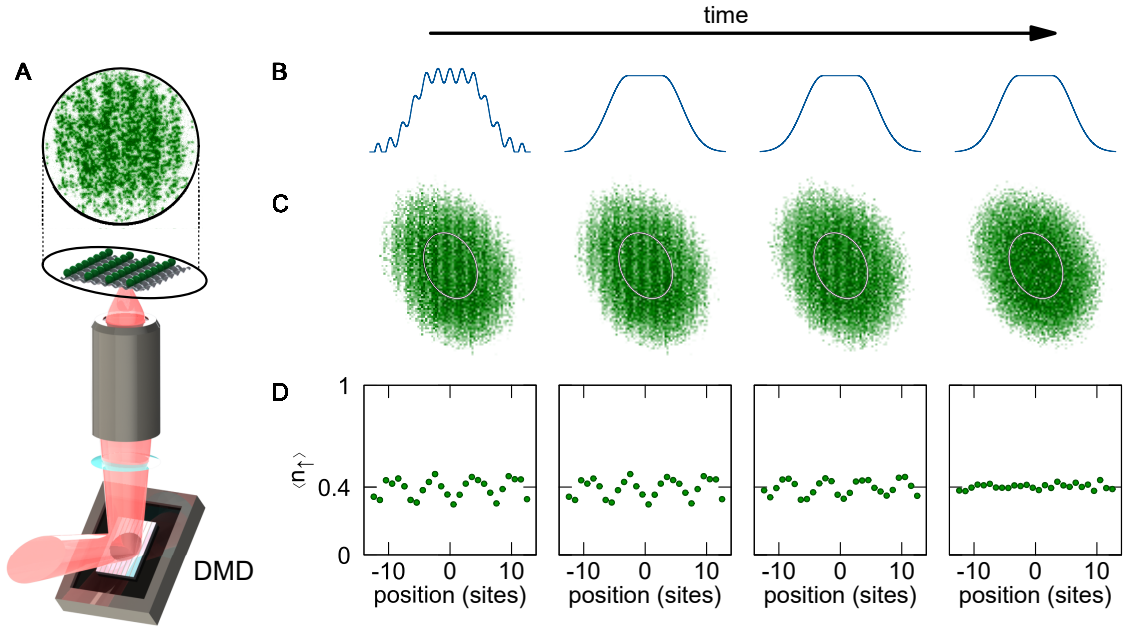


Figure 5.1: Measuring transport in the Hubbard model. **A,** Top: exemplary single shot fluorescence image of the atomic density for one spin component. Field of view diameter is approximately $60 \mu\text{m}$. Bottom: schematic of the setup for generating optical potentials. Far-off-resonant light is projected onto a digital micromirror device (DMD) and the resulting pattern is imaged onto the atoms using a high-resolution objective. We project a sinusoidally-modulated potential along one direction. **B,** One-dimensional cuts along the projected potential. The DMD is used to flatten the trap and project a sinusoidally-modulated potential (leftmost image). The confining potential comes from the optical lattice. After initial preparation, the sinusoidal potential is suddenly turned off, but the flattening potential is not. **C,** Average density of a single spin component, $\langle n_{\uparrow} \rangle$, versus time for approximately 30 images. Initially, the system is in thermal equilibrium with a spatially modulated density (leftmost image, $0 \mu\text{s}$ decay time). Immediately after the sinusoidal potential is turned off, the system is no longer in equilibrium but the density has not yet changed (second from left, $0 \mu\text{s}$ decay time). The density modulation decays with time (third from left, $50 \mu\text{s}$ decay time) until it is no longer visible (fourth from left, $500 \mu\text{s}$ decay time). The central flattened region of the potential is marked by a white ellipse. The field of view is approximately $75 \mu\text{m} \times 75 \mu\text{m}$. **D,** Atomic density from C averaged along the direction orthogonal to the modulation in the central flattened region of the potential.

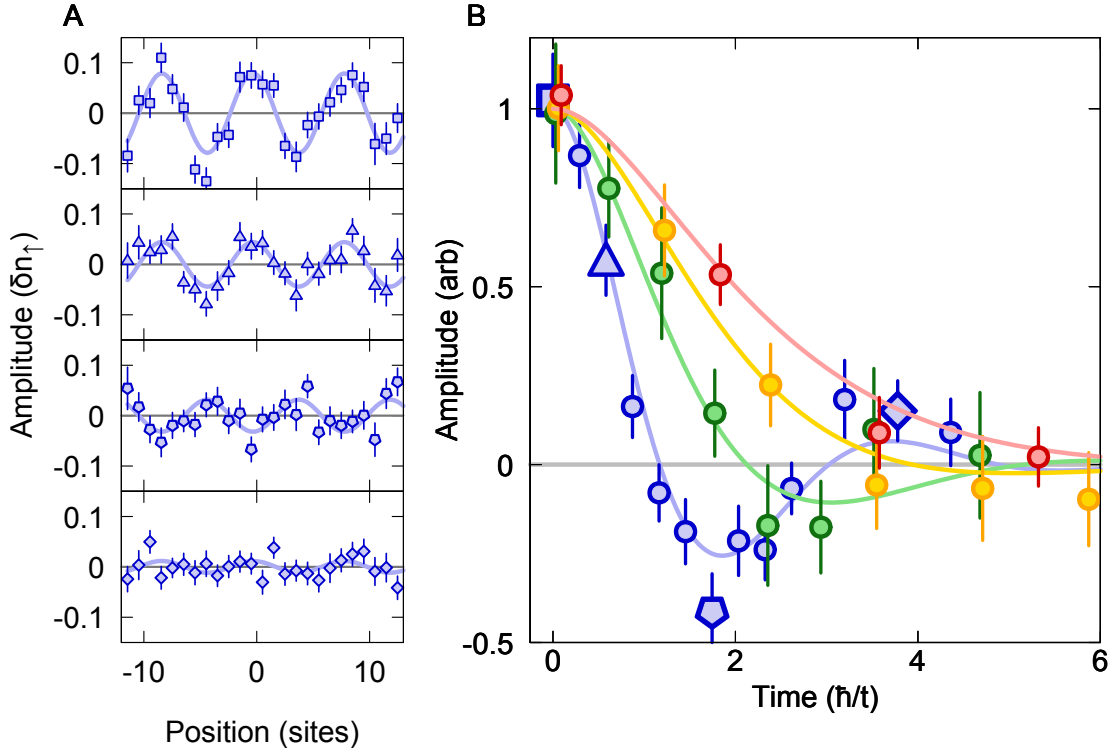


Figure 5.2: **Decay of density modulation pattern versus time.** **A**, Cloud profiles averaged along the direction of the modulation (points) and sinusoidal fits (lines) for modulation wavelength 8.1 sites and times 0 \hbar/t (top), 0.6 \hbar/t (second from top), 1.7 \hbar/t (third from top), and 3.8 \hbar/t (bottom). The average value obtained from the sinusoid fit has been subtracted. **B**, Sinusoid fit amplitudes (points) versus decay time for modulation periods 8.1 (blue), 11.8 (green), 15.6 (yellow), and 18.7 (red) sites. Each curve is scaled by the initial modulation amplitude. Lines are obtained from a simultaneous fit of the diffusion constant, D , and current relaxation rate, Γ , to all wavelengths and times. Different shaped points for period 8.1 correspond to different panels in A, 0 \hbar/t (square), 0.6 \hbar/t (triangle), 1.7 \hbar/t (pentagon), and 3.8 \hbar/t (diamond). The temperature for all wavelengths and decay times is $T/t = 0.57(8)$. Each point is the average of approximately 30 images. Error bars standard error of the mean.

The decay of the sinusoidal density pattern versus the wavelength of the modulation becomes consistent with diffusive transport at long wavelengths. In diffusive transport, the amplitude of a density pattern at wave vector $k = 2\pi/\lambda$ will decay exponentially with time constant $\tau = 1/Dk^2$, where D is the diffusion constant. We observe exponentially decaying amplitudes with diffusive scaling for wavelengths longer than 15 sites. However, the decay curves are flat at early times, showing clear deviation from exponential decay. For short wavelengths, we observe deviations from diffusive behavior in the form of underdamped oscillations, which can be understood as the damped limit of sound waves. Both of these effects are related to the fact that a density modulation does not instantaneously create a current, as implied by the diffusion equation. Rather, a current requires a finite amount of time to reach an equilibrium value after the creation of a density modulation.

5.4 Atomic tunneling time

We find that the density modulation decay times are in the range $2 - 6\hbar/t$ in fig. 5.2B. To establish a reference for this time scale, we estimate how long it takes a single fermion on a lattice to tunnel. Suppose we are working in 1D and initialize one atom at site n and time $T = 0$. We want to calculate the probability an atom is on site m at time T , i.e. $\langle 0 | c_n(0) c_m^\dagger(T) | 0 \rangle$.

We can write the time evolution of a particle initialized on site m using the fact the momentum states are eigenstates with energy given by the dispersion ϵ_k ,

$$c_m^\dagger(t) | 0 \rangle = \sum_k e^{-i\epsilon_k T} e^{-imk} c_k^\dagger | 0 \rangle. \quad (5.1)$$

Using the above equation to evaluate the time dependence and then Fourier transforming back to position space yields

$$\langle 0 | c_n(0)c_m^\dagger(t) | 0 \rangle = \sum_k e^{-i\epsilon_k T} e^{-imk} \langle 0 | c_n c_k^\dagger | 0 \rangle \quad (5.2)$$

$$= \sum_{k,l} e^{-i\epsilon_k T} e^{-imk} e^{ilk} \langle 0 | c_n c_l^\dagger | 0 \rangle \quad (5.3)$$

$$= \sum_k e^{-i\epsilon_k T} e^{i(n-m)k}. \quad (5.4)$$

Now we specialize to a 1D lattice system with dispersion $\epsilon_k = -2t \cos(k)$ and apply the Jacobi-Anger identity,

$$\sum_k e^{i2t \cos(k)t} e^{i(n-m)k} = \sum_{k,l} i^l J_l(2tT) e^{ilk} e^{i(n-m)k} \quad (5.5)$$

$$= \sum_l i^l J_l(2tT) \delta_{n-m+l} \quad (5.6)$$

$$= i^{m-n} J_{m-n}(2tT). \quad (5.7)$$

Here J_l is the l th Bessel function.

We can estimate the tunneling rate by determining when the probability that the atom is one site away from its initial position is maximum. The J_1 has its first maximum at $2tT \approx 1.8412$, which implies

$$T \approx 0.94 \hbar/t, \quad (5.8)$$

or this particle tunnels roughly once every \hbar/t .

This estimate also applies to a separable 2D lattice. Our science lattice is *not* separable due to $t_d \cos(k_x \pm k_y)$ terms in the dispersion relation (see eq. B.25). The above analysis does not strictly apply, but it is a good approximation because the diagonal tunneling t_d is extremely small.

The time scale for this non-interacting problem matches reasonably well with that observed in fig. 5.2B. We roughly expect that for a density pattern of wavelength λ particles from the maximum density region must reach the minimum, i.e. they must travel a distance $\lambda/2$.

5.5 Linear response theory

In the experiment we apply a spatially varying potential which couples to the atomic density, and then observe the effect this has on the atomic density. This implies that the dynamics can be understood in terms of the dynamical density susceptibility function. We make this connection here by describing the experiment in terms of the linear response theory introduced in section 3.7.

In the linear response formalism, we consider the effect of perturbing the system with the potential

$$v_i(t) = F(t) \cos(k \cdot r_i) \quad (5.9)$$

$$F(t) = F_o e^{\eta t} \theta(-t), \quad (5.10)$$

where we have supposed F is turned on slowly starting at $t = -\infty$ and switched off suddenly at $t = 0$. The turn on speed is parameterized by η , and we work in the limit $\eta \rightarrow 0$. The frequency domain representation of this force is $F(\omega) = \frac{F_o}{i\omega + \eta}$.

Using the notation introduced in section 3.7, we identifying the potential as the generalized force $h(r_i, t) = v_i(t)$ which is conjugate to the density response, $M(r_i, t) = n_i(t)$. We observe the system response by measuring the density, so $\mathcal{O}(r_i, t) = n_i(t)$. Following eq. 3.64, the response function is given by

$$\Phi_{nn}(k, t - t') = -\frac{i}{\hbar} \Theta(t - t') \langle [n_k(t), n_{-k}(t')] \rangle \quad (5.11)$$

where r_i is the position of site i , n_k is the spatial Fourier transform of the density, and we use translational invariance of the unperturbed system, which ensures that only v_k contributes to the density response at k . Note the $n_k = \sum_q c_{k+q}^\dagger c_q$ is the Fourier transform of the real space density operator, and *not* the momentum space occupation operator.

The density time response can be written in terms of the susceptibility as

$$\langle \delta n_k(t) \rangle = \int d\omega \chi(k, \omega) F(\omega) e^{-i\omega t}, \quad (5.12)$$

following from eqs. 3.60 and 3.62. To make further progress, an explicit form of χ is required. For example, we could calculate the dynamical response of the non-interacting Fermi gas using the expression we found for χ in eq. 3.34. In many cases, χ has a generic form in the long wavelength, long time limit determined by hydrodynamics. We consider this connection in the next section.

5.6 Phenomenological hydrodynamic model

To unify the description of modulation decay at all wavelengths considered in fig. 5.2, we develop a hydrodynamic description that accounts for conserved particle number and a finite momentum (or current) relaxation rate. Hydrodynamics is a long wavelength, low frequency limit which applies when there are few conserved quantities, typically only mass, momentum, and energy [219]. This is the situation in many isolated systems, with a notable exception being integrable systems, because these possess a large number of conserved quantities which must be accounted for. In most real materials electrons cannot be treated hydrodynamically because of couplings to phonons and lattice defects which can absorb energy or momentum.

The simplest hydrodynamic theory we can write down for an isolated Hubbard system accounts for conservation of mass and weak relaxation of momentum due to

umklapp scattering, and assumes that energy is decoupled from these two. The two equations describing this are

$$\partial_t n(r, t) = -\nabla \cdot \mathbf{J}(r, t) \quad (5.13)$$

$$\partial_t \mathbf{J}(r, t) = -\Gamma (D \nabla n(r, t) + \mathbf{J}(r, t)), \quad (5.14)$$

where the first equation is the continuity equation, and the second equation reduces to Fick's law, $\mathbf{J}(r, t) = -D \nabla n(r, t)$, in the steady state ($\partial_t \mathbf{J} = 0$). In the limit of strong current relaxation, a density modulation instantly creates a current satisfying Fick's law. However, for a finite relaxation rate Γ , the current responds with a time lag described by eq. 5.14. We can alternatively understand eq. 5.14 as a momentum "conservation" equation analogous to the Navier-Stokes equation including a weak momentum relaxation rate Γ , zero viscosity, and neglecting terms of higher order in linear response.

This model leads to a differential equation for the density decay,

$$\partial_t^2 n + \Gamma \partial_t n + \Gamma D k^2 n = 0, \quad (5.15)$$

where Γ is the momentum-relaxation rate and D is the diffusion constant. This oscillator model crosses over from an underdamped to an overdamped (approximately diffusive) regime at a modulation wavelength $4\pi\sqrt{D/\Gamma}$. In a system that can be described using quasiparticles, $\sqrt{D/\Gamma}$ is proportional to the mean free path.

In the overdamped limit, $\Gamma \gg \sqrt{\Gamma D} k$, eq. 5.15 describes diffusive behavior $n_k(t) \propto e^{-Dk^2 t}$ for finite k . In the underdamped limit, it describes sound waves whose amplitude decays at rate $\Gamma/2$. If we take the limit $k = 0$, the current decays exponentially at rate Γ , confirming that this is the current relaxation rate. The sound wave and current relaxation rates differ because the sound wave carries both kinetic and potential energy, shared equally, whereas the uniform ($k = 0$) current excitation carries only

kinetic energy. As only the kinetic energy is damped, the sound wave loses energy at half of the rate of the uniform current excitation.

This hydrodynamic model implies a specific form of the density susceptibility function χ . The density decay dynamics determined by eq. 5.15 must match the dynamics predicted by linear response through eq. 5.12. This implies χ must be the frequency space representation of the Green's function for eq. 5.15, which is

$$\chi(k, \omega) = \frac{\chi_c}{1 - \frac{i\omega}{k^2 D} - \frac{\omega^2}{k^2 D\Gamma}}, \quad (5.16)$$

where χ_c is the charge compressibility, D is the diffusion constant, and Γ is the current relaxation rate [180].

5.7 Determining experimental hydrodynamic parameters

Instead of assuming that D and Γ are dependent parameters linked through a Drude formula, as would be the case in a system that can be described using quasiparticles, we treat them separately and determine both by simultaneously fitting the amplitude decay patterns for all wavelengths to the hydrodynamic model data at fixed temperature. The results of such a fit are shown in fig. 5.2B.

We take images at a series of wave vectors and times (k_i, t_{ij}) , where $i = 1, \dots, N$ and $j = 1, \dots, j_i$, and determine a series of modulation amplitudes $a(k_i, t_{ij})$ and uncertainties σ_{ij} using the sinusoid fits illustrated in fig. 5.2. For a given wave vector, we first fit the earliest time ($t_{i1} = 0$) modulation pattern with the amplitude, period, phase, and offset as free parameters. For later times, we fix the phase and the period leaving only the amplitude and the offset as free parameters.

To compare our measurements with the hydrodynamic model, we consider the solutions to eq. 5.15 which satisfy the boundary condition $\dot{n}(t = 0) = 0$,

$$n(\Gamma, D, A, k, t) = \frac{A}{2} (e^{\tilde{\omega}t} + e^{-\tilde{\omega}t}) e^{-\Gamma t/2}, \quad (5.17)$$

where $\tilde{\omega} = \sqrt{\frac{\Gamma^2}{4} - \Gamma D k^2}$, and A is the amplitude. These can be obtained by applying χ given in eq. 5.16 to eq. 5.12. In the underdamped limit eq. 5.17 gives a damped cosine. In the overdamped limit it yields a product of a hyperbolic cosine factor and an exponential factor.

Finally, we determine Γ , D , and A_i , $i = 1, \dots, N$ with a nonlinear least squares fit which minimizes

$$\delta^2 = \sum_{i=1}^N \sum_{j=1}^{j_i} \frac{|a(k_i, t_{ij}) - n(\Gamma, D, A_i, k_i, t_{ij})|^2}{\sigma_{ij}^2}. \quad (5.18)$$

We determine the uncertainty in the fit parameters using a bootstrap technique [117].

5.8 Experimental hydrodynamic parameters versus temperature

The temperature dependence of D and Γ are the focus of the rest of this chapter. To prepare clouds at various temperatures, we use two different protocols. After the initial preparation, we either hold the atoms in the trap or modulate the lattice amplitude for a controlled time to heat the system. To reach temperatures in the range $T/t = 0.3 - 2$, we hold the cloud in the lattice and technical noise heats it at a rate of 3 t/s. To reach higher temperatures, we modulate the lattice depth at a frequency of 2 kHz. To avoid losses, we perform this modulation at 595 G where the interaction is weaker. For these higher temperatures, the compressibility of the gas

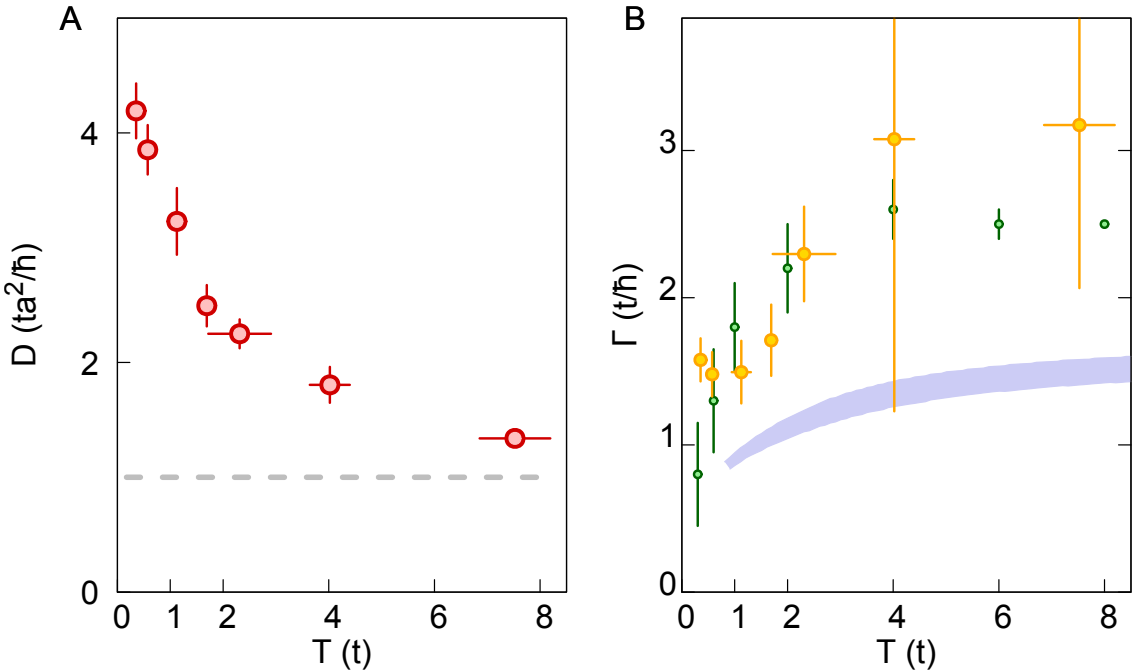


Figure 5.3: **Hydrodynamic model parameters.** **A**, Experimental diffusion constant, D , versus temperature (red) and the lower bound on D inferred from the Mott-Ioffe-Regel limit (gray). Each point is typically determined from 4 different modulation wavelengths each consisting of 10 different decay times with 30 images for each decay time. **B**, Results for the current relaxation rate, Γ , including experimental data (yellow), single-site dynamical mean-field theory results for $\langle n \rangle = 0.825$ and $U/t = 7.5$ (green), and finite-temperature Lanczos method results on a 16-site cluster for $\langle n \rangle = 0.8 - 0.85$ and $U/t = 7.5$ (blue band). Experimental error bars standard error of the mean.

is reduced and we provide extra radial confinement using a 1064 nm beam from the bottom to reach appropriate filling.

To determine the temperature of the cloud after the system has equilibrated we fit the measured singles density, $\langle n^s \rangle$ and nearest-neighbor spin-up density correlations $C_{\uparrow}(0, 1)$ versus total density $\langle n \rangle$ to determinantal quantum Monte Carlo (DQMC) simulations with T as the only free parameter (see section 3.6.2). For temperatures at the low end of the range we can access, between $0.3 < T/t < 1$, the density correlations are a sensitive thermometer. At higher temperature the singles density is a better thermometer.

As the temperature is lowered, Pauli blocking closes scattering channels, leading to an increased range of diffusion, in agreement with our observations in fig. 5.3A. At high temperatures, D is expected to saturate, eventually approaching an infinite temperature limiting value [176]. The diffusion constant is closely related to the mean-free-path, l , and is often estimated as $D = l \langle v \rangle / 2$, where $\langle v \rangle$ is the mean quasiparticle velocity [226]. Therefore, the MIR limit implies a lower bound on the diffusion constant, $D \gtrsim ta^2/\hbar$, where a is the lattice constant. Our measured diffusion constants approach this derived bound at high temperatures, but do not violate it. Because of the difficulty of measuring diffusion constants in materials, this limit has not been tested in real bad metals. We do not compare the measured diffusion constants with theory because determining D requires working in the limit $\lambda \rightarrow \infty$, and exact techniques such as diagonalization of finite systems and DQMC are limited to small system sizes. Even determining the infinite temperature limiting value is a non-trivial quantum dynamics problem [227, 228].

In a clean system like ours, momentum relaxation can only occur thanks to umklapp scattering, where a portion of the net momentum in a collision is transferred to the rigid lattice. Nevertheless, the current relaxation is strong at our interaction strength, which makes determining the temperature dependence of Γ challenging because Γ drops out of the model entirely in the overdamped limit. We find that Γ decreases weakly with decreasing temperature (fig. 5.3B). This trend may again be understood as Pauli blocking suppressing current relaxation at low temperatures.

We compare the experimental Γ to results from state-of-the-art finite-temperature Lanczos method (FTLM) and dynamical mean-field theory (DMFT) simulations by estimating the current relaxation rate as the half-width at half-maximum of the Drude peak in the optical conductivity. The optical conductivity has an additional peak at $\omega \sim U$, but we not expect this high-energy feature affects the low energy, long-wavelength dynamics considered here. Our experimental Γ agrees reasonably with

the DMFT results, but exceeds the FTLM results by up to a factor of two. FTLM is an exact technique expected to give correct results at high temperature.

5.9 Linearity

One possible explanation for the discrepancy between the measured and FTLM current relaxation rates is that Γ is sensitive to the amplitude of the density modulation. To test this, we measure Γ and D versus modulation amplitude. We find D is insensitive to the amplitude in the range explored. Γ shows some amplitude dependence but, because of the large error bars we can not conclusively say if this is the source of the discrepancy between experiment and FTLM (fig. 5.4).

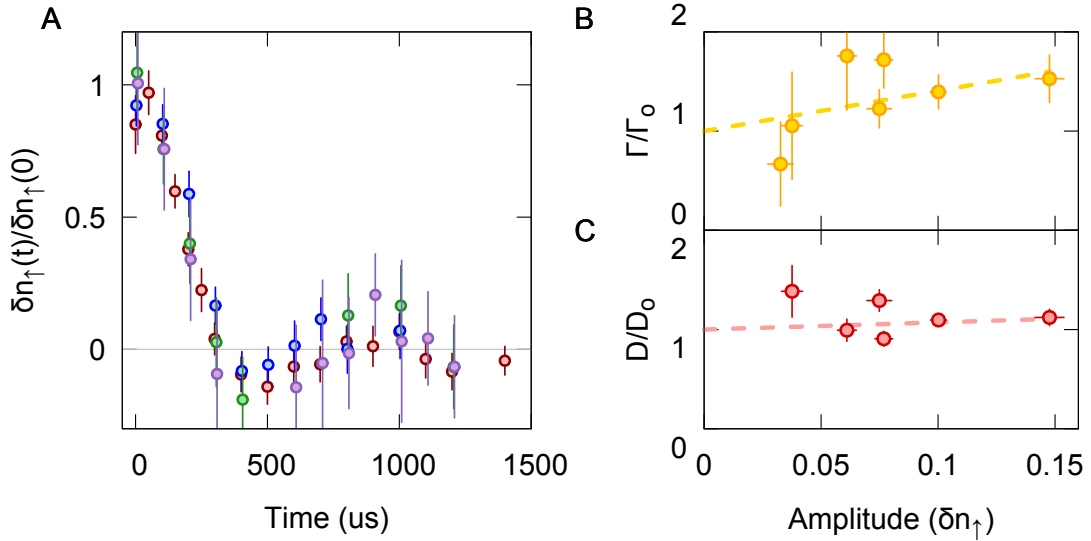


Figure 5.4: **Linearity of the density response.** **A**, Modulation amplitude versus decay time curves for selected initial amplitudes, $\delta n_{\uparrow}(t = 0) = 0.12$ (red), 0.08 (blue), 0.055 (green), and 0.035 purple. We see a collapse after scaling the curves to the initial modulation amplitude, $\delta n_{\uparrow}(0)$, obtained from a fit. Each point is the average of ≈ 30 images. **B**, Variation in fit parameter Γ versus amplitude for the curves shown in A (red) and a linear fit to the results (dashed line). Γ is normalized by the extrapolated zero-amplitude value, Γ_o . **C**, Variation in fit parameter D versus amplitude for the curves shown in A (red) and a linear fit to these results (dashed line). D is normalized by the extrapolated zero-amplitude value, D_o . Error bars standard error of the mean.

To assess the possibility of nonlinear effects which are not included in our hydrodynamic model, we vary the initial amplitude of the density modulation at a fixed wave vector. The amplitude versus time curves are shown in fig. 5.4A for $\lambda \approx 12$ sites and temperature $T/t = 0.4(1)$. For each curve, we fit a value for Γ and D to test how the fitted model parameters change with amplitude. We find no measurable difference between the temperature of the gas before switching off the potential modulation and after the density modulation has decayed.

We find the apparent Γ increases with increasing amplitude, and the apparent D is weakly affected by increasing amplitude. To establish an upper bound on the size of this effect, we perform a linear fit to the hydrodynamic parameters versus amplitude and extrapolate a “zero-amplitude” value. We normalize the curve fit parameters by these values in fig. 5.4B,C. Based on the statistical error in our fit lines, we find that at a typical experimental amplitude of $\delta n_\uparrow = 0.07$, Γ is increased by a factor of 1.4(4) and D by a factor of 1.06(10). Our extracted values for Γ appear to increase with amplitude, but the statistical error bar is quite large. This is due to the weak dependence of our model on the value of Γ . In the main text, we are able to obtain smaller error bars on Γ by simultaneously fitting decay curves at different modulation wavelengths. That approach is not feasible here because nonlinear effects may depend on wavelength.

A related but distinct type of nonlinearity is dependence of the charge compressibility on density. As the total density approaches half-filling, the compressibility decreases. Therefore, the chemical potential modulation we apply tends to decrease the density at the minimum chemical potential values more than it increases the density at the maximum chemical potential values. This can lead to the density modulation deviating from a sinusoid. At $T/t = 0.4$, the compressibility decreases by $\approx 20\%$ between $\langle n \rangle = 0.8 - 0.9$. At higher temperature, $T/t = 4$, the compressibility decreases by $\approx 2\%$. We resolve this effect as a shift in the average density between

the initial density modulation pattern and the long-time equilibrium density. This effect is largest at the coldest temperatures, and is at most $\delta n_\uparrow \approx 0.03$, which is comparable to the uncertainty in our density.

5.10 Thermoelectric effects

The hydrodynamic model we consider here neglects thermoelectric effects, which affect the measured density response by coupling local energy density modulations, and the resulting temperature gradients, to the particle current. We test this assumption by using local thermometry to search for dynamically generated thermal gradients. We infer local temperature by measuring the correlator $C_\uparrow(0, 1)$. To avoid the effects of varying density on the this correlator, we consider the time during the density modulation decay where the amplitude first crosses zero for a choice of wave vector with underdamped decay. At this time, any spatial variations in the correlator must be due to thermal gradients, however we find the correlator is flat within experimental precision.

Several simple theoretical approximations also suggest thermoelectric effects are small in our parameter regime. Thermoelectric coupling is primarily due to two effects. The first, which is thermodynamic in nature, is described by the thermoelectric susceptibility,

$$\zeta = -\frac{\partial^2 \Omega}{\partial \mu \partial T} = \left. \frac{\partial n}{\partial T} \right|_\mu = \left. \frac{\partial S}{\partial \mu} \right|_T, \quad (5.19)$$

where $\Omega = \epsilon - ST - n\mu$ is the grand potential and S is the entropy. This is a static quantity, and can be computed, e.g., by FTLM. In the whole temperature regime accessible by FTLM we find $|\zeta| \lesssim 0.015/t$. This is small in the sense that generating a density gradient of $0.01/a$ requires a large temperature gradient of $\nabla T \approx 0.8 t/a$.

The second thermoelectric coupling effect is the tendency of a temperature gradient to create a chemical potential gradient (and hence a current), described by the Seebeck coefficient. This is a transport coefficient, and hence more difficult to calculate. However, several approximation schemes suggest the Seebeck coefficient is small in our parameter regime due to a maximum of entropy which occurs close to $\langle n \rangle \approx 0.83$, including the Mott-Heikes approximation [229, 230] and the Kelvin formula [231, 232, 233]. This is in agreement with previous observations using different models or techniques [170, 229]. In the high- T regime where the Kelvin formula is a good approximation for the Seebeck coefficient [231, 233], the effect of thermoelectric coupling on particle diffusion is negligible.

5.11 The Nernst-Einstein relation

To draw a connection between the measured density response and the charge conductivity, we make use of charge conservation. Charge conservation imposes a connection between density and current expressed through the continuity equation (eq. 5.13).

Writing this in linear response we find

$$\sigma'(\omega) = \lim_{k \rightarrow 0} \frac{\omega}{k^2} \chi''(k, \omega), \quad (5.20)$$

where $\sigma'(\omega)$ is the real part of the conductivity and $\chi''(k, \omega)$ is the imaginary part of the density response function.

Inserting the expression for χ (eq. 5.16) into eq. 5.20, we find that the optical conductivity has a Lorentzian profile with half-width half-maximum Γ ,

$$\sigma'(\omega) = \frac{\chi_c D}{1 + \left(\frac{\omega}{\Gamma}\right)^2}, \quad (5.21)$$

and the Nernst-Einstein relationship holds for the DC conductivity,

$$\sigma = \chi_c D. \quad (5.22)$$

The Nernst-Einstein relation is a consequence of eq. 5.20 which holds if the density has a diffusive mode at long times and large wave vectors. It does not rely on the exact form of χ in eq. 5.16, but does require the same long wavelength behavior. We can, for example, take $D \rightarrow D_o + D_2 k^2$ or $\Gamma \rightarrow \Gamma_o + \Gamma_2 k^2$.

5.12 Compressibility versus temperature

To extract a resistivity using the Nernst-Einstein relation, we need the compressibility. It is determined in a separate experiment by measuring the variation of total density versus position in a harmonic trap and converting the position to chemical potential in the local density approximation [51, 234].

We first determine the harmonic trapping frequencies by fitting the density and nearest-neighbor density correlation profiles of a weakly interacting gas obtained at a field of 568.0(1) G, near the non-interacting point of the $|1\rangle - |3\rangle$ mixture, to the expected values for a non-interacting Fermi gas determined from eqs. 3.33 and 3.38.

Our cloud is slightly elliptic, with an aspect ratio of $\omega_x/\omega_y \approx 1.2$. Prior to determining the trapping frequency we perform an azimuthal average, which effectively rescales our coordinates $(x, y) \rightarrow \left(x\sqrt{\frac{\omega_x}{\omega_y}}, y\sqrt{\frac{\omega_y}{\omega_x}}\right)$. We measure r in these coordinates above, therefore our fitting procedures yields $\bar{\omega} = \sqrt{\omega_x\omega_y}$. Distance and energy scales are measured in units of the lattice constant and tunneling energy respectively. We assume a harmonic trapping potential, $\mu(r) = \mu_o - \frac{1}{2}m\omega^2r^2$ and fit our cloud profiles with μ_o , ω , and T as free parameters. For low temperatures, the lattice beams provide all the radial confinement, leading to $\bar{\omega} = (2\pi)185(10)$ Hz. For higher temperatures, we use a circular beam to provide extra confinement, leading to $\bar{\omega} = (2\pi)280(10)$ Hz.

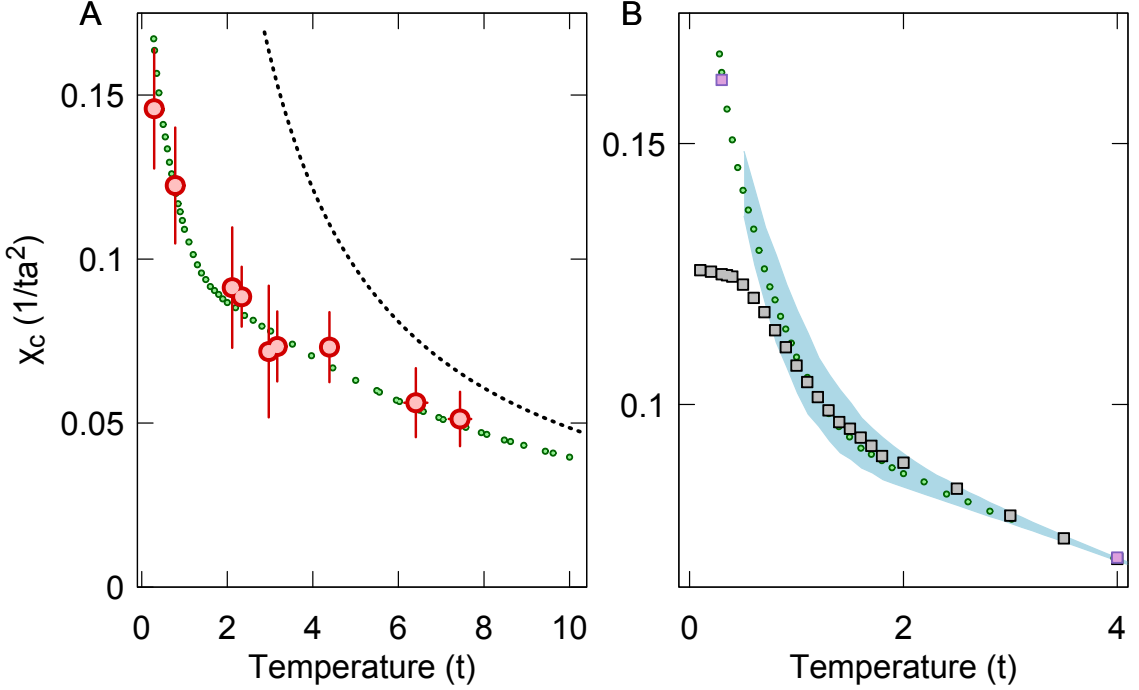


Figure 5.5: Hubbard compressibility versus temperature. **A**, Results for the charge compressibility, χ_c . Experimental results (red points), determinantal quantum Monte Carlo at $\langle n \rangle = 0.83$ and $U/t = 7.5$ (green points), and the high-temperature limit $1/T$ scaling (black dashed line). Each compressibility point is typically determined from 60 images. **B**, Charge compressibility at low temperature for FTLM (blue band), DQMC (as in A), single-site DMFT at $\langle n \rangle = 0.825$ and $U/t = 7.5$ (gray squares), and cellular DMFT (purple squares). Error bars standard error of the mean.

After determining the trapping frequency, we compute the compressibility for the interacting system density profiles according to

$$\left. \left(\frac{\partial n}{\partial \mu} \right) \right|_T = -\frac{1}{m\omega^2} \left(\frac{1}{r} \frac{\partial n}{\partial r} \right). \quad (5.23)$$

The measured compressibility increases with decreasing temperature (fig. 5.5A). For our highest experimental temperatures, χ_c approaches $n(1 - n/2)/T$, as expected in the high temperature limit, where $T \gg 8t$ [176]. At sufficiently low temperature χ_c is expected to saturate (see section 3.2.1), but we do not reach this limit at our lowest experimental temperature, $T/t = 0.3$. Our experimental results agree well with DQMC numerics over the full range of experimental temperatures.

We also compare our measured compressibility with FTLM, and DMFT in fig. 5.5B. The DQMC and FTLM compressibilities agree well with the experimental data and do not saturate at low temperatures. In contrast, the single-site DMFT compressibility saturates at $T/t \approx 1$. The increasing compressibility below this temperature may be associated with short-range correlations [226], which are not accounted for by single-site DMFT. Cellular DMFT results using a 2×2 plaquette gives excellent agreement with DQMC, supporting this interpretation.

5.13 Experimental DC conductivity

Having experimentally determined both the diffusion constant and the charge compressibility, we apply the Nernst-Einstein relation to determine the conductivity. We examine the temperature dependence of the resistivity $\rho = 1/\sigma$ in fig. 5.6, and observe that it rises without limit, showing no sign of saturation. Assuming the existence of quasiparticles, the maximum resistivity obtained from the Drude relation using the MIR limit is $\rho < \rho_{\max} \approx \sqrt{\frac{2\pi}{n}}\hbar$ [215, 226]. We find that our resistivity violates this bound for temperatures above $T/t \sim 1.3$. The temperature where ρ exceeds this limit is near the Brinkman-Rice temperature scale, defined by $T_{\text{BR}} = (1-n)W$, where $W = 8t$ is the band width, which is an estimate of the degeneracy temperature of quasiparticles in a doped Mott insulator. Similar violation of the resistivity bound at T_{BR} has been observed in DMFT studies [235, 236].

The failure of ρ to saturate at the resistivity bound is similar to behavior observed in bad metals at high temperatures [215]. In our system, the violation of the resistivity bound is not associated with the mean free path becoming shorter than the lattice spacing because the diffusion constant does not violate its derived bound, but rather with the temperature dependence of the compressibility [226]. This suggests a need for a more careful distinction between the MIR limit on the mean free path and the

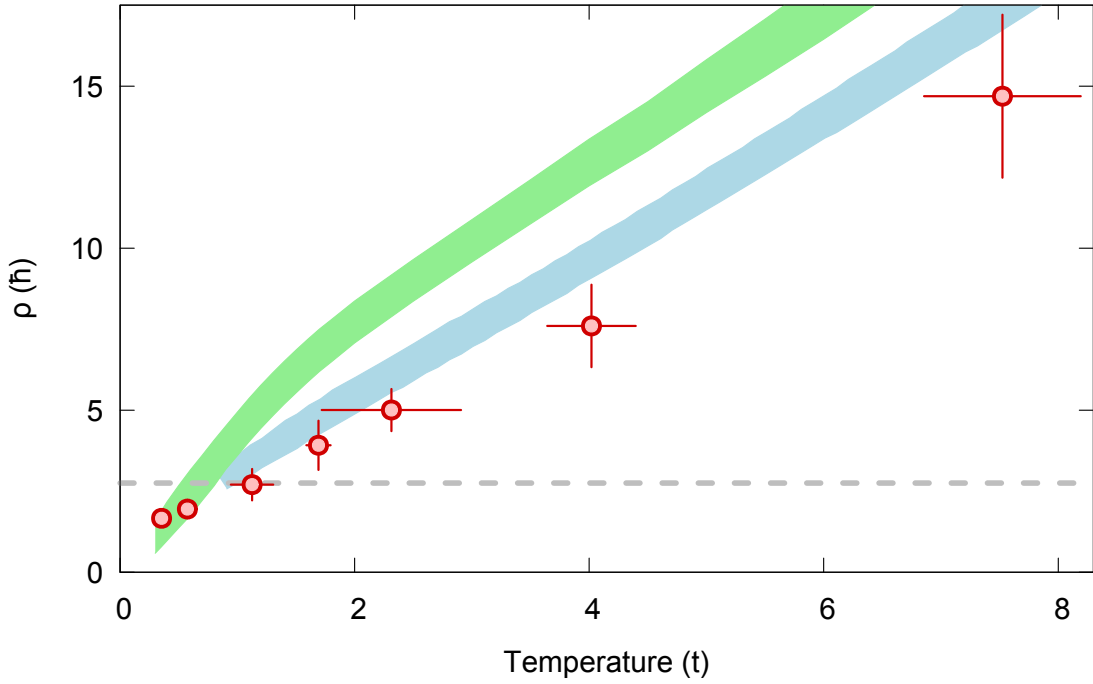


Figure 5.6: **Conductivity versus temperature.** Results for the resistivity, ρ . Experiment (red), 16-site finite-temperature Lanczos method for $U/t = 7.5$ and $\langle n \rangle = 0.8 - 0.85$ (light-blue band), single-site dynamical mean-field theory results for $U/t = 7.5$, $\langle n \rangle = 0.825$ (green band), and the lower bound on conductivity inferred from the Drude relation using the Mott-Ioffe-Regel limit, ρ_{max} (gray). Error bars standard error of the mean.

resistivity bound, despite the presumed equivalence of these concepts in condensed matter experiments.

To further elucidate the temperature dependence of ρ , we fit our results to the form $\rho(T) = \rho_o + AT + BT^2$. We find the temperature dependence is linear to good approximation as we obtain $\rho_o = 1.1(1)\hbar$, $A = 1.55(15)\frac{\hbar}{t}$, and $B = 0.03(3)\frac{\hbar}{t^2}$. Alternatively, a power law fit to the form $\rho(T) = \rho_o + (CT)^\alpha$ yields $\rho_o = 1.2(2)\hbar$, $C = 1.4(2)\frac{\hbar}{t}$, and $\alpha = 1.1(1)$. Similar fits show the inverse diffusion constant $1/D$ scales with $\alpha = 0.6(1)$ and the inverse charge compressibility scales with $\alpha = 0.85(20)$. In our temperature range, the linear resistivity is a combined result of the temperature dependence of the diffusivity and compressibility, both of which behave in a non-trivial

way. This behavior should be contrasted with the high-temperature regime, $T \gg W$, where D saturates to a limiting value and the resistivity inherits its temperature dependence from the compressibility, which scales as $\chi_c \propto 1/T$ [176]. It should also be contrasted with the low-temperature regime usually considered in condensed matter where the compressibility has saturated and the resistivity inherits its temperature dependence from the diffusion constant.

We end with more detailed comparison of resistivity with available theories. At our higher experimental temperatures we compare with FTLM, which is an exact technique, and find reasonable agreement (fig. 5.6). The experimental resistivity is systematically smaller than the FTLM calculation but within error bars. This may be a result of the uncertainty in determining U/t . At our lowest experimental temperatures, FTLM suffers from finite size effects which become relevant as correlation lengths approach the cluster size. For the 4×4 site cluster considered here, these effects limit FTLM resistivity calculations to $T/t \gtrsim 1$.

Because our experiment explores low temperatures which are inaccessible to FTLM, we also compare with an approximate technique, single-site DMFT [147] (fig. 5.6). We find the DMFT tends to overestimate the experimental resistivity at high temperatures. At our highest experimental temperatures, the DMFT resistivity is linear with a positive zero-temperature intercept. This linear scaling crosses over to a second linear scaling with a negative zero-temperature intercept around $T/t = 2$. This second linear region continues down to about $T/t = 0.8$ where the resistivity acquires a significant quadratic component. These regimes coincide with two different regimes observed in the DMFT compressibility (fig. 5.5B). Previous DMFT studies at stronger interaction strengths have also observed these two linear regimes at intermediate temperatures, finding evidence for resilient quasiparticles in the lower temperature regime [235, 236]. We do not observe the change of slope in the resistivity expected near $T/t = 2$ in either the experimental data (within uncertainties)

or the FTLM results. This suggests a need for comparison between more refined DMFT and exact theoretical approaches in the regime where this is possible. One recent comparison between DMFT and FTLM suggests vertex corrections, which are neglected by DMFT, may be important even at high temperatures [237].

5.14 Comparison of theory techniques

Each of the theory techniques considered in this chapter, DQMC, FTLM, and DMFT, have different strengths and weaknesses which makes one or another more suitable for certain comparisons with experiment. We provide a broad outline their strengths and weaknesses in this section.

DQMC is the method of choice for calculating static quantities because it is an exact technique which can access the lowest temperatures we reach in the experiment. On the other hand, dynamical quantities are difficult to extract, as DQMC yields imaginary time Green's functions which must be analytically continued to real time. Analytic continuation is an ill-posed problem, and the statistical uncertainty of DQMC data further complicates matters. In this experiment, we use DQMC to compute static quantities, including the singles density, spin-up density correlator, and compressibility.

Obtaining reliable dynamical quantities from DQMC is an active area of research, and recently resistivity versus temperature calculations for $U/t = 6$, $T/t = 0.2 - 8$ and diagonal-neighbor tunneling $t_d = -0.25t$ have been reported [238]. This study finds qualitatively similar results to those presented here.

FTLM is an exact technique which provides direct access to both static and dynamic correlators but is not capable of reaching either as large system sizes or as low temperature as DQMC. The minimum temperature it can access is limited by finite size effects. When correlation lengths exceed the size of the small system used, the

results no longer reflect the behavior of the system in the thermodynamic limit. In the main text we use FTLM to compute all dynamic quantities which can be obtained from correlators (current relaxation rate and conductivity). We also provide the FTLM compressibility in fig. 5.5B and verify that this agrees with the DQMC result.

DMFT is an *approximate* technique which maps an interacting problem onto a self-consistent quantum impurity problem. It becomes exact in infinite dimensions. The impurity problem can be solved using a variety of techniques. When exact diagonalization is used, dynamical quantities can be obtained directly without analytic continuation. DMFT calculations can be performed at lower temperatures than attainable by DQMC or DMFT. We use DMFT to compute all dynamical quantities which can be obtained from correlators. We also provide the DMFT compressibility in fig. 5.5B and verify that this agrees with the DQMC result. This comparison provides one test of the DMFT approximations.

More detailed descriptions of the FTLM and DMFT techniques used in this work are available in the supplement to [82].

5.15 Outlook

Our experiment paves the way for future studies of the optical conductivity and thermopower, which can be examined near equilibrium using a similar approach. Both of these quantities might be expected to show anomalous scalings, as in the cuprates [213, 217]. In line with theoretical work such as [235, 236], searching for direct signatures of resilient quasiparticles using spectroscopic techniques [239] would also be very interesting. Further experimental studies will also provide important benchmarks for approximate theoretical methods, as the combination of low temperature, finite-doping, and dynamics is challenging for exact theoretical approaches.

Chapter 6

Angle-resolved photoemission spectroscopy of a Fermi-Hubbard system

Portions of this chapter are based on work previously published as

P. T. Brown, E. Guardado-Sanchez, B. M. Spar, E. W. Huang, T. P. Devoreaux, and W. S. Bakr. [Angle-resolved photoemission spectroscopy of a Fermi-Hubbard system](#). arXiv:1903.05678v1.

In this chapter, we extend the program of the previous chapter, studying dynamical properties of the Fermi-Hubbard model, by developing a new technique to measure the single-particle spectral function in an attractive Fermi-Hubbard system. The single-particle spectral function is a dynamical observable that describes the allowed energy and momentum combinations for single-particle like excitations. The excitation spectrum reveals fundamental information about a correlated many-body system. If quasiparticles are present, they appear as sharp peaks in the spectral function. The spectral function is also sensitive to pairing physics and has been extensively explored using angle-resolved photoemission spectroscopy (ARPES) on cuprate ma-

terials to reveal information about the superconducting ground state — including playing a large role in determining the d -wave symmetry of the gap. ARPES on cuprates has also revealed a fascinating regime where the gas is in the normal state, but the spectral function contains an incomplete gap-like feature. This is referred to as the pseudogap regime, and its origin is not fully understood. There is broad interest in pseudogap phenomena, and it is now clear that pseudogap features appear in a variety of strongly correlated materials including continuum Fermi gases near unitarity.

6.1 Photoemission spectroscopy

Angle-resolved photoemission spectroscopy (ARPES) measures the single-particle excitations of a many-body quantum system with both energy and momentum resolution, providing detailed information about strongly interacting materials [240]. ARPES is a direct probe of fermion pairing, and hence a natural technique to study the development of superconductivity in a variety of experimental systems ranging from high temperature superconductors to unitary Fermi gases. In these systems a remnant gap-like feature persists in the normal state, which is referred to as a pseudogap [241]. A quantitative understanding of pseudogap regimes may elucidate details about the pairing mechanisms that lead to superconductivity, but developing this is difficult in real materials partly because the microscopic Hamiltonian is not known. Here we report on the development of ARPES to study strongly interacting fermions in an optical lattice using a quantum gas microscope. We benchmark the technique by measuring the occupied single-particle spectral function of an attractive Fermi-Hubbard system across the BEC-BCS crossover and comparing to quantum Monte Carlo calculations. We find evidence for a pseudogap in our system that opens well above the expected critical temperature for superfluidity. This technique may

also be applied to the doped repulsive Hubbard model, which is expected to exhibit a pseudogap at temperatures close to those achieved in recent experiments [73].

Photoemission spectroscopy measures the occupied single-particle spectral function [240, 242, 243], which describes the allowed energies for a single-particle excitation with given momentum. ARPES has been used to study the presence of a Fermi surface, the lifetime of quasiparticles, superconducting gaps and their symmetries, and surface states in topological materials [244, 245]. It is illustrative to consider some generic features of the spectral function as we introduce interactions. For a non-interacting system with dispersion ϵ_k , the single-particle excitations are eigenstates of the system implying they have a definite energy and infinite lifetime. The spectral function is a delta function, $A(k, \omega) = \delta(\hbar\omega - \epsilon_k + \mu)$ where μ is the chemical potential. Turning on weak interactions may create a Fermi liquid state, where the spectral function has a similar form but broadens along the energy axis reflecting the finite lifetime of the quasiparticles. In superconducting systems, more radical changes may occur including the development of a gap separating two disconnected spectral function branches. In weak coupling (BCS) superconductors, the gap vanishes at the critical temperature. However in many strongly-interacting superconducting systems, including the high-temperature cuprate superconductors (HTSC's) and the unitary Fermi gas, a depression in the spectral weight at the chemical potential persists in the normal state [241, 246, 247, 248, 249, 250, 251, 252]. These so called pseudogap states might arise from the same pairing mechanism as the superconducting ground states, and developing a better understanding of their properties may shed light on pairing physics in the HTSC's.

Photoemission spectroscopy with cold atoms has been used to study the pseudogap regime in strongly interacting Fermi gases without a lattice. The idea was first proposed using Raman techniques [253], but was realized with momentum-resolved radiofrequency (rf) spectroscopy [239]. Previous experiments have explored the BEC-

BCS crossover in 3D [239, 248, 254] and 2D [250, 255] continuum systems. These experiments inferred the presence of a pseudogap from spectral features that exhibit “back-bending” near the Fermi surface at temperatures above T_c , in analogy to the back-bending observed in the BCS dispersion. This interpretation has been criticized because back-bending can also arise due to other effects, including universal short range physics expected in continuum systems [256]. Exact theory techniques were not available for these systems, therefore experiments compared with various T -matrix approximation schemes [257, 258, 259] which become exact for weak interactions.

Here we extend photoemission spectroscopy to strongly-correlated lattice systems. We take advantage of quantum gas microscopy techniques to obtain high signal-to-noise data using a single layer 2D system, avoiding the complication of integration over a third axis of momentum space. Combining photoemission spectroscopy with quantum gas microscopy poses a technical challenge because photoemission spectroscopy relies on a large field of view for time-of-flight measurements to reach momentum space, whereas quantum gas microscopy is limited to a small field of view over which the atoms can be pinned during imaging. We solve this problem by developing a new measurement protocol which consists of four parts, illustrated in fig. 6.1A. First, we excite atoms from the interacting system to a non-interacting final state using a radiofrequency pulse. Next, we perform band mapping to adiabatically connect quasimomentum states in the lattice to real momentum states. Then, we allow the atoms to expand in a harmonic trap for a quarter period which maps the atomic momentum distribution to the real space distribution [260]. Finally, we turn on a deep optical lattice to freeze the atoms in place in preparation for site resolved imaging. The momentum detection portion of this protocol has been discussed in a recent proposal for measuring the spectral function in 1D systems using lattice modulation techniques [261].

We benchmark the ARPES technique by studying the pseudogap regime in the attractive Hubbard model. There has been comparatively little experimental work on this system [71, 79, 80, 262], but it has a number of advantages as a testing ground for our new protocol. Unlike the repulsive model, the attractive model does not have a sign problem, meaning it is possible to make high-precision theory calculations using DQMC at low temperatures. Furthermore, the 2D attractive model exhibits phenomenology similar to other strongly interacting superconducting systems. In particular, it exhibits a BCS-BEC crossover with increasing on-site interaction strength and a Berezinskii-Kosterlitz-Thouless (BKT) transition to an *s*-wave superconducting state at low temperatures [154]. At weak interactions the ground state is BCS-like, and pairing is destroyed at the critical temperature for superconductivity, T_c . As the interaction strength is increased, pairing persists above the critical temperature and is destroyed at some higher temperature $T^* > T_c$. Intermediate temperatures, $T_c < T < T^*$, exhibit a pseudogap which appears as a depression in either the density of states or spectral function at the Fermi energy [263, 264, 265]. As the interaction strength increases, the pairing changes character from momentum-space to real-space and from many-body to two-body, and the pseudogap temperature increases monotonically. In the BEC limit, the pseudogap represents a regime of real-space bosonic pairs which develop phase coherence below T_c .

6.2 Experimental preparation

In this experiment, we study an attractive Hubbard system with interactions ranging from intermediate coupling, $U/t = -4$, to strong coupling, $U/t = -8$, where t is the tunneling energy. We observe the emergence of a pseudogap as we increase the interaction at fixed temperature, $T/t \sim 0.5$. This is well above the theoretically calculated maximum T_c for this model $T/t \sim 0.15$ [154]. At strong coupling and

higher temperatures, we observe the presence of two branches in the occupied spectral function due to the coexistence of single and paired atoms.

To begin, we prepare an equal mixture of hyperfine states $|\uparrow\rangle = |3\rangle$ and $|\downarrow\rangle = |1\rangle$ in a 2D trap at a field of ~ 120 mG where the scattering length $a_{13} \sim -800$ a_0 [128], where a_0 is the Bohr radius and $|i\rangle$ denotes the i th lowest hyperfine state of lithium. We adiabatically load a 2D optical lattice with lattice spacing $a = 752$ nm to depths between 5 and $10 E_r$, where $E_r/h = 14.7$ kHz is the lattice recoil energy. The optical lattice provides harmonic confinement with a trapping frequency $\omega_l = (2\pi)160 - 200$ Hz depending on the final lattice depth. We then apply a 1 ms radiofrequency (rf) pulse to transfer $\sim 15\%$ of the $|\uparrow\rangle$ atoms to a third state $|f\rangle = |2\rangle$ (fig. 6.1A, left panel). Final state interactions are negligible because the scattering lengths $a_{12} \sim 0$ a_0 and $a_{23} \sim 25$ a_0 are small. We determine the initial quasimomentum distribution of the probed atoms by performing band mapping and subsequently expanding for a quarter period in a harmonic trap. To achieve this, we change the intensity of a harmonic trapping potential from zero to full in a few microseconds. At full intensity, this beam has trapping frequency $\omega = (2\pi)360$ Hz. Then, we ramp the lattice potential to zero linearly in 200 μ s before allowing the atoms to expand for $T/4 = 700$ μ s. The real space density distribution after the quarter period expansion reflects the initial quasimomentum distribution of the $|f\rangle$ atoms according to $\tilde{n}_f(k) = n_f(r)l^4$, where $l = \sqrt{\hbar/m\omega}$ is the harmonic oscillator length and $k = r/l^2$.

6.3 Radiofrequency spectroscopy

We obtain the energy dependence of the spectral function by measuring the density profile at a range of rf frequencies. For each frequency, ν , we obtain a two-dimensional image, $n_f(r, \nu)$ as shown in fig. 6.1B. Each pixel in the image is associated with a different quasimomentum. To improve our signal-to-noise, we spatially average using

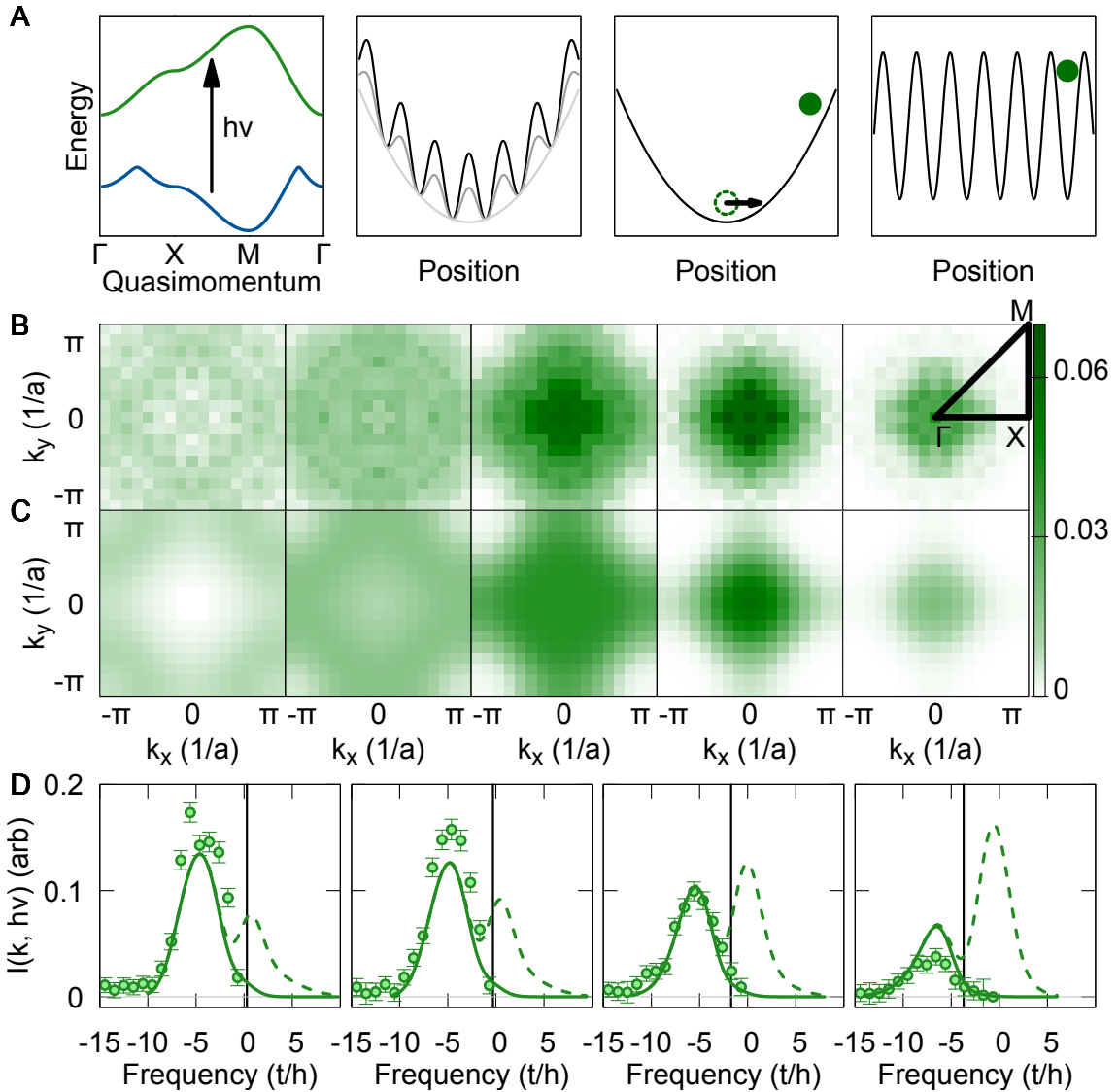


Figure 6.1: **ARPES technique and raw data.** **A**, A radiofrequency photon of energy $h\nu$ is incident on an interacting system with a dispersion (blue) and excites state $|\uparrow\rangle$ atoms to state $|f\rangle$ with a non-interacting final dispersion shown in green (far left). The dispersions are plotted along the high-symmetry lines of the Brillouin zone, with $\Gamma = (0, 0)$, $X = (\pi, 0)$, and $M = (\pi, \pi)$. We perform band mapping to map quasimomentum to momentum (second from left) by ramping down the lattice depth adiabatically with respect to the band gap. The atoms expand for a quarter period in a harmonic trap (third from left). Atoms (green ring) with initial momentum $\hbar k$ expand to position $r = k/l^2$ (solid green circle). Finally, we freeze the position of the atoms by ramping up an optical lattice to $\sim 60 E_r$ (right-most). **B**, Atomic density after the quarter period expansion for a range of frequencies ν at $U/t = -7.5(1)$ and $T/t = 0.55(3)$. From left to right, $h\nu/t = -10.5, -8.6, -6.6$, and -3.6 and -1.7 , measured with respect to the $|\uparrow\rangle - |f\rangle$ Zeeman splitting. Average of 40 pictures, binned, and averaged using the symmetry of the square. Field of view of $40 \mu\text{m} \times 40 \mu\text{m}$.

Figure 6.1: **C**, DQMC results for $A(k, \epsilon_k - h\nu)F(\epsilon_k - h\nu)$ at $U/t = -7.5$ and $T/t = 0.55$ for the same values of ν shown in B. **D**, Experimental (points) and DQMC (solid green lines) results for the occupied spectral function, DQMC results for the full spectral function (dashed lines), and chemical potential (black lines) at several quasimomenta in the Brillouin zone. From left to right, $(k_x, k_y) = (0, 0)$, $(\pi/4, 0)$, $(\pi/2, 0)$, and $(\pi, 0)$. Error bars standard error of the mean.

the symmetry of the square. The final density distribution of state $|f\rangle$ atoms is proportional to the occupied single-particle spectral function, $n_f(r, \nu) \propto A(\mathbf{k}, \epsilon_{\mathbf{k}} - h\nu - \mu)F(\epsilon_{\mathbf{k}} - h\nu - \mu)$, where F is the Fermi function. The energy of the final state is given by the tight-binding dispersion $\epsilon_{\mathbf{k}}/t = 4 - 2\cos(k_x a) - 2\cos(k_y a)$, and the energy of the initial state is $\epsilon_{\mathbf{k}} - h\nu$ where $h\nu$ is the rf photon energy. The rf photon carries negligible momentum, therefore the initial momentum is the same as the final momentum. This transition is illustrated schematically in momentum space (fig. 6.1A, left panel).

The density profiles change shape as the rf frequency is scanned, a characteristic of an interacting system. At large red detuning relative to the non-interacting transition, the transferred density is more heavily weighted towards the edges of the Brillouin zone (fig. 6.1B, leftmost). As the detuning is decreased, the density becomes peaked at the center and the transfer increases (center). Decreasing the detuning further leads to less transfer but does not significantly change the shape (rightmost). To further quantify the energy dependence of the spectral function we focus on individual quasimomenta and plot the corresponding energy distribution curves (EDC's) in fig. 6.1D. We compare our experimental results with determinantal quantum Monte Carlo (DQMC) calculations at $U/t = -7.5$ and $T/t = 0.55$, which are shown in fig. 6.1C and D and find good agreement. The full DQMC spectral function (fig. 6.1D) exhibits a depression near the central chemical potential, indicating a pseudogap at this temperature and interaction.

6.4 Band mapping simulation

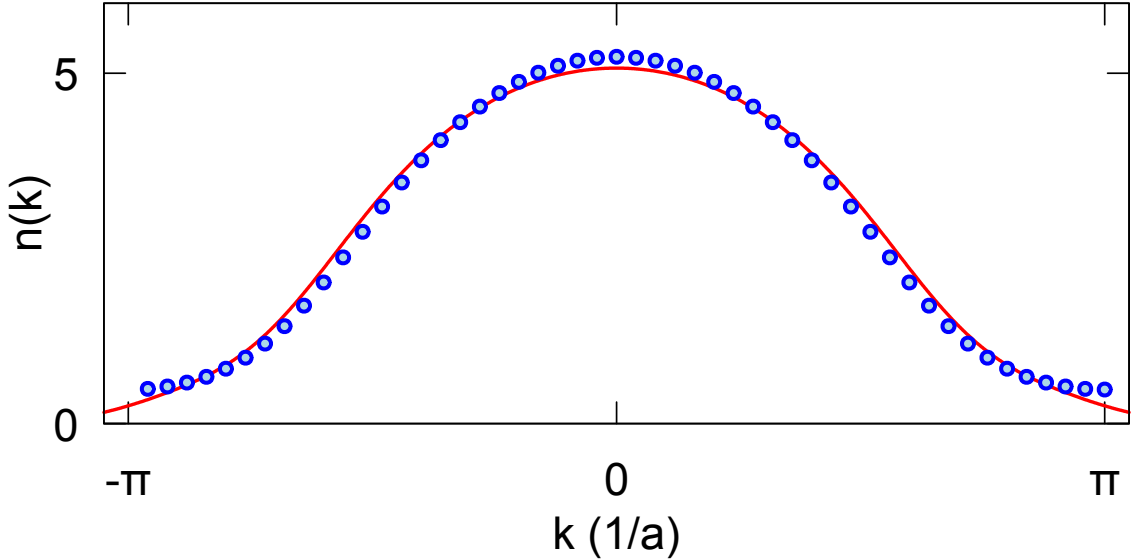


Figure 6.2: **Band mapping simulation.** Quasimomentum distribution (blue circles) and scaled atomic density after band mapping procedure (red line). These show good agreement for the parameters used in the experiment.

We perform a 1D simulation of the band mapping procedure used in the experiment following [266] to assess what effect atomic motion during the band mapping has on the final density profiles. This is an important verification step because the band mapping time, 200 μ s, is only a factor of ~ 3 shorter than the quarter period expansion time of 700 μ s.

To model the band mapping, we first find the lowest eigenstates of a single-particle Hamiltonian with potential given by the sum of a lattice and harmonic trap in real space. Then we change the lattice depth linearly from the initial depth to zero while time evolving the initial eigenstates using the Crank-Nicholson method. We simulate the quarter period expansion in the harmonic trap evolution using the propagator

$$U(x, t|x', 0) = \sqrt{\frac{1}{2\pi i \sin(\omega t) l^2}} \exp \left[i \frac{1}{2l^2 \sin(\omega t)} ((x^2 + x'^2) \cos(\omega t) - 2xx') \right], \quad (6.1)$$

where $l = \sqrt{\frac{\hbar}{m\omega}}$ is the harmonic oscillator length.

The results of this procedure are shown in fig. 6.2 for an initial temperature of $T/E_r = 1/30$, a lattice depth of $6.5 E_r$, a harmonic trapping frequency of $\omega_i = (2\pi)200$ Hz and a band mapping time of $200 \mu\text{s}$. The expansion trap frequency is $\omega_f = (2\pi)360$ Hz and one quarter period is $\sim 700 \mu\text{s}$.

We compare the results of the band mapping procedure to the initial quasimomentum distribution, which we determine by projecting the eigenstates of the initial trap on to the Bloch eigenstates of the lattice. We determine the scaling factor between the two using a least-squares fit as we do for the experimental data. This fit typically requires less than a 10% rescaling of the density. We find that the largest discrepancy occurs at the edges of the Brillouin zone where the gaps are smallest. The average fractional discrepancy between the quasimomentum distribution and the scaled band map density distribution is less than 10%.

6.5 The single-particle spectral function

In this section, we discuss the definition and physical interpretation of the single-particle spectral function. We also elucidate some of its useful properties and highlight its connection to the quantities measured in the experiment.

The single-particle spectral function can be thought of as a momentum-resolved density of states, and as such gives information about the allowed energies for an excitation with momentum k . It carries the frequency domain information associated with the single-particle retarded Green's function, which encodes information about the lifetime of these excitations. The single-particle retarded Green's function is given by,

$$G^R(k, t) = -\frac{i}{\hbar}\theta(t)\left\langle\left[c_k(t), c_k^\dagger(0)\right]_+\right\rangle. \quad (6.2)$$

The first term in the anticommutator, $\langle c_k(t)c_k^\dagger(0) \rangle$, describes what happens if we create a particle excitation with momentum k , watch this excitation propagate until time $t > 0$, and then measure the overlap of this state with the initial state. The second term, $\langle c_k^\dagger(0)c_k(t) \rangle$, can be interpreted similarly but for holes instead of particles.

We draw the connection between G^R and the spectral function by writing G^R in the spectral (Lehmann) representation. We arrive at this by Fourier transforming and expanding in a basis of eigenstates $|n\rangle$ with energies ϵ_n and partition function Z

$$G^R(k, \omega) = \frac{1}{Z} \sum_{n,m} e^{-\beta\epsilon_n} \frac{\left| \langle m | c_k^\dagger | n \rangle \right|^2}{\hbar\omega + \epsilon_n - \epsilon_m + i\eta} + e^{-\beta\epsilon_n} \frac{|\langle m | c_k | n \rangle|^2}{\hbar\omega - \epsilon_n + \epsilon_m + i\eta} \quad (6.3)$$

$$= G^+(k, \omega) + G^-(k, \omega). \quad (6.4)$$

Here $\eta \in \mathbb{R}^+$ and we always consider the limit $\eta \rightarrow 0^+$. The terms G^+ and G^- come from the anticommutator in G^R and can again be associated with creating a particle and hole excitation respectively.

The single-particle spectral function is the imaginary part of this above expression,

$$A(k, \omega) = -\frac{1}{\pi} \text{Im}\{G^R(k, \omega)\} \quad (6.5)$$

$$= \frac{1}{Z} \sum_{n,m} \left[e^{-\beta\epsilon_n} \left| \langle m | c_k^\dagger | n \rangle \right|^2 \delta(\hbar\omega + \epsilon_n - \epsilon_m) + e^{-\beta\epsilon_n} |\langle m | c_k | n \rangle|^2 \delta(\hbar\omega - \epsilon_n + \epsilon_m) \right]. \quad (6.6)$$

These two terms can also be written,

$$= A(k, \omega) [1 - F(\omega)] + A(k, \omega)F(\omega) \quad (6.7)$$

$$= A_{\text{unocc}}(k, \omega) + A_{\text{occ}}(k, \omega), \quad (6.8)$$

where A_{unocc} represents particle injection and A_{occ} , the occupied spectral function, represents photoemission.

The spectral function counts single-particle excitations at a given momentum and frequency. In this sense it may be thought of as a momentum resolved density of states. More precisely, we have the following relationship between the density of states, $\rho(\omega)$ and the spectral function

$$\rho(\omega) = \int dk A(k, \omega). \quad (6.9)$$

The spectral function is also closely related to the momentum distribution function

$$\langle n_k \rangle = \langle c_k^\dagger c_k \rangle = \int_{-\infty}^{\infty} d\omega A(k, \omega) F(\omega), \quad (6.10)$$

which follows from taking the limit $\tau \rightarrow 0$ in eq. 3.77.

Finally, the spectral function is normalized to unity

$$\int_{-\infty}^{\infty} d\omega A(k, \omega) = 1. \quad (6.11)$$

6.6 Linear response theory

To draw a connection between the experimental observable, the number of atoms transferred to the final state $|f\rangle$, and the single-particle spectral function, we outline the linear response theory describing the experiment following [242, 243, 267]. This approach works in the limit of a perturbatively weak radiofrequency drive.

The Hamiltonian of our system is $\mathcal{H} = \mathcal{H}_o + \mathcal{H}' + \mathcal{H}_f$, where the unperturbed Hamiltonians are given by

$$\mathcal{H}_o - \mu N = \sum_{\sigma k} \epsilon_k n_{k\sigma} + U \sum_i n_{i\uparrow} n_{i\downarrow} - \mu \sum_i n_i \quad (6.12)$$

$$\mathcal{H}_f = \sum_k \epsilon_k n_f - h\nu \sum_i n_{if}, \quad (6.13)$$

where \mathcal{H}_f describes the non-interacting final state particles. We choose the band minimum of the non-interacting dispersion as zero energy. This implies that half-filling occurs at $\mu = 4t + U/2$.

We work in the corotating frame of the radiofrequency drive, and we suppose the driving frequency is ν_d . The detuning is $\nu = \nu_d - \nu_o$, where $h\nu_o$ is the Zeeman splitting between non-interacting $|\uparrow\rangle$ and $|f\rangle$ atoms. We neglect Zeeman splitting between the $|\uparrow\rangle$ and $|\downarrow\rangle$ states which is not relevant here. The detuning appears analogous to a chemical potential for state $|f\rangle$. We assume that $\nu_o > 0$, otherwise the sign of ν should be reversed in eq. 6.13.

The perturbation term describing the radiofrequency probe in the rotating wave approximation is

$$\mathcal{H}' = \hbar \sum_{k,q} \left(\Omega(q, t) c_{k\uparrow}^\dagger c_{k+qf} + \Omega^*(q, t) c_{k+qf}^\dagger c_{k\uparrow} \right), \quad (6.14)$$

where $\Omega(q, t)$ is the spatial- and time-dependent Rabi frequency. If $\Omega(r, t) = \Omega(t)$ is spatially homogeneous, as is usually the case, then the rf does not contribute any momentum to the system and only the $q = 0$ term survives,

$$\mathcal{H}' = \hbar \sum_k \left(\Omega(t) c_{k\uparrow}^\dagger c_{kf} + \Omega^*(t) c_{kf}^\dagger c_{k\uparrow} \right). \quad (6.15)$$

In the experiment, we measure the total density of atoms transferred by the perturbation portion of the Hamiltonian acting for some time δt on our system. Assuming that the time is short enough and the perturbation is weak enough, we can apply linear response theory and the atom density is proportional to the atom current multiplied by δt . The atom current operator is given by

$$\dot{n}_f = \frac{i}{\hbar} [\mathcal{H}', n_f] = i \sum_k \left(\Omega c_{kf}^\dagger c_{k\uparrow} - \Omega^* c_{k\uparrow}^\dagger c_{kf} \right) \quad (6.16)$$

where we use the assumption that \mathcal{H}_o conserves particle number to drop it from the commutator in the first line and the fermionic anticommutation relations to simplify the commutator. We also take $\Omega(t) = \Omega$ to be time independent. We work with \dot{n}_f , effectively going to higher order in perturbation theory, because linear response in n_f vanishes.

Now we can apply a slight generalization of the linear response theory we developed in section 3.7. The only difference in this case is that $\mathcal{H}' = h(t)M(t) + h^*(t)M^\dagger(t)$ instead of $h(t)M(t)$. Making the identifications $h(t) = \hbar\Omega$, $M(k, t) = c_{k\uparrow}^\dagger c_{kf}$, and $\mathcal{O}(k, t) = \dot{n}_{kf}$, the time-dependent momentum-resolved current to the final state is given by the generalization of eq. 3.60,

$$I(k, h\nu, t) = \langle \dot{n}_{kf}(t) \rangle = \int_{-\infty}^{\infty} dt' \Phi(k, t - t')\Omega(t') + \text{h.c.}, \quad (6.17)$$

and the response function is given by eq. 3.61

$$\Phi(k, t) = -\frac{i}{\hbar}\theta(t) \left\langle \left[\dot{n}_{kf}(t), c_{k\uparrow}^\dagger c_{kf} \right] \right\rangle \quad (6.18)$$

$$= \theta(t)\Omega \left\langle \left[c_{kf}^\dagger(t)c_{k\uparrow}(t), c_{k\uparrow}^\dagger(0)c_{kf}(0) \right] \right\rangle, \quad (6.19)$$

where we drop terms like $\left\langle \left[c_{k\uparrow}^\dagger(t)c_{kf}(t), c_{k\uparrow}^\dagger(0)c_{kf}(0) \right] \right\rangle$ which vanish because states \uparrow and f are non-interacting.

The assumption f does not interact with the initial states allows us to simplify this response function using Wick's theorem. As Wick's theorem only applies to time-ordered correlation functions, we will exploit the relationship between the frequency representation of the response function and the Matsubara Green's function by first calculating the Matsubara Green's function and then analytically continuing to obtain the retarded Green's function in frequency space (see section 3.7.1). Passing to the Matsubara Green's function associated with the eq. 6.19 and applying Wick's

theorem,

$$G(k, \tau) = -\left\langle \mathcal{T} c_{kf}^\dagger(\tau^+) c_{k\uparrow}(\tau) c_{k\uparrow}^\dagger(0^+) c_{kf}(0) \right\rangle \quad (6.20)$$

$$= G_f(k, -\tau) G_\uparrow(k, \tau), \quad (6.21)$$

where $\tau^+ > \tau > 0^+ > 0$ and we again drop correlators between states \uparrow and f . We can write the single-particle Green's functions in terms of the single-particle spectral function using eqs. 3.76 and 3.77,

$$G(k, \tau) = \int d\omega d\omega' A_f(k, \omega) A_\uparrow(k, \omega') F(\omega) F(-\omega') e^{(\omega-\omega')\tau}, \quad (6.22)$$

where A_f and A_\uparrow are the spectral functions for the $|f\rangle$ and $|\uparrow\rangle$ states respectively.

Fourier transforming this result to imaginary frequency using eq. 3.72, we have

$$G(k, i\omega_n) = \int d\omega d\omega' A_f(k, \omega) A_\uparrow(k, \omega') \frac{F(\omega') - F(\omega)}{i\omega_n + \omega - \omega'}, \quad (6.23)$$

where $i\omega_n$ are the bosonic Matsubara frequencies. We analytically continue this to real frequency by taking $i\omega_n \rightarrow \sigma + i\eta$ to obtain the susceptibility

$$\chi(k, \sigma) = \Omega \int d\omega d\omega' A_f(k, \omega) A_\uparrow(k, \omega') \frac{F(\omega') - F(\omega)}{(\sigma + i\eta) + \omega - \omega'}, \quad (6.24)$$

where we reintroduce the factor of Ω from eq. 6.19. Taking the imaginary part of this expression introduces a factor of $-i\pi\delta(\sigma + \omega - \omega')$,

$$\text{Im}\{\chi(k, \sigma)\} = -\pi\Omega \int d\omega' A_f(k, \omega' - \sigma) A_\uparrow(k, \omega') [F(\omega') - F(\omega' - \sigma)] \quad (6.25)$$

The final state spectral function is known because we assume $|f\rangle$ is non-interacting, $A_f(k, \omega) = \delta(\hbar\omega - \epsilon_k + h\nu)$. If we additionally suppose the final state is initially unoccupied, then the second Fermi function in eq. 6.25 expression vanishes,

and we have

$$\text{Im}\{\chi(k, \sigma)\} = -\pi\Omega A_\uparrow(k, \epsilon_k - h\nu + \sigma)F(\epsilon_k + h\nu + \sigma). \quad (6.26)$$

This is nearly the final expression, but to obtain the correct *physical* frequency σ is a delicate issue related whether the time evolution is taken under the action of \mathcal{H}_o or $\mathcal{H}_o - \mu N$. In general, \mathcal{H}_o controls the dynamics of the system while $\mathcal{H}_o - \mu N$ controls the thermodynamics, but this distinction is often elided because the two are related by an energy offset in particle-number conserving systems. An equivalent point of view is that \mathcal{H}_o is related to $\mathcal{H}_o - \mu N$ by a change of reference frame using the unitary operator $U(t) = \exp[i\mu t \sum_i n_i]$. Up until now, we have considered time evolution under $\mathcal{H}_o - \mu N$. Changing frame from $\mathcal{H}_o - \mu N \rightarrow \mathcal{H}_o$ modifies the time dependence of $c_{k\uparrow}(t) \rightarrow c_{k\uparrow}(t)e^{-i\mu t}$. The effect of this change on the response function is $\Phi(k, t) \rightarrow \Phi(k, t)e^{-i\mu t}$ which implies that $\chi(k, \sigma) \rightarrow \chi(k, \sigma - \mu)$.

Passing back to the physical reference frame by taking by making this substitution,

$$\text{Im}\{\chi(k, \sigma)\} = -\pi\Omega A_\uparrow(k, \epsilon_k - h\nu - \mu + \sigma)F(\epsilon_k + h\nu - \mu + \sigma). \quad (6.27)$$

We obtain the momentum-resolved current from eq. 3.65 using the frequency domain expression for the Rabi frequency, $\Omega(\sigma) = \Omega\delta(\sigma)$ and taking the inverse Fourier transform,

$$I(k, h\nu, t) = -2\pi\Omega^2 A_\uparrow(k, \xi_k - h\nu)F(\xi_k - h\nu), \quad (6.28)$$

where $\xi_k = \epsilon_k - \mu$. As this expression is time independent, we will suppress the time argument and write $I(k, h\nu)$. We also suppress the spin index, writing $A = A_\uparrow$.

The origin of the $\epsilon_k - h\nu - \mu$ argument for the single-particle spectral function can be understood intuitively. The current of final state atoms depends on the com-

bination $\epsilon_k - h\nu$. ϵ_k is the energy of the outcoupled atom, implying that $\epsilon_k - h\nu$ is the initial energy. We must additionally subtract μ from the argument because the spectral function is defined such that $\omega = 0$ represents the system at the chemical potential.

We can rewrite eq. 6.28 to give the occupied spectral function at equal ω ,

$$A(k, \omega)F(\omega) \propto I(k, \epsilon_k - \omega - \mu). \quad (6.29)$$

This expression implies that the momentum resolved current is a measure of the occupied spectral function, however a measurement at a single frequency ν is a complicated surface in $k - \omega$ space.

6.7 Spectral function trap averaging

The spectral function is broadened by the presence of the harmonic trapping potential which causes the system to sample a range of chemical potentials. We account for this effect in our theory results using the local density approximation. We model the trapping potential as an effective spatial variation of the chemical potential according to $\mu_i = \mu - V_i$, where V_i is the potential at site i . The total current is given by

$$I(k, h\nu) = \sum_i A(k, \epsilon_k - h\nu - \mu_i, \mu_i)F(\epsilon_k - h\nu - \mu_i), \quad (6.30)$$

where we explicitly include the dependence of A on μ .

Determining the spectral function for the trapped system is more complicated than in the uniform system (eq. 6.29) because the convention is to reference ω to the chemical potential. This choice of reference is of little consequence when working at fixed density, but when working with multiple densities we must use a consistent reference point. In this case the physically meaningful quantity is $\omega + \mu$. In the

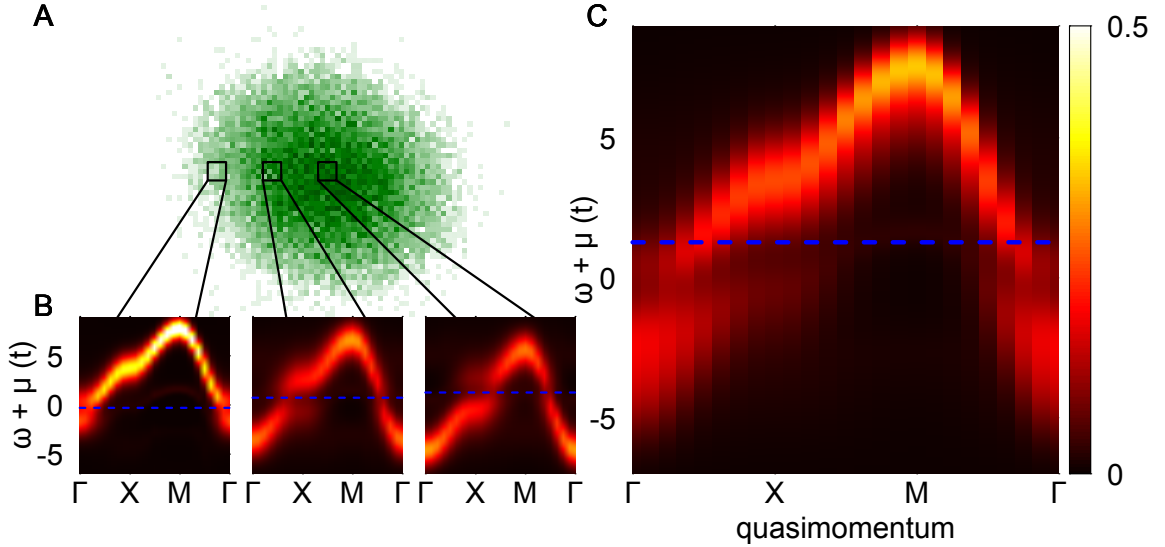


Figure 6.3: **Trap-averaged spectral function.** **A**, The total density, $\langle n \rangle$, of the trapped atoms. Field of view $50 \mu\text{m} \times 50 \mu\text{m}$. Black squares indicate regions of the trap with densities $n = 0.2, 0.8$, and 1.2 from left to right. **B**, Homogeneous system spectral functions calculated using DQMC at $U/t = -6$, $T/t = 0.5$ and $n = 0.2$ (left), 0.8 (center), and 1.2 (right). The chemical potential at each density is denoted by a horizontal blue line. The spectral functions for $n = 0.8$ and 1.2 reveal evidence of a pseudogap. **C**, The trap-average spectral function constructed by weighting the homogeneous system spectral functions by the area of the trapped cloud at each density. After trap averaging the pseudogaps at various densities in the trap are manifest as local minima in the spectral function at a fixed quasimomentum. The trap averaging blurs but does not destroy signatures of the pseudogap.

trapped system our energy reference is the central chemical potential, meaning that $\omega + \mu - \mu_i$ becomes the argument of the spectral functions

$$I(k, \epsilon_k - \omega - \mu) = \sum_i A(k, \omega + \mu - \mu_i, \mu_i) F(\omega + \mu - \mu_i). \quad (6.31)$$

As we expect eq. 6.28 to hold for the spectral function for the trap A_{trap} , we identify

$$A_{\text{occ, trap}}(k, \omega) = \frac{\sum_i A(k, \omega + \mu - \mu_i, \mu_i) F(\omega + \mu - \mu_i)}{\sum_i 1} \quad (6.32)$$

$$A_{\text{trap}}(k, \omega) = \frac{\sum_i A(k, \omega + \mu - \mu_i, \mu_i)}{\sum_i 1}, \quad (6.33)$$

where normalizing by the total number of sites in the trap ensures that the eqs. 6.9, 6.10, and 6.11 continue to hold.

The trap causes broadening of spectral features and tends to obscure signatures of gaps or pseudogaps. We illustrate this effect for an experimental density profile in fig. 6.3. The theoretical homogeneous system spectral functions shown in fig. 6.3B exhibit a pseudogap for densities $n > 0.2$. When these functions are combined using eq. 6.33, the pseudogap feature is broadened over the spread of chemical potentials where the uniform system exhibits a pseudogap (fig. 6.3C). This effect is also visible in fig. 6.1C, where the pseudogap feature appears shifted away from the central chemical potential. Before comparing these results with experiment, we account for Fourier broadening of the rf pulse by convolving the trap-average spectral function with a Gaussian with standard deviation $h \times 1 \text{ kHz}$.

6.8 LDA versus full trap simulation

To assess whether or not the LDA approach to computing the spectral function holds in our parameter regime, we compare the DQMC occupied spectral functions for a full trap simulations and for the LDA calculation described by eq. 6.33 in fig. 6.4 for $U/t = -3.7$ and $T/t = 0.48$. We expect any deviations from LDA to be more important at weak interaction, where the pair size is largest.

We choose a central chemical potential of $\mu/t = 2.45$ leading to a peak density of $\langle n \rangle \approx 1.2$, and a spatially varying potential of the form $V(x, y)/t = \frac{3}{256} (x^2 + y^2)$. This corresponds to a trapping frequency of $\omega = (2\pi)310 \text{ Hz}$ assuming $t/h = 1400 \text{ Hz}$, the tunneling rate in the experiment for the $U/t \sim -4$ data. This confinement is significantly stronger than that used in the experiment, which is at most $(2\pi)200 \text{ Hz}$, and therefore any deviations from the LDA prediction would be enhanced in this test compared with the experiment.

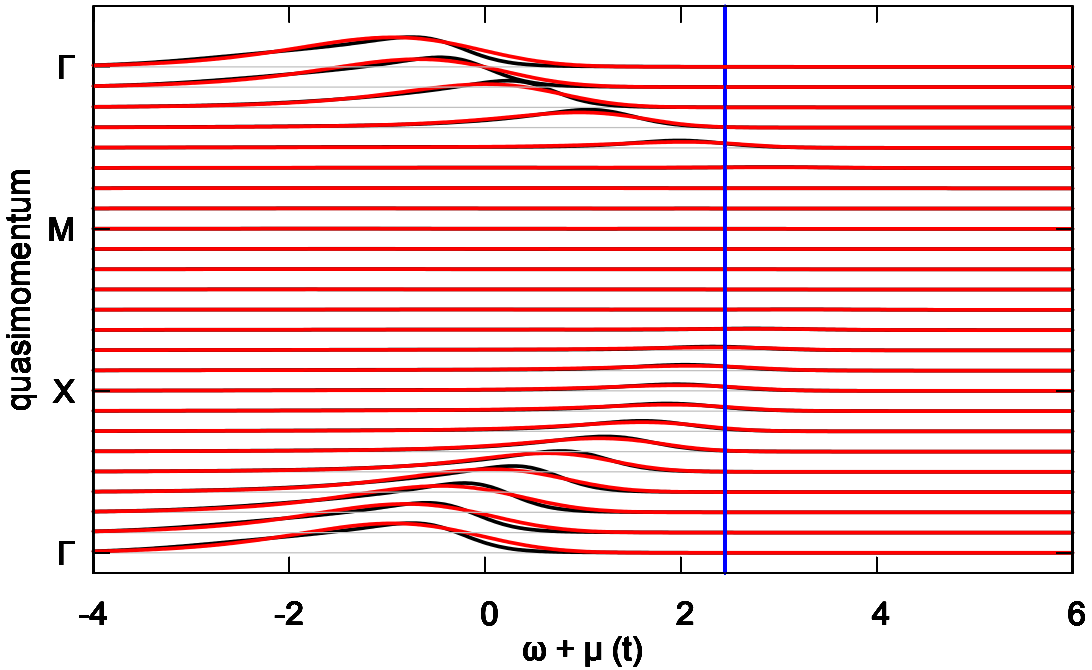


Figure 6.4: **Occupied spectral function from LDA versus trap simulation.** Occupied spectral function from DQMC calculated in the LDA (black) and from a full trap simulation (red) for a peak density of 1.2, and a trapping frequency of $\omega = (2\pi)310$ Hz. The two approaches match well, although small differences in the EDC shapes are visible.

We find good agreement between the full trap and LDA occupied spectral functions, indicating the LDA holds for the confinement considered here. There are small deviations between the shapes of the LDA and full trap simulation, with the LDA EDC's being somewhat more asymmetric. This relatively small discrepancy may have a number of origins, including the limited density resolution used to compute the LDA spectral function, difficulties in resolving fine details due to analytic continuation, or corrections to the LDA.

We do not compare the full trap and LDA spectral functions, as these are strongly dependent on the number of empty sites included in the calculation. This is because the full spectral function is sensitive to both occupied and unoccupied states. In the limit of a large but mostly empty system, the full spectral function will converge to that of a non-interacting gas.

6.9 Spectral function versus interaction

Having demonstrated the viability of this photoemission spectroscopy technique, we focus on elucidating the properties of the attractive Hubbard system by exploring the evolution of the spectral function with interaction strength and temperature. First, we consider the low temperature regime, $T/t \sim 0.5$, for a range of interactions $U/t = -4, -6$, and -7.5 . For each interaction strength we determine the temperature, interaction, and global chemical potential by fitting in-situ densities and correlators to DQMC results (see section 3.6.2). We determine the occupied spectral function from the density according to $A_{\text{occ}}(k, \omega) = n_f(k, \epsilon_k - \omega - \mu)$ and obtain the profiles shown in fig. 6.5. For the weakest interaction we consider, $U/t = -4$, the spectral weight is shifted to negative energy relative to the non-interacting dispersion and there is significant spectral weight near the chemical potential. As we increase the interaction, the spectral weight shifts further from the non-interacting dispersion and there is less spectral weight near the chemical potential.

We compare our measurements with DQMC calculations which account for both the presence of the trap and Fourier broadening of the rf pulse. These results, shown in the lower panels of fig. 6.5, display similar trends to the experiment. We determine the proportionality constant between the experimental data and the theoretical spectral function using a least squares fit. After scaling the experimental data, the theory agrees well at low quasimomentum (fig. 6.6). At larger quasimomentum near the X point, the experimental spectral function is systematically smaller than the theory. This may be due to imperfections in the band mapping process which are more significant near the edge of the band. A comparison of energy distribution curves (EDC's) for experiment and DQMC is shown in fig. 6.6.

We quantify the distribution of spectral weight by fitting each EDC to a Lorentzian profile and extracting the center position and half-width at half-maximum (HWHM) values. We emphasize that the resulting graph cannot be interpreted as a disper-

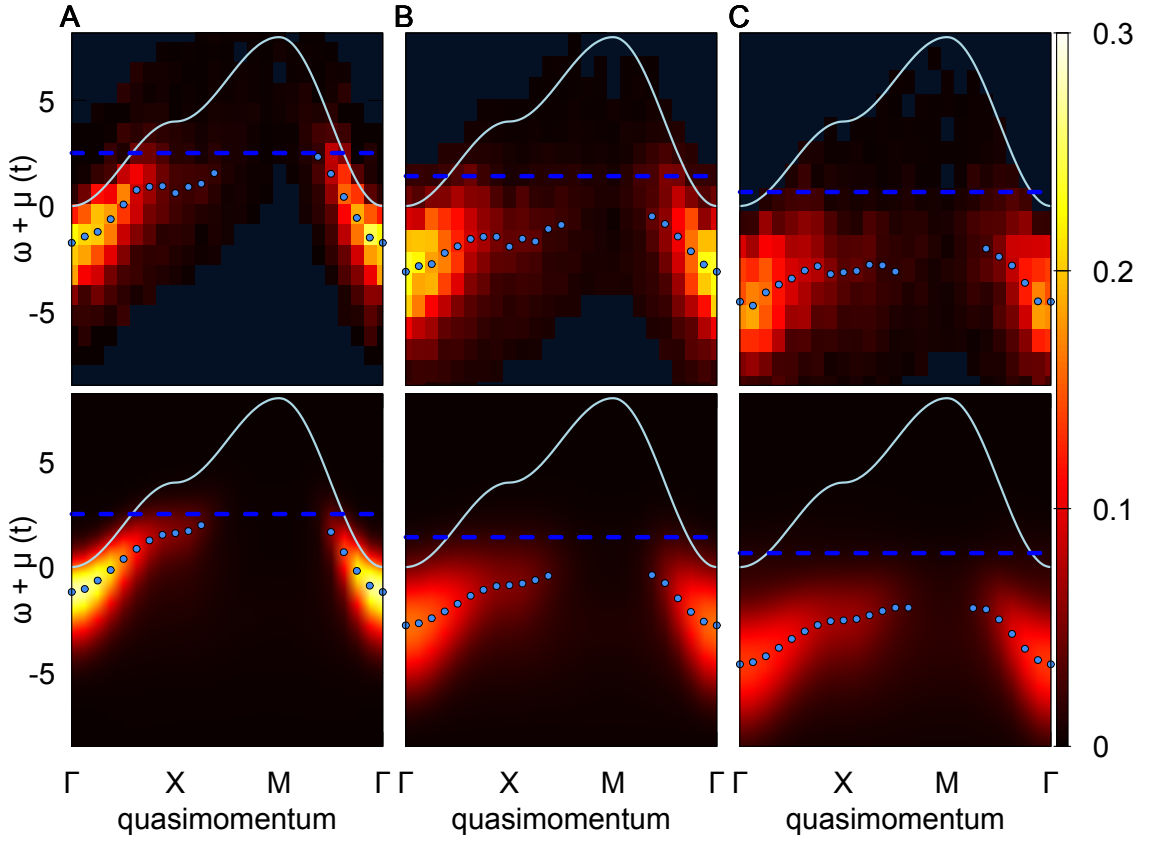


Figure 6.5: Occupied spectral function versus interaction. **A**, Experimental occupied spectral function (top) along directions of high symmetry in the Brillouin zone for $U/t = -3.7(1)$ and $T/t = 0.48(2)$ with the center position of Lorentzian fits to each EDC (light blue circles), the chemical potential (blue line) and the non-interacting dispersion relation (white line). DQMC results (bottom) for $U/t = -4$ and $T/t = 0.5$. At this temperature no pseudogap is present and the effective dispersion reaches the chemical potential. **B**, As the interaction is increased to $U/t = -6.0(1)$, a pseudogap develops at temperature $T/t = 0.50(2)$ and the dispersion pulls back from the chemical potential. **C**, At strong interaction $U/t = -7.5(1)$ and low temperature $T/t = 0.55(3)$ the pseudogap features are more pronounced.

sion for two reasons. First, there are trap averaging effects, and second even in a homogeneous system the Fermi function shifts the position of the peak in $A_{\text{occ}}(k, \omega)$ relative to $A(k, \omega)$, causing significant deviation from the true dispersion near and above the Fermi surface (see section 6.10). For $U/t = -4$, the center of the spectral weight reaches the chemical potential at a point along the $X - M$ line in momentum space (fig. 6.5A). For stronger interactions, $U/t = -6, -7.5$ the center of spectral weight no longer approaches the chemical potential. This pulling back of the spectral weight at the chemical potential is a signature of pseudogap behavior. The spectral width increases weakly with the interaction. At $U/t = -4$, the HWHM is $\sim 1.2t$ with little dependence on the quasimomentum. As we increase the interaction the width increases to $\sim 2t$ and $\sim 2.5t$ at $U/t = -6$ and $U/t = -7.5$ respectively. The measured width is larger than the Fourier broadening which is 1 kHz, corresponding to $\sim 0.7t$, $\sim 0.8t$, and $\sim 1t$ for these interactions. The width is not intrinsic, but due to the spread of chemical potentials across the harmonic trap.

Determining the presence of a pseudogap in the experimental system is complicated by the fact we measure the occupied spectral function. However, in the theory we can see the pseudogap open in the full spectral function. We display the full spectral functions in two ways, as EDC's in fig. 6.6 and as color plots in fig. 6.7. The EDC visualization makes it easier to compare the relative height of theoretical and experimental spectral functions, whereas the color plots emphasize the dispersion relation.

The EDC results for $U/t = -4$ (fig. 6.6A) show good agreement between the occupied spectral function line shapes in experiment and theory. No pseudogap is visible in the full spectral function EDC's at this interaction. For $U/t = -6$ (panel B), the theory systematically underestimates the height of the experimental occupied spectral function at low momenta, but agrees well at higher momenta. A pseudogap emerges in the full spectral EDC's along the $\Gamma - X$ and $M - \Gamma$ lines. For $U/t = -8$

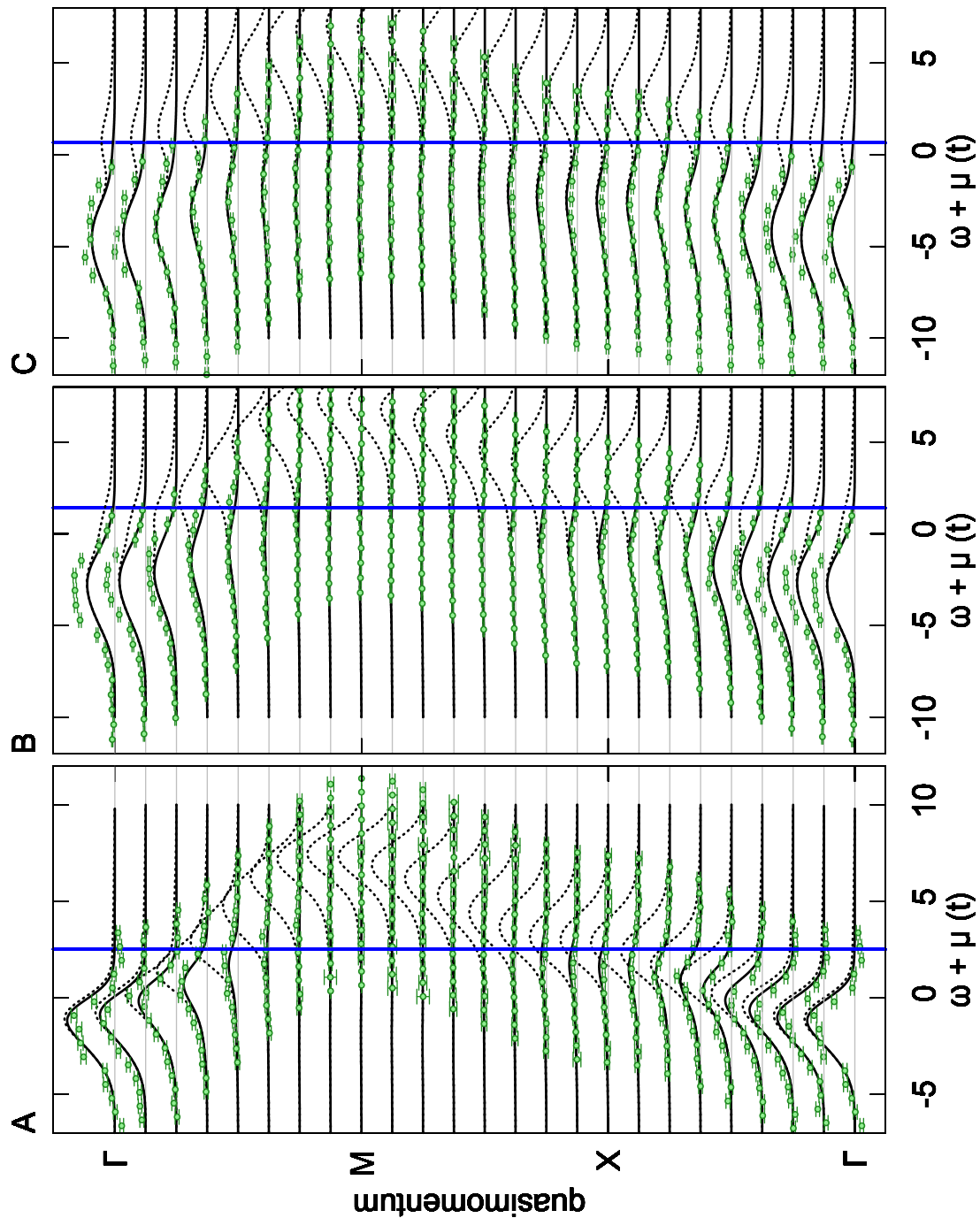


Figure 6.6: EDC's versus interaction. Caption continues on the following page.

Figure 6.6: **A**, EDC's from the experimental occupied spectral function (green points) and theory occupied spectral function (black solid lines) and theory spectral function (black dashed lines) for experiment at $U/t = -3.7(1)$ and $T/t = 0.48(2)$ and theory $U/t = -4$ and $T/t = 0.5$. The occupied spectral function has significant weight near the chemical potential at this weak interaction. **B**, experiment $U/t = -6.0(1)$ and $T/t = 0.50(2)$ and theory $U/t = -6$ and $T/t = 0.5$. At this intermediate interaction, the spectral weight pulls back from the chemical potential, and a pseudogap develops in the system. **C** experiment $U/t = -7.5(1)$ and $T/t = 0.55(3)$ and theory $U/t = -7.5$ and $T/t = 0.55$. At strong interaction, the pseudogap is clearly visible as a two-peaked structure in several of the spectral function EDC's.

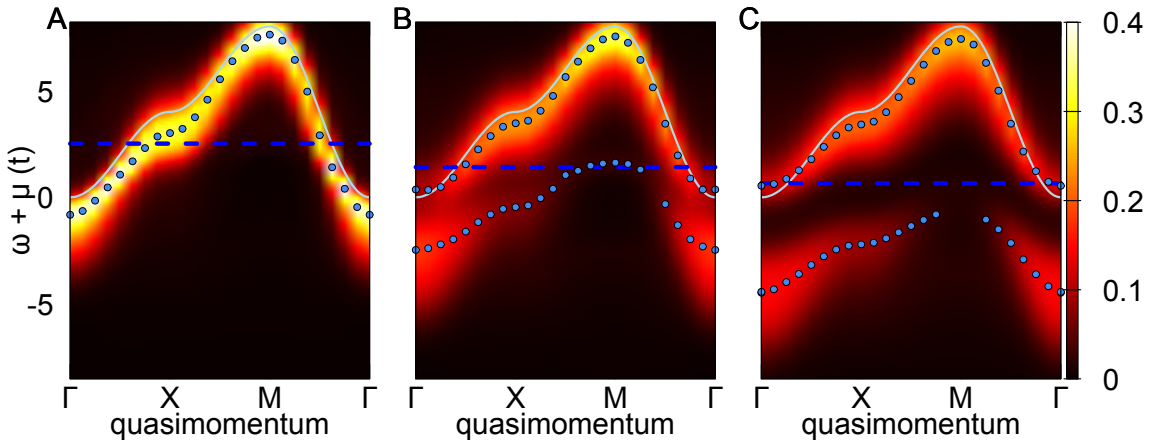


Figure 6.7: **Trap average spectral function versus interaction.** **A**, DQMC trap-average spectral function for $U/t = -4$ and $T/t = 0.5$. No pseudogap feature is present at this weak interaction. **B**, $U/t = -6$ and $T/t = 0.5$. A clear pseudogap emerges near intermediate coupling. **C**, $U/t = -7.5$ and $T/t = 0.55$. At strong coupling, the pseudogap feature is much stronger and present at all momenta.

(panel C), the theory and experiment show good agreement at all momenta. The pseudogap feature is visible at all momenta along the Γ - X and M - Γ lines.

The pseudogap is visible in the full spectral function color plots for $U/t = -6$ and -8 (fig. 6.7) and $T/t \sim 0.5$. The pseudogap is not present at $U/t = -4$, consistent with the calculations of [264]. We determine the peak locations using a peak-finding algorithm, which identifies multiple peaks more efficiently in the high quality numerical data. We do not include Gaussian broadening in this figure because it cannot be compared directly with the experimental results.

6.10 Dispersion from $A(k, \omega)$ versus $A_{\text{occ}}(k, \omega)$

The full spectral function is not accessible in the experiment, and existence of a pseudogap must be inferred from the occupied spectral function. Because this function has little weight above the chemical potential, the characteristic two peak pseudogap structure, which we considered in the previous section, is not directly observable. Instead, we must rely on other indicators, such as if the dispersion passes through the Fermi energy, to infer the presence of a pseudogap.

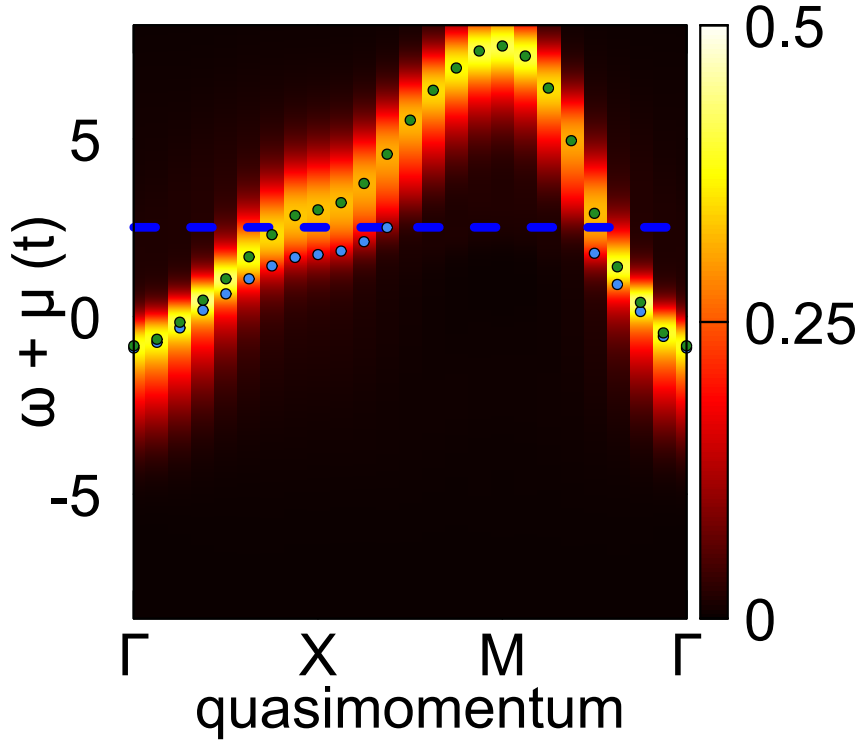


Figure 6.8: **Dispersion from $A(k, \omega)$ versus $A_{\text{occ}}(k, \omega)$.** The full spectral function along high symmetry points in the Brillouin zone, the chemical potential (blue line), and points of peak spectral weight for $A(k, \omega)$ (green points) and $A_{\text{occ}}(k, \omega)$ (blue points). The dispersion inferred from A_{occ} deviates from the true dispersion as the spectral weight approaches the chemical potential.

The dispersion inferred by determining the peak in the occupied spectral function at each momentum is significantly affected by the presence of the Fermi function. Near the chemical potential this causes the dispersion of the occupied spectral function to differ significantly from the real dispersion. This effect is most pronounced outside of

the pseudogap regime because in that case there is significant spectral weight at the chemical potential. To illustrate this effect, we perform the peak-finding procedure described in the text using both the full and occupied spectral functions. The results are displayed in fig. 6.8, showing only peaks with heights greater than 0.02.

6.11 Spectral function versus temperature

We also consider the evolution of the spectral function with increasing temperature at the strongest interaction, $U/t = -7.5$. At the lowest temperature, we find little weight at the Fermi level, fig. 6.9A. As the temperature is increased, a second peak emerges which approximately follows the non-interacting dispersion, fig. 6.9B,C,D. At the same time, the lower peak shifts to more negative energy and the spectral function is gapped at all momenta. At the highest temperatures (fig. 6.9C,D), the Fermi weighting approaches a constant value and occupied spectral function is proportional to the full spectral function, $A_{\text{occ}}(k, \omega) \sim A(k, \omega)/2$. In the limit of strong interactions, we can understand the upper and lower features as signatures of unpaired and paired atoms respectively.

We fit the EDC's to either one Lorentzian, for the lowest temperatures, or two Lorentzians, for the higher temperatures. We find temperature has a weak effect on the peak widths. The HWHM's of the upper and lower peak are $\sim 1.5t$ and $\sim 2.5t$ respectively. The theory results show that the dispersion obtained from the occupied spectral function nearly coincides with that obtained for the true spectral function $T/t \sim 0.5 - 3$. They also show that a pseudogap is present at $U/t = -8$ up to $T/t = 5$ (fig. 6.11). The large value of T^* is characteristic of strong coupling regime, and suggests that pairing near $U/t = -8$ is real-space and two-body in nature.

We plot the EDC's associated with the strong-coupling temperature scan in fig. 6.10. The results for $T/t = 0.55$ (panel A) show good agreement between experi-

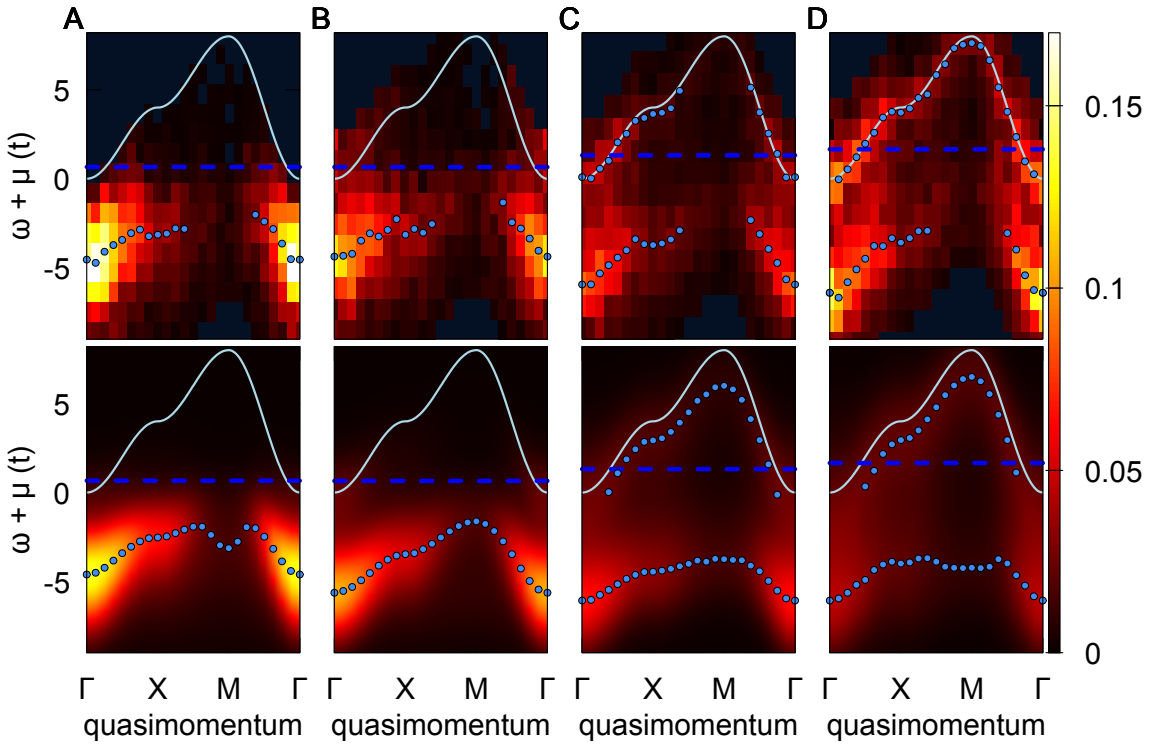


Figure 6.9: Occupied spectral function versus temperature at strong coupling. **A**, Experimental occupied spectral function along directions of high symmetry in the Brillouin zone (top) for $U/t = -7.5(1)$ and $T/t = 0.55(3)$ and DQMC (bottom) for $U/t = -7.5$ and $T/t = 0.55$. Also shown are the location of peaks in the occupied spectral function (light blue circle), the chemical potential (blue line), and the non-interacting dispersion (white line). For this interaction, a pseudogap is present at low temperatures. **B**, As the temperature is increased a small amount of spectral weight appears above the chemical potential. Experiment (top) for $U/t = -7.5$ and $T/t = 0.93(5)$ and DQMC (bottom) for $U/t = -8$ and $T/t = 1.04$. **C**, For even higher temperatures, a second branch of spectral weight emerges above the chemical potential. Experiment (top) for $U/t = -7.5$ and $T/t = 2.5(1)$ and DQMC (bottom) for $U/t = -8$ and $T/t = 2.83$. **D**, Even for the highest temperature considered here, a spectral gap persists at this interaction strength. Experiment (top) for $U/t = -7.5$ and $T/t = 4.5(1)$ and DQMC (bottom) for $U/t = -8$ and $T/t = 5$.

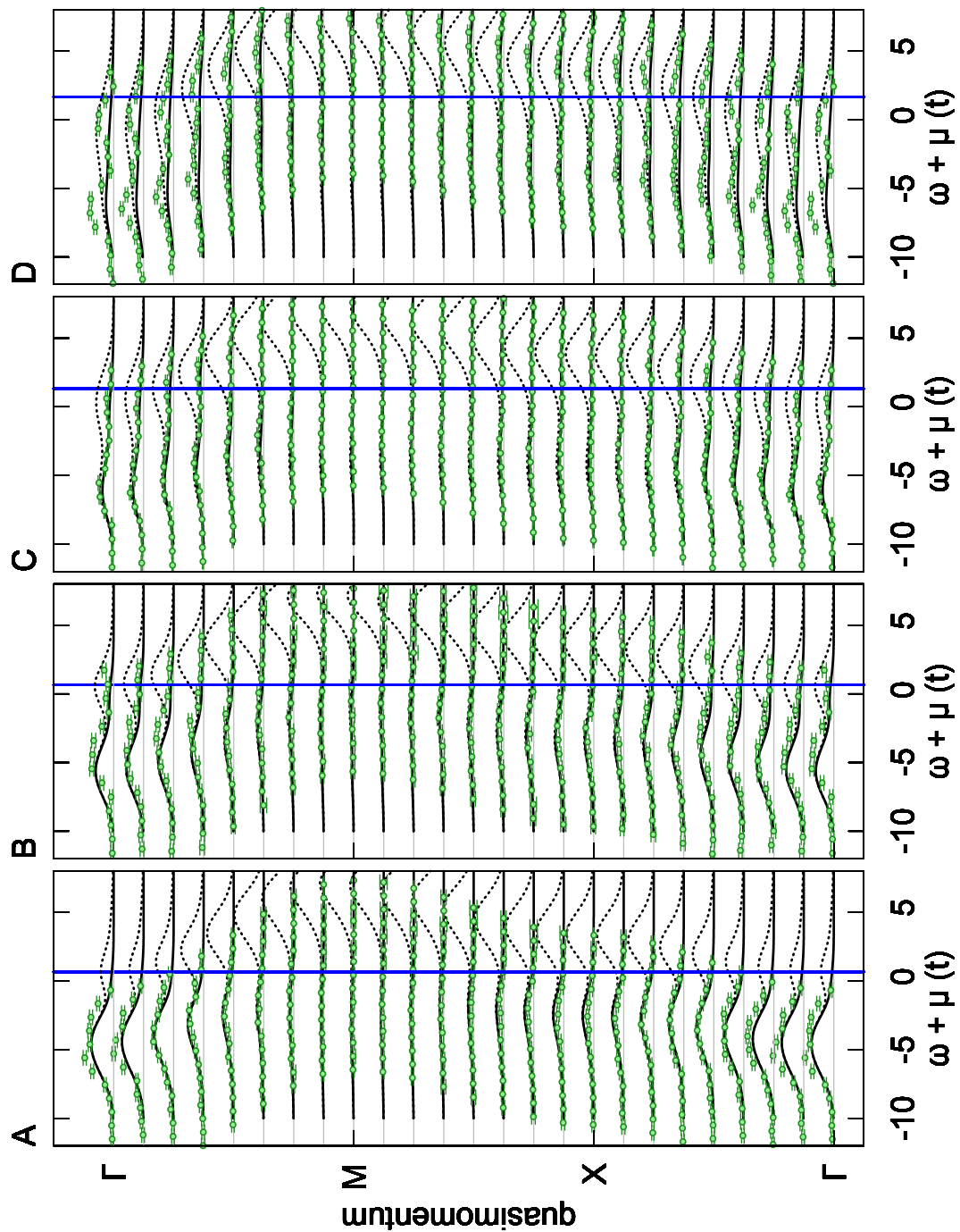


Figure 6.10: EDC's versus temperature. Caption continues on the following page.

Figure 6.10: **A**, EDC's from the experiment occupied spectral function (green points) and theory occupied spectral function (black solid lines) and theory spectral function (black dashed lines) for experiment at $U/t = -7.5(1)$ and $T/t = 0.55(3)$ and theory at $U/t = -7.5$, $T/t = 0.55$. A pseudogap is visible at low temperature and strong interaction. **B**, experiment $U/t = -7.5$ and $U/t = 0.93(5)$ and theory at $U/t = -8$ and $T/t = 1.04$. As the temperature is increased, weight starts to develop above the chemical potential in the occupied spectral function. **C**, experiment $U/t = -7.5$ and $T/t = 2.5(1)$ and theory $U/t = -8$ and $T/t = 2.83$. A second branch in the occupied spectral function emerges above the chemical potential. **D**, experiment $U/t = -7.5$ and $T/t = 4.5(1)$ and theory $U/t = -8$ and $T/t = 5.0$. The two-branch structure of the occupied spectral function persists even at temperature greater than half the band width.

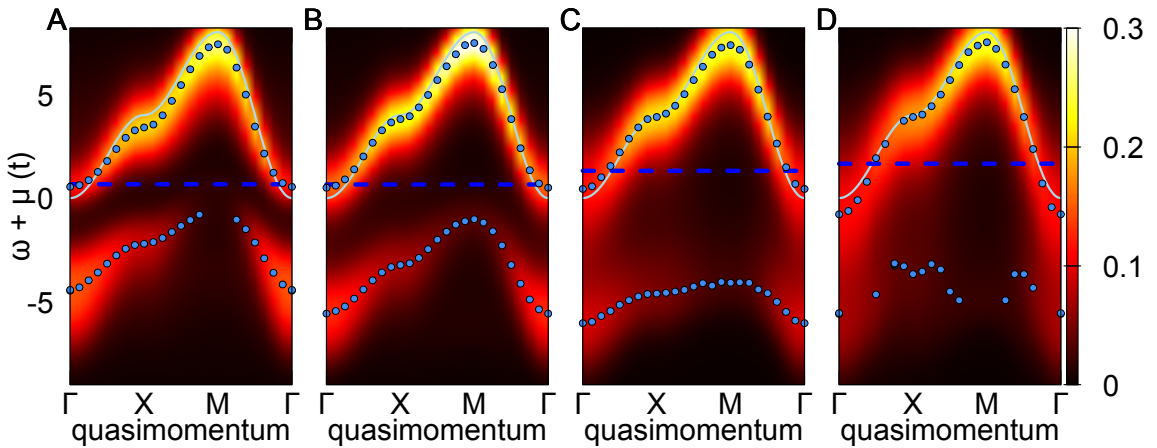


Figure 6.11: **Spectral function versus temperature.** **A**, DQMC trap-average spectral function for $U/t = -7.5$ and $T/t = 0.55$. At low temperature the pseudogap feature is pronounced and appears at all momenta. **B**, $U/t = -8$ and $T/t = 1.04$. The full spectral function is little affected by the increase in temperature from $T/t \sim 0.5$ to 1. **C**, $U/t = -8$ and $T/t = 2.83$. As the temperature approaches $T/t \sim 3$, the weight of the lower branch of the spectral function shrinks, and the apparent band width narrows. **D**, $U/t = -8$ and $T/t = 5.0$. At this temperature the majority of spectral weight is in the upper branch of the spectral function, and the pseudogap has nearly vanished.

ment and theory. The $T/t \sim 1$ results are similar (panel B). There is a small energy shift between experiment and theory, which is likely due to drift in the magnetic field during the course of this experiment. At $T/t \sim 2.5$ (panel C), the theory captures the emergence of a second peak in the spectral function. For $T/t \sim 5$ (panel D), the theory shows much weaker two peak structure than the experiment at low momenta.

The full spectral functions associated with the strong-coupling temperature scan reveal the presence of a pseudogap even at relatively high temperature, fig. 6.11. A pseudogap is visible for $T/t < 3$ (panels A-C), but the case of $T/t \sim 5$ (panel D) is more ambiguous, showing similar structure to $T/t \sim 2.5$, but without a clear gap.

6.12 Outlook

In conclusion, we have developed a technique to measure the single-particle spectral function in Hubbard systems using a quantum gas microscope. In combination with recent transport experiments [82, 85], this extends the toolkit for measuring dynamical properties of these systems, which is so far rather limited compared with the techniques available to study HTSC's and other real materials. Our experiment paves the way for future studies of the single-particle spectral function in the doped repulsive Hubbard model, a quantity which is difficult to calculate using exact theory techniques because of the fermionic sign problem. Such an experiment might elucidate properties of the Hubbard system at high temperature, where dynamical mean-field theory studies have suggested quasiparticles survive into the linear resistivity regime [235, 236] or test recent parton theories which may describe the doped antiferromagnetic regime [268]. At lower temperatures currently beyond the reach of exact theory methods, this technique could be used to study the symmetry of the pseudogap and superconducting states.

Chapter 7

Conclusion

The study of ultracold fermions in dilute atomic gases is, 20 years after the first degenerate atomic Fermi gas, a relatively mature field. Dozens of groups around the world routinely produce and study such systems. In light of this, the fact there are many open questions left to address highlights several key features of the field. First, the tremendous reconfigurability and tunability of these experiments allows new ideas from disparate areas of condensed matter, quantum information, and other fields to be quickly adapted and explored. Some of the most interesting avenues of recent progress, such as many-body localization [269], come from developing new paradigms for many-body physics. Second, many of the interesting, well-known problems related to fermions and many-body physics are very hard.

The extension of quantum gas microscopy to fermionic atoms has allowed several groups, including ours, to make headway on one difficult problem: understanding the low energy physics of the Fermi-Hubbard model. Much of this progress has come from using QGM's to explore new observables or study Hubbard systems in situations that are very far from what is done in condensed matter experiment, for example working with extremely large effective magnetic fields, exploring short-range correlations, or

working in T/t regimes which approach the melting temperatures of real materials. One surprise is that new physics has been observed in all of these regimes.

The tools developed in this thesis can be applied to a number of other important questions. For example, it would be interesting to measure the conductivity versus doping or interaction. The resistivity is expected to cross over from the linear temperature regime studied in chapter 5 to a Fermi liquid regime. Studying resistivity in the attractive Hubbard model may reveal signatures of the pseudogap or superfluid regimes. Similar techniques could be applied to measure other transport coefficients, such as the thermal conductivity and Seebeck coefficient. Comparing charge and thermal transport may shed light on the strange metal regime. On the other hand, the ARPES technique can be improved by working in a box potential to avoid the trap-averaging effects discussed in chapter 6. This technique could also probe the strange metal regime of the repulsive Hubbard model in search of resilient quasiparticles, or to search for the pseudogap regime. It would be interesting to apply several of these techniques to the same system to gain a more complete picture of the physics.

More progress can be made in studying the Fermi-Hubbard model even at present temperature scales by continuing to develop tools to explore new observables. As discussed in this thesis, many dynamical observables cannot be calculated in theory even at current temperatures. Cold atom quantum simulators are thus well positioned to assist in developing theory techniques capable of reliably calculating dynamical quantities at low temperature, which would have broad implications for understanding strongly-correlated systems. Other possible directions include the study of topology and interactions in Fermi-Hubbard systems. Recent experiments [270] suggest it may be possible to subvert heating effects common to various schemes for realizing artificial gauge fields [271, 272, 273]. Achieving the more narrow goal of determining the ground state of the repulsive Fermi-Hubbard model, on the other hand, will require new cooling techniques or other methods for achieving small T/t values.

Appendix A

Properties of ${}^6\text{Li}$

In this appendix we collect useful information about ${}^6\text{Li}$ matrix elements and Feshbach resonances. For more detailed information about the D_1 and D_2 lines of ${}^6\text{Li}$, see the appendix to [274].

A.1 Branching ratios

${}^6\text{Li}$ has 6 hyperfine states in the $2S_{1/2}$ ground state. Because of the weak hyperfine coupling lithium transitions from the low-field regime, where $|F m_f\rangle$ are good quantum numbers, to the high-field regime, where $|I m_i J m_j\rangle$ are good quantum numbers, in the range 50-100 G. In the other alkalis, the high-field regime is only reached well above 500 G. For this reason, nearly cycling transitions exist for all hyperfine ground states of ${}^6\text{Li}$ at modest magnetic bias fields.

To determine how cycling these transitions are, it is useful to consider the matrix elements between the hyperfine levels in the $2S_{1/2}$ ground state and the hyperfine levels in the $2P_{3/2}$ excited state. We display the results in fig. A.1, which shows the branching ratios from the $2P_{3/2}$ state versus magnetic field, revealing the nearly cycling transitions between the $2S_{1/2}$ $|m_j = \pm 1/2, m_i\rangle$ levels and the $2P_{3/2}$ $|m_j = \pm 3/2, m_i\rangle$ levels.

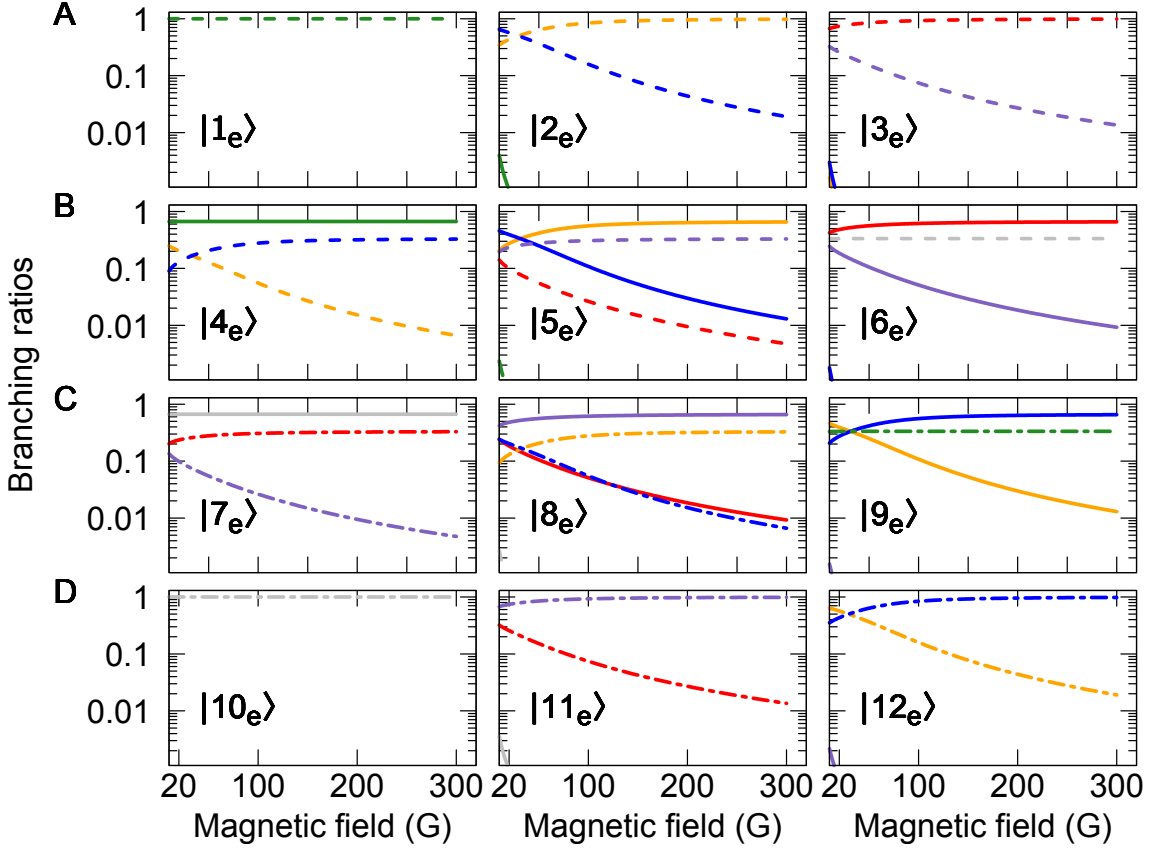


Figure A.1: **Lithium branching ratios from the D_2 line.** Lithium branching ratios from the 12 Zeeman sublevels of the D_2 line, which are denoted $|i_e\rangle$, numbered up from the lowest energy. Branching ratios to the $2S_{1/2}$ Zeeman sublevels, $|1_g\rangle$ (red), $|2_g\rangle$ (orange), $|3_g\rangle$ (green), $|4_g\rangle$ (blue), $|5_g\rangle$ (purple), and $|6_g\rangle$ (gray). π transitions are denoted by solid lines, σ^+ by dashed lines, and σ^- by dotted-dashed lines. **A**, branching ratios from the $|1_e\rangle$ (left), $|2_e\rangle$ (center), and $|3_e\rangle$ (right) states. These become the $m_j = -3/2$ states at high field. Driving the $|3_g\rangle$, $|2_g\rangle$, and $|1_g\rangle$ states with σ^- light gives nearly cycling transitions with these three states at high field. For the $|2_g\rangle$ and $|1_g\rangle$ states, there is finite probability to decay to the $|4_g\rangle$ and $|5_g\rangle$ states respectively. **B**, branching ratios from the $|4_e\rangle$ (left), $|5_e\rangle$ (center), and $|6_e\rangle$ (right) states. These become the $m_j = -1/2$ states at high-field. **C**, branching ratios from the $|7_e\rangle$ (left), $|8_e\rangle$ (center), and $|9_e\rangle$ (right) states. These become the $m_j = 1/2$ states at high-field. **D**, branching ratios from the $|10_e\rangle$ (left), $|11_e\rangle$ (center), and $|12_e\rangle$ (right) states. These becomes the $m_j = 3/2$ states at high-field. Driving the $|6_g\rangle$, $|5_g\rangle$, and $|4_g\rangle$ states with σ^+ light gives nearly cycling transitions with these three states at high field. For the $|5_g\rangle$ and $|4_g\rangle$ states, there is finite probability to decay to the $|1_g\rangle$ and $|2_g\rangle$ states respectively.

To calculate these matrix elements, we first determine the eigenstates of the Breit-Rabi problem for both the ground and excited states. This gives the matrices $B_\alpha = \langle (LSJI)Fm_f | i_\alpha \rangle$ where i is the i th lowest eigenstate and $\alpha = g, e$. Expressing the eigenstates in terms of the hyperfine basis states yields $|i_\alpha\rangle = \sum_{F,m_f} \langle (LSJI)Fm_f | i_\alpha \rangle |(LSJI)Fm_f\rangle$.

Next, we determine the decay rates from $|j_e\rangle$ to $|i_g\rangle$ for photons of angular momentum q which are given by

$$\Gamma_{ij} = \frac{\omega_o^3}{3\pi\epsilon_o\hbar c^3} \sum_q |\langle i_g | \mu(q) | j_e \rangle|^2 \quad (\text{A.1})$$

$$\propto \sum_q \left| \sum_{F,m_f,F',m'_f} \langle i_g | (J)Fm_f \rangle \langle (J)Fm_f | \mu(q) | (J')F'm'_f \rangle \langle (J')F'm'_f | j_e \rangle \right|^2 \quad (\text{A.2})$$

where we have suppressed the L, S, I labels. Using the Wigner-Eckhart theorem we can rewrite the middle term as the product of a combinatorial factor and a reduced matrix element common to the entire transition [274, 275],

$$\begin{aligned} M(q) &= \langle (LSJI)Fm_f | \mu(q) | (L'S'J'I')F'm'_f \rangle \\ &= (-1)^{F'-m'_f+J+I+F+1+L'+S+J+1+L'} \times \\ &\quad \sqrt{(2F+1)(2F'+1)(2J+1)(2J'+1)(2L+1)(2L'+1)} \delta_{II'} \delta_{SS'} \times \\ &\quad \begin{pmatrix} F' & 1 & F \\ -m'_f & q & m_f \end{pmatrix} \begin{Bmatrix} J' & I & F' \\ F & 1 & J \end{Bmatrix} \begin{Bmatrix} L' & S & J' \\ J & 1 & L \end{Bmatrix} \begin{pmatrix} L & 1 & L' \\ 0 & 0 & 0 \end{pmatrix} R_{nl,n'l'}. \quad (\text{A.3}) \end{aligned}$$

In fact, we only need to write the matrix element in terms of the reduced matrix elements $\langle (LS)J \| \mu(1) \| (L'S')J' \rangle$, but there are two common conventions for these which differ by a factor of $\sqrt{2J+1}$. There is no such confusion with the above expression written in terms of the radial matrix elements.

The problem reduces to calculating a product of known matrices

$$\Gamma_{ij} = \frac{\omega_o^3}{3\pi\epsilon_o\hbar c^3} \sum_q |B_g^\dagger M(q) B_e|^2, \quad (\text{A.4})$$

from which we obtain the branching ratios Γ_{ij}/Γ . For a given excited state level $|j_e\rangle$, the branching ratios are the probabilities that this level decays to $|i_g\rangle$. This follows because the decay rate from any of the excited state Zeeman sublevels is Γ , i.e. $\sum_i \Gamma_{ij} = \Gamma$ independent of j_e [274].

A.2 Feshbach resonances

${}^6\text{Li}$ exhibits broad Feshbach resonances [276] among all the states which are high-field seeking in the high-field regime, i.e. the $|12\rangle$, $|13\rangle$ and $|23\rangle$ channels. These Feshbach resonances occur where the least bound vibrational level in the singlet (i.e. the $X^1\Sigma_g^+$) potential, $|\nu = 38\rangle$ in ${}^6\text{Li}$, becomes degenerate with the entrance channel. We number the vibrational states up from the bottom of the potential, with $|\nu = 0\rangle$ being the ground state. No Feshbach resonances can occur in the low field seeking channels, because these have positive magnetic moments, and therefore cannot cross the molecular states. The binding energies and other properties of the molecular states are well known from photoassociation studies [277, 278, 279, 280, 281]. We identify the molecular state using the quantum numbers $S = S_1 + S_2$, $I = I_1 + I_2$ and l the orbital angular momentum. The molecular singlet state has two allowed nuclear spin quantum numbers, $I = I_1 + I_2 = 0, 2$ which give rise to the broad and narrow features in each channel [282]. Various experimental studies have measured the position of these Feshbach resonances or other features in the ${}^6\text{Li}$ scattering lengths [94, 128, 282, 283, 284, 285, 286, 287].

The location of the narrow Feshbach resonance due to the $\nu = 38$, $I = 2$ state of the singlet potential in the $|12\rangle$ channel is well known, but to our knowledge no group

has reported the location of the corresponding feature in the other channels. In the process of working with a $|23\rangle$ mixture in [71] we discovered a loss feature near 714 G which we believe to be the corresponding resonance in this channel.

The least bound state of the triplet (i.e. the $a^3\Sigma_u^+$) potential, $|\nu = 9\rangle$ is predicted to lead to Feshbach resonances among these channels at fields approaching 4000 G and 9000 G [288]. The resonances have not been observed experimentally. The triplet potential also supports a “nearly bound” state which leads to the large negative triplet scattering length in ${}^6\text{Li}$ [280].

We summarize the various known Feshbach resonances of ${}^6\text{Li}$ in table A.1. More detailed information can be found in the given references.

Channel	Type	Symmetry	Field	Reference
$ 12\rangle$	zero-crossing		527.32(25) G	[94]
$ 12\rangle$	resonance	<i>s</i> -wave	543.286(3) G	[94]
$ 12\rangle$	resonance	<i>s</i> -wave	832.18(8) G	[94]
$ 23\rangle$	zero-crossing		589 G	[94]
$ 23\rangle$	resonance?	<i>s</i> -wave?	714 G	unpublished
$ 23\rangle$	resonance	<i>s</i> -wave	809.76(5) G	[94]
$ 13\rangle$	zero-crossing		568 G	[94]
$ 13\rangle$	resonance	<i>s</i> -wave	689.68(8) G	[94]
$ 11\rangle$	resonance	<i>p</i> -wave	160.2(6) G	[282]
$ 12\rangle$	resonance	<i>p</i> -wave	186.2(6) G	[282]
$ 22\rangle$	resonance	<i>p</i> -wave	215.2(6) G	[282]

Table A.1: Known Feshbach resonances and scattering length zero-crossings for ${}^6\text{Li}$.

Appendix B

Optical lattice

In this section we briefly summarize a method for obtaining the tunneling and interaction energies for atoms in an optical lattice with contact interactions from a band structure calculations. Similar calculations are discussed in [30, 289, 290]. We also discuss features of the four-fold symmetric lattice used in the experiment (see section 2.5). More information about this geometry is available in [118, 291].

B.1 Band structure for an arbitrary periodic potential

Suppose we have a periodic potential $V(\mathbf{r})$ with lattice basis vectors \mathbf{a}_i and reciprocal lattice basis vectors \mathbf{b}_j . By definition, the potential satisfies $V(\mathbf{r} + \mathbf{R}) = V(\mathbf{r})$ for any $\mathbf{R} = \sum_i n_i \mathbf{a}_i$ with $n_i \in \mathbb{Z}$ and the reciprocal lattice basis vectors satisfy $\mathbf{a}_i \cdot \mathbf{b}_j = 2\pi\delta_{ij}$.

The periodicity requirement implies that the potential only has non-zero Fourier components at the *reciprocal lattice vectors*, $\mathbf{K} = \sum_j n_j \mathbf{b}_j$. Expanding the potential

in Fourier components yields

$$V(\mathbf{r}) = \sum_{\mathbf{K}} V_{\mathbf{K}} e^{i\mathbf{K}\cdot\mathbf{r}} \quad (\text{B.1})$$

$$V_{\mathbf{K}} = \frac{1}{\mathcal{V}} \int_{\text{unit cell}} d\mathbf{r} V(r) e^{-i\mathbf{K}\cdot\mathbf{r}}, \quad (\text{B.2})$$

where \mathcal{V} is the volume of the unit cell. The integrals are performed over the unit cell because the potential is a periodic function, which avoids any convergence issues for the infinite integral.

The wave function is not periodic, therefore we consider its Fourier transform over the full real line

$$\psi(\mathbf{r}) = \int_{-\infty}^{\infty} d\mathbf{q} \psi_{\mathbf{q}} e^{i\mathbf{q}\cdot\mathbf{r}} \quad (\text{B.3})$$

$$\psi_{\mathbf{q}} = \frac{1}{2\pi} \int_{-\infty}^{\infty} d\mathbf{r} \psi(\mathbf{r}) e^{-i\mathbf{q}\cdot\mathbf{r}} \quad (\text{B.4})$$

Suppose that our space is periodic after N_i lattice sites in each direction respectively. The wave functions must also be periodic,

$$\psi_{\mathbf{q}}(\mathbf{r}) = \psi_{\mathbf{q}} \left(\mathbf{r} + \sum_i N_i \mathbf{a}_i \right) \quad (\text{B.5})$$

$$1 = \exp \left(i \sum_i N_i \mathbf{q} \cdot \mathbf{a}_i \right), \quad (\text{B.6})$$

which requires $N_i \mathbf{q} \cdot \mathbf{a}_i = 2\pi n$ for some integer n . Comparing with the orthogonality relationship for the reciprocal lattice vectors, the allowed spatial frequencies are

$$\mathbf{q} = \sum_i \frac{n_i}{N_i} \mathbf{b}_i, \quad n_i \in \{0, \dots, N_i\}. \quad (\text{B.7})$$

Writing the single-particle Schrodinger equation in Fourier space after accounting for the structure imposed on V and ψ gives

$$\frac{\hbar^2 \mathbf{q}^2}{2m} \psi_{\mathbf{q}} + \frac{1}{a^2} \sum_{\mathbf{K}} V_{\mathbf{K}} \psi_{\mathbf{q}-\mathbf{K}} = E \psi_{\mathbf{q}}. \quad (\text{B.8})$$

Two basis states are only coupled if the potential has a Fourier component at their momentum difference — a manifestation of momentum conservation. Due to the periodicity of the potential, only states with momenta that differ by a reciprocal lattice vector are coupled.

Now, we write \mathbf{q} in terms of its corresponding quasimomentum in the Brillouin zone, $\mathbf{q} = \mathbf{q}' - \mathbf{Q}$, where \mathbf{Q} is a particular reciprocal lattice vector. The previous equation becomes

$$\begin{aligned} \frac{\hbar^2(\mathbf{q}' - \mathbf{Q})^2}{2m} \psi_{\mathbf{q}'-\mathbf{Q}} + \frac{1}{a^2} \sum_{\mathbf{K}} V_{\mathbf{K}} \psi_{\mathbf{q}'-\mathbf{Q}-\mathbf{K}} &= E \psi_{\mathbf{q}'-\mathbf{Q}} \\ \frac{\hbar^2(\mathbf{q}' - \mathbf{Q})^2}{2m} \psi_{\mathbf{q}'-\mathbf{Q}} + \frac{1}{a^2} \sum_{\mathbf{K}'} V_{\mathbf{K}'-\mathbf{Q}} \psi_{\mathbf{q}'-\mathbf{K}'} &= E \psi_{\mathbf{q}'-\mathbf{Q}}, \end{aligned}$$

where we took $\mathbf{K}' = \mathbf{K} + \mathbf{Q}$ in the second line.

We cast this as a matrix equation by taking the \mathbf{Q} 's as indices for the vectors $\psi_{\mathbf{Q}}^{\mathbf{q}} = \psi_{\mathbf{q}-\mathbf{Q}}$ and defining a potential matrix $V_{\mathbf{K}\mathbf{Q}} = V_{\mathbf{K}-\mathbf{Q}}$. The fact that only momenta different by a reciprocal lattice vector are coupled implies that this problem is decoupled for the different \mathbf{q} 's in the Brillouin zone. There are $N_{\text{sites}} = \prod N_i$ eigenvalue problems

$$\sum_{\mathbf{K}} \left(\frac{\hbar^2}{2m} (\mathbf{q} - \mathbf{Q})^2 \delta_{\mathbf{K}\mathbf{Q}} + V_{\mathbf{K}\mathbf{Q}} \right) \psi_{\mathbf{K}}^{\mathbf{q}} = E \psi_{\mathbf{Q}}^{\mathbf{q}}, \quad (\text{B.9})$$

which yield the Bloch eigenvectors $\psi_{n\mathbf{Q}}^{\mathbf{q}}$ and the band energies $E_n(\mathbf{q})$. Solving this equation on a computer requires truncating the number of reciprocal lattice vectors

included in the computation. For a 2D or 3D lattice it also requires picking some ordering for the reciprocal lattice vectors $\mathbf{Q} = \sum_i n_i \mathbf{b}_i$, i.e. mapping the 2- or 3-index tuples given by the n_i to a single index.

The choice of origin for our potential $V(\mathbf{r})$ is still a degree of freedom in the problem, and it has an effect on the Bloch states. Suppose we shift our coordinates to be centered at position \mathbf{r}_o (labeled in the original coordinate system), i.e. we take $\tilde{V}(\mathbf{r}) = V(\mathbf{r} - \mathbf{r}_o)$. The Fourier components of the two potentials are identical up to a phase factor, $\tilde{V}_K = e^{-i\mathbf{K}\cdot\mathbf{r}_o}$. Writing the analog of eq. B.9 for \tilde{V} and collecting terms we find,

$$\sum_{\mathbf{K}} \left(\frac{\hbar^2}{2m} (\mathbf{q} - \mathbf{Q})^2 \delta_{\mathbf{KQ}} + V_{\mathbf{KQ}} \right) e^{-i\mathbf{K}\cdot\mathbf{r}_o} \tilde{\psi}_{\mathbf{K}}^{\mathbf{q}} = E e^{-i\mathbf{Q}\cdot\mathbf{r}_o} \tilde{\psi}_{\mathbf{Q}}^{\mathbf{q}}, \quad (\text{B.10})$$

which shows that the Bloch vectors in the new coordinates are related to those in the old through

$$\tilde{\psi}_{\mathbf{Q}}^{\mathbf{q}} = e^{i\mathbf{Q}\cdot\mathbf{r}_o} \psi_{\mathbf{Q}}^{\mathbf{q}}. \quad (\text{B.11})$$

B.2 Wannier Functions

Given a set of Bloch wave functions, we define the *Wannier function* on site $\mathbf{R} = \sum_i n_i \mathbf{a}_i$

$$w_{\mathbf{R}}(\mathbf{r}) = \sum_{\mathbf{q}} e^{-i\mathbf{q}\cdot\mathbf{R}} \psi_{\mathbf{q}}(\mathbf{r}). \quad (\text{B.12})$$

For some choice of the phases of the $\psi_{\mathbf{q}}$, this gives the maximally localized wave function in the ground band of the lattice.

Wannier functions centered at different sites have the same shape. Since the Bloch wave functions are the product of an exponential factor and a periodic function,

$\psi_{\mathbf{q}}(\mathbf{r}) = e^{i\mathbf{q}\cdot\mathbf{r}}u_{\mathbf{q}}(\mathbf{r})$, we find

$$w_{\mathbf{R}}(\mathbf{r}) = \sum_{\mathbf{q}} e^{-i\mathbf{q}\cdot\mathbf{R}} e^{i\mathbf{q}\cdot\mathbf{r}} u_{\mathbf{q}}(\mathbf{r}) \quad (\text{B.13})$$

$$= w_{\mathbf{R}+\mathbf{R}'}(\mathbf{r} + \mathbf{R}'), \quad (\text{B.14})$$

where we multiply by $e^{i\mathbf{q}\cdot\mathbf{R}'}e^{-i\mathbf{q}\cdot\mathbf{R}'} = 1$ and use the periodicity of $u_{\mathbf{q}}$ to obtain the second line.

We can also write the Wannier function in terms of the Bloch wave functions in momentum space, which gives a recipe for calculating Wannier functions using the results of eq. B.9,

$$\psi_{\mathbf{q}}(\mathbf{r}) = \sum_{\mathbf{Q}} \psi_{\mathbf{Q}}^{\mathbf{q}} e^{-i(\mathbf{q}-\mathbf{Q})\cdot\mathbf{r}} \quad (\text{B.15})$$

$$w_{\mathbf{R}}(\mathbf{r}) = \sum_{\mathbf{Q}, \mathbf{q}} \psi_{\mathbf{Q}}^{\mathbf{q}} e^{-i(\mathbf{q}-\mathbf{Q})\cdot\mathbf{r}} e^{-i\mathbf{q}\cdot\mathbf{R}}. \quad (\text{B.16})$$

We can ask what the relationship between this Wannier function is and a Wannier function defined with respect to a shifted coordinate system. Inserting eq. B.11 in the above,

$$\begin{aligned} \tilde{w}_{\mathbf{R}}(\mathbf{r}) &= \sum_{\mathbf{Q}, \mathbf{q}} \psi_{\mathbf{q}}(\mathbf{Q}) e^{i\mathbf{Q}\cdot\mathbf{r}_o} e^{-i(\mathbf{q}-\mathbf{Q})\cdot\mathbf{r}} e^{-i\mathbf{q}\cdot\mathbf{R}} \\ \tilde{w}_{\mathbf{R}+\mathbf{r}_o}(\mathbf{r} - \mathbf{r}_o) &= w_{\mathbf{R}}(\mathbf{r}) \end{aligned} \quad (\text{B.17})$$

The definition of the Wannier function (eq. B.12) is non-unique up to a choice of phase factors for the Bloch wave functions. The maximally localized function is obtained when the phases of the $\psi_{\mathbf{q}}(r)$ vary smoothly with \mathbf{q} [292]. But if we have obtained Bloch wave functions from a computer simulation, this is not guaranteed to be the case. Before computing the Wannier function, we must fix the phases of the Bloch wave functions.

If Bloch functions are obtained from eq. B.9, the $\psi_{\mathbf{Q}}^{\mathbf{q}}$ will be real. In this case, fixing the phase of each wave functions amounts to choosing the sign of each Bloch function. We choose an ordering for the \mathbf{q} vectors, and take the overlap of the two adjacent wave functions

$$\sum_{\mathbf{Q}} \psi_{\mathbf{q}_i}(\mathbf{Q}) \psi_{\mathbf{q}_{i+1}}(\mathbf{Q}), \quad (\text{B.18})$$

and check whether it is less than or greater than zero. If it is less than zero, we take $\psi_{\mathbf{q}_{i+1}} \rightarrow -\psi_{\mathbf{q}_{i+1}}$. In 1D, the \mathbf{q} vectors are naturally ordered. In 2D, we pick some convenient ordering. On a square lattice we might begin with $\mathbf{q} = (-\pi/2, \pi/2)$ and fix the phases along the line $\mathbf{q} = (q_x, \pi/2)$ using the same prescription as in 1D. Then we can fix phases along each of the lines $\mathbf{q} = (q_x, q_y)$.

Note that this overlap is not the inner product of two wave functions, which is given by

$$\langle \phi | \eta \rangle = \int_{-\infty}^{\infty} d\mathbf{k} \phi^*(\mathbf{k}) \eta(\mathbf{k}) \quad (\text{B.19})$$

$$= \sum_{\mathbf{Q}} \int_{\text{BZ}} d\mathbf{q} \phi^*(\mathbf{q} - \mathbf{Q}) \eta(\mathbf{q} - \mathbf{Q}), \quad (\text{B.20})$$

where $\phi(\mathbf{q} - \mathbf{Q}) = \psi_{\mathbf{q}}(\mathbf{Q}) \delta(\mathbf{q} - \mathbf{q}_1)$ and $\eta(\mathbf{q} - \mathbf{Q}) = \psi_{\mathbf{q}}(\mathbf{Q}) \delta(\mathbf{q} - \mathbf{q}_2)$ are Bloch functions. Two Bloch functions in the same band are orthogonal because they are never non-zero at the same $\mathbf{k} = \mathbf{q} - \mathbf{Q}$.

B.3 Determining tight-binding parameters

The Wannier states are a natural basis for the Hamiltonian. If we are working at low energies where only the lowest band is relevant and we define the creation operators

$c_{i\sigma}^\dagger$ as creating a particle in state $w_{\mathbf{R}_i}$, then the free particle Hamiltonian is

$$\mathcal{H} = - \sum_{i,j,\sigma} t_{ij} \left(c_{i\sigma}^\dagger c_{j\sigma} + \text{h.c.} \right) \quad (\text{B.21})$$

$$t_{ij} = - \int_{-\infty}^{\infty} d\mathbf{r} w_{\mathbf{R}_i}(\mathbf{r}) \left(-\frac{\hbar^2}{2m} \nabla^2 + V(\mathbf{r}) \right) w_{\mathbf{R}_j}(\mathbf{r}). \quad (\text{B.22})$$

For a sufficiently deep lattice, long-distance tunneling terms are suppressed compared with nearest-neighbor tunneling. In that case, we say we are in the *tight-binding* limit.

In the tight-binding limit the tunneling integrals can be determined directly from the band structure, avoiding any calculation of the Wannier functions. Here we demonstrate this for a two-dimensional square lattice with nearest-neighbor tunneling t_x and t_y , and diagonal neighbor tunneling t_d . Then we have the following tight-binding model

$$\begin{aligned} \mathcal{H} = & - \sum_{i,j} t_x c_{(i_x, j_x)}^\dagger c_{(i_x+1, j_x)} + t_y c_{(i_x, j_x)}^\dagger c_{(i_x, j_x+1)} \\ & + t_d c_{(i_x, j_x)}^\dagger c_{(i_x+1, j_x+1)} + t_d c_{(i_x, j_x)}^\dagger c_{(i_x-1, j_x+1)} \end{aligned} \quad (\text{B.23})$$

$$= \sum_{\mathbf{k}} \epsilon_{\mathbf{k}} n_{\mathbf{k}} \quad (\text{B.24})$$

$$\epsilon_{\mathbf{k}} = -2 [t_x \cos(k_x) + t_y \cos(k_y) + t_d \cos(k_x + k_y) + t_d \cos(k_x - k_y)]. \quad (\text{B.25})$$

Evaluating the dispersion at several points in the Brillouin zone and combining these judiciously yields the tunneling parameters,

$$t_x = \frac{1}{8} \{ [\epsilon(\pi, 0) - \epsilon(0, 0)] + [\epsilon(\pi, \pi) - \epsilon(0, \pi)] \} \quad (\text{B.26})$$

$$t_y = \frac{1}{8} \{ [\epsilon(0, \pi) - \epsilon(0, 0)] + [\epsilon(\pi, \pi) - \epsilon(\pi, 0)] \} \quad (\text{B.27})$$

$$t_{\text{avg}} = \frac{1}{8} [\epsilon(\pi, \pi) - \epsilon(0, 0)] \quad (\text{B.28})$$

$$t_d = \frac{1}{16} \{ \epsilon(0, \pi) + \epsilon(\pi, 0) - \epsilon(0, 0) - \epsilon(\pi, \pi) \}. \quad (\text{B.29})$$

For the first two expressions, either of the terms in square brackets would give $t_{x,y}$ in the absence of diagonal tunneling.

B.4 Interactions in the tight-binding model

So far, we have considered the problem of non-interacting particles in a periodic potential. Now, consider what happens if we include two species of atoms interacting with contact interactions given by the pseudopotential $\frac{4\pi a_s \hbar^2}{m} \delta(\mathbf{r})$. As usual we label the species by their spins $\sigma = \uparrow, \downarrow$. If the interaction is sufficiently weak that it does not modify the shape of the Wannier function, the on-site interaction is

$$\mathcal{H}_U = U \sum_i n_{i\uparrow} n_{i\downarrow} \quad (\text{B.30})$$

$$U = \frac{4\pi a_s \hbar^2}{m} \int d\mathbf{r} |w_0(\mathbf{r})|^4 \quad (\text{B.31})$$

$$U = \frac{4\pi a_s \hbar^2}{m} \sqrt{\frac{m\omega_z}{h}} \int_{\mathbb{R}^2} d\mathbf{r} |w_0^{2D}(\mathbf{r})|^4 \quad (\text{quasi-2D}). \quad (\text{B.32})$$

Stronger interactions can distort the Wannier function by mixing higher bands into the problem. To reach this regime, the interaction energy must be a substantial fraction of the band-gap. Multi-band effects can be estimated using various techniques [192, 293].

To arrive at the quasi-2D expressions, we consider a situation where the z -direction is much more tightly-confining than the other two. The z -direction is assumed to have a trapping frequency ω_z which is much larger than other energy scales in the problem. We estimate the wave function in the z -direction by the ground state harmonic oscillator wave function, and find

$$w^{3D}(\mathbf{r}) = \left(\frac{m\omega}{\pi\hbar} \right)^{1/4} e^{-m\omega_z z^2/2\hbar} w^{2D}(\mathbf{x}, \mathbf{y}) \quad (\text{B.33})$$

$$\int_{\mathbb{R}^3} d\mathbf{r} |w^{3D}(\mathbf{r})|^4 = \sqrt{\frac{m\omega_z}{h}} \int_{\mathbb{R}^2} d\mathbf{r} |w^{2D}(\mathbf{r})|^4 \quad (\text{B.34})$$

where $w^{2D}(\mathbf{r})$ and $w^{3D}(\mathbf{r})$ are the 3D and 2D Wannier functions respectively.

B.5 Four-fold interfering lattice

Here we consider the same lattice geometry we discuss in detail in section 2.5, but now allowing for an arbitrary linear polarization characterized by α , the angle the polarization vector makes with the z -axis. The lattice potential is a sum of Fourier components as in eq. B.1. We summarize the Fourier components in table B.1 in terms of the lattice depth, V_o , the attenuation factor of the retro-reflected electric fields, r , and the angle the beams make with the x -axis, $\theta/2$. For $\alpha = 0$ these reduce to the potential given by eq. 2.27 and table 2.2. We write the total depth in terms of the intensity of the first incident beam, I , and atomic polarizability α ,

$$V_o = \left(\frac{1}{2\epsilon c} |\alpha| I \right) 4 \left[(1 + r^2) (\cos^2(\alpha) + \cos(\theta) \sin^2(\alpha)) + 2r \right]. \quad (\text{B.35})$$

K_x	K_y	$V_{\mathbf{K}}$
0	0	$-V_o \frac{2(1+r^2)}{4[(1+r^2)(\cos^2(\alpha)+\cos(\theta)\sin^2(\alpha))+2r]}$
$\pm 2k \sin(\theta/2)$	0	$-V_o \frac{2r(\cos^2(\alpha)+\cos(\theta)\sin^2(\alpha))}{4[(1+r^2)(\cos^2(\alpha)+\cos(\theta)\sin^2(\alpha))+2r]}$
0	$\pm 2k \cos(\theta/2)$	$-V_o \frac{(1+r^2)(\cos^2(\alpha)+\cos(\theta)\sin^2(\alpha))}{4[(1+r^2)(\cos^2(\alpha)+\cos(\theta)\sin^2(\alpha))+2r]}$
$\pm 2k \sin(\theta/2)$	$\pm 2k \cos(\theta/2)$	$-V_o \frac{r}{4[(1+r^2)(\cos^2(\alpha)+\cos(\theta)\sin^2(\alpha))+2r]}$
$\pm 2k \sin(\theta/2)$	$\mp 2k \cos(\theta/2)$	$-V_o \frac{r}{4[(1+r^2)(\cos^2(\alpha)+\cos(\theta)\sin^2(\alpha))+2r]}$

Table B.1: Fourier components of the four-fold interfering lattice for arbitrary polarization angle α .

Appendix C

Static spin structure factor

In this appendix we present unpublished measurements of the static spin structure factor for a repulsive Hubbard system at a range of dopings and compare these measurements with DQMC results. Similar results were obtained in [55, 73].

The static spin structure factor is the spatial Fourier transform of the spin correlation functions considered previously,

$$SF(q) = \sum_d C_{\text{spin}}^z(d) e^{iq \cdot d}. \quad (\text{C.1})$$

Near half-filling, the spin structure factor exhibits a peak at $q = (\pi, \pi)$ due to the presence of antiferromagnetic spin correlations.

The static structure factor for various cuprate materials has been measured using neutron scattering, which reveals the emergence of antiferromagnetic order incommensurate with the lattice spacing at finite doping [294, 295, 296]. Similar behavior might be expected at small dopings in a 2D Hubbard system. Such incommensurate order has been observed previously in 1D systems [77].

We observe that static structure factor is strongly peaked at $k = (\pi, \pi)$ at half-filling, interaction $U/t = 8$, and temperature $T/t = 0.4$ (fig. C.1). We find good agreement between experiment and DQMC results. As the doping is increased, (fig. C.2),

the sharp peak in the structure factor broadens. We do not find any evidence for a sharp peak away from the (π, π) momentum.

We also consider the static structure factor at the weaker interaction $U/t = 4$ (fig. C.3). We observe weaker antiferromagnetic correlations at this interaction. As in the $U/t = 8$ data, the antiferromagnetic peak in the structure factor disappears quickly upon doping (fig. C.3).

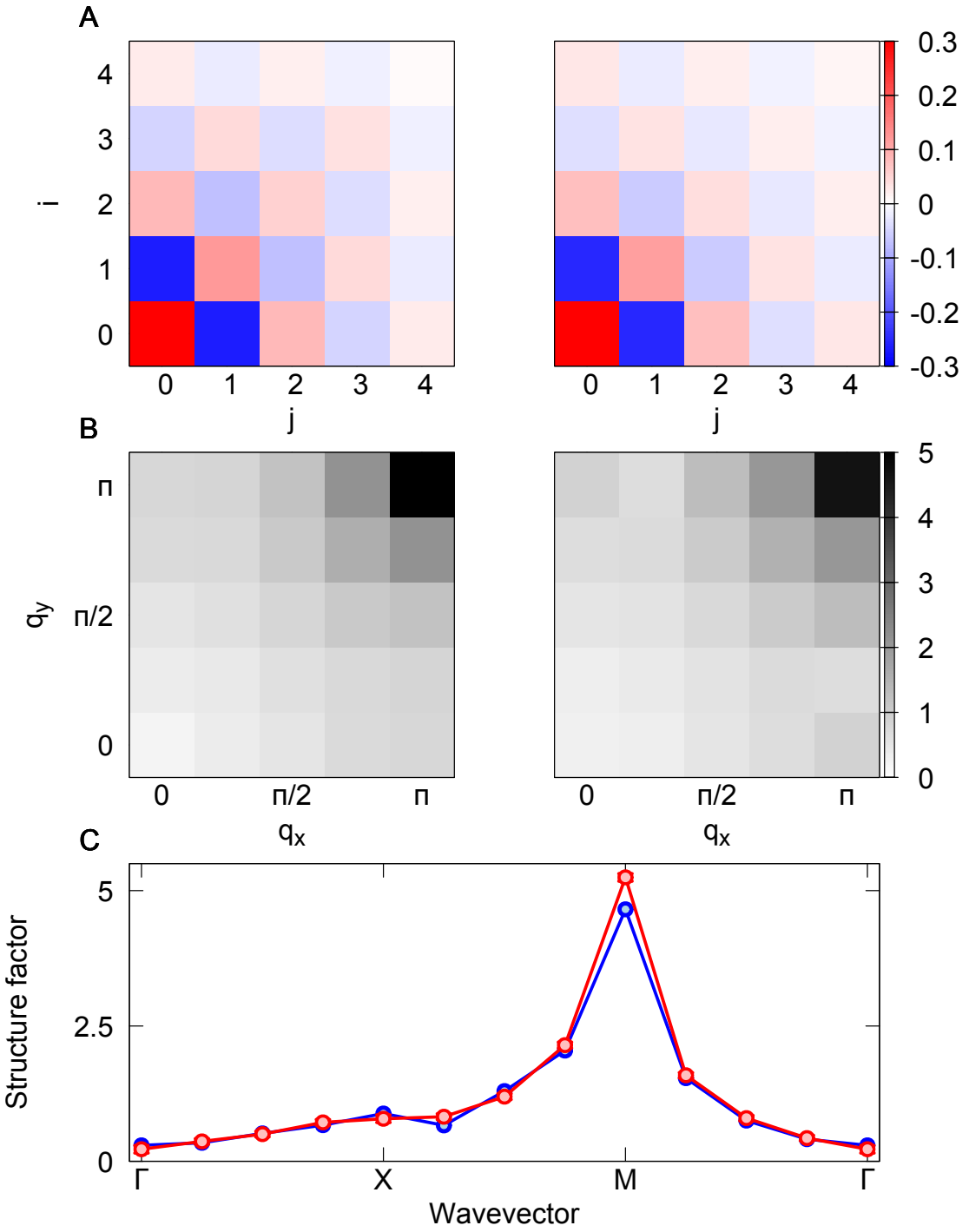


Figure C.1: **Static spin structure factor near half-filling, $U/t = 8$.** **A**, Experiment (left) and DQMC (right) spin correlations versus distance, $C_{\text{spin}}^z(j, i)$. DQMC parameters are $U/t = 8$, $T/t = 0.3$, and $n = 1$. **B**, Experiment (left) and DQMC (right) static spin structure factor versus distance, $SF(q_x, q_y)$. **C**, Experiment (red) and DQMC (blue) static spin structure factor along the high symmetry $\Gamma - X - M - \Gamma$ line. Error bars standard error of the mean.

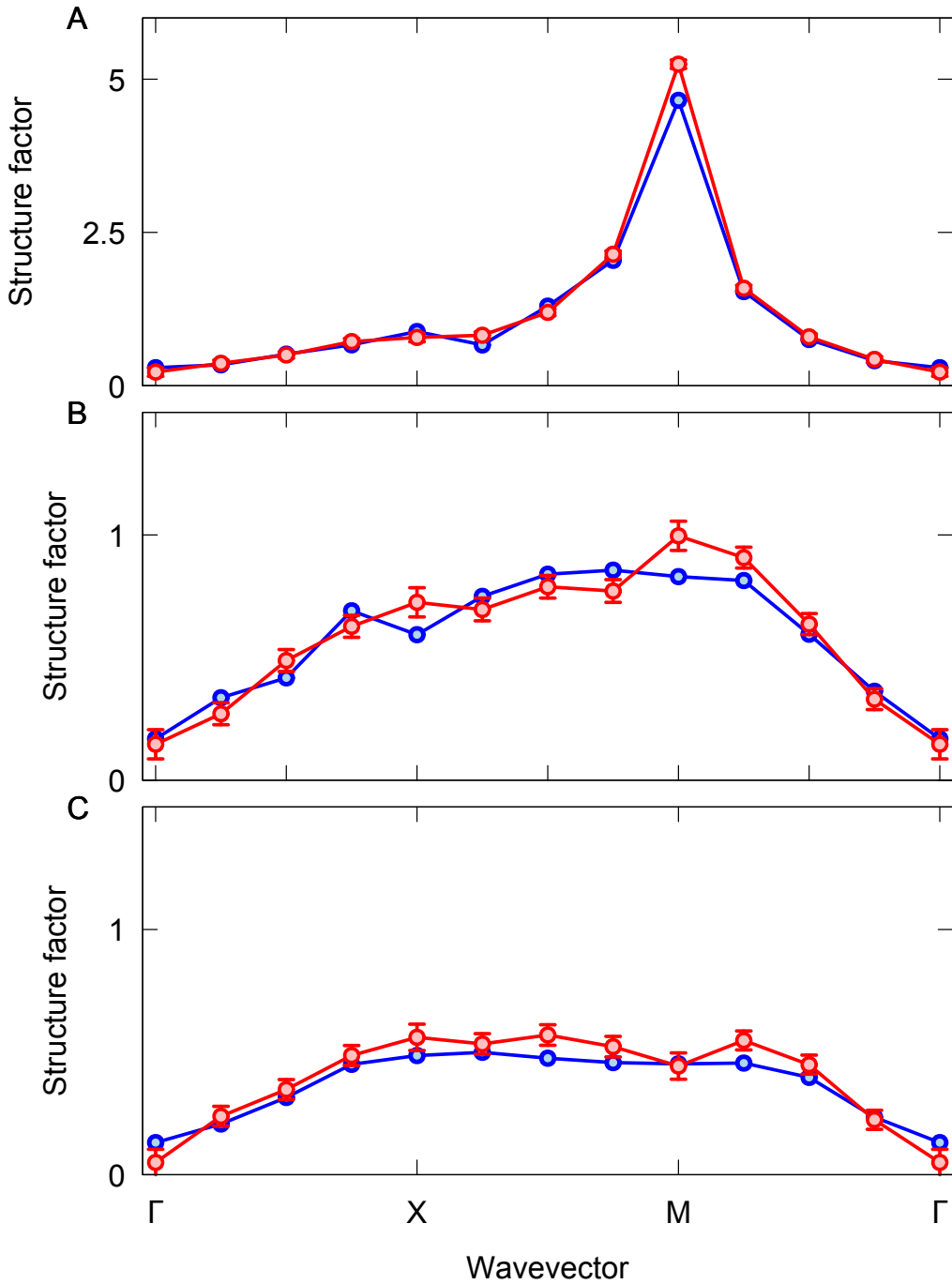


Figure C.2: **Static spin structure factor versus doping at $U/t = 8$ and $T/t = 0.3$.** **A**, Static spin structure factor along the high symmetry $\Gamma - X - M - \Gamma$ line for doping $n = 1.00$. A sharp peak appears at the antiferromagnetic wave vector, $M = (\pi, \pi)$ in both the experiment (red) and DQMC (blue). **B**, As the doping is increased to $n = 0.66$ the sharp peak vanishes and the structure factor exhibits a broad plateau along the $X - M$ line. **C**, At quarter filling, $n = 0.50$, the strength of the broad plateau also diminishes. Error bars standard error of the mean.

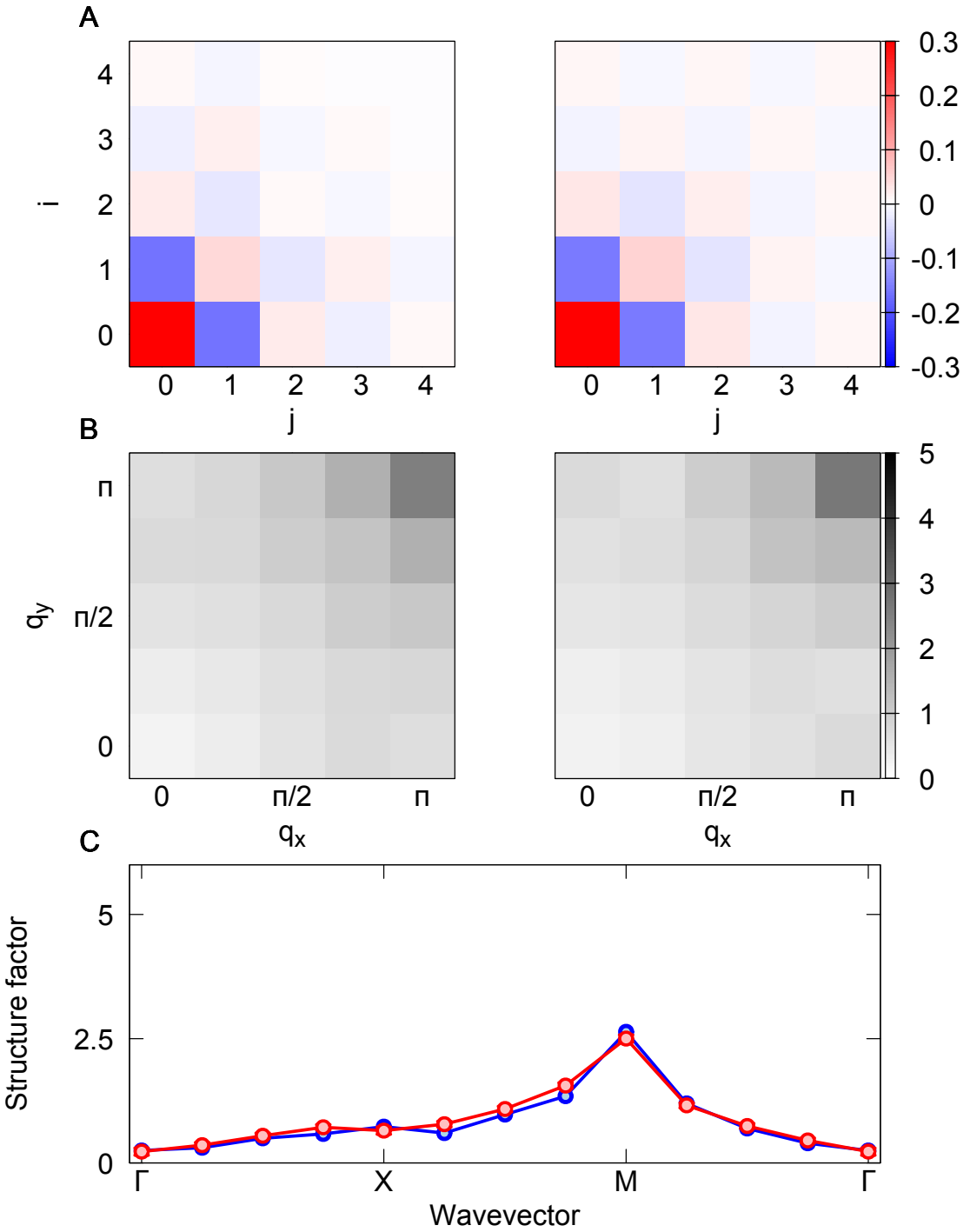


Figure C.3: **Static spin structure factor near half-filling, $U/t = 4$.** **A**, Experiment (left) and DQMC (right) spin correlations versus distance, $C_{\text{spin}}^z(j, i)$. DQMC parameters are $U/t = 4$, $T/t = 0.3$, and $n = 1$. **B**, Experiment (left) and DQMC (right) static spin structure factor versus distance, $SF(q_x, q_y)$. **C**, Experiment (red) and DQMC (blue) static spin structure factor along the high symmetry $\Gamma - X - M - \Gamma$ line. Error bars standard error of the mean.

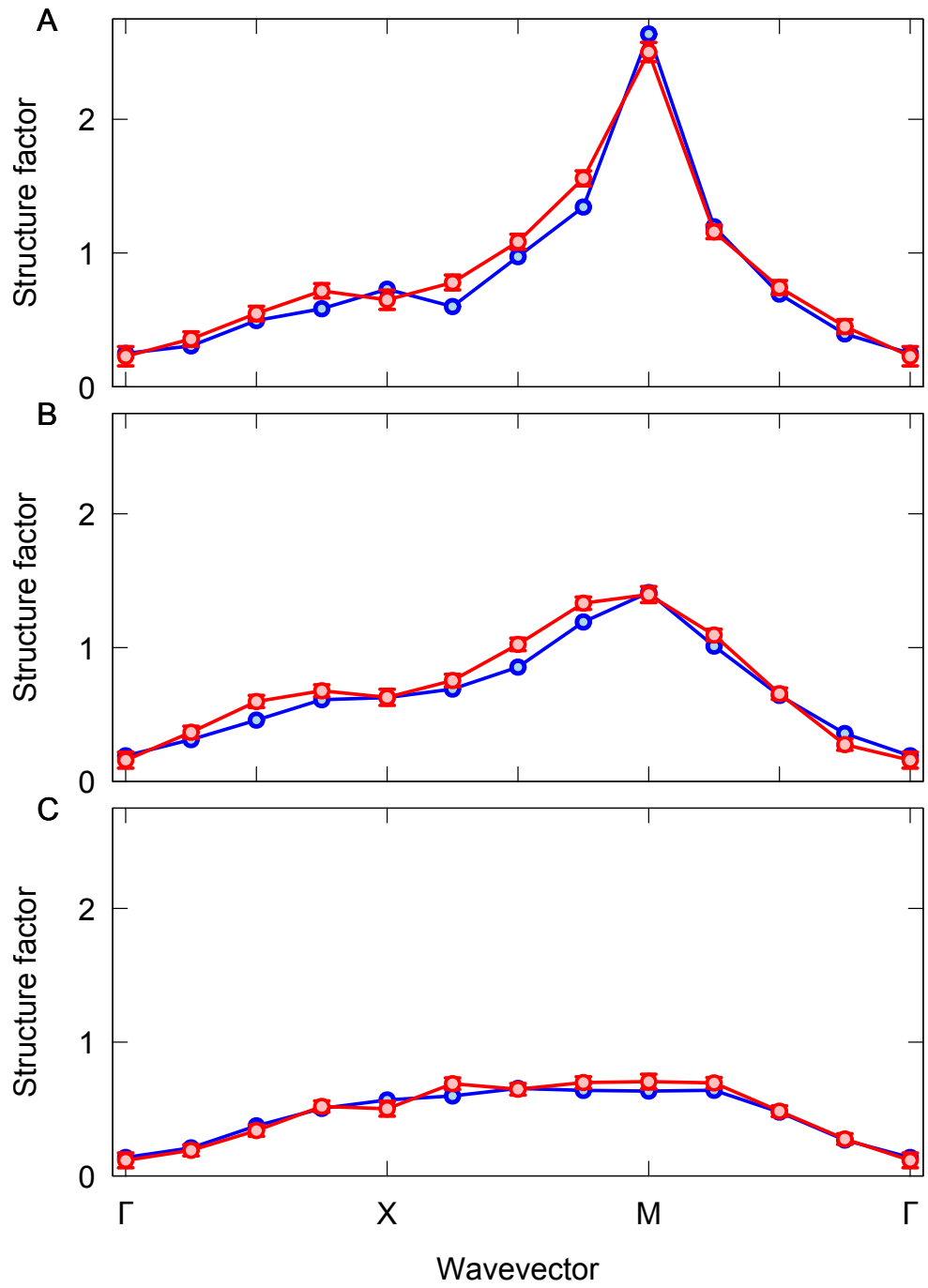


Figure C.4: **Static spin structure factor versus doping at $U/t = 4$ and $T/t = 0.3$.** **A**, $\Gamma - X - M - \Gamma$ line for doping $n = 1.00$. A sharp peak appears at the antiferromagnetic wave vector, $M = (\pi, \pi)$ in both the experiment (red) and DQMC (blue). The peak is weaker than at $U/t = 8$, as the antiferromagnetic correlations are less strong. **B**, As the doping increases to $n = 0.84$ the peak broadens and diminishes in height. **C**, At large doping, $n = 0.55$, a plateau develops along the $X - M$ line. Error bars standard error of the mean.

Bibliography

- [1] R. P. Feynman. **Simulating physics with computers**. *Int. J. Theor. Phys.* **21**, 6-7, 467–488 (1982).
- [2] J. Bardeen, L. N. Cooper, and J. R. Schrieffer. **Microscopic theory of superconductivity**. *Phys. Rev.* **106**, 162–164 (1957).
- [3] H. K. Onnes. **Communication from the Physical Laboratory of the University of Leiden** **122b** (1911).
- [4] W. L. McMillan. **Transition temperature of strong-coupled superconductors**. *Phys. Rev.* **167**, 331–344 (1968).
- [5] J. G. Bednorz and K. A. Müller. **Possible high T_c superconductivity in the Ba-La-Cu-O system**. *Z. Phys. B* **64**, 2, 189–193 (1986).
- [6] M. K. Wu, J. R. Ashburn, C. J. Torng, P. H. Hor, R. L. Meng, L. Gao, Z. J. Huang, Y. Q. Wang, and C. W. Chu. **Superconductivity at 93 K in a new mixed-phase Y-Ba-Cu-O compound system at ambient pressure**. *Phys. Rev. Lett.* **58**, 908–910 (1987).
- [7] M. Imada, A. Fujimori, and Y. Tokura. **Metal-insulator transitions**. *Rev. Mod. Phys.* **70**, 1039–1263 (1998).
- [8] J. Orenstein and A. J. Millis. **Advances in the physics of high-temperature superconductivity**. *Science* **288**, 5465, 468–474 (2000).
- [9] P. A. Lee, N. Nagaosa, and X.-G. Wen. **Doping a Mott insulator: Physics of high-temperature superconductivity**. *Rev. Mod. Phys.* **78**, 1, 17–85 (2006).
- [10] P. W. Anderson. **The resonating valence bond state in La_2CuO_4 and superconductivity**. *Science* **235**, 4793, 1196–1198 (1987).
- [11] J. Hubbard. **Electron correlations in narrow energy bands**. *Proc. Roy. Soc. A* **276**, 1365, 238–257 (1963).
- [12] J. Kanamori. **Electron correlation and ferromagnetism of transition metals**. *Prog. Theor. Phys.* **30**, 3, 275–289 (1963).
- [13] M. C. Gutzwiller. **Effect of correlation on the ferromagnetism of transition metals**. *Phys. Rev. Lett.* **10**, 159–162 (1963).

- [14] J. Hubbard. Electron correlations in narrow energy bands. II. The degenerate band case. *Proc. Royal Soc. A* **277**, 1369, 237–259 (1964).
- [15] C. Varma, S. Schmitt-Rink, and E. Abrahams. Charge transfer excitations and superconductivity in “ionic” metals. *Solid State Commun.* **62**, 10, 681–685 (1987).
- [16] V. J. Emery. Theory of high- T_c superconductivity in oxides. *Phys. Rev. Lett.* **58**, 2794–2797 (1987).
- [17] V. J. Emery and G. Reiter. Mechanism for high-temperature superconductivity. *Phys. Rev. B* **38**, 4547–4556 (1988).
- [18] F. C. Zhang and T. M. Rice. Effective Hamiltonian for the superconducting Cu oxides. *Phys. Rev. B* **37**, 3759–3761 (1988).
- [19] F. C. Zhang and T. M. Rice. Validity of the $t - J$ model. *Phys. Rev. B* **41**, 7243–7246 (1990).
- [20] L. Pietronero, P. Benedetti, E. Cappelluti, C. Grimaldi, S. Strässler, and G. Varelogiannis. Nonadiabatic superconductivity: Electron phonon interaction beyond Migdal's theorem. *J. Low Temp. Phys.* **99**, 3-4, 535–543 (1995).
- [21] J. P. F. LeBlanc, A. E. Antipov, F. Becca, I. W. Bulik, G. K.-L. Chan, C.-M. Chung, Y. Deng, M. Ferrero, T. M. Henderson, C. A. Jiménez-Hoyos, E. Kozik, X.-W. Liu, A. J. Millis, N. V. Prokof'ev, M. Qin, G. E. Scuseria, H. Shi, B. V. Svistunov, L. F. Tocchio, I. S. Tupitsyn, S. R. White, S. Zhang, B.-X. Zheng, Z. Zhu, and E. Gull. Solutions of the two-dimensional Hubbard model: Benchmarks and results from a wide range of numerical algorithms. *Phys. Rev. X* **5**, 041041 (2015).
- [22] M. H. Anderson, J. R. Ensher, M. R. Matthews, C. E. Wieman, and E. A. Cornell. Observation of Bose-Einstein condensation in a dilute atomic vapor. *Science* **269**, 5221, 198–201 (1995).
- [23] K. B. Davis, M. O. Mewes, M. R. Andrews, N. J. van Druten, D. S. Durfee, D. M. Kurn, and W. Ketterle. Bose-Einstein condensation in a gas of sodium atoms. *Phys. Rev. Lett.* **75**, 3969–3973 (1995).
- [24] B. DeMarco and D. Jin. Onset of Fermi degeneracy in a trapped atomic gas. *Science* **285**, 5434, 1703–1706 (1999).
- [25] W. Ketterle and M. W. Zwierlein. Making, probing and understanding ultracold Fermi gases. *La Rivista del Nuovo Cimento*, 5–6, 247–422 (2008).
- [26] W. Ketterle, D. S. Durfee, and D. M. Stamper-Kurn. *Bose-Einstein Condensation in Atomic Gases*, volume 140 of *Proceedings of the International School of Physics "Enrico Fermi"*, chapter Making, probing and understanding Bose-Einstein condensates, pages 67–176. IOS Press, (1999).

- [27] D. Jaksch, C. Bruder, J. I. Cirac, C. W. Gardiner, and P. Zoller. **Cold bosonic atoms in optical lattices**. *Phys. Rev. Lett.* **81**, 3108–3111 (1998).
- [28] C. I. Westbrook, R. N. Watts, C. E. Tanner, S. L. Rolston, W. D. Phillips, P. D. Lett, and P. L. Gould. **Localization of atoms in a three-dimensional standing wave**. *Phys. Rev. Lett.* **65**, 33–36 (1990).
- [29] M. Greiner, O. Mandel, T. Esslinger, T. W. Hänsch, and I. Bloch. **Quantum phase transition from a superfluid to a Mott insulator in a gas of ultracold atoms**. *Nature* **415**, 6867, 39–44 (2002).
- [30] M. Greiner. *Ultracold quantum gases in three-dimensional optical lattice potentials*. PhD thesis, Ludwig-Maximilians-Universität München, (2003).
- [31] I. Bloch. **Ultracold quantum gases in optical lattices**. *Nat. Phys.* **1**, 1, 23–30 (2005).
- [32] M. Lewenstein, A. Sanpera, V. Ahufinger, B. Damski, A. Sen(De), and U. Sen. **Ultracold atomic gases in optical lattices: Mimicking condensed matter physics and beyond**. *Adv. Phys.* **56**, 2, 243–379 (2007).
- [33] I. Bloch, J. Dalibard, and W. Zwerger. **Many-body physics with ultracold gases**. *Rev. Mod. Phys.* **80**, 885–964 (2008).
- [34] W. Hofstetter, J. I. Cirac, P. Zoller, E. Demler, and M. D. Lukin. **High-temperature superfluidity of fermionic atoms in optical lattices**. *Phys. Rev. Lett.* **89**, 220407 (2002).
- [35] M. Köhl, H. Moritz, T. Stöferle, K. Günter, and T. Esslinger. **Fermionic atoms in a three dimensional optical lattice: Observing Fermi surfaces, dynamics, and interactions**. *Phys. Rev. Lett.* **94**, 080403 (2005).
- [36] M. Köhl. **Thermometry of fermionic atoms in an optical lattice**. *Phys. Rev. A* **73**, 031601 (2006).
- [37] T. Stöferle, H. Moritz, K. Günter, M. Köhl, and T. Esslinger. **Molecules of fermionic atoms in an optical lattice**. *Phys. Rev. Lett.* **96**, 030401 (2006).
- [38] T. Rom, T. Best, D. van Oosten, U. Schneider, S. Fölling, B. Paredes, and I. Bloch. **Free fermion antibunching in a degenerate atomic Fermi gas released from an optical lattice**. *Nature* **444**, 7120, 733–736 (2006).
- [39] R. Jördens, N. Strohmaier, K. Günter, H. Moritz, and T. Esslinger. **A Mott insulator of fermionic atoms in an optical lattice**. *Nature* **455**, 7210, 204–207 (2008).
- [40] U. Schneider, L. Hackermüller, S. Will, T. Best, I. Bloch, T. A. Costi, R. W. Helmes, D. Rasch, and A. Rosch. **Metallic and insulating phases of repulsively interacting fermions in a 3D optical lattice**. *Science* **322**, 5907, 1520–1525 (2008).

- [41] T. Esslinger. **Fermi-Hubbard physics with atoms in an optical lattice**. *Annu. Rev. Condens. Matter Phys.* **1**, 1, 129–152 (2010).
- [42] D. Greif, L. Tarruell, T. Uehlinger, R. Jördens, and T. Esslinger. **Probing nearest-neighbor correlations of ultracold fermions in an optical lattice**. *Phys. Rev. Lett.* **106**, 145302 (2011).
- [43] D. Greif, T. Uehlinger, G. Jotzu, L. Tarruell, and T. Esslinger. **Short-range quantum magnetism of ultracold fermions in an optical lattice**. *Science* **340**, 6138, 1307–1310 (2013).
- [44] S. Taie, R. Yamazki, S. Sugawa, and Y. Takahashi. **An SU(6) Mott insulator of an atomic Fermi gas realized by large-spin Pomeranchuk cooling**. *Nat. Phys.* **8**, 825–830 (2012).
- [45] C. Hofrichter, L. Riegger, F. Scazza, M. Höfer, D. R. Fernandes, I. Bloch, and S. Fölling. **Direct probing of the Mott crossover in the SU(n) Fermi-Hubbard model**. *Phys. Rev. X* **6**, 021030 (2016).
- [46] T. Uehlinger, G. Jotzu, M. Messer, D. Greif, W. Hofstetter, U. Bissbort, and T. Esslinger. **Artificial graphene with tunable interactions**. *Phys. Rev. Lett.* **111**, 185307 (2013).
- [47] M. Messer, R. Desbuquois, T. Uehlinger, G. Jotzu, S. Huber, D. Greif, and T. Esslinger. **Exploring competing density order in the ionic Hubbard model with ultracold fermions**. *Phys. Rev. Lett.* **115**, 115303 (2015).
- [48] P. M. Duarte, R. A. Hart, T.-L. Yang, X. Liu, T. Paiva, E. Khatami, R. T. Scalettar, N. Trivedi, and R. G. Hulet. **Compressibility of a fermionic Mott insulator of ultracold atoms**. *Phys. Rev. Lett.* **114**, 070403 (2015).
- [49] R. A. Hart, P. M. Duarte, T.-L. Yang, X. Liu, T. Paiva, E. Khatami, R. T. Scalettar, N. Trivedi, D. A. Huse, and R. G. Hulet. **Observation of antiferromagnetic correlations in the Hubbard model with ultracold atoms**. *Nature* **519**, 7542, 211–214 (2015).
- [50] D. Greif, G. Jotzu, M. Messer, R. Desbuquois, and T. Esslinger. **Formation and dynamics of antiferromagnetic correlations in tunable optical lattices**. *Phys. Rev. Lett.* **115**, 260401 (2015).
- [51] E. Cocchi, L. A. Miller, J. H. Drewes, M. Koschorreck, D. Pertot, F. Brennecke, and M. Köhl. **Equation of state of the two-dimensional Hubbard model**. *Phys. Rev. Lett.* **116**, 175301 (2016).
- [52] J. H. Drewes, E. Cocchi, L. A. Miller, C. F. Chan, D. Pertot, F. Brennecke, and M. Köhl. **Thermodynamics versus local density fluctuations in the metal-Mott-insulator crossover**. *Phys. Rev. Lett.* **117**, 135301 (2016).

- [53] E. Cocchi, L. A. Miller, J. H. Drewes, C. F. Chan, D. Pertot, F. Brennecke, and M. Köhl. **Measuring entropy and short-range correlations in the two-dimensional Hubbard model.** *Phys. Rev. X* **7**, 031025 (2017).
- [54] J. H. Drewes, L. A. Miller, E. Cocchi, C. F. Chan, N. Wurz, M. Gall, D. Pertot, F. Brennecke, and M. Köhl. **Antiferromagnetic correlations in two-dimensional fermionic Mott-insulating and metallic phases.** *Phys. Rev. Lett.* **118**, 170401 (2017).
- [55] N. Wurz, C. F. Chan, M. Gall, J. H. Drewes, E. Cocchi, L. A. Miller, D. Pertot, F. Brennecke, and M. Köhl. **Coherent manipulation of spin correlations in the Hubbard model.** *Phys. Rev. A* **97**, 051602 (2018).
- [56] W. S. Bakr, J. I. Gillen, A. Peng, S. Fölling, and M. Greiner. **A quantum gas microscope for detecting single atoms in a Hubbard-regime optical lattice.** *Nature* **462**, 7269, 74–77 (2009).
- [57] J. F. Sherson, C. Weitenberg, M. Endres, M. Cheneau, I. Bloch, and S. Kuhr. **Single-atom-resolved fluorescence imaging of an atomic Mott insulator.** *Nature* **467**, 7311, 68–72 (2010).
- [58] W. S. Bakr, A. Peng, M. E. Tai, R. Ma, J. Simon, J. I. Gillen, S. Folling, L. Pollet, and M. Greiner. **Probing the superfluid-to-Mott insulator transition at the single-atom level.** *Science* **329**, 5991, 547–550 (2010).
- [59] C. Gross and I. Bloch. **Quantum simulations with ultracold atoms in optical lattices.** *Science* **357**, 6355, 995–1001 (2017).
- [60] M. F. Parsons, F. Huber, A. Mazurenko, C. S. Chiu, W. Setiawan, K. Wooley-Brown, S. Blatt, and M. Greiner. **Site-resolved imaging of fermionic ${}^6\text{Li}$ in an optical lattice.** *Phys. Rev. Lett.* **114**, 213002 (2015).
- [61] A. Omran, M. Boll, T. A. Hilker, K. Kleinlein, G. Salomon, I. Bloch, and C. Gross. **Microscopic observation of Pauli blocking in degenerate fermionic lattice gases.** *Phys. Rev. Lett.* **115**, 263001 (2015).
- [62] E. Haller, J. Hudson, A. Kelly, D. A. Cotta, B. Peaudecerf, G. D. Bruce, and S. Kuhr. **Single-atom imaging of fermions in a quantum-gas microscope.** *Nat. Phys.* **11**, 9, 738–742 (2015).
- [63] L. W. Cheuk, M. A. Nichols, M. Okan, T. Gersdorf, V. V. Ramasesh, W. S. Bakr, T. Lompe, and M. W. Zwierlein. **Quantum-gas microscope for fermionic atoms.** *Phys. Rev. Lett.* **114**, 193001 (2015).
- [64] G. J. A. Edge, R. Anderson, D. Jervis, D. C. McKay, R. Day, S. Trotzky, and J. H. Thywissen. **Imaging and addressing of individual fermionic atoms in an optical lattice.** *Phys. Rev. A* **92**, 063406 (2015).

- [65] D. Greif, M. F. Parsons, A. Mazurenko, C. S. Chiu, S. Blatt, F. Huber, G. Ji, and M. Greiner. **Site-resolved imaging of a fermionic Mott insulator**. *Science* **351**, 6276, 953–957 (2016).
- [66] L. W. Cheuk, M. A. Nichols, K. R. Lawrence, M. Okan, H. Zhang, and M. W. Zwierlein. **Observation of 2D fermionic Mott insulators of ^{40}K with single-site resolution**. *Phys. Rev. Lett.* **116**, 235301 (2016).
- [67] M. Boll, T. A. Hilker, G. Salomon, A. Omran, J. Nespolo, L. Pollet, I. Bloch, and C. Gross. **Spin- and density-resolved microscopy of antiferromagnetic correlations in Fermi-Hubbard chains**. *Science* **353**, 6305, 1257–1260 (2016).
- [68] L. W. Cheuk, M. A. Nichols, K. R. Lawrence, M. Okan, H. Zhang, E. Khatami, N. Trivedi, T. Paiva, M. Rigol, and M. W. Zwierlein. **Observation of spatial charge and spin correlations in the 2D Fermi-Hubbard model**. *Science* **353**, 6305, 1260–1264 (2016).
- [69] M. F. Parsons, A. Mazurenko, C. S. Chiu, G. Ji, D. Greif, and M. Greiner. **Site-resolved measurement of the spin-correlation function in the Fermi-Hubbard model**. *Science* **353**, 6305, 1253–1256 (2016).
- [70] P. T. Brown, D. Mitra, E. Guardado-Sánchez, P. Schauß, S. S. Kondov, E. Khatami, T. Paiva, N. Trivedi, D. A. Huse, and W. S. Bakr. **Spin-imbalance in a 2D Fermi-Hubbard system**. *Science* **357**, 6358, 1385–1388 (2017).
- [71] D. Mitra, P. T. Brown, E. Guardado-Sánchez, S. S. Kondov, T. Devakul, D. A. Huse, P. Schauß, and W. S. Bakr. **Quantum gas microscopy of an attractive Fermi–Hubbard system**. *Nat. Phys.* **14**, 2, 173–177 (2017).
- [72] J. Koepsell, J. Vijayan, P. Sompet, F. Grusdt, T. A. Hilker, E. Demler, G. Salomon, I. Bloch, and C. Gross. **Imaging magnetic polarons in the doped Fermi–Hubbard model**. arXiv:1811.06907v1.
- [73] A. Mazurenko, C. S. Chiu, G. Ji, M. F. Parsons, M. Kanász-Nagy, R. Schmidt, F. Grusdt, E. Demler, D. Greif, and M. Greiner. **A cold-atom Fermi–Hubbard antiferromagnet**. *Nature* **545**, 7655, 462–466 (2017).
- [74] C. S. Chiu, G. Ji, A. Mazurenko, D. Greif, and M. Greiner. **Quantum state engineering of a Hubbard system with ultracold fermions**. *Phys. Rev. Lett.* **120**, 243201 (2018).
- [75] C. S. Chiu, G. Ji, A. Bohrdt, M. Xu, M. Knap, E. Demler, F. Grusdt, M. Greiner, and D. Greif. **String patterns in the doped Hubbard model**. *Science* **365**, 6450, 251–256 (2019).
- [76] T. A. Hilker, G. Salomon, F. Grusdt, A. Omran, M. Boll, E. Demler, I. Bloch, and C. Gross. **Revealing hidden antiferromagnetic correlations in doped Hubbard chains via string correlators**. *Science* **357**, 6350, 484–487 (2017).

- [77] G. Salomon, J. Koepsell, J. Vijayan, T. A. Hilker, J. Nespolo, L. Pollet, I. Bloch, and C. Gross. **Direct observation of incommensurate magnetism in Hubbard chains**. *Nature* **565**, 7737, 56–60 (2018).
- [78] H. Ott, E. de Mirandes, F. Ferlaino, G. Roati, G. Modugno, and M. Inguscio. **Collisionally induced transport in periodic potentials**. *Phys. Rev. Lett.* **92**, 160601 (2004).
- [79] N. Strohmaier, Y. Takasu, K. Günter, R. Jördens, M. Köhl, H. Moritz, and T. Esslinger. **Interaction-controlled transport of an ultracold Fermi gas**. *Phys. Rev. Lett.* **99**, 220601 (2007).
- [80] U. Schneider, L. Hackermüller, J. P. Ronzheimer, S. Will, S. Braun, T. Best, I. Bloch, E. Demler, S. Mandt, D. Rasch, and A. Rosch. **Fermionic transport and out-of-equilibrium dynamics in a homogeneous Hubbard model with ultracold atoms**. *Nat. Phys.* **8**, 3, 213–218 (2012).
- [81] W. Xu, W. McGehee, W. Morong, and B. DeMarco. **Bad-metal relaxation dynamics in a Fermi lattice gas**. arXiv:1606.06669v5.
- [82] P. T. Brown, D. Mitra, E. Guardado-Sánchez, R. Nourafkan, A. Reymbaut, C.-D. Hébert, S. Bergeron, A.-M. S. Tremblay, J. Kokalj, D. A. Huse, P. Schauß, and W. S. Bakr. **Bad metallic transport in a cold atom Fermi-Hubbard system**. *Science* **363**, 6425, 379–382 (2019).
- [83] P. T. Brown, E. Guardado-Sánchez, B. M. Spar, E. W. Huang, T. P. Devereaux, and W. S. Bakr. **Angle-resolved photoemission spectroscopy of a Fermi-Hubbard system**. arXiv:1903.05678v1.
- [84] R. Anderson, F. Wang, P. Xu, V. Venu, S. Trotzky, F. Chevy, and J. H. Thywissen. **Conductivity spectrum of ultracold atoms in an optical lattice**. *Phys. Rev. Lett.* **122**, 153602 (2019).
- [85] M. A. Nichols, L. W. Cheuk, M. Okan, T. R. Hartke, E. Mendez, T. Senthil, E. Khatami, H. Zhang, and M. W. Zwierlein. **Spin transport in a Mott insulator of ultracold fermions**. *Science* **363**, 6425, 383–387 (2019).
- [86] J. Vijayan, P. Sompet, G. Salomon, J. Koepsell, S. Hirthe, A. Bohrdt, F. Grusdt, I. Bloch, and C. Gross. **Time-resolved observation of spin-charge deconfinement in fermionic hubbard chains**. arXiv:1905.13638v1.
- [87] D. Mitra. *Exploring attractively interacting fermions in 2D using a quantum gas microscope*. PhD thesis, Princeton University, (2018).
- [88] F. Serwane. **The setup of a magneto optical trap for the preparation of a mesoscopic degenerate Fermi gas**. Diploma thesis, University of Heidelberg, (2007).

- [89] P. Simon. *Apparatus for the preparation of ultracold Fermi gases*. Diploma thesis, University of Heidelberg, (2010).
- [90] M. F. Parsons. *Probing the Hubbard model with single-site resolution*. PhD thesis, Harvard University, (2016).
- [91] A. Omran. *A microscope for Fermi gases*. PhD thesis, LMU München, (2016).
- [92] J. Dalibard and C. Cohen-Tannoudji. *Laser cooling below the Doppler limit by polarization gradients: simple theoretical models*. *J. Opt. Soc. Am.* **6**, 11, 2023 (1989).
- [93] A. T. Grier, I. Ferrier-Barbut, B. S. Rem, M. Delehaye, L. Khaykovich, F. Chevy, and C. Salomon. *Λ -enhanced sub-Doppler cooling of lithium atoms in D_1 gray molasses*. *Phys. Rev. A* **87**, 063411 (2013).
- [94] G. Zürn, T. Lompe, A. N. Wenz, S. Jochim, P. S. Julienne, and J. M. Hutson. *Precise characterization of ^6Li Feshbach resonances using trap-sideband-resolved rf spectroscopy of weakly bound molecules*. *Phys. Rev. Lett.* **110**, 135301 (2013).
- [95] R. A. Williams, J. D. Pillet, S. Al-Assam, B. Fletcher, M. Shotter, and C. J. Foot. *Dynamic optical lattices: two-dimensional rotating and accordion lattices for ultracold atoms*. *Opt. Express* **16**, 21, 16977 (2008).
- [96] J. L. Ville, T. Bienaimé, R. Saint-Jalm, L. Corman, M. Aidelsburger, L. Chomaz, K. Kleinlein, D. Perconte, S. Nascimbène, J. Dalibard, and J. Beugnon. *Loading and compression of a single two-dimensional Bose gas in an optical accordion*. *Phys. Rev. A* **95**, 013632 (2017).
- [97] G. Morigi, J. Eschner, and C. H. Keitel. *Ground state laser cooling using electromagnetically induced transparency*. *Phys. Rev. Lett.* **85**, 4458–4461 (2000).
- [98] J. Bechhoefer. *Feedback for physicists: A tutorial essay on control*. *Rev. Mod. Phys.* **77**, 783–836 (2005).
- [99] L. Qiu and K. Zhou. *Introduction to Feedback Control*. Prentice Hall, (2010). ISBN 0132353962.
- [100] R. W. P. Drever, J. L. Hall, F. V. Kowalski, J. Hough, G. M. Ford, A. J. Munley, and H. Ward. *Laser phase and frequency stabilization using an optical resonator*. *Appl. Phys. B* **31**, 2, 97–105 (1983).
- [101] W. Lenth. *Optical heterodyne spectroscopy with frequency- and amplitude-modulated semiconductor lasers*. *Opt. Lett.* **8**, 11, 575 (1983).
- [102] J. H. Shirley. *Modulation transfer processes in optical heterodyne saturation spectroscopy*. *Opt. Lett.* **7**, 11, 537 (1982).

- [103] H. N. Rutt. **A heterodyne frequency offset locking technique for pulsed or CW lasers.** *J. Phys. E* **17**, 8, 704–709 (1984).
- [104] U. Schünemann, H. Engler, R. Grimm, M. Weidemüller, and M. Zielonkowski. **Simple scheme for tunable frequency offset locking of two lasers.** *Rev. Sci. Instrum.* **70**, 1, 242–243 (1999).
- [105] K. Kuboki and M. Ohtsu. **Frequency offset locking of AlGaAs semiconductor lasers.** *IEEE J. Quantum Electron.* **23**, 4, 388–394 (1987).
- [106] M. Zhu and J. L. Hall. **Stabilization of optical phase/frequency of a laser system: application to a commercial dye laser with an external stabilizer.** *J. Opt. Soc. Am. B* **10**, 5, 802 (1993).
- [107] T. Stace, A. N. Luiten, and R. P. Kovacich. **Laser offset-frequency locking using a frequency-to-voltage converter.** *Meas. Sci. Technol.* **9**, 9, 1635–1637 (1998).
- [108] G. Ritt, G. Cennini, C. Geckeler, and M. Weitz. **Laser frequency offset locking using a side of filter technique.** *Appl. Phys. B* **79**, 3, 363–365 (2004).
- [109] G. Puentes. **Laser frequency offset locking scheme for high-field imaging of cold atoms.** *Appl. Phys. B* **107**, 1, 11–16 (2012).
- [110] E. Guardado-Sánchez. **A laser system for trapping and cooling of ${}^6\text{Li}$ atoms.** Bachelor's thesis, Massachusetts Institute of Technology, (2015).
- [111] K. Aikawa. **All-optical selective formation of ultracold molecules in the rovibrational ground state.** PhD thesis, The University of Tokyo, (2011). Department of Applied Physics.
- [112] J. Hall, M. Taubman, and J. Ye. **Handbook of Optics Volume II**, chapter Laser Stabilization. Optical Society of America, (1999).
- [113] J. G. Ziegler and N. B. Nichols. **Optimum settings for automatic controllers.** *Transactions of the ASME* **64**, 759–768 (1942).
- [114] B. Carter. **High-speed notch filters.** *Analog Applications Journal* (2006).
- [115] A. Ryou and J. Simon. **Active cancellation of acoustical resonances with an FPGA FIR filter.** *Rev. Sci. Instrum.* **88**, 1, 013101 (2017).
- [116] T. C. Briles, D. C. Yost, A. Cingöz, J. Ye, and T. R. Schibli. **Simple piezoelectric-actuated mirror with 180 kHz servo bandwidth.** *Opt. Express* **18**, 10, 9739 (2010).
- [117] B. Efron and R. Tibshirani. **Bootstrap methods for standard errors, confidence intervals, and other measures of statistical accuracy.** *Stat. Sci.* **1**, 1, 54–75 (1986).

- [118] J. Sebby-Strabley, M. Anderlini, P. S. Jessen, and J. V. Porto. **Lattice of double wells for manipulating pairs of cold atoms**. *Phys. Rev. A* **73**, 033605 (2006).
- [119] G. K. Campbell. *⁸⁷Rubidium Bose-Einstein Condensates in Optical Lattices*. PhD thesis, MIT, (2006).
- [120] M. E. Gehm, K. M. O’Hara, T. A. Savard, and J. E. Thomas. **Dynamics of noise-induced heating in atom traps**. *Phys. Rev. A* **58**, 3914–3921 (1998).
- [121] S. Blatt, A. Mazurenko, M. F. Parsons, C. S. Chiu, F. Huber, and M. Greiner. **Low-noise optical lattices for ultracold ${}^6\text{Li}$** . *Phys. Rev. A* **92**, 021402 (2015).
- [122] F. Etzold. **Laser beam shaping with a digital micromirror device**. Diploma thesis, Johannes Gutenberg-Universität, (2010).
- [123] D. Bellem. **Generation of spatially and temporally varying light potentials in optical lattices**. Diploma thesis, Ludwig-Maximilians-Universität München, (2011).
- [124] P. P. J. Zupancic. **Dynamic holography and beamshaping using digital micromirror devices**. Master’s thesis, Ludwig-Maximilians-Universität, (2013).
- [125] E. C. Cook, P. J. Martin, T. L. Brown-Heft, J. C. Garman, and D. A. Steck. **High passive-stability diode-laser design for use in atomic-physics experiments**. *Rev. Sci. Instrum.* **83**, 4, 043101 (2012).
- [126] R. W. Floyd and L. Steinberg. **An adaptive algorithm for spatial grey scale**. *Proc. Soc. Inf. Displays* **17**, 2, 75–77 (1976).
- [127] K. Hueck, A. Mazurenko, N. Luick, T. Lompe, and H. Moritz. **Suppression of kHz-frequency switching noise in digital micro-mirror devices**. *Rev. Sci. Instrum.* **88**, 1, 016103 (2017).
- [128] K. M. O’Hara, M. E. Gehm, S. R. Granade, S. Bali, and J. E. Thomas. **Stable, strongly attractive, two-state mixture of lithium fermions in an optical trap**. *Phys. Rev. Lett.* **85**, 2092–2095 (2000).
- [129] C. J. Dedman, R. G. Dall, L. J. Byron, and A. G. Truscott. **Active cancellation of stray magnetic fields in a Bose-Einstein condensation experiment**. *Rev. Sci. Instrum.* **78**, 2, 024703 (2007).
- [130] S. Hild, T. Fukuhara, P. Schauß, J. Zeiher, M. Knap, E. Demler, I. Bloch, and C. Gross. **Far-from-equilibrium spin transport in Heisenberg quantum magnets**. *Phys. Rev. Lett.* **113**, 147205 (2014).
- [131] E. Ercolessi, G. Morandi, and P. Pieri. **An introduction to the Hubbard model**. In G. Sierra and M. A. Martín-Delgado, editors, *Strongly Correlated Magnetic and Superconducting Systems*, volume 478 of *Lecture Notes in Physics*, pages 1–32. Springer, (1997). ISBN 978-3-540-49734-9.

- [132] H. Tasaki. **The Hubbard model - An introduction and selected rigorous results.** *J. Phys. Condens. Matter* **10**, 20, 4353–4378 (1998).
- [133] S. A. Jafari. **Introduction to Hubbard model and exact diagonalization.** arXiv:0807.4878v1.
- [134] R. T. Scalettar. *Quantum Materials: Experiments and Theory*, volume 6 of *Modeling and Simulation*, chapter An Introduction to the Hubbard Hamiltonian. Forschungszentrum Jülich, (2016). ISBN 978-3-95806-159-0.
- [135] R. Eder. *The Physics of Correlated Insulators, Metals, and Superconductors*, volume 7 of *Modeling and Simulation*, chapter Introduction to the Hubbard Model. Forschungszentrum Jülich, (2017). ISBN 978-3-95806-224-5.
- [136] M. Rasetti. *The Hubbard Model: Recent Results*, volume 7 of *Series on Advances in Statistical Mechanics*. World Scientific, (1991). ISBN 9810206232.
- [137] A. Montorsi, editor. *The Hubbard Model: A reprint volume*. World Scientific, (1992).
- [138] D. Baeriswyl, D. K. Campbell, J. M. P. Carmelo, F. Guinea, and E. Louis, editors. *The Hubbard Model - Its Physics and Mathematical Physics*. Springer, (1995). ISBN 978-1-4899-1044-8.
- [139] P. Fazekas. *Lecture Notes on Electron Correlation and Magnetism*. World Scientific, (1999).
- [140] F. Gebhard. *The Mott Metal-Insulator Transition*. Springer, (2000).
- [141] E. H. Lieb and F. Y. Wu. **Absence of Mott transition in an exact solution of the short-range, one-band model in one dimension.** *Phys. Rev. Lett.* **20**, 1445–1448 (1968).
- [142] Y. Nagaoka. **Ferromagnetism in a narrow, almost half-filled s band.** *Phys. Rev.* **147**, 392–405 (1966).
- [143] W. Metzner and D. Vollhardt. **Correlated lattice fermions in $d = \infty$ dimensions.** *Phys. Rev. Lett.* **62**, 324–327 (1989).
- [144] E. Müller-Hartmann. **Correlated fermions on a lattice in high dimensions.** *Z. Phys. B* **74**, 4, 507–512 (1989).
- [145] A. Georges and G. Kotliar. **Hubbard model in infinite dimensions.** *Phys. Rev. B* **45**, 12, 6479–6483 (1992).
- [146] A. Georges, G. Kotliar, W. Krauth, and M. J. Rozenberg. **Dynamical mean-field theory of strongly correlated fermion systems and the limit of infinite dimensions.** *Rev. Mod. Phys.* **68**, 1, 13–125 (1996).

- [147] G. Kotliar, S. Y. Savrasov, K. Haule, V. S. Oudovenko, O. Parcollet, and C. A. Marianetti. **Electronic structure calculations with dynamical mean-field theory**. *Rev. Mod. Phys.* **78**, 3, 865–951 (2006).
- [148] H. Kramers. **L'interaction entre les atomes magnétogènes dans un cristal paramagnétique**. *Physica* **1**, 1-6, 182–192 (1934).
- [149] P. W. Anderson. **Antiferromagnetism. Theory of superexchange interaction**. *Phys. Rev.* **79**, 350–356 (1950).
- [150] N. D. Mermin and H. Wagner. **Absence of ferromagnetism or antiferromagnetism in one- or two-dimensional isotropic Heisenberg models**. *Phys. Rev. Lett.* **17**, 1133–1136 (1966).
- [151] P. C. Hohenberg. **Existence of long-range order in one and two dimensions**. *Phys. Rev.* **158**, 383–386 (1967).
- [152] V. L. Berezinsky. **Destruction of long range order in one-dimensional and two-dimensional systems having a continuous symmetry group. I. Classical systems**. *Sov. Phys. JETP* **32**, 493–500 (1971). [Zh. Eksp. Teor. Fiz. 59, 907(1971)].
- [153] J. M. Kosterlitz and D. J. Thouless. **Ordering, metastability and phase transitions in two-dimensional systems**. *J. of Phys. C* **6**, 7, 1181–1203 (1973).
- [154] T. Paiva, R. R. dos Santos, R. T. Scalettar, and P. J. H. Denteneer. **Critical temperature for the two-dimensional attractive Hubbard model**. *Phys. Rev. B* **69**, 184501 (2004).
- [155] N. Bulut. **$d_{x^2-y^2}$ superconductivity and the Hubbard model**. *Adv. Phys.* **51**, 7, 1587–1667 (2002).
- [156] O. Andersen, A. Liechtenstein, O. Jepsen, and F. Paulsen. **LDA energy bands, low-energy hamiltonians, t' , t'' , $t \perp (k)$, and $j \perp$** . *J. Phys. Chem. Solids* **56**, 12, 1573–1591 (1995).
- [157] A. L. Solov'ev and V. M. Dmitriev. **Fluctuation conductivity and pseudogap in YBCO high-temperature superconductors**. *Low Temp. Phys.* **35**, 3, 169–197 (2009).
- [158] M. Gurvitch and A. T. Fiory. **Resistivity of $\text{La}_{1.825}\text{Sr}_{0.175}\text{CuO}_4$ and $\text{YBa}_2\text{Cu}_3\text{O}_7$ to 1100 K: Absence of saturation and its implications**. *Phys. Rev. Lett.* **59**, 12, 1337–1340 (1987).
- [159] A. Schilling, M. Cantoni, J. D. Guo, and H. R. Ott. **Superconductivity above 130 K in the Hg–Ba–Ca–Cu–O system**. *Nature* **363**, 6424, 56–58 (1993).
- [160] H. Shiba. **Thermodynamic properties of the one-dimensional half-filled-band Hubbard model. II: Application of the grand canonical method**. *Prog. Theor. Phys.* **48**, 6, 2171–2186 (1972).

- [161] C. N. Yang. η pairing and off-diagonal long-range order in a Hubbard model. *Phys. Rev. Lett.* **63**, 2144–2147 (1989).
- [162] S. Zhang. Pseudospin symmetry and new collective modes of the Hubbard model. *Phys. Rev. Lett.* **65**, 120–122 (1990).
- [163] E. Mele. Spin analog method for collective modes of the Hubbard model. *Solid State Commun.* **79**, 6, 515–519 (1991).
- [164] E. Demler, S.-C. Zhang, N. Bulut, and D. J. Scalapino. A class of collective excitations of the Hubbard model: η excitation of the negative-U model. *Int. J. Mod. Phys. B* **10**, 17, 2137–2166 (1996).
- [165] C. N. Yang and S. Zhang. SO₄ symmetry in a Hubbard model. *Mod. Phys. Lett. B* **04**, 11, 759–766 (1990).
- [166] M. Pernici. Spin and pairing algebras and ODLRO in a Hubbard model. *EPL* **12**, 1, 75–80 (1990).
- [167] S. Zhang. SO(4) symmetry of the Hubbard model and its experimental consequences. *Int. J. Mod. Phys. B* **5**, 1&2, 153–168 (1991).
- [168] S.-C. Zhang. A unified theory based on SO(5) symmetry of superconductivity and antiferromagnetism. *Science* **275**, 5303, 1089–1096 (1997).
- [169] J. R. Schrieffer and P. A. Wolff. Relation between the Anderson and Kondo Hamiltonians. *Phys. Rev.* **149**, 491–492 (1966).
- [170] J. Jaklič and P. Prelovšek. Finite-temperature properties of doped antiferromagnets. *Adv. Phys.* **49**, 1, 1–92 (2000).
- [171] C. L. Cleveland and R. M. A. Obtaining a Heisenberg Hamiltonian from the Hubbard model. *Am. J. Phys* **44**, 1, 44–46 (1976).
- [172] J. E. Hirsch and D. J. Scalapino. Enhanced superconductivity in quasi two-dimensional systems. *Phys. Rev. Lett.* **56**, 2732–2735 (1986).
- [173] G. C. Wick. The evaluation of the collision matrix. *Phys. Rev.* **80**, 268–272 (1950).
- [174] H. Bruus and K. Flensberg. *Many-body quantum theory in condensed matter physics - An introduction*. Oxford University Press, United States, (2004). ISBN 0198566336.
- [175] P. Coleman. *Introduction to Many-Body Physics*. Cambridge University Press, (2015). ISBN 0521864887.
- [176] E. Perepelitsky, A. Galatas, J. Mravlje, R. Žitko, E. Khatami, B. S. Shastry, and A. Georges. Transport and optical conductivity in the Hubbard model: A high-temperature expansion perspective. *Phys. Rev. B* **94**, 235115 (2016).

- [177] C. N. Varney, C.-R. Lee, Z. J. Bai, S. Chiesa, M. Jarrell, and R. T. Scalettar. **Quantum Monte Carlo study of the two-dimensional fermion Hubbard model.** *Phys. Rev. B* **80**, 075116 (2009).
- [178] A. M. Tremblay. **A refresher in many-body theory.** (2008). <https://www.physique.usherbrooke.ca/tremblay/cours/phy-892/joucence.pdf>.
- [179] R. Kubo. **Statistical-mechanical theory of irreversible processes. I. General theory and simple applications to magnetic and conduction problems.** *J. Phys. Soc. Jpn.* **12**, 6, 570–586 (1957).
- [180] L. P. Kadanoff and P. C. Martin. **Hydrodynamic equations and correlation functions.** *Ann. Phys.* **24**, 419–469 (1963).
- [181] R. Kubo. **The fluctuation-dissipation theorem.** *Rep. Prog. Phys.* **29**, 1, 255 (1966).
- [182] D. Bergeron and A.-M. S. Tremblay. **Algorithms for optimized maximum entropy and diagnostic tools for analytic continuation.** *Phys. Rev. E* **94**, 023303 (2016).
- [183] L. Landau. **Diamagnetismus der metalle.** *Z. Phys.* **64**, 9-10, 629–637 (1930).
- [184] P. Fulde. *Correlated Electrons in Quantum Matter.* World Scientific, (2012). ISBN 9814390925.
- [185] A. Auerbach. *Interacting Electrons and Quantum Magnetism.* Springer, New York, (1990). ISBN 978-1-4612-0869-3.
- [186] R. T. Scalettar, E. Y. Loh, J. E. Gubernatis, A. Moreo, S. R. White, D. J. Scalapino, R. L. Sugar, and E. Dagotto. **Phase diagram of the two-dimensional negative- U Hubbard model.** *Phys. Rev. Lett.* **63**, 218–218 (1989).
- [187] R. Yamamoto, J. Kobayashi, T. Kuno, K. Kato, and Y. Takahashi. **An ytterbium quantum gas microscope with narrow-line laser cooling.** *New J. Phys.* **18**, 2, 023016 (2016).
- [188] A. Koetsier, F. van Liere, and H. T. C. Stoof. **Imbalanced antiferromagnet in an optical lattice.** *Phys. Rev. A* **81**, 2, 023628 (2010).
- [189] B. Wunsch, L. Fritz, N. T. Zinner, E. Manousakis, and E. Demler. **Magnetic structure of an imbalanced Fermi gas in an optical lattice.** *Phys. Rev. A* **81**, 013616 (2010).
- [190] M. Snoek, I. Titvinidze, and W. Hofstetter. **Canted antiferromagnetic order of imbalanced Fermi-Fermi mixtures in optical lattices by dynamical mean-field theory.** *Phys. Rev. B* **83**, 5, 054419 (2011).

- [191] D. Mitra, P. T. Brown, P. Schauß, S. S. Kondov, and W. S. Bakr. Phase separation and pair condensation in a spin-imbalanced 2D Fermi gas. *Phys. Rev. Lett.* **117**, 093601 (2016).
- [192] Z. Idziaszek and T. Calarco. Two atoms in an anisotropic harmonic trap. *Phys. Rev. A* **71**, 050701 (2005).
- [193] R. Blankenbecler, D. J. Scalapino, and R. L. Sugar. Monte Carlo calculations of coupled boson-fermion systems. I. *Phys. Rev. D* **24**, 2278–2286 (1981).
- [194] T. Paiva, R. Scalettar, M. Randeria, and N. Trivedi. Fermions in 2D optical lattices: Temperature and entropy scales for observing antiferromagnetism and superfluidity. *Phys. Rev. Lett.* **104**, 066406 (2010).
- [195] M. Rigol, T. Bryant, and R. R. P. Singh. Numerical linked-cluster approach to quantum lattice models. *Phys. Rev. Lett.* **97**, 187202 (2006).
- [196] E. Khatami and M. Rigol. Thermodynamics of strongly interacting fermions in two-dimensional optical lattices. *Phys. Rev. A* **84**, 053611 (2011).
- [197] E. Batyev and L. Braginskii. Antiferromagnet in a strong magnetic field: analogy with Bose gas. *JETP* **60**, 4, 781–786 (1984).
- [198] V. Zapf, M. Jaime, and C. D. Batista. Bose-Einstein condensation in quantum magnets. *Rev. Mod. Phys.* **86**, 563–614 (2014).
- [199] J. B. Torrance, A. Bezing, A. I. Nazzal, T. C. Huang, S. S. P. Parkin, D. T. Keane, S. J. LaPlaca, P. M. Horn, and G. A. Held. Properties that change as superconductivity disappears at high-doping concentrations in $\text{La}_{2-x}\text{Sr}_x\text{CuO}_4$. *Phys. Rev. B* **40**, 8872–8877 (1989).
- [200] D. C. Johnston. Magnetic susceptibility scaling in $\text{La}_{2-x}\text{Sr}_x\text{CuO}_{4-y}$. *Phys. Rev. Lett.* **62**, 957–960 (1989).
- [201] H. Takagi, T. Ido, S. Ishibashi, M. Uota, S. Uchida, and Y. Tokura. Superconductor-to-nonsuperconductor transition in $(\text{La}_{1-x}\text{Sr}_x)_2\text{CuO}_4$ as investigated by transport and magnetic measurements. *Phys. Rev. B* **40**, 2254–2261 (1989).
- [202] R. L. Glenister and R. R. P. Singh. Temperature and doping dependence of the magnetic susceptibility in the cuprates. *J. Appl. Phys.* **73**, 10, 6329 (1993).
- [203] A. Moreo. Magnetic susceptibility of the two-dimensional Hubbard model. *Phys. Rev. B* **48**, 3380–3382 (1993).
- [204] J. Gukelberger, S. Liener, E. Kozik, L. Pollet, and M. Troyer. Fulde-Ferrell-Larkin-Ovchinnikov pairing as leading instability on the square lattice. *Phys. Rev. B* **94**, 075157 (2016).

- [205] P. Medley, D. M. Weld, H. Miyake, D. E. Pritchard, and W. Ketterle. **Spin gradient demagnetization cooling of ultracold atoms**. *Phys. Rev. Lett.* **106**, 195301 (2011).
- [206] K. v. Klitzing, G. Dorda, and M. Pepper. **New method for high-accuracy determination of the fine-structure constant based on quantized hall resistance**. *Phys. Rev. Lett.* **45**, 494–497 (1980).
- [207] D. C. Tsui, H. L. Stormer, and A. C. Gossard. **Two-dimensional magnetotransport in the extreme quantum limit**. *Phys. Rev. Lett.* **48**, 1559–1562 (1982).
- [208] M. Banerjee, M. Heiblum, V. Umansky, D. E. Feldman, Y. Oreg, and A. Stern. **Observation of half-integer thermal hall conductance**. *Nature* **559**, 7713, 205–210 (2018).
- [209] J. A. N. Bruin, H. Sakai, R. S. Perry, and A. P. Mackenzie. **Similarity of scattering rates in metals showing T -linear resistivity**. *Science* **339**, 6121, 804–807 (2013).
- [210] S. A. Hartnoll. **Theory of universal incoherent metallic transport**. *Nat. Phys.* **11**, 1, 54–61 (2014).
- [211] A. Ioffe and A. Regel. **Non-crystalline amorphous, and liquid electronic semiconductors**. *Prog. Semicond.* **4**, 237–291 (1960).
- [212] N. F. Mott. **Conduction in non-crystalline systems IX. the minimum metallic conductivity**. *Philos. Mag.* **26**, 4, 1015–1026 (1972).
- [213] N. E. Hussey. **Phenomenology of the normal state in-plane transport properties of high- T_c cuprates**. *J. Phys.: Condens. Matter* **20**, 12, 123201 (2008).
- [214] G. R. Stewart. **Non-Fermi-liquid behavior in d- and f-electron metals**. *Rev. Mod. Phys.* **73**, 4, 797–855 (2001).
- [215] O. Gunnarsson, M. Calandra, and J. E. Han. **Colloquium: Saturation of electrical resistivity**. *Rev. Mod. Phys.* **75**, 4, 1085–1099 (2003).
- [216] P. W. Anderson. **Hidden Fermi liquid: The secret of high- T_c cuprates**. *Phys. Rev. B* **78**, 174505 (2008).
- [217] C. M. Varma, P. B. Littlewood, S. Schmitt-Rink, E. Abrahams, and A. E. Ruckenstein. **Phenomenology of the normal state of Cu-O high-temperature superconductors**. *Phys. Rev. Lett.* **63**, 18, 1996–1999 (1989).
- [218] J. Vučičević, D. Tanasković, M. J. Rozenberg, and V. Dobrosavljević. **Bad-metal behavior reveals Mott quantum criticality in doped Hubbard models**. *Phys. Rev. Lett.* **114**, 246402 (2015).
- [219] S. A. Hartnoll, A. Lucas, and S. Sachdev. *Holographic Quantum Matter*. MIT Press, (2018). ISBN 0262038439.

- [220] D. J. Scalapino. *Handbook of High-Temperature Superconductivity*, chapter Numerical Studies of the 2D Hubbard Model, pages 463–493. Springer, (2007).
- [221] J.-P. Brantut, J. Meineke, D. Stadler, S. Krinner, and T. Esslinger. **Conduction of ultracold fermions through a mesoscopic channel**. *Science* **337**, 6098, 1069–1071 (2012).
- [222] G. Valtolina, A. Burchianti, A. Amico, E. Neri, K. Xhani, J. A. Seman, A. Trombettoni, A. Smerzi, M. Zaccanti, M. Inguscio, and G. Roati. **Josephson effect in fermionic superfluids across the BEC-BCS crossover**. *Science* **350**, 6267, 1505–1508 (2015).
- [223] S. Krinner, T. Esslinger, and J.-P. Brantut. **Two-terminal transport measurements with cold atoms**. *J. Phys.: Condens. Matter* **29**, 34, 343003 (2017).
- [224] M. Lebrat, P. Grišins, D. Husmann, S. Häusler, L. Corman, T. Giamarchi, J.-P. Brantut, and T. Esslinger. **Band and correlated insulators of cold fermions in a mesoscopic lattice**. *Phys. Rev. X* **8**, 011053 (2018).
- [225] N. S. Vidhyadhiraja, A. Macridin, C. Šen, M. Jarrell, and M. Ma. **Quantum critical point at finite doping in the 2D Hubbard model: A dynamical cluster quantum Monte Carlo study**. *Phys. Rev. Lett.* **102**, 206407 (2009).
- [226] J. Kokalj. **Bad-metallic behavior of doped Mott insulators**. *Phys. Rev. B* **95**, 041110 (2017).
- [227] S. Mukerjee, V. Oganesyan, and D. Huse. **Statistical theory of transport by strongly interacting lattice fermions**. *Phys. Rev. B* **73**, 035113 (2006).
- [228] E. Leviatan, F. Pollmann, J. H. Bardarson, D. A. Huse, and E. Altman. **Quantum thermalization dynamics with matrix-product states**. arXiv:1702.08894v2.
- [229] G. Pálsson and G. Kotliar. **Thermoelectric response near the density driven Mott transition**. *Phys. Rev. Lett.* **80**, 21, 4775–4778 (1998).
- [230] B. S. Shastry. **Electrothermal transport coefficients at finite frequencies**. *Rep. Prog. Phys.* **72**, 1, 016501 (2009).
- [231] M. R. Peterson and B. S. Shastry. **Kelvin formula for thermopower**. *Phys. Rev. B* **82**, 195105 (2010).
- [232] L.-F. Arsenault, B. S. Shastry, P. Sémond, and A.-M. S. Tremblay. **Entropy, frustration, and large thermopower of doped Mott insulators on the fcc lattice**. *Phys. Rev. B* **87**, 035126 (2013).
- [233] J. Kokalj and R. H. McKenzie. **Enhancement of thermal expansion of organic charge-transfer salts by strong electronic correlations**. *Phys. Rev. B* **91**, 205121 (2015).

- [234] A. F. Ho, M. A. Cazalilla, and T. Giamarchi. **Quantum simulation of the Hubbard model: The attractive route.** *Phys. Rev. A* **79**, 033620 (2009).
- [235] X. Deng, J. Mravlje, R. Žitko, M. Ferrero, G. Kotliar, and A. Georges. **How bad metals turn good: Spectroscopic signatures of resilient quasiparticles.** *Phys. Rev. Lett.* **110**, 086401 (2013).
- [236] W. Xu, K. Haule, and G. Kotliar. **Hidden Fermi liquid, scattering rate saturation, and Nernst effect: A dynamical mean-field theory perspective.** *Phys. Rev. Lett.* **111**, 036401 (2013).
- [237] J. Vučičević, J. Kokalj, R. Žitko, N. Wentzell, D. Tanasković, and J. Mravlje. **Conductivity in the square lattice Hubbard model at high temperatures: Importance of vertex corrections.** *Phys. Rev. Lett.* **123**, 036601 (2019).
- [238] E. W. Huang, R. Sheppard, B. Moritz, and T. P. Devereaux. **Strange metallicity in the doped Hubbard model.** arXiv:1806.08346v2.
- [239] J. T. Stewart, J. P. Gaebler, and D. S. Jin. **Using photoemission spectroscopy to probe a strongly interacting Fermi gas.** *Nature* **454**, 7205, 744–747 (2008).
- [240] A. Damascelli, Z. Hussain, and Z.-X. Shen. **Angle-resolved photoemission studies of the cuprate superconductors.** *Rev. Mod. Phys.* **75**, 2, 473–541 (2003).
- [241] E. J. Mueller. **Review of pseudogaps in strongly interacting Fermi gases.** *Rep. Prog. Phys.* **80**, 10, 104401 (2017).
- [242] Q. Chen, Y. He, C.-C. Chien, and K. Levin. **Theory of radio frequency spectroscopy experiments in ultracold Fermi gases and their relation to photoemission in the cuprates.** *Rep. Prog. Phys.* **72**, 12, 122501 (2009).
- [243] P. Törmä. **Physics of ultracold Fermi gases revealed by spectroscopies.** *Phys. Scr.* **91**, 4, 043006 (2016).
- [244] I. M. Vishik, W. S. Lee, R.-H. He, M. Hashimoto, Z. Hussain, T. P. Devereaux, and Z.-X. Shen. **ARPES studies of cuprate fermiology: Superconductivity, pseudogap and quasiparticle dynamics.** *New J. Phys.* **12**, 10, 105008 (2010).
- [245] M. Z. Hasan and C. L. Kane. **Colloquium: Topological insulators.** *Rev. Mod. Phys.* **82**, 3045–3067 (2010).
- [246] C. Chin, M. Bartenstein, A. Altmeyer, S. Riedl, S. Jochim, and G. R. Denschlag, J. Hecker. **Observation of the pairing gap in a strongly interacting Fermi gas.** *Science* **305**, 5687, 1128–1130 (2004).
- [247] C. H. Schunck, Y. Shin, A. Schirotzek, M. W. Zwierlein, and W. Ketterle. **Pairing without superfluidity: The ground state of an imbalanced Fermi mixture.** *Science* **316**, 5826, 867–870 (2007).

- [248] J. P. Gaebler, J. T. Stewart, T. E. Drake, D. S. Jin, A. Perali, P. Pieri, and G. C. Strinati. **Observation of pseudogap behaviour in a strongly interacting Fermi gas**. *Nat. Phys.* **6**, 8, 569–573 (2010).
- [249] S. Nascimbène, N. Navon, S. Pilati, F. Chevy, S. Giorgini, A. Georges, and C. Salomon. **Fermi-liquid behavior of the normal phase of a strongly interacting gas of cold atoms**. *Phys. Rev. Lett.* **106**, 215303 (2011).
- [250] M. Feld, B. Fröhlich, E. Vogt, M. Koschorreck, and M. Köhl. **Observation of a pairing pseudogap in a two-dimensional Fermi gas**. *Nature* **480**, 7375, 75–78 (2011).
- [251] A. T. Sommer, L. W. Cheuk, M. J. H. Ku, W. S. Bakr, and M. W. Zwierlein. **Evolution of fermion pairing from three to two dimensions**. *Phys. Rev. Lett.* **108**, 045302 (2012).
- [252] P. A. Murthy, M. Neidig, R. Klemt, L. Bayha, I. Boettcher, T. Enss, M. Holten, G. Zürn, P. M. Preiss, and S. Jochim. **High-temperature pairing in a strongly interacting two-dimensional Fermi gas**. *Science* **359**, 6374, 452–455 (2017).
- [253] T.-L. Dao, A. Georges, J. Dalibard, C. Salomon, and I. Carusotto. **Measuring the one-particle excitations of ultracold fermionic atoms by stimulated Raman spectroscopy**. *Phys. Rev. Lett.* **98**, 240402 (2007).
- [254] Y. Sagi, T. E. Drake, R. Paudel, R. Chapurin, and D. S. Jin. **Breakdown of the Fermi liquid description for strongly interacting fermions**. *Phys. Rev. Lett.* **114**, 075301 (2015).
- [255] B. Fröhlich, M. Feld, E. Vogt, M. Koschorreck, M. Köhl, C. Berthod, and T. Giamarchi. **Two-dimensional Fermi liquid with attractive interactions**. *Phys. Rev. Lett.* **109**, 130403 (2012).
- [256] W. Schneider and M. Randeria. **Universal short-distance structure of the single-particle spectral function of dilute Fermi gases**. *Phys. Rev. A* **81**, 021601 (2010).
- [257] V. M. Loktev, R. M. Quick, and S. G. Sharapov. **Phase fluctuations and pseudogap phenomena**. *Phys. Rep.* **349**, 1, 1–123 (2001).
- [258] A. Perali, P. Pieri, G. C. Strinati, and C. Castellani. **Pseudogap and spectral function from superconducting fluctuations to the bosonic limit**. *Phys. Rev. B* **66**, 024510 (2002).
- [259] A. Perali, F. Palestini, P. Pieri, G. C. Strinati, J. T. Stewart, J. P. Gaebler, T. E. Drake, and D. S. Jin. **Evolution of the normal state of a strongly interacting Fermi gas from a pseudogap phase to a molecular Bose gas**. *Phys. Rev. Lett.* **106**, 060402 (2011).

- [260] P. A. Murthy, D. Kedar, T. Lompe, M. Neidig, M. G. Ries, A. N. Wenz, G. Zürn, and S. Jochim. **Matter-wave Fourier optics with a strongly interacting two-dimensional Fermi gas.** *Phys. Rev. A* **90**, 043611 (2014).
- [261] A. Bohrdt, D. Greif, E. Demler, M. Knap, and F. Grusdt. **Angle-resolved photoemission spectroscopy with quantum gas microscopes.** *Phys. Rev. B* **97**, 125117 (2018).
- [262] L. Hackermüller, U. Schneider, M. Moreno-Cardoner, T. Kitagawa, T. Best, S. Will, E. Demler, E. Altman, I. Bloch, and B. Paredes. **Anomalous Expansion of Attractively Interacting Fermionic Atoms in an Optical Lattice.** *Science* **327**, 5973, 1621–1624 (2010).
- [263] J. M. Singer, M. H. Pedersen, T. Schneider, H. Beck, and H.-G. Matuttis. **From BCS-like superconductivity to condensation of local pairs: A numerical study of the attractive Hubbard model.** *Phys. Rev. B* **54**, 1286–1301 (1996).
- [264] J. M. Singer, T. Schneider, and M. H. Pedersen. **On the phase diagram of the attractive Hubbard model: Crossover and quantum critical phenomena.** *Eur. Phys. J. B* **2**, 1, 17–30 (1998).
- [265] J. M. Singer, T. Schneider, and P. F. Meier. **Spectral properties of the attractive Hubbard model.** *Eur. Phys. J. B* **7**, 1, 37–51 (1999).
- [266] D. McKay, M. White, and B. DeMarco. **Lattice thermodynamics for ultracold atoms.** *Phys. Rev. A* **79**, 063605 (2009).
- [267] P. Törmä and P. Zoller. **Laser probing of atomic cooper pairs.** *Phys. Rev. Lett.* **85**, 487–490 (2000).
- [268] F. Grusdt, M. Kánavsz-Nagy, A. Bohrdt, C. S. Chiu, G. Ji, M. Greiner, D. Greif, and E. Demler. **Parton theory of magnetic polarons: Mesonic resonances and signatures in dynamics.** *Phys. Rev. X* **8**, 011046 (2018).
- [269] D. A. Abanin, E. Altman, I. Bloch, and M. Serbyn. **Colloquium: Many-body localization, thermalization, and entanglement.** *Rev. Mod. Phys.* **91**, 021001 (2019).
- [270] F. Görg, M. Messer, K. Sandholzer, G. Jotzu, R. Desbuquois, and T. Esslinger. **Enhancement and sign change of magnetic correlations in a driven quantum many-body system.** *Nature* **553**, 7689, 481–485 (2018).
- [271] Y.-J. Lin, R. L. Compton, K. Jiménez-García, J. V. Porto, and I. B. Spielman. **Synthetic magnetic fields for ultracold neutral atoms.** *Nature* **462**, 7273, 628–632 (2009).
- [272] M. Aidelsburger, M. Atala, S. Nascimbène, S. Trotzky, Y.-A. Chen, and I. Bloch. **Experimental realization of strong effective magnetic fields in an optical lattice.** *Phys. Rev. Lett.* **107**, 255301 (2011).

- [273] J. Struck, C. Ölschläger, M. Weinberg, P. Hauke, J. Simonet, A. Eckardt, M. Lewenstein, K. Sengstock, and P. Windpassinger. Tunable gauge potential for neutral and spinless particles in driven optical lattices. *Phys. Rev. Lett.* **108**, 225304 (2012).
- [274] M. E. Gehm. *Preparation of an Optically-Trapped Degenerate Fermi Gas of ^6Li : Finding the Route to Degeneracy*. PhD thesis, Duke University, (2003).
- [275] Z. Chen and A. Z. Msezane. Reduced dipole matrix element for photoionization calculation of two open-shell atoms or ions. *Phys. Rev. A* **68**, 054701 (2003).
- [276] C. Chin, R. Grimm, P. Julienne, and E. Tiesinga. Feshbach resonances in ultracold gases. *Rev. Mod. Phys.* **82**, 1225–1286 (2010).
- [277] E. R. I. Abraham. *Photoassociative Spectroscopy of Collisions between Ultracold Lithium Atoms*. PhD thesis, Rice University, (1996).
- [278] E. R. I. Abraham, W. I. McAlexander, J. M. Gerton, R. G. Hulet, R. Côté, and A. Dalgarno. Singlet s-wave scattering lengths of ^6Li and ^7Li . *Phys. Rev. A* **53**, R3713–R3715 (1996).
- [279] E. R. I. Abraham, W. I. McAlexander, H. T. C. Stoof, and R. G. Hulet. Hyperfine structure in photoassociative spectra of $^6\text{Li}_2$ and $^7\text{Li}_2$. *Phys. Rev. A* **53**, 3092–3097 (1996).
- [280] E. R. I. Abraham, W. I. McAlexander, J. M. Gerton, R. G. Hulet, R. Côté, and A. Dalgarno. Triplet s-wave resonance in ^6Li collisions and scattering lengths of ^6Li and ^7Li . *Phys. Rev. A* **55**, R3299–R3302 (1997).
- [281] M. Houbiers, H. T. C. Stoof, W. I. McAlexander, and R. G. Hulet. Elastic and inelastic collisions of ^6Li atoms in magnetic and optical traps. *Phys. Rev. A* **57**, R1497–R1500 (1998).
- [282] J. Zhang, E. G. M. van Kempen, T. Bourdel, L. Khaykovich, J. Cubizolles, F. Chevy, M. Teichmann, L. Tarruell, S. J. J. M. F. Kokkelmans, and C. Salomon. p-wave Feshbach resonances of ultracold ^6Li . *Phys. Rev. A* **70**, 030702 (2004).
- [283] K. M. O’Hara. *Optical Trapping and Evaporative Cooling of Fermionic Atoms*. PhD thesis, Duke University, (2000).
- [284] K. M. O’Hara, S. L. Hemmer, S. R. Granade, M. E. Gehm, J. E. Thomas, V. Venturi, E. Tiesinga, and C. J. Williams. Measurement of the zero crossing in a Feshbach resonance of fermionic ^6Li . *Phys. Rev. A* **66**, 041401 (2002).
- [285] K. Dieckmann, C. A. Stan, S. Gupta, Z. Hadzibabic, C. H. Schunck, and W. Ketterle. Decay of an ultracold fermionic lithium gas near a Feshbach resonance. *Phys. Rev. Lett.* **89**, 203201 (2002).

- [286] M. Bartenstein, A. Altmeyer, S. Riedl, R. Geursen, S. Jochim, C. Chin, J. H. Denschlag, R. Grimm, A. Simoni, E. Tiesinga, C. J. Williams, and P. S. Julienne. Precise determination of ${}^6\text{Li}$ cold collision parameters by radio-frequency spectroscopy on weakly bound molecules. *Phys. Rev. Lett.* **94**, 103201 (2005).
- [287] C. H. Schunck, M. W. Zwierlein, C. A. Stan, S. M. F. Raupach, W. Ketterle, A. Simoni, E. Tiesinga, C. J. Williams, and P. S. Julienne. Feshbach resonances in fermionic ${}^6\text{Li}$. *Phys. Rev. A* **71**, 045601 (2005).
- [288] W. I. McAlexander. *Collisional Interactions in an Ultracold Lithium Gas*. PhD thesis, Rice University, (2000).
- [289] N. W. Ashcroft and N. Mermin. *Solid State Physics*. Cengage Learning, Inc, (1976). ISBN 0030839939.
- [290] M. P. Marder. *Condensed Matter Physics*. John Wiley & Sons, (2010). ISBN 0470617985.
- [291] K. Sun, W. V. Liu, A. Hemmerich, and S. Das Sarma. Topological semimetal in a fermionic optical lattice. *Nat. Phys.* **8**, 1, 67–70 (2011).
- [292] W. Kohn. Analytic properties of Bloch waves and Wannier functions. *Phys. Rev.* **115**, 809–821 (1959).
- [293] T. Busch, B.-G. Englert, K. Rzażewski, and M. Wilkens. Two cold atoms in a harmonic trap. *Found. Phys.* **28**, 4, 549–559 (1998).
- [294] H. Yoshizawa, S. Mitsuda, H. Kitazawa, and K. Katsumata. An incommensurate magnetic diffuse scattering in superconducting $\text{La}_{1.92}\text{Sr}_{0.08}\text{CuO}_{4-\delta}$. *J. Phys. Soc. Jpn.* **57**, 11, 3686–3689 (1988).
- [295] R. J. Birgeneau, Y. Endoh, K. Kakurai, Y. Hidaka, T. Murakami, M. A. Kastner, T. R. Thurston, G. Shirane, and K. Yamada. Static and dynamic spin fluctuations in superconducting $\text{La}_{2-x}\text{Sr}_x\text{CuO}_4$. *Phys. Rev. B* **39**, 2868–2871 (1989).
- [296] M. A. Kastner, R. J. Birgeneau, G. Shirane, and Y. Endoh. Magnetic, transport, and optical properties of monolayer copper oxides. *Rev. Mod. Phys.* **70**, 897–928 (1998).